UNIVERSITÉ DE STRASBOURG

ÉCOLE DOCTORALE physique et chimie-physique (ED 182)

Institut de Physique et Chimie des Matériaux de Strasbourg

THÈSE présentée par :

Aditi Raman MOGHE

soutenue le : **22 mai 2024**

pour obtenir le grade de : **Docteur de l'université de Strasbourg**

Discipline/ Spécialité : Physique/Physique de la matière condensée

Interfacial coupling and electrical control of light-matter interactions in van der Waals heterostructures made of two-dimensional semiconductors and graphene

THÈSE dirigée par :

[M. BERCIAUD Stéphane]	Professeur, Université de Strasbourg

RAPPORTEURS :

[Mme. MARTY Laëtitia]	Chargée de recherches, Institut Néel, CNRS
[Mme. WURSTBAUER Ursula]	Professeur, Universität Münster

AUTRES MEMBRES DU JURY :

[M. SHUKLA Abhay]	Professeur, IMPMC, Sorbonne Université
[M. WEINMANN Dietmar]	Directeur de recherches, IPCMS, Université de Strasbourg
[M. NEUMAN Tomáš]	Scientifique sénior, FZU-CAS

Contents

Acknowledgements

This PhD thesis is a culmination of work of three and a half years at IPCMS, which was possible with the help of many people in various small and big ways.

I would like to thank the jury reporters Laëtitia Marty and Ursula Wurstbauer for reviewing my manuscript in detail as well as Abhay Shukla, Dietmar Weinmann and Tomáš Neuman for being examiners in my jury.

I thank my thesis supervisor Stéphane Berciaud for giving me this opportunity and always being there to guide me throughout this journey. Dear Stéphane, I consider myself very lucky to have had a considerate, kind and optimistic supervisor like you! I really appreciate that you motivated me through the difficult times and always had confidence in me and my projects. After working under you for three and a half years, I have really become much more confident in my own abilities when it comes to research. Thank you very much!

As I started my PhD, I met Arnaud Gloppe, whose enthusiasm, helpfulness and efficient working ways motivated me a lot. Dear Arnaud, it was great to work with you and get feedback from someone like you who is experienced in research and yet not too far from the student days.

During the three and a half years in the research group, I had the pleasure to interact with many incredible people. A huge thanks goes to Loïc Moczko for teaching me about handling many things in the lab as well as for having open-minded fruitful discussions (scientific and non-scientific) with me. During the first two months of my PhD, you were one of my few friends in a radius of thousands of kilometers and I appreciate you for listening to my many stories. A few months later, Joanna Wolff joined the group and I had the pleasure of having her company throughout the rest of my PhD. I learned a lot about French culture from you and I hope that I have imparted a considerable amount of knowledge about India to you! I would like to thank Etienne Lorchat for teaching me how to fabricate samples and also for the good time we shared. I thank Luis Parra López and Léo Colombier for helping me in the labs. I really appreciated the few months I spent with Jules Maistret, Simón Rincón and Satyam Sahu. I also thank the newer kids in the group: Quentin Fenoy and Elise Jouaiti for motivating me during my thesis writing phase. Dear Elise, I will never forget looking at your smiling face during my thesis presentation!

I thank Michelangelo Romeo for all the many ways in which he has contributed to my measurements. I would like to thank STnano personnels Hicham Majjad, Sabine Siegwald and in particularly, Romain Bernard, who has spent hours for the difficult wire bonding on my samples. I also appretiate the help given by Tom Ferté, Fabrice Scheurer, Fabien

Chevrier and Virginie Speisser. I would like to express my gratitude towards Catherine Bonnin for administrative support. I wholeheartedly thank all people at IPCMS who have helped me in innumerable ways.

For part of the measurements in my thesis work, a big thanks goes to Delphine Lagarde, Maxime Mauguet, Xavier Marie and Cedric Robert at LPCNO. I also want to thank all my collaborators for giving me a chance to be involved in interesting projects.

The time at IPCMS was very enjoyable, all thanks to the many amazing and interesting people I had met: Aleena, Jinu, Arvind, Krishna, Samiul, Ulrich, Mohamed Soliman, Satakshi, Ankita (my dear senior from IISERB), José, Nivedita, Davy, Quentin, Louis, Suvidya, Saeel and many more. I thank Deeksha Gupta for feeding me snacks throughout my thesis writing time! I would also like to thank Guillaume Weick, Jean-François Dayen, David Hagenmuller, Yves Henry and all the members of the team of Guillaume Schull (including Anna, Alex, Song, Katharina, Kirill) that I have met during my time at IPCMS for enriching my doctoral experience.

I would like to express my gratitude to Surajit Saha and the members of his research team at IISER Bhopal for introducing me to the world of two dimensional materials during my Master's thesis project and motivating me towards further research in it.

I thank my high school teachers, Madam Vasundhara Sathe and Madam Sangeeta Chaudhary, for encouraging me to pursue research in science.

Reaching the level to be a PhD student would have been very difficult without the support of all of my friends from IISER Bhopal, in particular, Aditi Maheshwari, Mamta Yadav, Jatin Khaimani and Ajinkya Khandare. The last of whom is also a part of my amazing school friends circle that includes Himanshu Aglave and Ambarish Mangrulkar.

A big thanks goes to Ramakant and Deepali Bagmare and their daughters Payal and Sakshi for all the support and motivation they have given me. I would like to express my gratitude to all the members of Bondre family for helping me in many small and big ways since my school days. I thank my father's friends, late Shyam Indoliya and Arvind Yadav and his family.

I wholeheartedly thank my cousins (or, as I usually refer to them by affection, my brothers and sisters): Apurva, Atharva, Gauri, Hrishikesh, Kalyani, Ketan and Renuka as well as my Aunts and Uncles: Rajendra and Sandhya Joshi, Madhavi and Balakrishna Dande and Kishori and Shrikant Naik for always encouraging me in my studies since my childhood. I wouldn't be where I am without the support from each one of you.

I would like to thank Alexandre Gris from the bottom of my heart. This journey of PhD would have been much more difficult and much less enjoyable if you had not been there by my side.

I cannot truly describe in words how grateful I am to my parents Jyoti Moghe and Raman Moghe. Aai and baba, I couldn't have reached anywhere in my life without your continuous encouragement, support and blessings. You two have made countless sacrifices for my education, I hope me receiving the highest degree possible makes you proud. This thesis is dedicated to you.

From arriving in France during a pandemic, having a lockdown from the next day after my arrival in Strasbourg and subsequent curfews, being ’administratively special’, visiting home after a gap of two years and many twists and turns in the research projects, this journey has been quite challenging; but very special and cherished at the same time because of the interesting projects and the opportunity to perform my research, meeting many amazing people, being able to be part of a great research team as well as an excellent scientific community, learning about a new country and adjusting my life in it to a point that it became a home away from home, learning many new things about life and myself and being able to fulfill some of my dreams!

This has been an incredible adventure!

Introduction

Atomically thin two-dimensional (2D) materials can be isolated from their bulk crystals by virtue of these individual layers being held together with weak van der Waals forces and strong in-plane covalent bonds. The isolation of atomically thin graphene layer, which is a semimetal, from graphite by [1] was the advent of discovering a wide range of 2D materials with different properties ranging from semiconductors like transition metal dichalcogenides, insulators like hexagonal Boron Nitride, metals, superconductors as well as magnetic materials, with the properties of thinned down 2D materials being different than their bulk counterparts. In order to isolate 2D materials from bulk crystals, many techniques including mechanical exfoliation, chemical vapour deposition, molecular beam epitaxy and liquid assisted exfoliation have been explored and utilized.

Beyond the isolation of these 2D materials, due to the absence of the dangling bonds on their surfaces, these 2D layers can be stacked on top of each other in any desired sequence to fabricate van der Waals hetrostructures (vdWH) [2]. During the fabrication of vdWH, the self cleaning mechanism [3] makes the contaminants/impurities get grouped together which provides atomically flat clean interfaces between the 2D materials. Because of this, even if some ripples or bubbles get created in the vdWH, one can easily find clean areas to study in the vdWH. The wide range of known 2D materials means that an enormous number of different vdWH are possible to be made. The band alignment between 2D materials in vdWH depends upon their band offsets with respect to one another, making it possible to obtain various types of heterojunctions depending upon the bandgaps of chosen 2D materials. Moreover, the lattice mismatch between the 2D materials involved in vdWH can give rise to Moiré patterns for specific twist angles.

The 2D materials are very sensitive to their surroundings and the properties of a vdWH depend upon the properties of all the individual materials it consists of as well as the interactions and interfacial coupling between these materials. Thus, the properties of 2D materials can be tailored by the materials attached to them in the vdWH. Moreover, the adsorbates, defects and other irregularities can strongly affect the properties of vdWH. In this two-dimensional system, the interactions between materials in this near-field are different compared to interactions between three-dimensional bulk materials, making the vdWH a very intriguing system to study the physics in 2D limit.

This thesis aims to understand the interlayer coupling between vdWH consisting of graphene and transition metal dichalcogenides and then, achieving the control of light emission from it by tuning its electrical properties. The electrical and optical properties of graphene can be controlled by tuning the charge density in it. The phonon dispersion in graphene and the inelastic scattering of photons with these phonons (i.e. Raman scattering) has been studied well over the past decades. This makes it possible to accurately probe the effects of external parameters like charge doping, strain, temperature, dielectric screening and more on the graphene layer. The electronic structure of monolayer graphene is quite unique as its bandgap is zero.

On the other hand, transition metal dichalcogenides (TMDs) have a direct bandgap in the monolayer limit. Thus, they provide intense light emission and their emission properties are dominated by rich exciton physics with the excitons in TMDs being stable even at room temperature. Because of this, TMDs are used as efficient building blocks in optoelectronic applications like photovoltaics [4] and light-emitting diodes [5].

When a monolayer TMD is well coupled to a graphene layer, it is interesting to wonder what processes can happen between these two layers and their dependence upon different external conditions like illumination, temperature and charge doping. The vdWH made up of TMD and graphene is an interesting system for both fundamental research (see chapter 1, which also describes the relevant properties for graphene, TMD and their vdWH) as well as in applied sciences such as opto-electronics, spin- and valley-tronics [6, 7] and photodetection [8].

In this work, the vdWH made up of graphene and monolayer $MoSe_2$ (a type of TMD) is used as a building block (schematic of vdWH is given in figure 1) as it is an ideal system to study the interlayer coupling and different near-field transfer processes occurring between the layers in the 2D limit. Harnessing these transfer mechanisms, we tune the charge carrier density in this vdWH and thereby control their light emission.

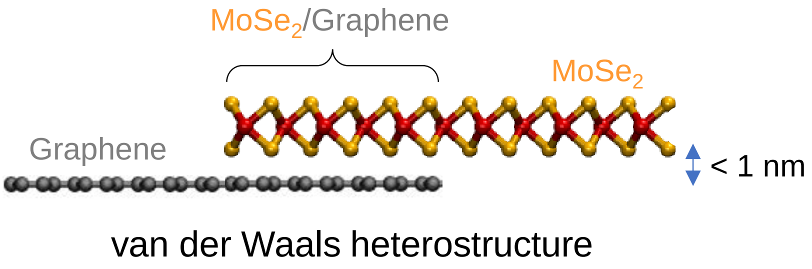

Figure 1: Schematic of vdWH made up of monolayer graphene and monolayer $MoSe_2$, having three different regions of interest: $MoSe_2$, $MoSe_2$/graphene and graphene.

As detailed in this thesis, the question of which type of transfer processes occur and dominate between graphene and TMDs has been an ongoing field of active research through different measurement techniques (see chapter 3). As these transfer mechanisms between 2D materials are dependent upon the distance between layers, the extent and efficiency of these processes can be studied through exploiting their distance dependence. In this work, we have approached this question by using the staircase-like $MoSe_2$/n-layered graphene heterostructures to explore the distance dependence of transfer processes using the changing thickness of graphene. The coupling of graphene to TMD causes the emission yield of TMD to be strongly reduced and a filtering of charged exciton which are results of transfer mechanisms between them. Although these effects of coupling of graphene to TMD on its excitonic properties has been observed [9], the mechanisms behind them remain hidden. This study is done to further understand the charge and energy transfer mechanisms between graphene and TMD and the extent to which they can occur. As long-range Forster energy transfer is actively being researched for applications in light-harvesting devices [10] and short-range charge transfer mechanisms are at the heart of photodetectors [11], studying these processes is very important to progress towards their applications.

After studying the interlayer transfer mechanisms, we have worked on controlling the interlayer interactions between $MoSe_2$ and graphene and thereby achieving electrical control of light emission from this vdWH (see chapter 4). This study is done to fundamentally understand and estimate the band offsets between graphene and $MoSe_2$. Controlling light-matter interactions is very intriguing from the viewpoint of optoelectronics. This requires tuning the charge carrier density in $MoSe_2$/graphene and our approach to do this is by externally doping graphene with charges by applying a gate voltage and then charge doping the $MoSe_2$ layer through the charge doping in graphene. Graphene layers are often used as electrodes in charge tunable devices, but their photoresponse where the graphene layer is coupled to TMD is not studied thoroughly yet. These 2D materials are very sensitive to external effects like charge doping, which causes changes in the Fermi level in these materials. In this work, we have focused on shifting the Fermi level in graphene significantly such that charges can be possibly injected from graphene into $MoSe_2$, making the voltage dependence of the region with $MoSe_2$ covering graphene very intriguing to study, which has largely remained unexplored so far. Moreover, most of the voltage dependent research on TMDs done over the years were performed at cryogenic temperatures; however, in this thesis, we have worked primarily at room temperature as well as at cryogenic temperatures. Experimentally, this shift in the Fermi level in graphene by hundreds of meV requires a charge density of $\approx 10^{14}$ cm^{-2} and is very hard to reach.

In this work, this high charge density is achieved by using ionic glass LaF_3 as a gate dielectric and substrate. As the leakage current in LaF_3 is high at room temperature (it could reach a few hundred nA), the experiments are quite challenging to perform, but samples on LaF_3 substrate are known to reach charge density of $\approx 10^{14}$ cm^{-2}. The changes caused because of external charge doping can be probed through observing excitonic species in $MoSe_2$ by photoluminescence (PL) spectroscopy and peaks in Raman spectra of graphene arising from vibrational phonon modes. Raman spectroscopy is a very accurate probe to determine the charge density in graphene and we have used it as a doping meter for the vdWH. The robustness of charge doping methodology in graphene layers on LaF_3 substrate at room temperature was also explored by checking its reversibility, reproducibility and the influence of defects on it via Raman spectroscopy. In this thesis, we have studied the effects of charge doping on graphene, $MoSe_2$ as well as $MoSe_2$/graphene and achieved the electrical control of light-matter interactions in this vdWH which also reveals details about the band alignment between these two layers.

This project started in November 2020 with the objective of advancing the research on interlayer transfer mechanisms between 2D materials that had been started in 2017 in my host team at IPCMS, by exploring the distance dependence of these mechanisms with $MoSe_2$/n-layered graphene heterostructures tuned in a microcavity-like structure that removes the problems about resolution caused because of instrument response function observed during TRPL measurements. With the understanding of the interlayer interactions, the natural next step was to attain control over them. Although the effects of charge doping in graphene as well as in some of the TMD monolayers has been studied extensively; the tuning of light emission by controlling charge density in TMD/graphene heterostructures is relatively unexplored, which gave us the motivation to investigate this in the case of $MoSe_2$/graphene under a wide range of charge density variation to gain understanding about the band alignment between these layers. For this purpose, a methodology for fabrication of electrically gated heterostructures on LaF_3 and performing applied gate voltage dependent optical spectroscopy measurements on them has been developed. A comprehensive set of voltage dependent measurements could be performed with this methodology on multiple samples to observe consistent trends.

Manuscript organization

This manuscript is divided into four chapters.

Chapter 1 is dedicated towards the introduction of 2D materials concerned with this work i.e. monolayer to few layered graphene, monolayer TMDs, hexagonal Boron Nitride as well as the TMD/graphene heterostructures and the description of their properties relevant to the next chapters.

Chapter 2 gives details about the experimental methods utilized in this work. It includes methods for sample fabrication and optical spectroscopy measurement techniques and setups where they were performed.

Chapter 3 is dedicated to understanding near-field interactions between monolayer $MoSe_2$ and graphene using $MoSe_2$/n-layer graphene heterostructures. The chapter first introduces the known transfer mechanisms between 2D materials and then gives details about the results observed towards understanding changes in PL of $MoSe_2$ caused by coupling to n-layered graphene.

Chapter 4 focuses on tuning the charge density over a large range in monolayer $MoSe_2$/monolayer graphene heterostructures by charge doping $MoSe_2$ through graphene and thereby controlling the light emission from the three regions of interest: graphene, $MoSe_2$/graphene and $MoSe_2$. The methodology of charge doping in samples using LaF_3 is also described in detail.

The last chapter is dedicated for conclusion and perspectives.

Supplementary figures concerned with $MoSe_2$/n-layer graphene heterostructures in chapter 3 are given in appendix A.

CHAPTER 1

Introducing 2D materials and van der Waals heterostructures

The 2D materials is a large family of various types of materials that can be thinned down to atomic level. For this thesis, we have used graphene, transition metal dichalcogenide (in particular, $MoSe_2$) and hBN to make van der Waals heterostructures. In this chapter, we will discuss about the properties of these materials and their heterostructues.

1.1 Graphene

1.1.1 Crystal structure

Graphene is an allotrope of carbon in which the atoms are arranged in a honeycomb lattice structure. The carbon atoms in this structure are bound together by sp^2 hybrid orbitals which means that each carbon atom will form three localized σ-bonds and one delocalized π-bond. The honeycomb lattice structure (shown in figure 1.1a) which can be visualized as two triangular sublattices is made by the carbon atoms connected by σ-bonds at two inequivalent sites A and B. The neighbouring atoms in this crystal structure are separated by a distance of a = 1.42 Å. The unit cell in monolayer graphene has two carbon atoms and is shown in figure 1.1a as dashed part. The unit cell is defined by basis vectors [12]

$$\boldsymbol{a}_1 = \frac{a}{2}\begin{pmatrix} 3 \\ \sqrt{3} \end{pmatrix} \text{ and } \boldsymbol{a}_2 = \frac{a}{2}\begin{pmatrix} 3 \\ -\sqrt{3} \end{pmatrix}. \tag{1.1}$$

The three nearest neighbouring atoms to lattice site B are located in lattice sites A (or vice versa) and their corresponding vectors are given by

$$\boldsymbol{\delta}_1 = \frac{a}{2}\begin{pmatrix} 1 \\ \sqrt{3} \end{pmatrix}, \boldsymbol{\delta}_2 = \frac{a}{2}\begin{pmatrix} 1 \\ -\sqrt{3} \end{pmatrix} \text{ and } \boldsymbol{\delta}_3 = -a\begin{pmatrix} 1 \\ 0 \end{pmatrix}. \tag{1.2}$$

The first Brillouin zone of graphene in reciprocal space is hexagonal and is shown in figure 1.1b. There are four high symmetry points in the Brillouin zone: Γ, K, K' and M. The basis vectors in the reciprocal lattice in momentum space are given by

$$\boldsymbol{b}_1 = \frac{2\pi}{3a}\begin{pmatrix} 1 \\ \sqrt{3} \end{pmatrix} \text{ and } \boldsymbol{b}_2 = \frac{2\pi}{3a}\begin{pmatrix} 1 \\ -\sqrt{3} \end{pmatrix}. \tag{1.3}$$

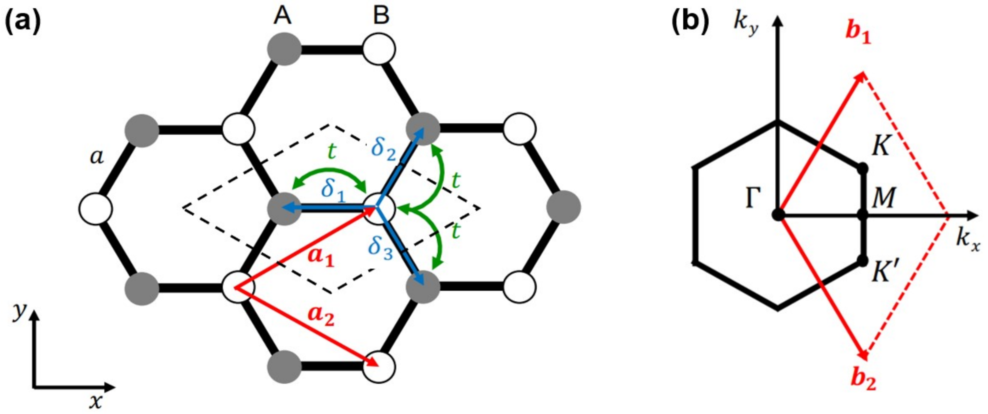

Figure 1.1: (a) Sketch of honeycomb lattice structure and (b) the first Brillouin zone of monolayer graphene. Adapted from [13].

In this thesis, we have studied interactions of different graphene thicknesses with transition metal dichalcogenides (materials to be discussed in section 1.2) and this makes it important to understand the properties of graphene with respect to changes in layer thickness. In the case of graphene thicker than monolayer, the individual layers are stacked in the AB i.e. Bernal stacking for the crystal used in this work (it should be noted that a rhombohedral ABC polytype also exists). In this type of stacking, the vacant centers of the hexagons in one layer are overlapped by carbon atoms at the hexagonal corner sites in the two adjacent graphene layers (figure 1.2a); while one of the carbon sites (B carbon sites in figure 1.2) is overlapped in all layers. For bilayer graphene, the unit cell (figure 1.2b) consists of four carbon atoms at sites: A_1, B_1, A_2 and B_2 ; while the unit cell of trilayer graphene is made up of 6 carbon atoms at sites: A_1, B_1, A_2, B_2, A_3 and B_3 (figure 1.2c) where the subscript in name of site denotes the layer number to which the atom site belongs [14].

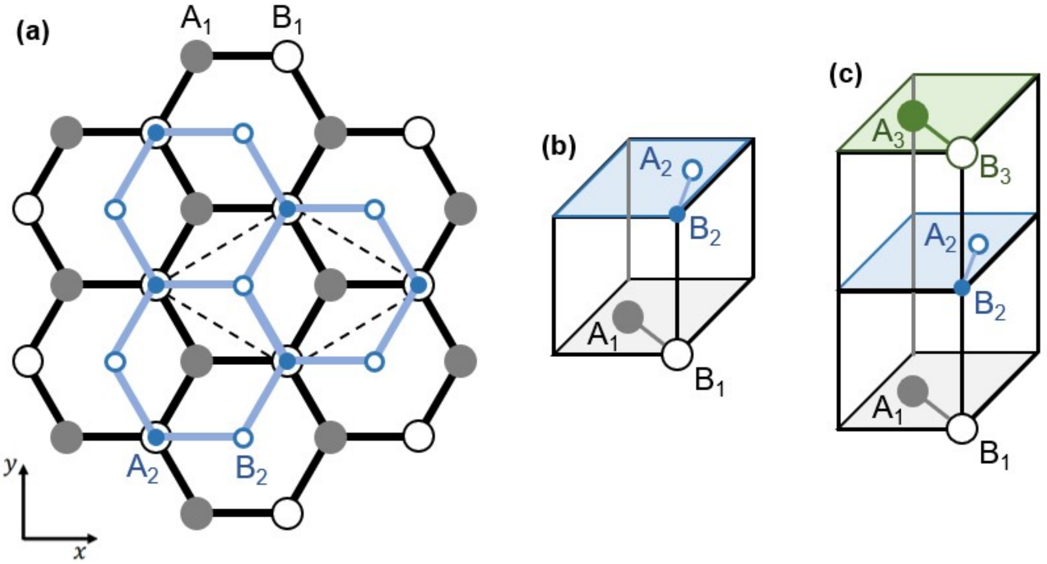

Figure 1.2: (a) Sketch of honeycomb lattice structure in Bernal stacking where the black and blue hexagons with filled/hollow gray/blue circles, respectively belong to two adjacent layers. (b) The unit cell of bilayer (c) and trilayer. Adapted from [14].

1.1.2 Electronic properties

Band structure

The 2s, $2p_x$ and $2p_y$ orbitals in carbon atoms of monolayer graphene interact and form three hybrid sp^2 orbitals. The σ-bonds (bonding molecular orbitals) mentioned in previous subsection as well as the σ^* antibonding orbitals are formed by combination of sp^2 orbitals of adjacent carbon atoms. Similarly, remaining $2p_z$ orbitals of adjacent carbon atoms give rise to π and π^* molecular orbitals. When a graphene lattice is considered, the molecular orbitals form bands. The π and π^* bands are energetically closer to the Fermi level; whereas the σ and σ^* bands are far away and can be ignored in most cases [15]. Thus, the electronic structure considering only the π and π^* bands is sufficient to understand the properties of graphene in this work [16].

Considering only the interactions between first nearest neighbours and next-nearest neighbors in tight - binding model with a nearest-neighbor hopping parameter t $\approx$ 2.7 eV (as in figure 1.1a, it concerns hopping of an electron of a carbon atom to its nearest neighbours) and next nearest-neighbor hopping parameter t', the electronic dispersion of π (lower) and π^* (upper) bands is given by

$$E_\pm(\boldsymbol{k}) = \pm t\sqrt{3 + f(\boldsymbol{k})} - t' f(\boldsymbol{k}) \tag{1.4}$$

in which the plus and minus signs apply for π^* and π bands, respectively and $f(\boldsymbol{k})$ is

$$f(\boldsymbol{k}) = 2\cos\left(\sqrt{3}k_y a\right) + 4\cos\left(\frac{\sqrt{3}}{2}k_y a\right)\cos\left(\frac{3}{2}k_x a\right) \tag{1.5}$$

where $\boldsymbol{k}$ is the wavevector. This electronic dispersion in equation (1.4) is plotted in figure 1.3 with t'$= -0.2$t.

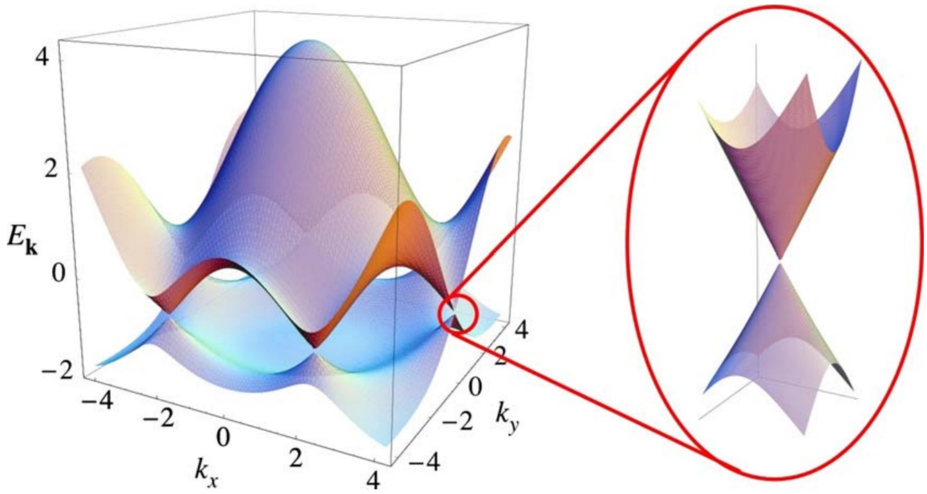

Figure 1.3: Electronic structure of graphene with a zoom in on the Dirac cone. Adapted from [12].

It should be noted that the electronic dispersion obtained from equation (1.4) is asymmetric for π^* and π bands (electron-hole asymmetry) at K and K' points due to t'≠0. Although if only nearest neighbours interactions are considered while ignoring the ones beyond (i.e. t'=0), then this dispersion becomes symmetric with respect to zero energy. In any case, the bands are degenerate at K and K' points which are the corners of the Brillouin zones.

For the graphene with thickness of a few layers, the upper and lower bands in electronic dispersion get split into the same number of bands as the numbers of graphene layers [17]. The electronic band structure of few layer graphene can be obtained by methods like zone folding of 3D graphite crystal [18], allowing possible intraband transitions due to splitting of bands.

Dirac cones

As seen in figure 1.3, the electronic band dispersion of graphene is degenerate at points K and K', which form Dirac cones and these points are referred to as Dirac points. Their positions in momentum space are given by

$$\boldsymbol{K} = \begin{pmatrix} 2\pi/3a \\ 2\pi/3\sqrt{3}a \end{pmatrix} \text{ and } \boldsymbol{K'} = \begin{pmatrix} 2\pi/3a \\ -2\pi/3\sqrt{3}a \end{pmatrix}. \tag{1.6}$$

The dispersion at these Dirac points can be obtained by Taylor expansion of equation (1.4) with t'=0 and wavevector $\boldsymbol{k} = \boldsymbol{K} + \boldsymbol{q}$, where $|\boldsymbol{q}| \ll |\boldsymbol{K}|$ to be

$$E_{\pm}(\boldsymbol{q}) = \pm\vartheta_F|\boldsymbol{q}| \tag{1.7}$$

where ϑ_F is the Fermi velocity and is given by $\vartheta_F = 3\mathrm{ta}/2 \approx 1 \times 10^6$ m/s [19].

The electronic dispersion at K and K' points satisfies Dirac equation for massless fermions.

It should be kept in mind that for higher wavevectors $|\boldsymbol{q}|$, considering higher-order terms in Taylor expansion adds non-linear terms to equation (1.7), which causes the deformation of cone into a triangular shape and this effect is called as trigonal warping [20].

For few layer graphene with an even number of layers, all components are chiral massive (electrons with finite masses and described by a pair of hyperbolic bands); while for graphene with an odd number of layers, all components are chiral massive except for one massless component [18].

Density of states

The density of states in monolayer graphene near Dirac cones assuming t' = 0 is given by

$$g(E) = \frac{2E}{\pi\ v_{\mathrm{F}}^2} \tag{1.8}$$

in which the two-fold spin and valley degeneracy are considered. The expression is valid for both electrons and holes. It scales linearly with energy E and goes to zero at Dirac points. The density of states is symmetric for electrons and holes.

1.1.3 Optical absorption

Graphene layers can absorb light from both interband and intraband transitions (represented in figure 1.4a). Whether the intraband transitions dominate or the interband ones depend upon spectral range and doping level. For undoped graphene, intraband transitions dominate the optical absorption in the far infrared regime (photon energies $\leq$ 50meV) and scattering by phonons or defects is required to fulfill momentum conservation.

In the near infrared to visible range, the interband transitions dominate the absorption. This absorption coefficient is constant (in case of no trigonal warping), independent of Fermi velocity and can be calculated by taking the ratio of absorbed power to incident power. The incident power is given by $P_{\text{abs}} = \eta_{\text{abs}}\hbar\omega$ where ω is the frequency of incident photons and η_{abs} is the probability of absorption. The latter can be calculated using Fermi's golden rule by [21]

$$\eta_{\text{abs}} = \frac{2\pi}{\hbar}|M|^2 g(E) \tag{1.9}$$

where M is the matrix element of the 2D Dirac electron light-matter interaction hamiltonian and $|M|^2 = (e|\boldsymbol{\epsilon}|v_{\text{F}})^2/8\omega^2$, in which $\boldsymbol{\epsilon}$ is the electric field of incoming light and e is the elementary charge. Using equation (1.8),

$$P_{\text{abs}} = \frac{(e|\epsilon|)^2}{4\hbar} \tag{1.10}$$

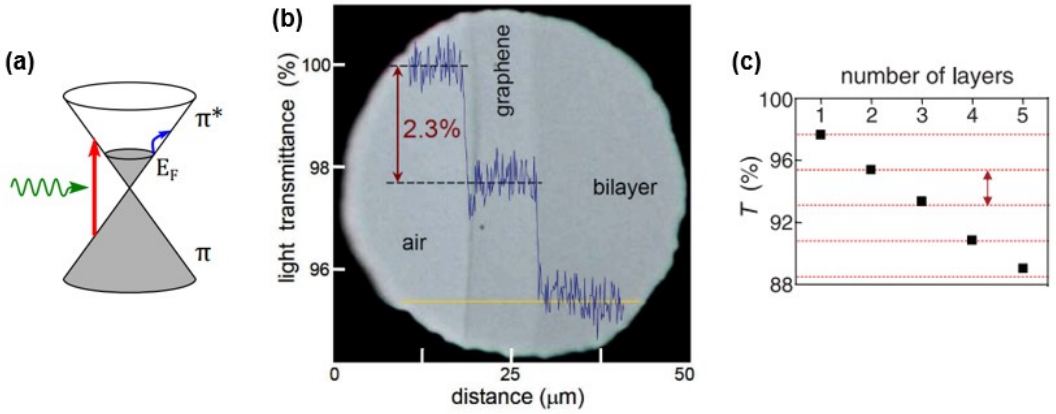

Figure 1.4: (a) Schematic of intraband (blue arrow) and interband (red arrow) transitions from initial occupied states (gray shaded area) to final state in graphene caused by absorption of photon (wavy green arrow). (b) Optical image of monolayer and bilayer graphene suspended over a hole and percentage of light transmittance taken over the yellow line (c) the percentage of light transmission vs the number of graphene layers, the dashed lines correspond to a reduction by 2.3% with each added graphene layer. Adapted from [21].

The absorbed power is given by

$$P_{\text{in}} = \frac{c|\epsilon|^2}{4\pi} \tag{1.11}$$

where c is the speed of light. Using equations (1.9) and (1.10), the absorption coefficient is

$$\mathcal{A} = \frac{P_{\text{abs}}}{P_{\text{in}}} = \pi\alpha \approx 2.3\% \tag{1.12}$$

where $\alpha = e^2/\hbar c = 1/137$ is the fine structure constant. This can also be seen in figures 1.4b and 1.4c which show a decrease in light transmittance percentage by about 2.3% with each added graphene layer [21].

1.1.4 Vibrational properties

Phonon dispersion of graphene

As the graphene monolayer has two carbon atoms per unit cell, there are six phonon branches possible. Out of these, three of them are acoustic (A) and the other three are optical phonon (O) branches. Furthermore, there are two in-plane longitudinal branches (iLA and iLO), two are in-plane transverse branches (iTA and iTO) and the remaining two are out-of-plane transverse phonon branches (oTA and oTO). The phonon dispersion of monolayer graphene is shown in figure 1.5.

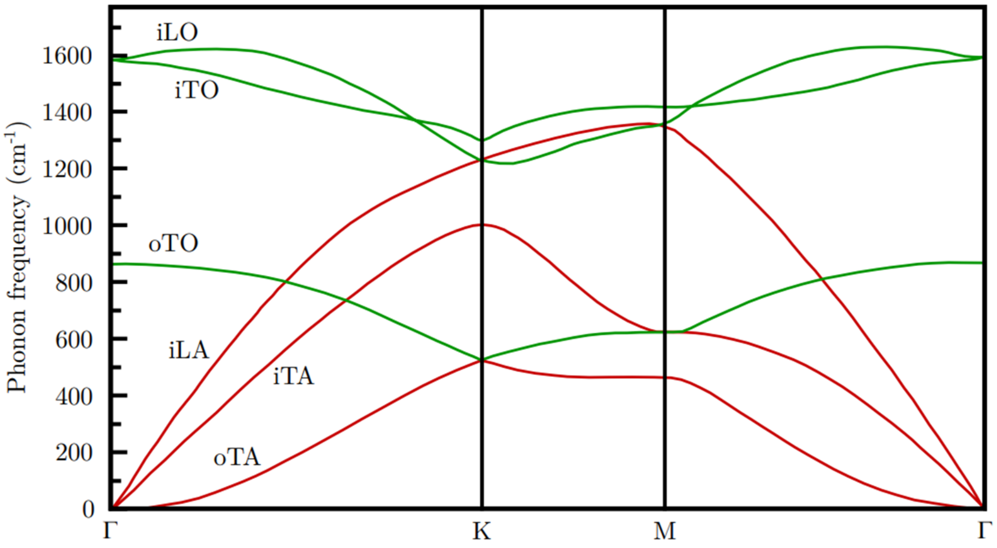

Figure 1.5: Phonon dispersion of graphene. Adapted from [22]

In this figure, some kinks, known as Kohn anomalies [23], can be seen in the phonon dispersion. A Kohn anomaly occurs due to an abrupt decrease in ability of conduction electrons to screen ionic charge distribution produced by lattice vibrations of ions. The Kohn anomalies can occur for phonon wavevectors $\boldsymbol{q}$ in Brillouin zone such that there are two electronic states with wavevectors $\boldsymbol{k_1}$ and $\boldsymbol{k_2} = \boldsymbol{k_1}+\boldsymbol{q}$ on the Fermi surface. In the case of graphene, the only points for which Kohn anomalies can occur are $\boldsymbol{q} = \boldsymbol{\Gamma}$ and $\boldsymbol{q} = \boldsymbol{K}, \boldsymbol{K'}$. The figure 1.5 shows two Kohn anoalies in graphene: one for iLO phonons at Γ point and the other one for iTO phonons at K or K' points. At these points, the electron-phonon coupling is quite strong due to energy and momentum conservation in electron-phonon scattering [24]. The electron-phonon coupling at the Γ point is smaller than at the K point, which influences the Raman peak intensity of modes accordingly, as will be discussed in the coming subsection.

The phonon frequencies in graphene can be observed by Raman spectroscopy while also probing the effects of external parameters on intrinsic properties of graphene.

Introduction to Raman spectroscopy

Raman spectroscopy is an optical spectroscopy technique based upon the inelastic scattering of photons with phonons in a material. The shift in frequency of scattered photon as compared to incident photon is called as Raman shift (δ) and is typically measured in wavenumbers with cm^{-1} as units:

$$\delta = \frac{\Delta\omega}{2\pi c} = \frac{1}{\lambda_{\mathrm{inc}}} - \frac{1}{\lambda_{\mathrm{s}}} \tag{1.13}$$

in which $\Delta\omega$ is the shift in frequency between incident and scattered photon, λ_{inc} is the wavelength of incident light and λ_{s} is the wavelength of scattered light.

Classical picture

In this section, Raman spectroscopy is initially described in the classical picture [25]. In this classical picture, let us consider an incident monochromatic electromagnetic wave of the form

$$\boldsymbol{E}(\boldsymbol{r},t) = \boldsymbol{E}_0 \cos(\boldsymbol{k}_0.\boldsymbol{r} - \omega_0 t) \tag{1.14}$$

with amplitude $\boldsymbol{E}_0$, wavevector $\boldsymbol{k}_0$ and frequency ω_0. When this wave is incident on a material with electric susceptibility $\bar{\boldsymbol{\chi}}$, it induces a polarization of the form

$$\boldsymbol{P} = \epsilon_0 \bar{\boldsymbol{\chi}} \boldsymbol{E} \tag{1.15}$$

where ϵ_0 is the vacuum permittivity. The incident wave induces lattice vibrations and the atomic displacement related to a phonon is of the form

$$\boldsymbol{u}(\boldsymbol{r},t) = \boldsymbol{u}_0 \cos(\boldsymbol{q}.\boldsymbol{r} - \Omega t) \tag{1.16}$$

with wavevector $\boldsymbol{q}$ and frequency Ω. These lattice vibrations cause changes in $\bar{\boldsymbol{\chi}}$ and it can be expanded as a Taylor series in $\boldsymbol{u}$ with respect to the equilibrium position of atoms. The first order expansion gives

$$\bar{\boldsymbol{\chi}} \approx \bar{\boldsymbol{\chi}}_0 + \left(\frac{\partial \bar{\boldsymbol{\chi}}}{\partial \boldsymbol{u}}\right)_0 .\boldsymbol{u} \tag{1.17}$$

where $\bar{\boldsymbol{\chi}}_{\mathbf{0}}$ as the first term is the electric susceptibility tensor without fluctuations and the second term describes the effect of lattice vibrations on $\bar{\boldsymbol{\chi}}$. By substituting equation (1.17) into equation (1.15), we get the polarization wave of the form

$$\boldsymbol{P}(\boldsymbol{r},t,\boldsymbol{u}) = \boldsymbol{P}_0(\boldsymbol{r},t) + \boldsymbol{P}_{\mathrm{ind}}(\boldsymbol{r},t,\boldsymbol{u}) \tag{1.18}$$

where the first term $\boldsymbol{P}_0$ is resonant with the incident frequency. Using 1.14, this term is

$$\boldsymbol{P}_0(\boldsymbol{r},t) = \epsilon_0 \bar{\boldsymbol{\chi}}_0 \boldsymbol{E}_0 \cos(\boldsymbol{k}_0.\boldsymbol{r} - \omega_0 t) \tag{1.19}$$

and it describes elastic Rayleigh scattering.

The second term $\boldsymbol{P}_{ind}$ in 1.18 represents the changes in $\bar{\boldsymbol{\chi}}$ caused by phonons and is obtained from the second term in 1.17. Thus, using equations (1.16)and (1.14), we get

$$\boldsymbol{P}_{\mathrm{ind}}(\boldsymbol{r},t,\boldsymbol{u}) = \epsilon_0 \left(\frac{\partial \bar{\boldsymbol{\chi}}}{\partial \boldsymbol{u}}\right)_0 .\boldsymbol{u}_0 \cos(\boldsymbol{q}.\boldsymbol{r} - \Omega t) \boldsymbol{E}_0 \cos(\boldsymbol{k}_0.\boldsymbol{r} - \omega_0 t). \tag{1.20}$$

By linearizing the cosine product in equation (1.20), we obtain

$$\boldsymbol{P}_{\text{ind}}(\boldsymbol{r},t,\boldsymbol{u}) = \frac{\epsilon_0}{2}\left(\frac{\partial\bar{\boldsymbol{\chi}}}{\partial\boldsymbol{u}}\right)_0 .\boldsymbol{u}_0\boldsymbol{E}_0\left[\cos([\boldsymbol{k}_0+\boldsymbol{q}].\boldsymbol{r}-[\omega_0+\Omega]t)+\cos([\boldsymbol{k}_0-\boldsymbol{q}].\boldsymbol{r}-[\omega_0-\Omega]t)\right]$$

in which the first and second terms on the right hand side describe anti-Stokes and Stokes Raman scattering with frequencies $\omega_0+\Omega$ and $\omega_0-\Omega$ and wavevectors $\boldsymbol{k}_0+\boldsymbol{q}$ and $\boldsymbol{k}_0-\boldsymbol{q}$ respectively. Both energy and momentum are conserved for anti-stokes and Stokes Raman scattering. Thus, the anti-Stokes Raman scattering is a type of inelastic scattering that involves annihilation of a phonon of frequency Ω and wavevector $\boldsymbol{q}$ and it emits scattered light blue-shifted in frequency compared to incident light. On the other hand, the Stokes Raman scattering is a type of inelastic scattering that involves the creation of a phonon of frequency Ω and wavevector $\boldsymbol{q}$ and it emits scattered light red-shifted in frequency compared to incident light.

For understanding processes involving two phonons, $\bar{\boldsymbol{\chi}}$ has to be expanded in terms of $\boldsymbol{u}$ up to the second order term in Taylor expansion. The second order in this the Taylor expansion for two phonons $\boldsymbol{u}_a$ and $\boldsymbol{u}_b$ with respective wavevectors $\boldsymbol{q}_a$ and $\boldsymbol{q}_b$ and frequencies Ω_a and Ω_b adds four terms to $\boldsymbol{P}_{ind}$ with frequencies $\omega_0 \pm (\Omega_a \pm \Omega_b)$.

The intensity of the Raman peak is proportional to the power of the induced polarization. Thus, for scattered light with frequency ω_s and polarization $\boldsymbol{e}_\text{s}$, the intensity is given by [26]

$$I(\omega_\text{s}) \propto |\boldsymbol{e}_\text{i}.\left(\frac{\partial\bar{\boldsymbol{\chi}}}{\partial\boldsymbol{u}}\right)_0 .\frac{\boldsymbol{u}_0}{|\boldsymbol{u}_0|}.\boldsymbol{e}_\text{s}|^2|\boldsymbol{u}_0|^2\omega_\text{s}^4 \tag{1.21}$$

in which $\boldsymbol{e}_\text{i}$ is the polarization of incident light.

In equation (1.21), the Raman tensor is defined as

$$\bar{\boldsymbol{R}} = \left(\frac{\partial\bar{\boldsymbol{\chi}}}{\partial\boldsymbol{u}}\right)_0 .\frac{\boldsymbol{u}_0}{|\boldsymbol{u}_0|}. \tag{1.22}$$

If the Raman tensor is null, then the phonon mode is not Raman active. In case the Raman tensor is not null, then the phonon mode is Raman active and the intensity of the corresponding Raman peak depends upon polarization of incident and scattered light as shown in equation (1.21). Thus, the equation (1.21) works as a selection rule for determining the Raman peaks that are present in Raman spectroscopy performed in a particular experimental setting. As the Raman tensor has the same symmetry as the corresponding phonon, the symmetries of phonon modes can be observed by using polarization dependent Raman spectroscopy.

Quantum picture

The description of Raman spectroscopy from a classical view discussed so far tells us about the conservation of energy and momentum in Raman scattering, interactions between photons and phonons and the selection rule for Raman intensity; but a microscopic understanding of Raman scattering with a quantum approach described here onwards will give information about interactions between electrons and photons.

In a quantum picture (figure 1.6), the system is initially considered to be in state $|i\rangle$. The incident photon with frequency ω_0 creates an electron-hole pair and excites the electron from this initial state into the first intermediate state $|e_1\rangle$. This $|e_1\rangle$ interacts with the lattice and absorbs or emits a phonon of frequency Ω for Anti-Stokes or Stokes Raman scattering respectively. Then, the electron reaches the second intermediate state $|e_2\rangle$. This $|e_2\rangle$ relaxes to $|i\rangle$ by recombining of electron-hole pair and emitting a scattered photon of frequency ω_s. The intermediate states $|e_1\rangle$ and $|e_2\rangle$ can be real or virtual states. If at least one of these intermediate states is real, then the process is resonant Raman scattering.

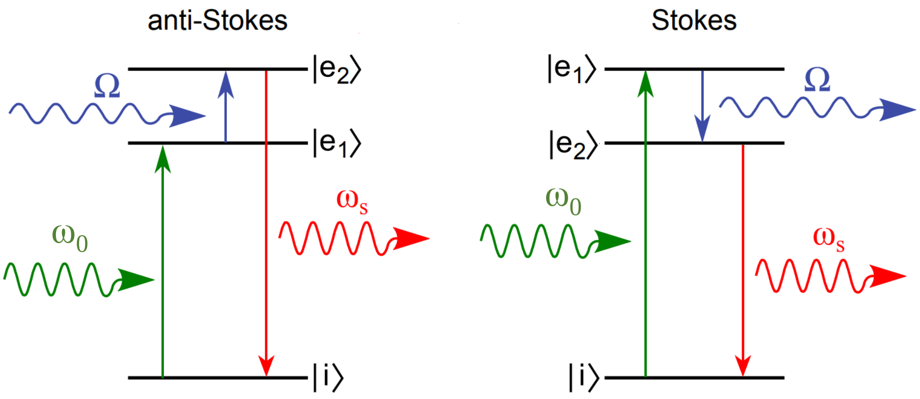

Figure 1.6: Quantum picture of Raman spectroscopy. Adapted from [13].

The Raman intensity is proportional to the scattering probability corresponding to the Feynman diagram of the scattering process:

$$I(\omega_\mathrm{s}) \propto \left| \sum_{|e_1\rangle,|e_2\rangle} \frac{\langle i|\hat{\mathcal{H}}_{\mathrm{e-l}}|e_2\rangle\langle e_2|\hat{\mathcal{H}}_{\mathrm{e-v}}|e_1\rangle\langle e_1|\hat{\mathcal{H}}_{\mathrm{e-l}}|i\rangle}{[\hbar\omega_\mathrm{i} - (E_1 - E_i)][\hbar\omega_0 - \hbar\Omega - (E_2 - E_i)]} \right|^2 \tag{1.23}$$

in which electron-photon interactions are described by $\hat{\mathcal{H}}_{\mathrm{e-l}}$ hamiltonian and electron-phonon interactions are given by $\hat{\mathcal{H}}_{\mathrm{e-v}}$ hamiltonian. The states $|i\rangle$, $|e_1\rangle$ and $|e_2\rangle$ have energies E_i, E_1 and E_2 respectively.

As phonons are bosons, the average number of phonons with frequency Ω is dependent on temperature T and is given by

$$N_{\boldsymbol{q}} = \frac{1}{e^{\hbar\Omega/k_\mathrm{B}T} - 1} \tag{1.24}$$

where k_B is the Boltzmann constant. In Stokes Raman scattering, the number of phonons in the material increases by 1 after the scattering process and thus, the $I(\omega_\mathrm{s})$ for the Stokes scattering is proportional to $N_{\boldsymbol{q}} + 1$.

In this PhD work, we have focused on measuring Stokes Raman scattering on graphene at room temperature.

Raman spectroscopy of graphene

In graphene, only iTO and iLO phonon branches give rise to Raman active phonons and thus, detectable Raman peaks in a typical Raman spectrum are seen in top panel of figure

1.7. In this section, we will be discussing about G and 2D modes as well as other Raman modes including the ones observed in monolayer graphene with defects (bottom panel of figure 1.7).

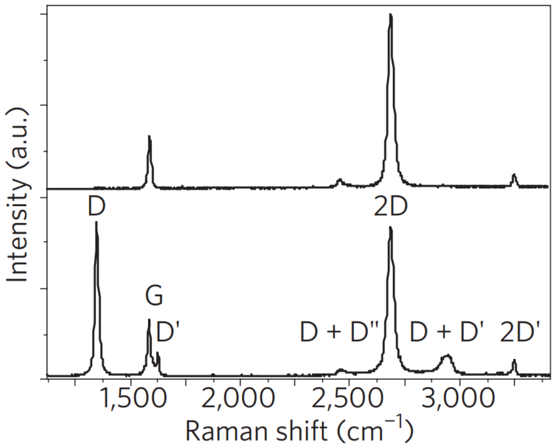

Figure 1.7: Typical Raman spectra of pristine monolayer graphene (top panel) and graphene with defects (bottom panel). Adapted from [27].

G mode

The G mode seen near 1585 cm^{-1} originates from a doubly degenerate phonon mode with E_{2g} symmetry from phonon branches iTO and iLO at Brillouin zone center Γ. The vibrational mode in real space is represented in figure 1.8a and it involves out-of-phase vibration of A and B sublattices with respect to each other. It occurs from a first order Raman scattering process as shown in figure 1.8a. The Kohn anomaly at Γ point in the phonon dispersion of graphene occurs in E_{2g} mode.

The G peak in Raman spectrum can be fitted quite well with a Lorentzian profile which gives its center, FWHM (full width at half maximum) and integrated intensity of the peak. These parameters can be used to observe effects of external perturbations on the sensitive G mode.

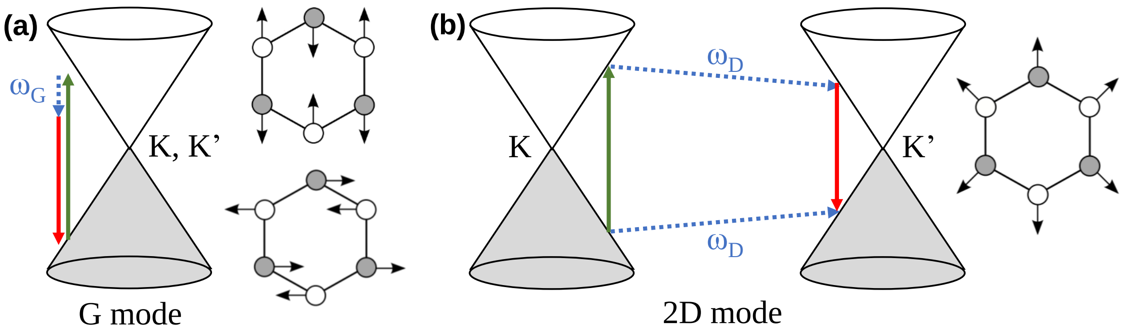

Figure 1.8: Representation and vibrational modes of (a) G mode and (b) 2D mode. The gray shaded part shows filled states. Adapted from [27, 28].

2D mode and 2D' mode

The 2D mode usually seen near 2650 cm^{-1} arises mainly from a fully resonant two phonon process between the K and K' points (intervalley process). The scattering process for 2D mode is shown in figure 1.8b in which the steps of excitation of an electron around the K point to a real state creating an electron-hole pair, scattering of an electron from K point to a real state in K' point after interacting with first phonon and the backscattering of electron from K' to K point after interacting with second phonon are all resonant processes as all the intermediate states involved are real states. A small contribution to the 2D mode can also come from double resonant scattering processes. The two phonons involved in the scattering process come from iTO branch at K and K' points and they have the same frequency with opposite momenta. These phonons have A_1' symmetry and vibrational mode involves breathing vibration of carbon atoms (figure 1.8b). The 2D Raman peak is fit with a Voigt profile in this work.

A Raman peak can be seen at around 3240 cm^{-1} named as 2D' mode which occurs due to double resonant intravalley (at K or K' point) scattering process involving scattering by two phonons from iLO branch near Γ point having opposite momenta. As the electron-phonon coupling at Γ point is smaller compared to that of K point, the intensity of 2D' mode is much smaller than that of 2D mode.

Defect associated D, D', D+D' and D+D" modes

When defects are created in graphene, the defect related Raman peaks D, D' and D+D' appear in Raman spectrum (figure bottom panel of figure 1.7) because of Raman scattering processes involving scattering by defects. Understanding these defect related Raman modes in graphene is important for this work as we will be checking the effects of creation of defects on charge doping of graphene in chapter 4.

The D mode arises from double resonant intervalley scattering process involving scattering of electron by one phonon from iTO branch at K point and then by a defect around K' point. This phonon is the same as the two phonons mentioned in aforementioned description of 2D mode which means that 2D mode is an overtone (involving two phonons having same frequency) of D mode, which makes the D mode appear near 1325 cm^{-1} i.e. half of the frequency of 2D mode. The intensity of D peak in Raman spectrum increases with increase in density of defects in graphene.

The D' mode mainly originates from double resonant scattering process at K (or K') point (intravalley process) in which electron is scattered by a phonon from the iLO branch and a defect. The D' Raman peak can be seen just alongside the G mode, at around 1620 cm^{-1}. The aforementioned 2D' mode is an overtone of D' mode.

It should be noted that second order scattering processes for the D and D' modes involve only one phonon and one defect, which makes one of the scattering events elastic and the other one inelastic.

The D+D' Raman mode involves one intervalley (between K and K' points) and one defect-assisted intravalley (at K or K' point) scattering process by phonons. This is a triple resonant scattering process which gives a broad Raman peak near 2950 cm^{-1}.

The D+D" mode is a combination of scattering from phonon related to D mode and a phonon belonging to iLA branch seen at around 1100 cm^{-1} named as D" peak. Thus, the

D+D" Raman peak can be seen near 2450 cm^{-1} in the Raman spectrum. This mode mainly arises from a triple resonant scattering process similar to 2D mode and is visible even in defect-free samples.

For this thesis, we have focused on the G and 2D modes and their behaviour with respect to external charge doping which is well-known in literature. We will also be observing the emergence of defect related Raman modes with electrochemical reactions that give rise to defects in graphene layer (in chapter 4). The Raman modes also show dependence on the thickness of graphene, which is also discussed in the upcoming subsection.

Raman spectroscopy of graphene as a probe

The peaks in the Raman spectrum of graphene can be analyzed to know information about the effects of external perturbations and parameters like strain, doping, incident photon energy, temperature, dielectric screening, thickness of layers etc. on properties of graphene.

When the graphene layer is exposed to external strain, the lattice parameter and force constant change, causing changes in phonon dispersion. Hence, under tensile or compressive strain, the Raman mode frequency shows downshift or upshift respectively [29]. Although exploring the effects of strain on TMD/Graphene heterostructures is not an objective of this thesis, we will be checking for possible intrinsic strain on samples when they are externally charge doped in chapter 4.

The Raman mode parameters i.e. frequency, linewidth and intensity are very sensitive to charge doping because of changes caused in lattice parameter, phonon renormalization and quantum interference between Raman pathways.

In this section, we will focus on the changes in Raman modes with respect to doping of charges and thickness of graphene, which is important to understand for the chapters 3 and 4.

Charge doping

In this subsection, the effects of external charge doping on Raman peaks of monolayer graphene are described which will be important for understanding the results in chapter 4. For intrinsic and charge neutral monolayer graphene, the Fermi level (E_{F}) is at the Dirac points and charge doping shifts this Fermi level in energy. The charge carrier density n in monolayer graphene is related to E_{F} as [30]

$$E_F = \mathrm{sgn(n)}\hbar\vartheta_{\mathrm{F}}\sqrt{\pi|\mathrm{n}|} \tag{1.25}$$

The G and 2D modes Raman peaks are sensitive to charge doping, thus the parameters frequency, FWHM and intensity of these modes can be analyzed with respect to changes in charge doping.

G mode frequency:

The frequency of G mode (ω_{G}) is very sensitive to addition of charges and with changes in E_{F}, ω_{G} shows clear shift denoted by $\Delta\omega_{\mathrm{G}}$ with respect to ω_{G}^0 which is ω_{G} at $E_{\mathrm{F}} = 0$.

When charges are added to graphene, the carbon-carbon bond strength is modified which in turn, causes modification in equilibrium lattice parameter. Electron and hole doping to antibonding orbitals causes softening and hardening of carbon-carbon bonds and thereby a downshift and upshift in ω_{G} respectively [31]. The Born-Oppenheimer approximation, which assumes that the electrons remain in their instantaneous ground state and adjust adiabatically to the motion of heavier nuclei is used to obtain this contribution [32, 33]

$$\Delta\omega_{\mathrm{G}}^{\mathrm{A}} = -2.13n_1 - 0.0360n_1^2 - 0.00329n_1^3 - 0.226|n_1|^{3/2} \tag{1.26}$$

in which n_1 represents the charge carrier density in units of 10^{13} cm^{-2} and $\Delta\omega_{\mathrm{G}}^{\mathrm{A}}$ is in cm^{-1}.

Moreover, a second non-adiabatic contribution to changes in ω_{G} with charge doping originates from a renormalization of the G mode phonon energy due to the interaction between phonon and virtual electron-hole pair which is caused by electron-phonon interaction. This strong electron-phonon coupling which is directly connected to the Kohn anomaly at the Γ point, makes the phonon spend part of its time as a virtual electron-hole pair (as represented in left inset in figure 1.9a), causing changes in phonon energy that can be described by the real-part of phonon self energy. The change in phonon energy cannot be calculated by Born-Oppenheimer approximation because in this non-adiabatic case, electrons do not have time to relax to their instantaneous ground state [32]. For calculating the non-adiabatic contribution to $\Delta\omega_{\mathrm{G}}$, the perturbation is considered to be dynamic and time-dependent perturbation theory has to be used [33] which gives

$$\Delta\omega_{\mathrm{G}}^{\mathrm{NA}} = \frac{\lambda_\Gamma}{2\pi\hbar} P \int_{-\infty}^{\infty} \frac{[f(E - E_{\mathrm{F}}) - f(E)]E^2 \mathrm{sgn}(E)}{E^2 - (\hbar\omega_{\mathrm{G}}^0)^2/4} \mathrm{d}E \tag{1.27}$$

where λ_Γ is electron-phonon coupling constant at the Γ point [34], P denotes the Cauchy principal value and

$$f(E) = [1 + \exp((E)/k_{\mathrm{B}}T)]^{-1} \tag{1.28}$$

is the Fermi-Dirac distribution.

From these adiabatic and non-adiabatic contributions, $\Delta\omega_{\mathrm{G}}$ with respect to external charge doping is given by

$$\Delta\omega_{\mathrm{G}} = \Delta\omega_{\mathrm{G}}^{\mathrm{A}} + \Delta\omega_{\mathrm{G}}^{\mathrm{NA}}. \tag{1.29}$$

It should be noted that although $\Delta\omega_{\mathrm{G}}^{\mathrm{A}}$ is negligible as compared to $\Delta\omega_{\mathrm{G}}^{\mathrm{NA}}$ for $n < 10^{13}$ cm^{-2}, it becomes sizeable above this limit and will be considered alongwith the $\Delta\omega_{\mathrm{G}}^{\mathrm{NA}}$ in chapter 4.

The $\Delta\omega_{\mathrm{G}}$ obtained from 1.29 with respect to charge carrier density at T=300 K is shown in figure 1.9b as continuous line [33]. The asymmetry seen in $\Delta\omega_{\mathrm{G}}$ between electron and hole doping is due to $\Delta\omega_{\mathrm{G}}^{\mathrm{A}}$ because $\Delta\omega_{\mathrm{G}}^{\mathrm{NA}}$ is an even function of E_{F}.

G mode FWHM:

The evolution of G mode FWHM Γ_{G} and $\Delta\omega_{\mathrm{G}}^{\mathrm{NA}}$ as a function of charge doping is deeply connected (as seen in figure 1.9a) because the imaginary-part of phonon self energy explains the variation in Γ_{G} as the G mode phonon decays spontaneously into an electron-hole pair

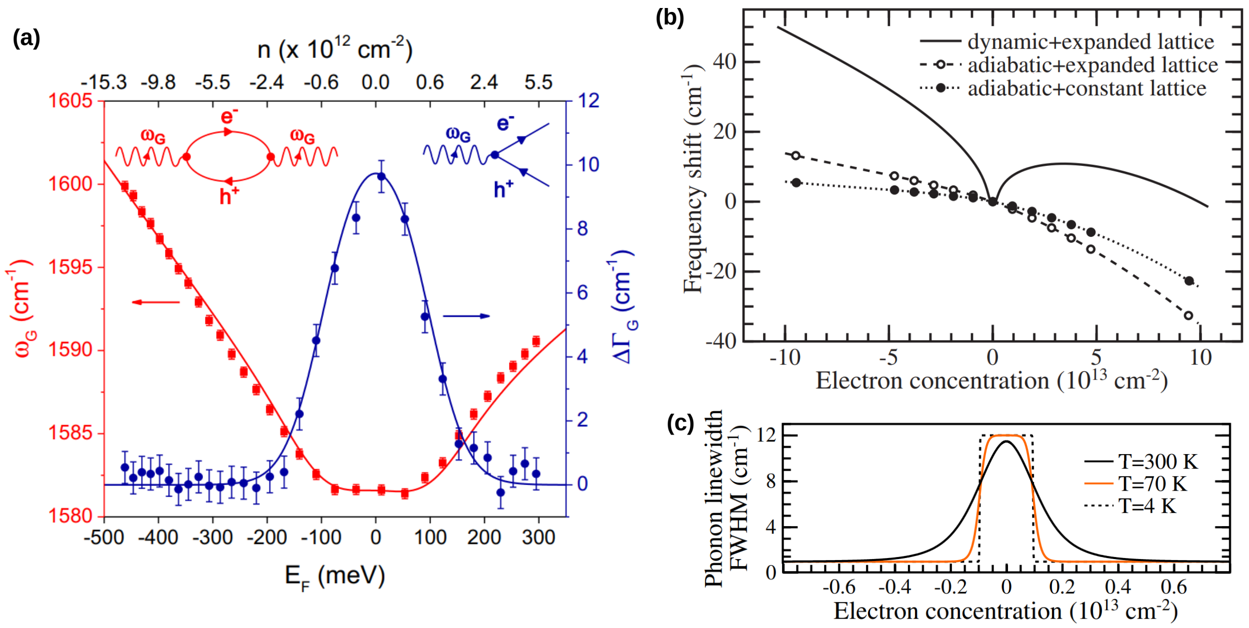

Figure 1.9: (a) ω_G and $\Delta\Gamma_\mathrm{G}$ as a function of charge doping adapted from [30](b) Frequency Raman shift of G mode as a function of charge concentration at T=300 K shown by solid line and (c) Linewidth of G mode as a function of charge concentration at different temperatures, adapted from [35].

(right inset of figure 1.9a). The change in Γ_G from addition of charges can be calculated using Fermi Golden rule to be [32]

$$\Delta\Gamma_\mathrm{G} = \frac{\lambda_\Gamma}{2c}\omega^0_\mathrm{G}\pi\left[f\left(-\frac{\hbar\omega^0_\mathrm{G}}{2} - E_\mathrm{F}\right) - f\left(\frac{\hbar\omega^0_\mathrm{G}}{2} - E_\mathrm{F}\right)\right] \tag{1.30}$$

which vanishes for $|E_\mathrm{F}| > \hbar\omega_\mathrm{G}/2$ because the scattering process is forbidden by Pauli exclusion principle [35]. The calculated Γ_G with respect to charge doping at different T is given in figure 1.9c.

G mode intensity:

The intensity of G mode I_G remains constant while $|E_\mathrm{F}| \ll E_\mathrm{L}/2$ (where E_L is the incident laser energy), but gets enhanced strongly as $|E_\mathrm{F}|$ reaches $E_\mathrm{L}/2$. This sudden increase in I_G can be understood by looking at the quantum interference between Raman pathways for Raman G mode [36]. Figure 1.10a shows two representative Raman G mode pathways, denoted by I and II. These pathways have different intermediate excited energy states. The pathway I is resonant, while pathway II is close to resonance. All such possible pathways for Raman G mode having different quantum phases and amplitudes interfere with each other. Depending upon the relative phases of these quantum pathways, blocking one pathway can influence I_G by interfering with other quantum pathways. The following explanation emphasizes on the quantum nature of Raman scattering. For a particular E_L, I_G depends upon the interference between pathways as [37, 31, 36, 38]

$$I_\mathrm{G} = \left|\sum_{\boldsymbol{k}} M_{\boldsymbol{k}} R_{\boldsymbol{k}}\right|^2 \tag{1.31}$$

in which $M_{\boldsymbol{k}}$ is a third-order transition matrix element and $R_{\boldsymbol{k}}$ is the resonance factor given by

$$R_{\boldsymbol{k}} = \frac{1}{(E_{\mathrm{L}} - E_{\boldsymbol{k}} - i\gamma)(E_{\mathrm{L}} - \hbar\omega_{\mathrm{G}} - E_{\boldsymbol{k}} - i\gamma)} \tag{1.32}$$

where $E_{\boldsymbol{k}}$ is the vertical transition energy at wavevector $\boldsymbol{k}$ and γ is the energy broadening of excited state containing contributions from electron-electron interactions and electron-phonon coupling. The summation over $\boldsymbol{k}$ gives interference of quantum pathways depending upon the phase of allowed pathways. Pathways resonant with incident light have $E_{\boldsymbol{k}} = E_L$ and the ones that are resonant with scattered light have $E_{\boldsymbol{k}} = E_L - \hbar\omega_{\mathrm{G}}$.

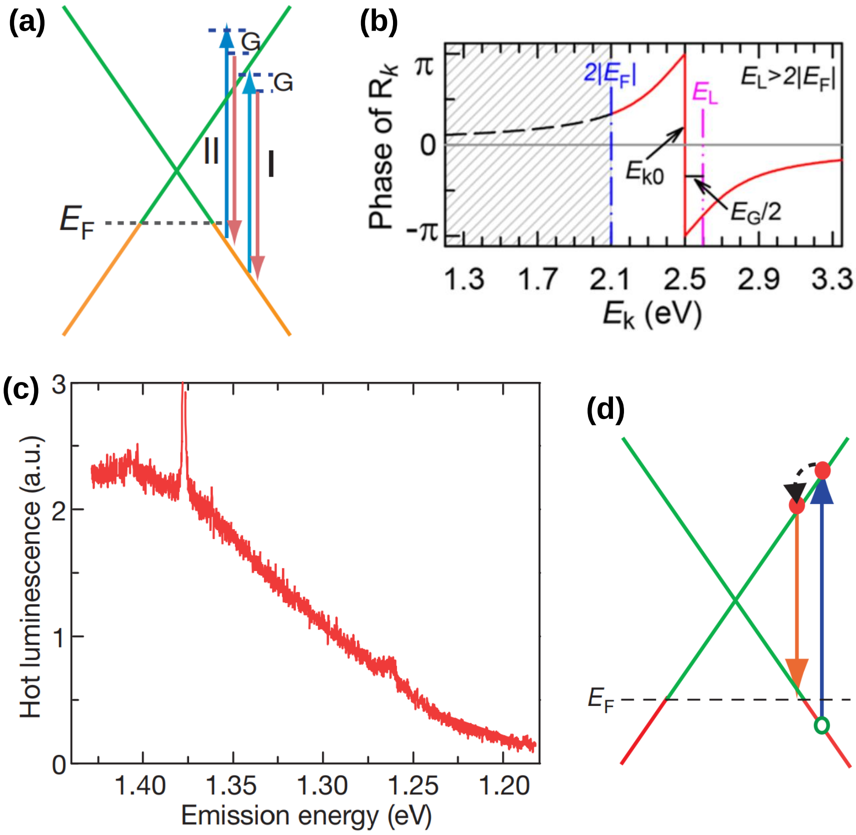

Figure 1.10: (a) Two representative Raman G mode pathways I and II occurring through two different intermediate excited states (b) Phase of $R_{\boldsymbol{k}}$ for pathways at E_L=2.6 eV and $|2E_{\mathrm{F}}|$=2.1 eV, the diagonally shaded area shows Pauli blocked pathways (c) Hot luminescence seen with E_L=1.58 eV at $|2E_{\mathrm{F}}|$=1.4 eV (d) Hot luminescence generation mechanism. Adapted from [36, 38].

For intrinsic graphene, all pathways are allowed and they interfere destructively with each other, which gives a weak I_{G}. This is because the quantum pathways with $E_{\boldsymbol{k}}$ above and below $E_{\boldsymbol{k_0}} = E_L - \hbar\omega_{\mathrm{G}}/2$ have an average phase difference of π leading to destructive interference (figure 1.10b).

As graphene is doped increasing $|E_{\mathrm{F}}|$, the pathways with $E_{\boldsymbol{k}} < 2|E_{\mathrm{F}}|$ are blocked by Pauli exclusion principle. Hence, the corresponding pathways antisymmetric to the blocked pathways having $E_{\boldsymbol{k}} > 2E_{\boldsymbol{k_0}} - 2|E_{\mathrm{F}}|$ are the only ones contributing to G mode, which enhances I_{G}. Accordingly, I_{G} reaches a maximum for $E_L = 2|E_{\mathrm{F}}| + \hbar\omega_{\mathrm{G}}/2$ [36, 38].

When E_{F} approaches $E_{\mathrm{L}}/2$ with hole doping, hot luminescence can be seen over a broad range in the Raman spectrum (figure 1.10c). The figure 1.10d shows a schematic of hot luminescence generation. An incident photon excites an electron into an excited state creating a hole. The charges then relax to E_{F} by interacting with electrons and phonons. The hot electron can emit a photon during the relaxation process only if the final state in valence band is empty and this leads to broad luminescence with energy below $2|E_{\mathrm{F}}|$ [36]. It should be noted that the D mode expected at ≈ 1.42 eV remains faint in figure 1.10 implying low defect density.

2D mode frequency:

The 2D mode frequency ω_{2D} shows weak variation under moderate electron and hole doping (figure 1.12a)[30]. The shift in ω_{2D} with respect to external charge doping is denoted here by $\Delta\omega_{\mathrm{2D}}$ and it is a combination of adiabatic and non-adiabatic terms. But since the phonons concerned here are far from the Kohn anomalies at K and K' points, the non-adiabatic term in $\Delta\omega_{\mathrm{2D}}$ is weak and the adiabatic term dominates [39]. The correlation between $\Delta\omega_{\mathrm{G}}$ and $\Delta\omega_{\mathrm{2D}}$ given in the following subsection of correlations is quite helpful in visualizing $\Delta\omega_{\mathrm{2D}}$.

2D mode FWHM:

As 2D mode has contributions from the inner and outer loop [20] (represented in figures 1.8b and 1.11a respectively), the FWHM of 2D mode denoted by Γ_{2D} has weak lineshape as it is not really a single peak and remains almost constant under moderate charge doping as seen in figure 1.12a. This lack of significant variation in $\Delta\Gamma_{\mathrm{2D}}$ in moderate doping is because the corresponding phonons in 2D mode cannot undergo resonant decay into an electron-hole pair due to momentum conservation [30]. Although, at high charge density ($> 10^{12}$ cm^{-2}), Γ_{2D} increases because of electron-electron interactions and possible electron-defect elastic scattering [40, 41].

2D mode intensity:

The 2D mode intensity I_{2D} shows continuous decrease with both moderate electron and hole doping as compared to I^0_{2D} which is I_{2D} at $E_{\mathrm{F}} = 0$. Assuming a fully resonant process and ignoring trigonal warping, I_{2D} is given by [34]

$$I_{\mathrm{2D}} \propto \left(\frac{\gamma_{\mathrm{K}}}{\gamma_{\mathrm{e-ph}} + \gamma_{\mathrm{D}} + \gamma_{\mathrm{ee}}} \right)^2 \tag{1.33}$$

in which $\gamma_{\mathrm{e-ph}} + \gamma_{\mathrm{D}} + \gamma_{\mathrm{ee}}$ is the total electron scattering rate with $\gamma_{\mathrm{e-ph}}$ is the electron-phonon scattering rate, γ_{D} is electron-defect scattering rate and γ_{ee} the electron-electron scattering rate. γ_{K} is scattering rate for zone-edge phonons and γ_{Γ} is scattering rate for zone-centre phonons making $\gamma_{\mathrm{e-ph}} = \gamma_{\mathrm{K}} + \gamma_{\Gamma}$. In the total electron scattering rate, γ_{D} and $\gamma_{\mathrm{e-ph}}$ do not depend upon E_{F}, but γ_{ee} scales linearly with $|E_{\mathrm{F}}|$.

As $|E_{\mathrm{F}}|$ reaches $E_{\mathrm{L}}/2$, I_{2D} starts to reduce rapidly beyond the threshold of $E_L = 2|E_{\mathrm{F}}| + \hbar\omega_{\mathrm{2D}}$. The changes in I_{2D} can be understood with interference of quantum pathways. Figure 1.11a shows two representative pathways I and II for 2D mode. For a two-phonon process, the intensity is given by [36]

$$I_{\mathrm{2D}} = \left| \sum_{\boldsymbol{k}} L_{\boldsymbol{k}} R_{\boldsymbol{k}} \right|^2 \tag{1.34}$$

where $L_{\boldsymbol{k}}$ is the transition matrix element and $R_{\boldsymbol{k}}$ is the resonance factor that is dependent upon relative phase between pathways given by

$$R_{\boldsymbol{k}} = \frac{1}{(E_{\mathrm{L}} - E_{\boldsymbol{k}} - i\gamma)(E_{\mathrm{L}} - \hbar\omega_{\mathrm{2D}}/2 - E_{\boldsymbol{k}'} - i\gamma)(E_{\mathrm{L}} - \hbar\omega_{\mathrm{2D}} - E_{\boldsymbol{k}''} - i\gamma)} \tag{1.35}$$

where $E_{\boldsymbol{k}}$ is vertical transition energy at wavevector $\boldsymbol{k}$, $E_{\boldsymbol{k}'}$ and $E_{\boldsymbol{k}''}$ are energies of intermediate states and γ is the energy broadening.

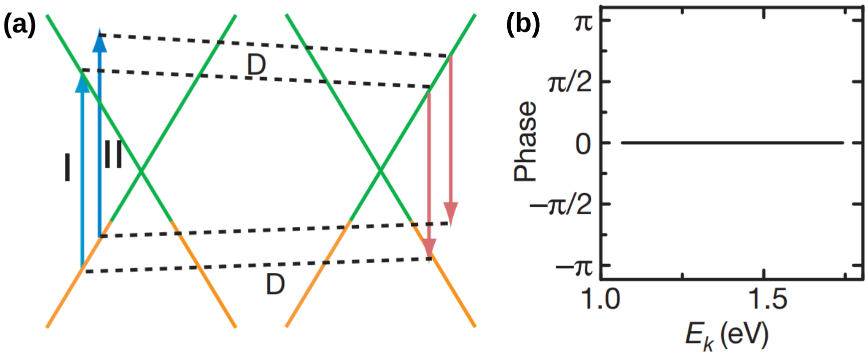

Figure 1.11: (a) Two representative Raman 2D mode pathways I and II (b) Phase of $R_{\boldsymbol{k}}$ for pathways at E_L=1.58 eV. Adapted from [36].

Figure 1.11b shows the phase of quantum pathways with respect to $E_{\boldsymbol{k}}$ for processes like I and II in figure 1.11a. Thus, the pathways involved in 2D mode are all in phase and their interference is constructive. Because of this, blocking of Raman pathways cause reduction in I_{2D}. When all resonant pathways are blocked due to high doping ($|E_{\mathrm{F}}| \to E_{\mathrm{L}}/2$), the 2D mode becomes negligible and $I_{\mathrm{2D}} \to 0$.

Correlations and comparison between G and 2D mode parameters:

The different charge doping dependence of I_{G} and I_{2D} makes their ratios $I_{\mathrm{2D}}/I_{\mathrm{G}}$ and $\sqrt{I_{\mathrm{G}}/I_{\mathrm{2D}}}$ with respect to E_{F} quite informative. Figure 1.12b shows these intensity ratios under moderate charge doping to be symmetric with respect to $E_{\mathrm{F}} = 0$. For $|E_{\mathrm{F}}| \ll E_{\mathrm{L}}/2$ and assuming that $\gamma_{\mathrm{D}} \ll \gamma_{\mathrm{e-ph}}$ i.e. graphene remains pristine under charge doping [34],

$$\sqrt{\frac{I_{\mathrm{G}}}{I_{\mathrm{2D}}}} = \frac{\sqrt{\frac{I_{\mathrm{G}}}{I_{\mathrm{2D}}}|_0}}{\gamma_{\mathrm{e-ph}} + \gamma_{\mathrm{D}}}(\gamma_{\mathrm{e-ph}} + \gamma_{\mathrm{D}} + 0.06|E_{\mathrm{F}}|) \tag{1.36}$$

where $\frac{I_{\mathrm{G}}}{I_{\mathrm{2D}}}|_0$ is the ratio at $E_{\mathrm{F}} = 0$. Thus, the above equation (1.36) (dashed line in figure 1.12b) can be used to estimate the different scattering rates.

The correlations between parameters can be used to observe a universal behaviour between different samples. Figure 1.12c shows correlation between $\Delta\omega_{\mathrm{G}}$ and $\Delta\Gamma_{\mathrm{G}}$ seen in [30] that agrees with equations (1.30) and (1.29). The other correlation shown by figure 1.12d is

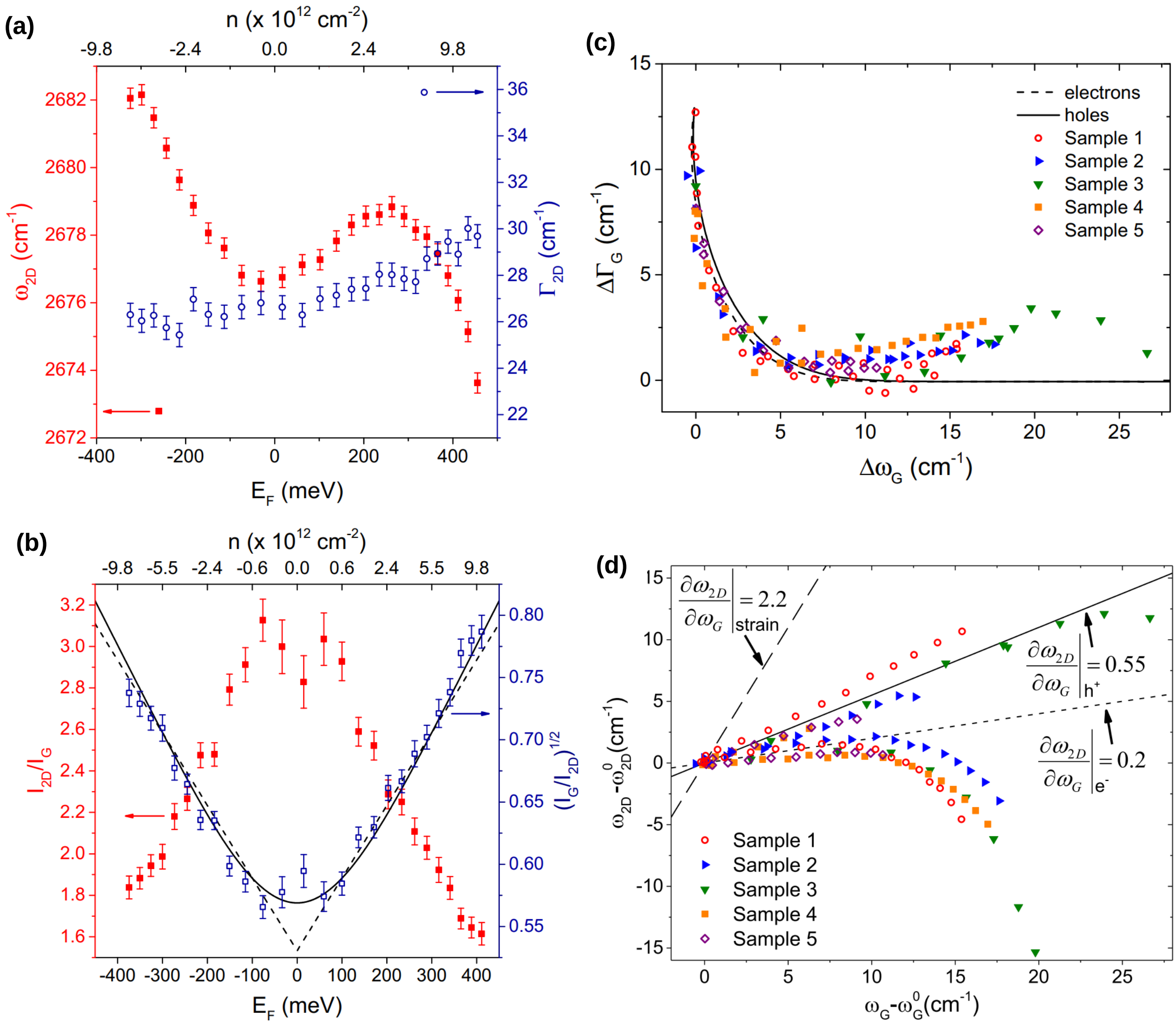

Figure 1.12: (a) ω_{2D} and Γ_{2D} and (b) I_{2D}/I_G and $\sqrt{I_G/I_{2D}}$ as a function of doping, dashed line corresponds to equation1.36 (c) correlations between $\Delta\omega_G$ and $\Delta\Gamma_G$ (d) and between $\Delta\omega_G$ and $\Delta\omega_{2D}$ in which the short dashed, continuous and long dashed lines represent electron doping, hole doping and strain. Adapted from [30].

between $\Delta\omega_G$ and $\Delta\omega_{2D}$ from [30] and is more dispersed than the correlation between $\Delta\omega_G$ and $\Delta\Gamma_G$ because of the non-universal dependence of ω_{2D} on E_F.

2D' mode:

The 2D' mode shows a reduction in its frequency for both electron and hole doping [42]. The intensity of 2D' mode is given by [34, 41]

$$I_{2D'} \propto \left(\frac{\gamma_\Gamma}{\gamma_{e-ph}+\gamma_D+\gamma_{ee}}\right)^2 \tag{1.37}$$

As hole or electron charge carrier density gets higher, the intensity of the relatively weak 2D' mode decreases, making its observation difficult during experiments.

Defect related modes:

When graphene is under a high gate bias, defects can be created in it leading to changes in overall Raman spectrum as shown in the bottom panel figure 1.7. The Raman modes D, D' and D+D' are seen to emerge when defects are created in graphene. Since the 2D mode is the overtone of the D mode, the trend of variation $\Delta\omega_{2D}$ is the same as change in ω_D with charge doping [30] and the doping dependence of D and 2D modes is similar [43]. The density of defects can be quantified by the ratio of intensities of G and D mode [44]. The behaviour of the D mode and D' mode in defected graphene under charge doping has been studied in [43, 45].

Thickness of graphene

The Raman spectrum of a given flake can be used to determine the number of graphene layers present in it. The low-frequency Raman modes of graphene can give information about its thickness [46] as well as the stacking order of layers [47, 48]. The lineshape of 2D mode and the number of peaks that are needed to fit it have also been used to estimate the number of layers [14].

The number of layers in a graphene flake also influences the G and 2D mode significantly. In this thesis, we have used I_G to estimate the number of layers as in figure 1.13 from [49].

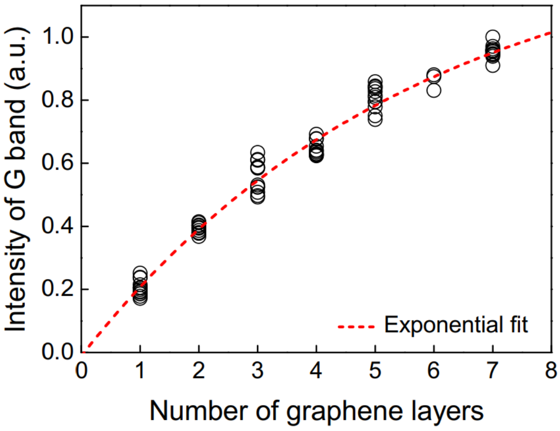

Figure 1.13: I_G as a function of the number of graphene layers. Adapted from [49].

In this section, we have discussed about the electronic and vibrational properties of graphene, including the Raman modes of graphene and their usage as a probe for charge doping, which are utilized extensively in this thesis. We now move on to discussing the other 2D material used in our vdWH of TMD/graphene, the transition metal dichalcogenides.

1.2 Transition metal dichalcogenides

The transition metal dichalcogenides (TMDs) is a group of 2D materials that were thinned down to monolayer limit soon after the isolation of monolayer graphene [50], which are of particular interest due to them being direct bandgap semiconductors [51, 52, 53] with rich exciton physics. Although the Raman modes of TMDs are also interesting, they are not studied in this work because the excitons in TMDs are sufficient to study the interactions between TMD and graphene due to the effects of graphene on excitons of TMDs that can be easily probed, as discussed in section 1.4.2.

1.2.1 Crystal structure

TMDs have chemical formula MX_2 in which M is a transition metal and X is a chalcogen atom. The layer of M atoms is sandwiched between two layers of X atoms. In this thesis, we have mainly used monolayer $MoSe_2$, a type of TMD, in crystalline phase 2Hc. The crystal structure of TMDs in 2Hc phase is shown in figure 1.14a, which shows a hexagonal structure when viewed from top, similar to that of graphene. It should be noted that the TMDs in 2Hc phase have broken inversion symmetry because the atoms in A and B sites are different [13]. The first Brillouin zone is hexagonal as well analogous to that of graphene (figure 1.14b) [54].

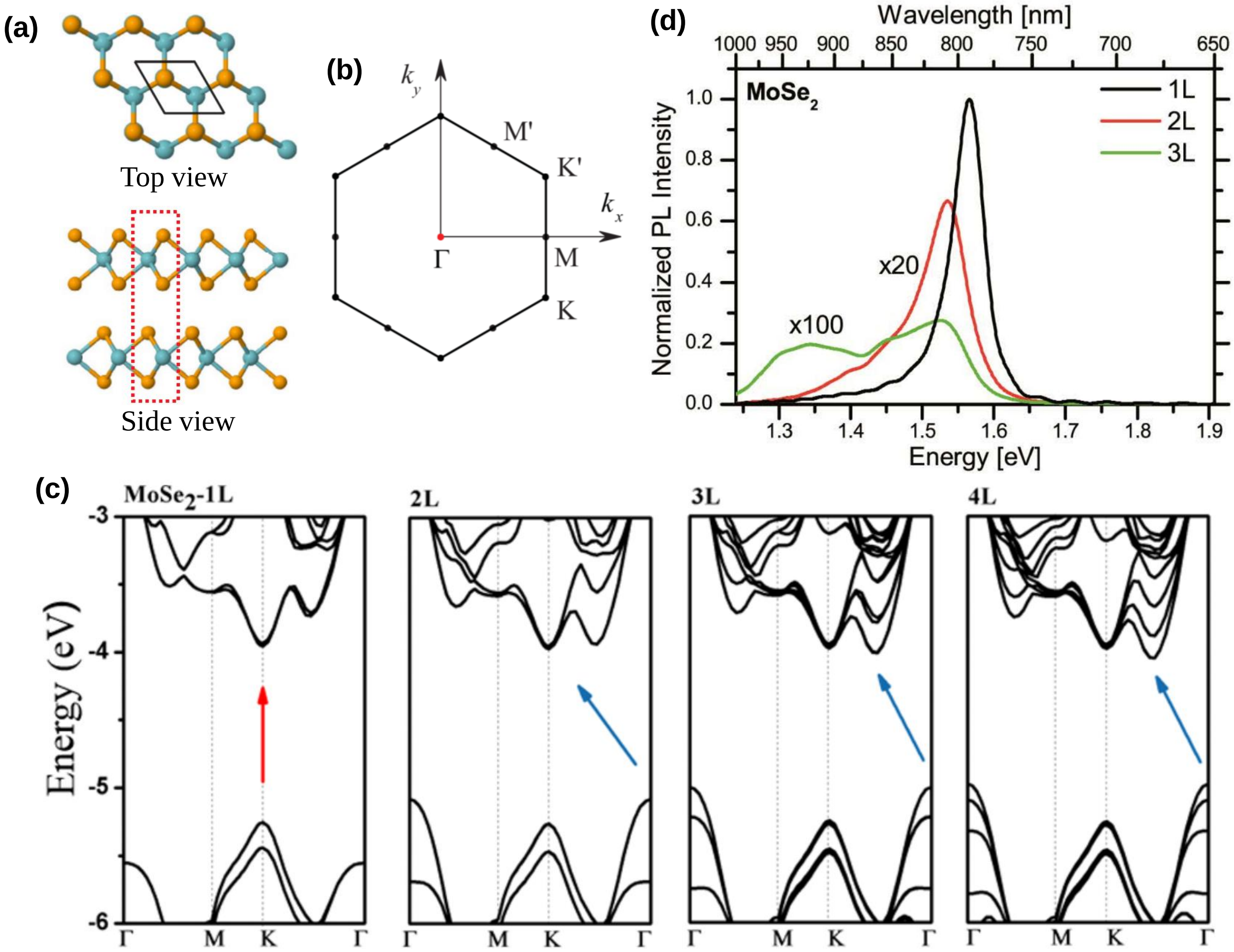

Figure 1.14: (a) Top and side view of TMDs in 2Hc polytype with M atom and X atoms represented by blue and orange spheres respectively, the black rhombus and red box shows primitive unit cell. (b) First Brillouin zone of monolayer TMD (c) evolution of calculated band structure of $MoSe_2$ with the changing layer thickness (d) photoluminescence of $MoSe_2$ as a function of layer thickness. Adapted from [55, 54, 53, 56].

1.2.2 Band structure

Indirect to direct bandgap transition

The Molybdenum and Tungsten based TMDs undergo an indirect to direct bandgap conversion when thinned down from bulk to monolayer limit [51, 52, 53]. Figure 1.14c shows the evolution of calculated band structure of $MoSe_2$ with the changing layer thickness [53]. In these TMDs, the electronic states at the Γ point contain contributions from the d_{z^2} orbitals of the M atom and the p_z orbitals of the X atom. On the other hand, the K or K' point have conduction band (CB) and valence band (VB) states that are strongly localized in the M atom plane because they have contributions from $d_{x^2y^2} \pm id_{xy}$ orbitals (for VB) and d_{z^2} orbitals (for CB) of M atom slightly mixed with the $p_x \mp ip_y$ orbitals of the X atom respectively. There is significant spatial overlap between adjacent layers of the orbitals for Γ point in VB and the points along Γ - K direction in CB. Thus, when these TMDs are thinned down from bulk to monolayer, the indirect bandgap energy related to the separation between Γ point and a point along Γ - K increases while the CB and VB at K or K' point remain almost unaffected making the direct bandgap smaller than the indirect one [57, 58].

The indirect to direct bandgap conversion results in a huge increase in emission efficiency because the lowest energy transition does not need interaction with a phonon to conserve the momentum anymore. Hence, the photoluminescence signals of the monolayers are massively increased as compared to the thicker layers, as can be seen in figure 1.14d for the case of $MoSe_2$ [56].

Spin-orbit coupling

As the band structure of these TMDs involve d orbitals of relatively heavy elements, there is a strong spin-orbit coupling that lifts the degeneracy of spin of the bands resulting in splitting of electronic bands [57, 54]. At the K point in monolayer TMDs, VB has splitting of about 200 meV and 400 meV for Mo based and W based TMDs respectively [59]. This splitting in VB gives rise to two valence sub-bands and therefore, to two possible excitonic transitions: A and B excitons. For CB, a smaller splitting (of the order of a few 10s of meV) occurs because of partial compensation between contributions from p and d orbitals [60, 61]. In $MoSe_2$ and $MoTe_2$, the direction of splitting of CB is the opposite as compared to the direction of splitting in VB. On the other hand, for W based TMDs and MoS_2, the direction of splitting of CB is same as that of VB. This dependence of splitting direction upon the TMDs is represented in figure 1.15a for $MoSe_2$ and $MoTe_2$ and 1.15b for W based TMDs and MoS_2 from [57]. As a consequence of this, the lowest energy transitions in Mo based TMDs (except MoS_2) are spin allowed and optically active, making these TMDs to be referred to as 'bright' TMDs. However, the lowest energy transitions in W based TMDs and MoS_2 are spin forbidden and optically inactive, making them 'dark' TMDs. Moreover, the K and K' points have the bands splitting in opposite directions (figure 1.15). The K and K' valleys can be selectively excited by circularly polarized σ^+ and σ^- light respectively, giving rise to valley degree of freedom.

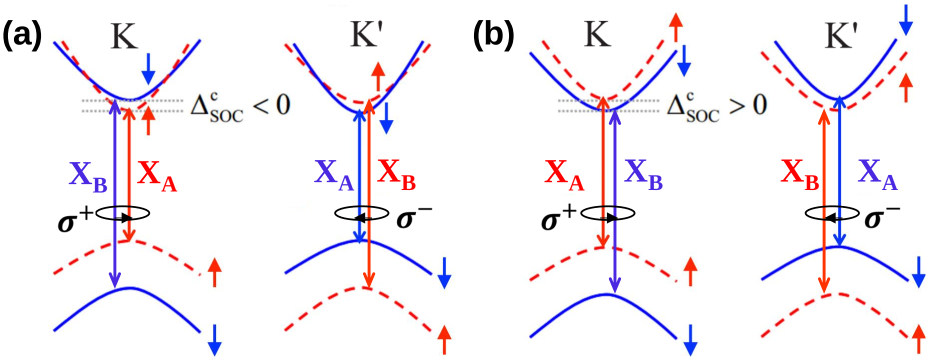

Figure 1.15: Sketch of fine structure at K and K' valleys for (a) $MoSe_2$ and $MoTe_2$ (bright TMDs) and (b) MoS_2 and W based TMDs (dark TMDs) in momentum-energy space. Adapted from [57, 62].

1.2.3 Excitonic properties

Excitons

When a photon with energy higher than that of the optical gap is incident on it, its absorption causes an electron to be excited from VB into CB, creating a hole in VB (figure 1.16a). The electron and hole interact with phonons and decay to the conduction band minimum and valence band maximum respectively. The charges then recombine emitting a photon. In case the charges recombine without relaxing to the band extrema, then the emission is called as 'hot luminescence'. In TMDs, there is a very strong Coulomb interaction between the electron-hole pair and it can be considered as a quasiparticle called as an exciton [25]. While the direct term in the Coulomb interaction corresponds to the binding energy of the excitons (to be discussed in the next subsection), the exchange term at short distances defines the fine structure of excitons i.e. splitting of dark and bright transitions [57]. The splitting of bands leads to two allowed transitions denoted by A exciton (X^0) and B exciton as shown in figure 1.15 out of which the former is a lower energy transition than the latter.

Rydberg series of excitons

Excitons in TMDs have a Rydberg like series anologous to a hydrogen-like system [64]. The exciton momentum is $\boldsymbol{K}_{\mathrm{exc}} = \boldsymbol{k}_{\mathrm{e}} + \boldsymbol{k}_{\mathrm{h}}$ where $\boldsymbol{k}_{\mathrm{e}}$ and $\boldsymbol{k}_{\mathrm{h}}$ are electron and hole momentum respectively and the exciton mass is $M_{\mathrm{exc}} = m_{\mathrm{e}} + m_{\mathrm{h}}$ where m_{e} and m_{h} are electron and hole effective masses respectively. Thus, the dispersion relation of an exciton can be given by [65]

$$E^{(n)}_{\mathrm{exc}} = E_{\mathrm{g}} + \frac{\hbar \boldsymbol{K}^2_{\mathrm{exc}}}{2M_{\mathrm{exc}}} - E^{(n)}_{\mathrm{b}} \tag{1.38}$$

and is represented in figure 1.16b where E_g is the electronic gap energy (which corresponds to single particle gap renormalized by electron electron interaction [66]) and $E^{(n)}_{\mathrm{b}}$ is the exciton binding energy of the nth state in Rydberg series. The lowest possible E_{exc} is $E^{(0)}_{exc}$ called as the optical gap for which $\boldsymbol{K}_{\mathrm{exc}} = 0$. In the 2D limit, the electron and hole are spatially

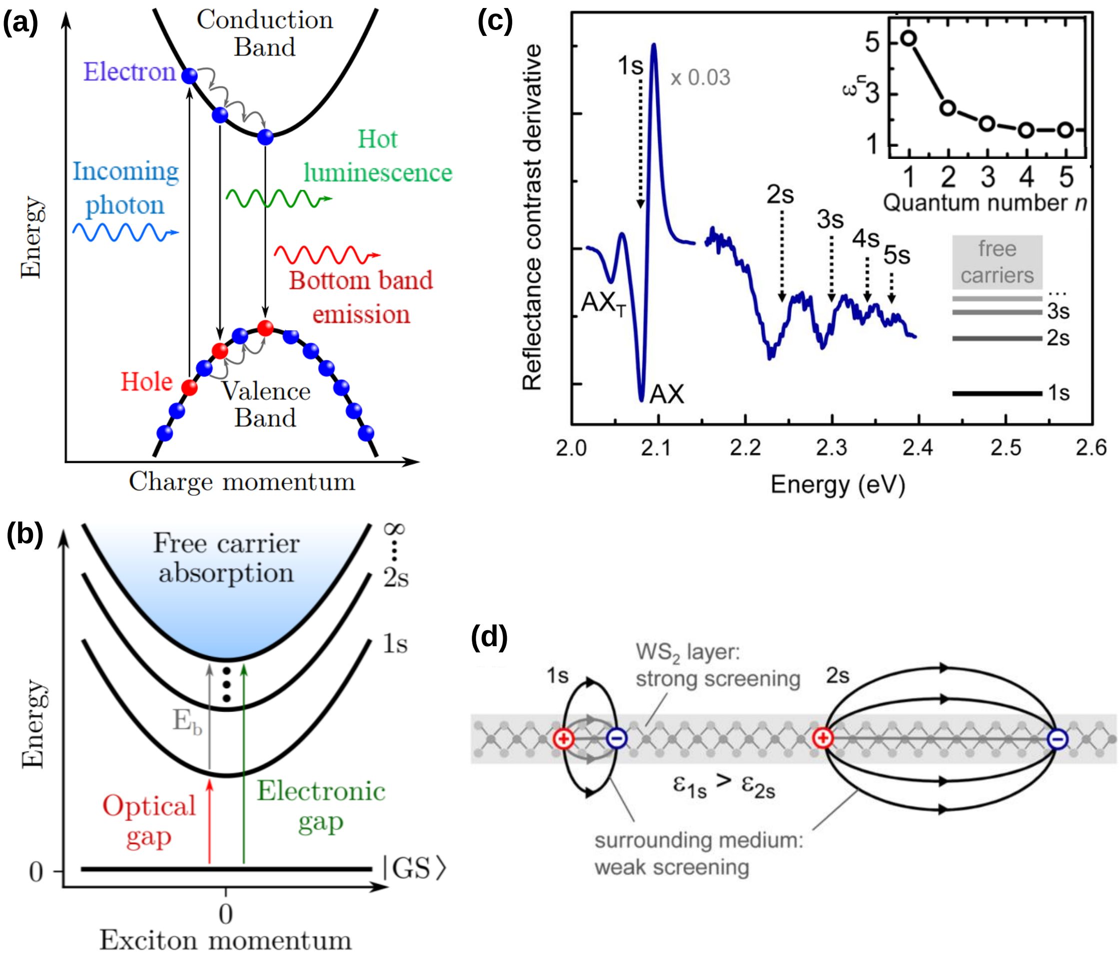

Figure 1.16: (a) Schematic of free carrier absorption and photoluminecence process (b) Exciton dispersion of Rydberg states in energy-momentum space (c) Reflectance contrast derivative of WS_2 taken at low temperature showing absorption lines of Rydberg states of the A exciton up to $n = 5$, inset: effective dielectric constant as a function of quantum number n (d) Schematic representation of 1s and 2s excitons in a nonuniform dielectric environment. Adapted from [22, 63].

confined leading to smaller Bohr radii and stronger oscillator strengths as compared to 3D hydrogen model [63, 65]. Assuming a homogeneous effective dielectric constant ϵ_{eff}, the binding energy is [65]

$$E_{\mathrm{b}}^{(n)} = \frac{\mu \mathrm{Ry}}{m_0 \epsilon_{\mathrm{eff}}^2 (n - 1/2)^2} \tag{1.39}$$

where $\mu = m_{\mathrm{e}} m_{\mathrm{h}} / (m_{\mathrm{e}} + m_{\mathrm{h}})$ is the reduced mass of the electron-hole pair, Ry is the hydrogen Rydberg constant and m_0 is the free electron mass. Considering $\mu \approx 0.25 m_0$ and $\epsilon_{\mathrm{eff}} \approx 5$, $E_{\mathrm{b}}^{(n=1)}$ can be estimated to be around 500 meV [67, 68], a much higher value as compared to other semiconductors like bulk GaAs having binding energy of about 4.3 meV [69]. Moreover, as $E_{\mathrm{b}}^{(n)}$ also defines exciton stability with respect to temperature by it being compared to thermal fluctuations, the excitons in TMDs are stable even at room temperature because $E_{\mathrm{b}}^{(n)}$ is larger than $k_{\mathrm{B}} T \approx 26$ meV.

However, comparing values obtained from equation (1.39) of 2D-hydrogen model to the observed values in [63] obtained using the experimental reflectance contrast derivative spectrum of WS_2 (figure 1.16c) reveals that 1.39 overestimates $E_b^{(n)}$ for smaller values of n. This deviation is because of effective dielectric constant changing significantly for $n = 1, 2$ (figure 1.16c inset). As the electric field between electron and hole in an exciton permeating both the TMD and the surrounding medium changes with the spatial distance between charges, the effective screening changes as well (figure 1.16d)[63, 70, 71]. The Rytova-Keldysh potential can be used as an improved expression with considerations for dielectric properties of the surrounding medium [63, 70, 72, 68] :

$$V(r) = -\frac{\pi e^2}{2r_0}\left[H_0\left(\frac{r}{r_0}\right) - Y_0\left(\frac{r}{r_0}\right)\right] \tag{1.40}$$

in which r is the distance between electron and hole, r_0 is called as the screening length related to 2D polarizability of TMD, H_0 and Y_0 are Struve and Bessel functions respectively [70, 72]. When $r > r_0$, one obtains $V(r) \sim 1/r$ recovering the potential in 2D-hydrogen model. When $r < r_0$, the electric field is confined inside TMD increasing the effective screening and gives $V(r) \sim \ln(\mathrm{r})$.

Temperature dependent photoluminescence in TMDs

The PL spectrum of TMDs changes significantly as a function of temperature as shown in figure 1.17a for $MoSe_2$ [73]. As we have performed PL spectroscopy measurements on $MoSe_2$ at both low temperature (< 20 K) and at room temperature in this work, understanding the known changes in PL of TMDs with changing temperature is important. The PL spectra show two clear features: the first is the exciton X^0 (which will denote A_{1s} from here onwards) and the second is its charged exciton or trion denoted by X^* here onwards. Trions can be either positively charged (X^+) or negatively charged (X^-) and have a binding energy of around a few 10s of meV [73, 74]. It should be noted that the thermal fluctuations energy at room temperature $k_\mathrm{B}T$ is very close to the X^* binding energy, making its observation as a low energy shoulder to exciton.

Figure 1.17a and the ratio of areas shown in figure 1.17c show that X^* diminishes as $T >$ 55 K which happens because of electrons escape the trion bound state because of thermal fluctuations [73].

The other change in PL spectra with respect to decrease in temperature is the blueshift of both X^0 and X^* and their peak positions (as shown in figure 1.17b) can be fit by a modified Varshni equation [75, 76].

A broadening of X^0 peak is seen in figure 1.17a with increase in temperature. The homogeneous thermal broadening is dominant at all temperatures, while the increase in linewidth with increase in temperature is attributed to scattering of excitons with phonons at Γ point and Λ point (halfway between Γ point and K point of first Brillouin zone) [77, 78].

1.2.4 Exciton dynamics

The dynamics of excitons can be understood using the three-level model as shown in figure 1.18a with the following steps:

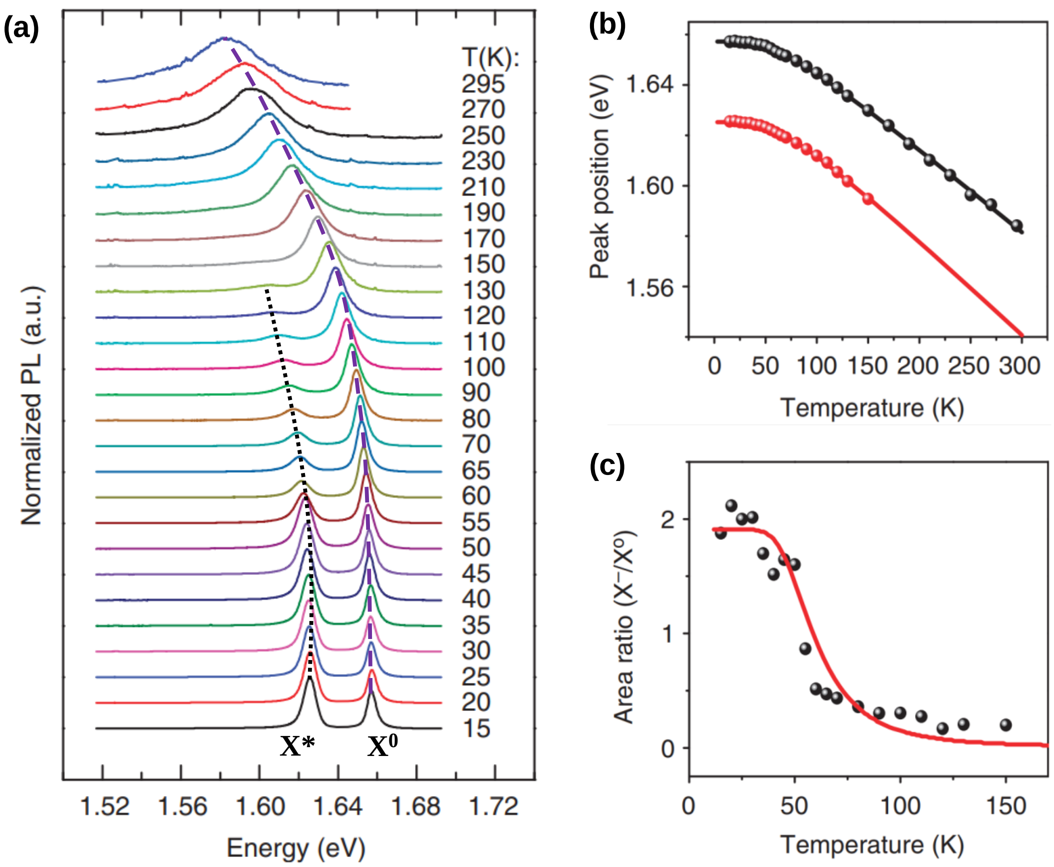

Figure 1.17: (a) Temperature dependence of PL spectra of $MoSe_2$, the dotted and dashed lines are a guide to eye for X* and X^0 respectively (b) Peak positions of X^0 and X* and (c) ratio of areas X^*/X^0 as a function of temperature. Adapted from [73].

Hot exciton formation

A population of hot excitons can be formed in TMDs (i.e. the excitons formed outside of lightcone shown in figure 1.18b,c) by resonant as well as non-resonant excitation with energy smaller than free carrier bandgap. As will be discussed in section 3.3.6, the intensity in PL spectra depends upon the initial population of hot excitons that is formed.

Relaxation

This hot exciton population relaxes with a timescale of τ_{relax} to the energy level of excitons. The timescale of τ_{relax} depends upon electron-phonon, electron-photon and electron-hole interactions. The exciton density formed at this stage is related to the possible non linear processes like Auger recombination (to be discussed in section 3.3.3).

Exciton recombination

This exciton population recombines with the ground state via nonradiative or radiative pathways. Exciton recombination depends upon both intrinsic and extrinsic factors. The extrinsic factors like strain, temperature, surrounding materials, adsorbates, defects etc. influence nonradiative recombination that occurs through pathways like scattering by phonons or defects which bypass photon emission. Radiative recombination is an intrinsic process which describes the exciton recombination via emitting a photon. In general, exciton PL recombination time τ_{X^0} is given by

$$\frac{1}{\tau_{\mathrm{X}^0}} = \frac{1}{\tau_{\mathrm{rad}}} + \frac{1}{\tau_{\mathrm{nr}}} \tag{1.41}$$

where τ_{rad} is radiative recombination time and τ_{nr} is nonradiative recombination time.

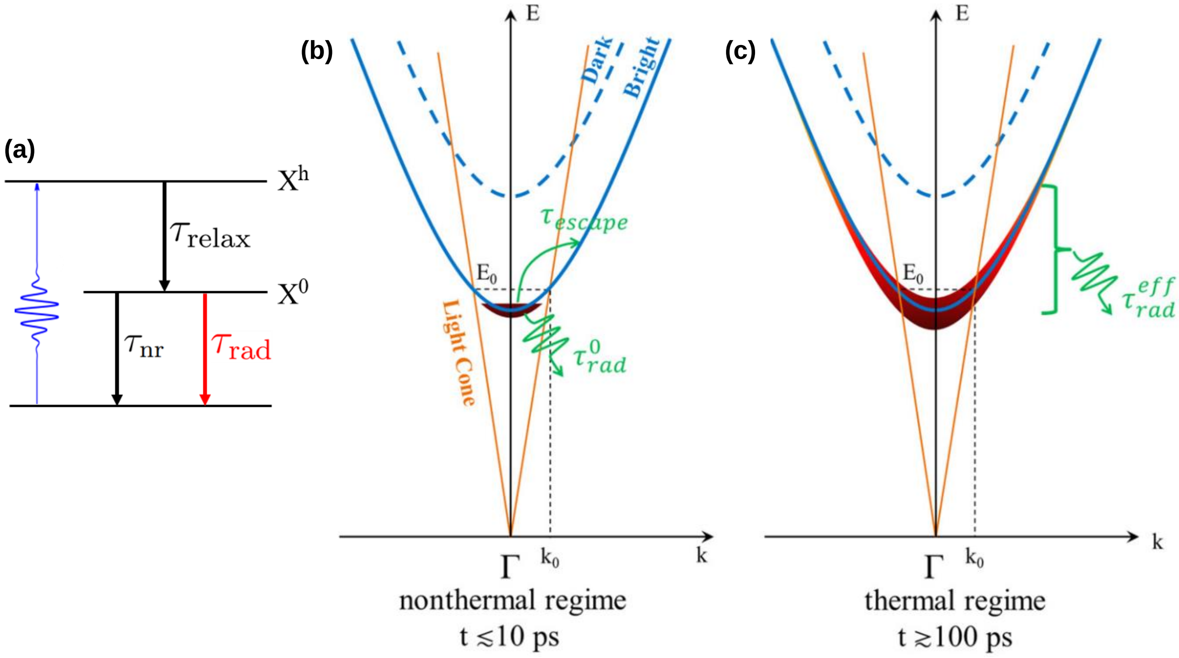

Figure 1.18: (a) Three-level model for exciton dynamics, laser excitation is show in blue wavy arrow. Schematic of exciton population (b) before thermalization and (c) after thermalization. Adapted from [79].

For radiative recombination to occur, the excitons have to fulfill momentum conservation condition and only the excitons having momentum $|\boldsymbol{K}_{\mathrm{exc}}| \leq 2\pi/\lambda$ can recombine radiatively by emitting photon having wavelength λ. This condition defines a lightcone as shown in figure 1.18b,c which is 10^3 smaller than the first Brillouin zone, making only the excitons with $|\boldsymbol{K}_{\mathrm{exc}}| \approx 0$ to be able undergo radiative recombination. The excitons outside of the lightcone can give away their momentum to phonons or defects in order to recombine radiatively. The intrinsic exciton radiative recombination time is given by [79, 80]

$$\tau^0_{\mathrm{rad}} = \frac{1}{2\Gamma_{rad}} = \frac{\hbar\epsilon'}{2\boldsymbol{k_0}} \left(\frac{E_{X^0}}{e\hbar\nu}\right)^2 \left(a_B^{2D}\right)^2 \tag{1.42}$$

where Γ_{rad} is the radiative recombination rate, ϵ' is the dielectric constant, $\boldsymbol{k}_0 = E_{X^0}\sqrt{\epsilon'}/(\hbar c)$ is the light wavevector (in which E_{X^0} is the exciton transition energy), ν the Kane velocity related to the interband matrix element of the electron momentum and a_B^{2D} is the 2D Bohr radius.

With the increase in temperature, the X^0 population can be thermalized by exciton-exciton and exciton-phonon interactions. In this case, the recombination rate of the exciton is given by the thermal average of the exciton recombination rate which depends on the kinetic energy E_0 of the excitons recombining radiatively and the thermal energy $k_B T$. The effective exciton lifetime as a function of temperature is given by [80]

$$\tau_{\mathrm{rad}}^{\mathrm{eff}} = \frac{3}{2} \frac{k_B T}{E_0} \tau_{\mathrm{rad}}^{0} \tag{1.43}$$

which is valid for $k_B T \gg \gamma_h, E_0$ where γ_h is homogeneous linewidth of X^0 [81]. The excitons can escape out from the radiative window because of exciton-phonon interactions at a timescale of τ_{esc} (figure 1.18b).

For 7 K $< T <$ 40 K, inset of figure 1.19a shows that the decay time of $MoSe_2$ monolayer remains constant in ps range, implying that τ_{rad}^0 is faster than exciton-phonon interaction time, making the exciton decay driven by τ_{rad}^0. The X^0 PL intensity for 7 K $< T <$ 70 K plotted in inset of figure 1.19b is quite constant showing that there is no signature from nonradiative recombination of excitons [79].

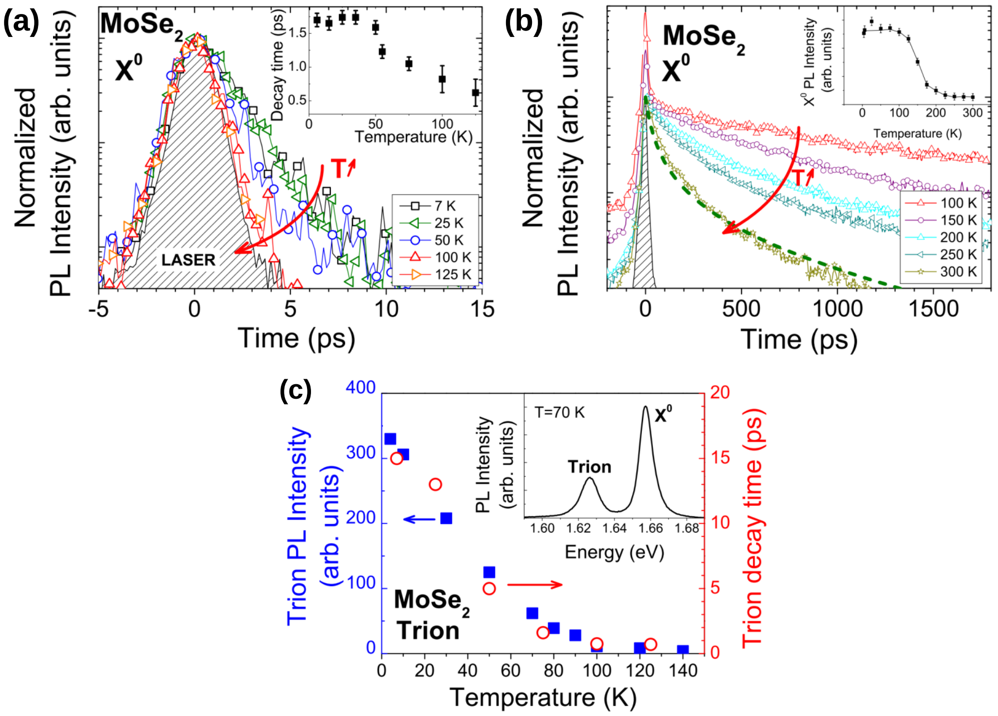

Figure 1.19: (a) Temperature dependence dynamics of monolayer $MoSe_2$, inset: PL decay time as a function of T (b) time resolved PL of X^0 for T = 100–300 K, inset: temperature dependence of the time integrated X^0 PL intensity (c) Temperature dependence X^* PL intensity and the X^* PL decay time, inset: PL spectrum of the monolayer $MoSe_2$ at T = 70 K. Adapted from [79].

As the temperature increases beyond a few 10s of K, the fraction of excitons lying in the lightcone becomes very small and the X^0 PL intensity decreases (inset of figure 1.19b) giving a long radiative decay time. For thermalized regime (figure 1.18c), τ_{X^0} is estimated by $1/\tau_{X^0} = 1/\tau_{\mathrm{rad}}^{\mathrm{eff}} + 1/\tau_{\mathrm{nr}}$. When $T >$ 100 K, the τ_{X^0} decreases with temperature and is in ns range (figure 1.19) and nonradiative recombination is the main channel of recombination for the thermalized population [79]. There are two nonradiative processes: (i) trapping of photogenerated excitons on defects and (ii) exciton-exciton annihilation process called as Auger recombination [82, 83, 84].

Figure 1.19c shows trion decay time and X* intensity as a function of temperature. At $T =$ 7 K, the trion radiative recombination time is longer than that of exciton attributed to a reduction in oscillator strength due to a stronger localization [79, 85, 86]. The continuous decrease of trion decay time with increase in temperature beyond 50 K can be explained by the trion-phonon interaction time becoming shorter than the trion radiative recombination time.

1.2.5 Excitonic properties in charge tunable samples

TMDs are excellent candidates for optoelectronic devices because of their strong light-matter interactions. Figure 1.20a shows the schematic of an FET device made with $MoSe_2$. The PL spectrum of this device taken at T =30 K (figure 1.20b) shows X^0 and X^- peaks, with the binding energy of X^- being 30 meV [73].

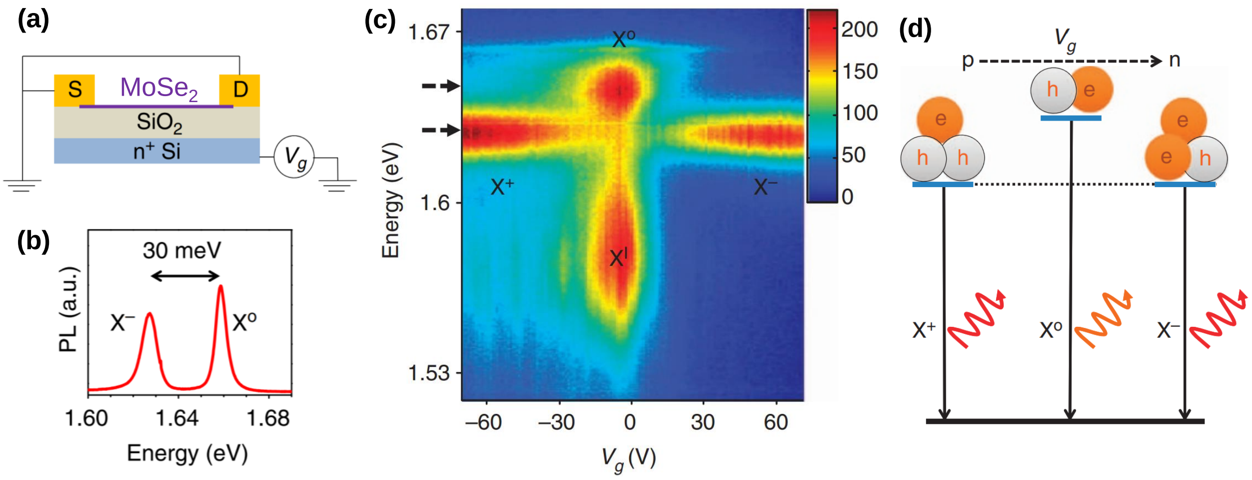

Figure 1.20: (a) Schematic of back-gated $MoSe_2$ device (b) PL spectrum of device (c) PL contourplot as a function of voltage (d) schematic of formation of X^- and X^+ because of p-doping and n-doping respectively with back-gate voltage. Adapted from [73].

The effect of gate bias on the PL is shown in figure 1.20c as a contourmap. Four features can be seen in this contourmap: X^0, X^-, X^+ and X^I. Near V_g=0 V, X^0 can be seen near 1.65 eV and a low-energy broad peak X^I, the latter is caused because of excitons trapped to impurities. The peaks X^- and X^+ become more intense with the gate voltage increasing in positive and negative directions respectively. As voltage is increased in positive direction, more electrons are injected into the $MoSe_2$ layer causing it to be n-doped and turning X^0 into X^-. A similar formation mechanism for X^+ upon hole doping can also be thought of and they are represented in figure 1.20d [73]. Similar trends in PL intensity of monolayer $MoSe_2$ as a function of applied voltage have also been seen in other studies [87, 88].

The PL emission from TMDs used in charge tunable samples can be controlled by tuning the charge carrier density in them. As the changing charge carrier density shifts the Fermi level, the excitons interact with the charge carrier density [89]. The presence of these charge carriers and the trions that can be formed from them can strongly influence the emission properties [90]. The control of trion dynamics to tune its optical response is also an active field of work [88]. Also, the optoelectronic properties of TMDs can be altered by coupling the TMD to other layers in vdWH [87, 91, 92, 93] by virtue of their band offsets.

1.3 hBN

Hexagonal boron nitride (hBN) is a stable polytype of Boron nitride [94], a 2D material made up of Boron and Nitrogen. The crystal structure of hBN is given in figure 1.21a and it has lattice constant of 2.5 Å [95] and is anologous to that of graphene (figure 1.1a). It is a wide gap semiconductor with a bandgap of 6 eV and is considered as an insulator [96].

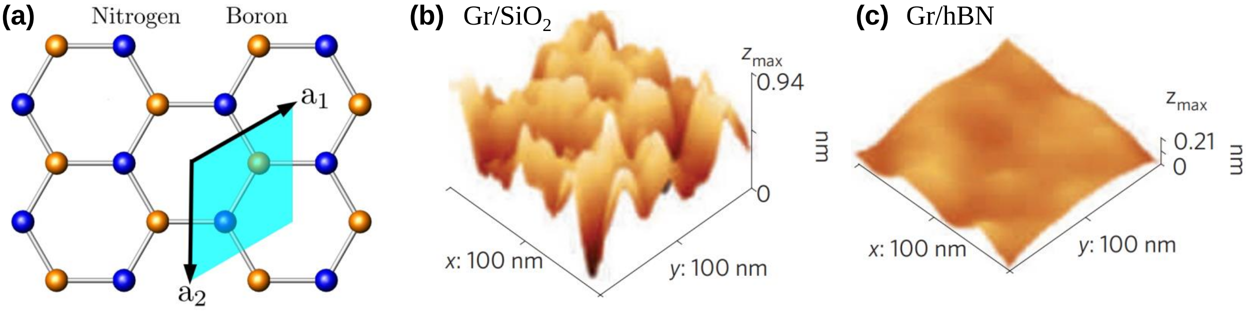

Figure 1.21: (a) Crystal structure of monolayer hBN, highlighted region shows the unit cell with lattice vectors. STM images of (a) SiO_2 supported graphene and (c) hBN supported graphene. Adapted from [97, 98].

1.4 van der Waals heterostructures

The 2D materials can be stacked in a sequence to form a heterostructure in order to study and tune their properties and interactions with each other. The 2D materials have no out-of plane dangling bonds and can be stacked without issues related to lattice mismatch [1]. In their bulk counterparts, individual layers are held together by van der Waals forces. When the 2D materials are stacked on top of each other, these van der Waals interaction forces at the interfaces hold the materials together. Thus, the van der Waals heterostructures (vdWH) can be fabricated (by processes described in upcoming section 2.1.2) with the 2D materials in a desired sequence to unlock their full potential [2]. The vdWH can be made to tailor and engineer properties of 2D materials.

hBN as a protective layer and a substrate

Due to its high thermal stability, chemical inertness and electrical insulation, hBN is considered as a very good protective layer for other 2D materials when exfoliated in the form of large uniform few layers [99, 100, 101].

Furthermore, hBN can also be used as a substrate when it is uniformly flat. Figure 1.21b and figure 1.21c show the scanning tunnelling microscopy (STM) images of graphene supported on top of SiO_2 and hBN respectively. This demonstrates how making hBN as a substrate or the bottom layer of vdWH can reduce the surface roughness [102]. In fact, the first vdWH was fabricated with monolayer graphene deposited on hBN flake [103]. Moreover, this can also help getting rid of photodoping in vacuum [104].

The 2D layers of interest used in making the vdWH can be encapsulated/capped by hBN in order to protect them from both external disturbances and substrate roughness. Such encapsulation provides a homogeneous dielectric environment, which reduces the fluctuations in exciton energy [105]. The PL spectra taken at low temperature on hBN encapsulated TMDs (figure 1.22a) are cleaner with linewidths as narrow as 2 meV, approaching the homogeneous limit [77].

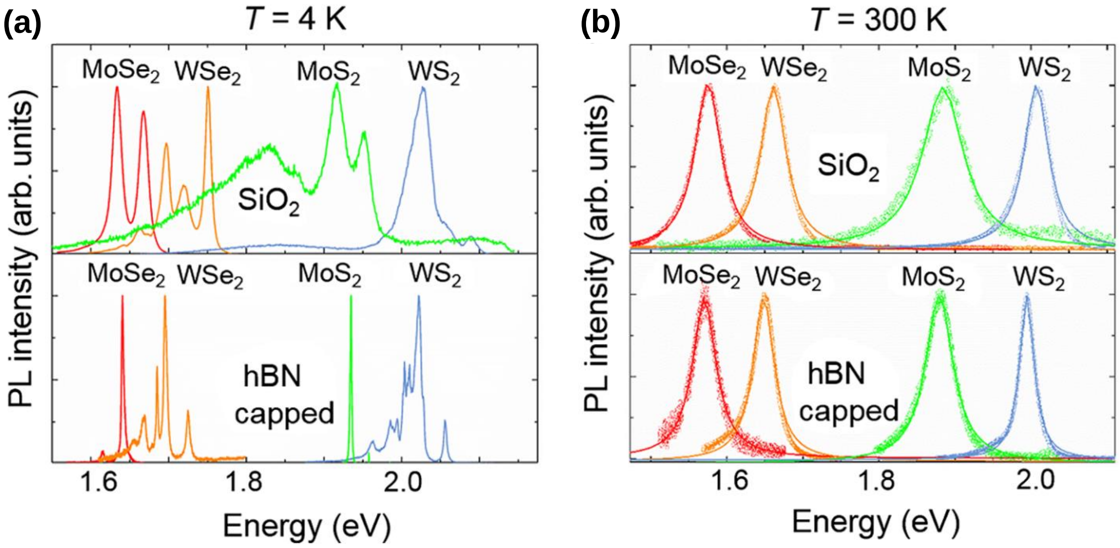

Figure 1.22: PL spectra of $MoSe_2$ (red), WSe_2 (orange), MoS_2 (green) and WS_2 (blue) when deposited on SiO_2 (top panel) and encapsulated/capped by hBN (bottom panel) taken at (a) T=4 K and (b) T=300 K. Adapted from [77].

hBN as a spacer

On virtue of its inert nature, hBN can be used as an atomically thin spacer between other 2D materials. A layer of hBN of a particular thickness, measured by AFM or estimated by optical contrast [106, 107], can be a part of vdWH in a charge tunable device [108, 109].

The hBN spacers of different thicknesses deposited between layers of 2D materials (figure 1.23) have been used to observe the distance dependence of charge and energy transfer mechanisms (which will be detailed in section 3.2.4) [110, 111], much like the distance dependent studies of transfer mechanisms between graphene and nanoplatelets or nanocrystals with MgO spacer [112], graphene and fluorescent emitters with TiO_2 spacer [113] and graphene and quantum dots with poly(methyl methacrylate) (PMMA) as a spacer [114], etc.

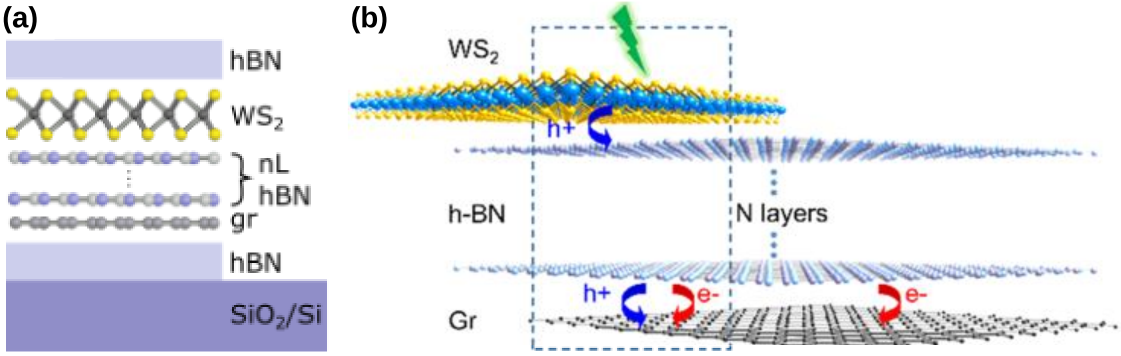

Figure 1.23: (a) and (b) are schematics of samples in which hBN spacers are used for studying distance dependence of charge and energy transfer mechanisms. Adapted from [110, 111].

1.4.1 Controlling exciton radiative timescale in TMDs with hBN

The encapsulation of heterostructure by hBN also causes changes in exciton dynamics as the dielectric environment changes the radiative recombination time. Such a control of exciton radiative dynamics was achieved with sample geometry shown in figure 1.24a where the top and bottom hBN layers form a microcavity-like structure for the $MoSe_2$ monolayer [115]. The weak coupling regime in this structure increases spontaneous emission of photons [116]. The radiative recombination lifetime τ_{rad} of X^0 at low temperature in the $MoSe_2$ monolayer can be tuned by varying the structure of this microcavity, like changing the bottom hBN thickness (as shown in figure 1.24b). According to Fermi's golden rule, the changes in local density of optical modes in the microcavity causes tuning of the spontaneous emission probability which is proportional to the amplitude of the electromagnetic field. This tuning of exciton radiative lifetime in TMDs using hBN will be thoroughly exploited in chapter 3.

Moreover, the X^0 linewidth is also tuned with varying thickness of bottom hBN that results in control of spontaneous lifetime of excitons (as shown in figure 1.24c) [115, 117, 118].

Normalized PL spectra of X^* as a function of time shown in figure 1.24d reveals that the radiative lifetime of X^* denoted by τ^*_{rad} also changes with varying bottom hBN thickness by a factor smaller than the one seen for X^0 (figure 1.24b) [115].

1.4.2 Heterostructures of graphene and TMD

The near field interactions happening at the interfaces of the layers in vdWH strongly influence its optical and electronic properties. The graphene/TMD heterostructures are excellent candidates for understanding the near-field interactions between layers as well as control of their optoelectronic properties. In this section, we will discuss about band alignment of such vdWH and the effects of coupling graphene to TMD.

Band alignment

In 3D limit, the electronic bands of two semiconductors deform to make a continuation of band structure by forming a depletion region [119] and in the case of semiconductor-metal

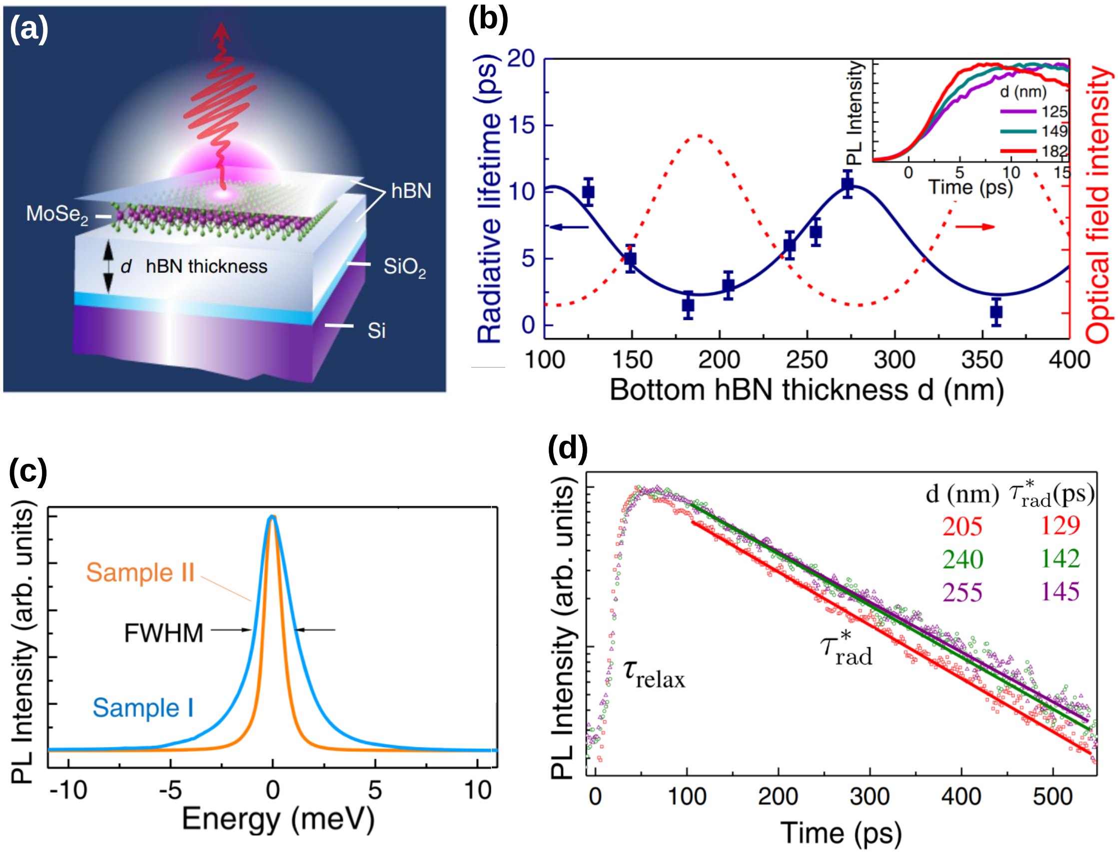

Figure 1.24: (a) Schematic of sample geometry to tune radiative lifetime of $MoSe_2$ layer encapsulated by hBN (b) Calculated (blue line) and measured (blue symbols) τ_{rad} and intensity of electromagnetic field (red dashed line) as a function of bottom hBN thickness d, inset: normalized time resolved PL intensity with changing d (c) normalized PL spectra with different FWHM observed in sample I and II having d = 180 nm and d = 273 nm respectively (d) normalized PL intensity of the X* as a function of time for different bottom hBN layer thicknesses d, the lines are exponential fits. Adapted from [115].

interfaces, the semiconductor bands will bend forming Schottky barriers [62].

But in the 2D limit, the typical size of the depletion region is much larger than the thin layers. Thus, the band structure for the heterostructure of thin layers can be considered as a superposition of bands of the materials involved [120]. The calculated band alignments of Mo based and W based TMDs with respect to graphene are shown in figure 5.2. This relative band alignments between TMDs and graphene have been experimentally studied via techniques like nanoangle-resolved photoemission spectroscopy (nano-ARPES) [121], submicrometer angle-resolved photoemission spectroscopy (µ-ARPES) [122], transport measurements [91], etc.

For the graphene/TMD heterostructures, the Dirac point of neutral graphene lying between the conduction band minimum and valence band maximum (figure 5.2) implies that it is a model donor-acceptor system for both electrons and holes.

Figure 1.25: Calculated band alignments of Mo based and W based monolayer TMDs and monolayer graphene. Adapted from [123, 124].

Importance of coupling between layers

A good coupling between layers of TMD/graphene heterostructure is very important as impurities can cause the layers to decouple affecting the optical properties of the heterostructure. Figure 1.26 shows the influence of coupling between layers determined by atomic force microscopy on the PL spectra of TMD and Raman spectra of graphene [125]. The PL spectra taken at room temperature (figure 1.26b) show a strong quenching or reduction in PL intensity on coupled MoSe$_2$/graphene as compared to bare MoSe$_2$. However, the PL intensity on decoupled MoSe$_2$/graphene is similar to that of bare MoSe$_2$ due to the decoupling between layers [125, 126]. The coupled MoSe$_2$/graphene shows an upshift and sharpening of G mode (due to difference in intrinsic doping) , upshift of 2D mode alongwith decrease in intensity ratio I_{2D}/I_G in Raman spectra as compared to the decoupled MoSe$_2$/graphene (figure 1.26c).

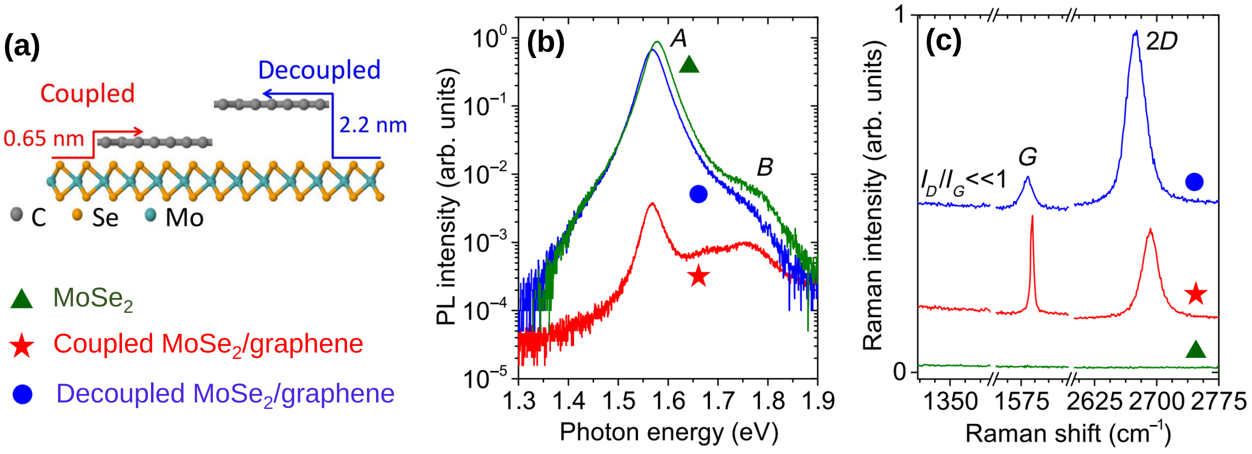

Figure 1.26: (a) Height difference between MoSe$_2$ and graphene measured by atomic force microscopy used to determine the coupled and decoupled regions (b) PL spectra in log scale and (c) Raman spectra taken on the denoted three different regions at room temperature. Adapted from [125].

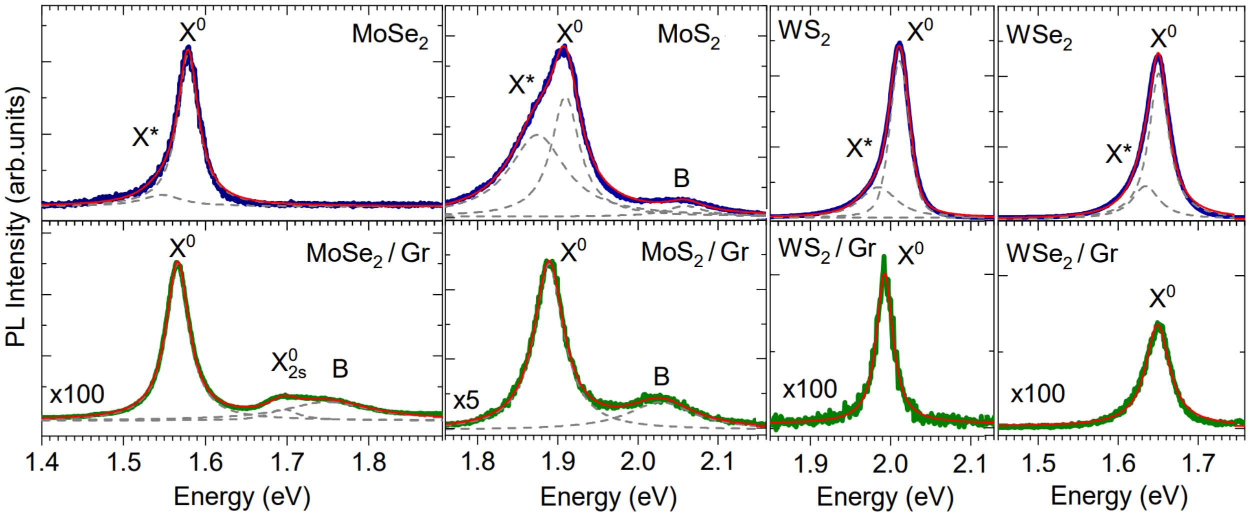

Figure 1.27: Neutralization and PL quenching of TMD by graphene at room temperature: PL spectra of Mo and W based TMDs compared when coupled to graphene, recorded under 2.33 eV and a photon flux of 10^{21} cm^{-2}. Adapted from [9].

Filtering and quenching of PL in TMD by graphene

The coupling of graphene to TMDs causes many interesting effects on excitonic physics in TMD that can be probed precisely through PL spectroscopy.

At room temperature, the TMDs have an X^0 lifetime in ns range (figure 1.28a) [127, 125], much longer than the typical ps range energy transfer process. Coupling of TMD to graphene opens up an efficient non-radiative recombination channel for A exciton in TMDs transferring to graphene, resulting in the strong PL quenching [125]. Although, since the B exciton has a lifetime shorter than that of A exciton, its intensity is only marginally effected by the presence of graphene.

The charges in TMD can tunnel to graphene by static charge transfer (detailed in section 3.2.1) resulting in the neutralization of the TMD layer by graphene. The PL spectra taken at room temperature on Mo based and W based TMDs shown in figure 1.27 depict the neutralization of X^* feature formed due to native dopants on monolayer TMD coupled to monolayer graphene.

At low temperatures (below 100 K), the TMDs have X^0 radiative lifetime in ps range (detailed in section 1.2.4 and shown in left panel of figure 1.28b) [127, 79], comparable to the timescale of energy transfer mechanisms from TMD to graphene [9]. This makes the quenching of X^0 intensity in PL spectra when TMDs are coupled to graphene seen at cryogenic temperatures much lesser than observed in room temperature (figure 1.29a compared to figure 1.27).

On the other hand, the excitonic species in TMDs with longer lifetimes (compared to X^0), like X^* (generally having a lifetime of few 10s of ps at low temperature, detailed in section 1.2.4 and right panel of figure 1.28b), are efficiently filtered out by attached graphene layer due to energy transfer processes and through neutralization by static charge transfer [9]. This leads to the filtering of the X^* and other absorption features via non-radiative pathways in TMD/graphene causing the absence of these features in bottom panel of figure 1.29a.

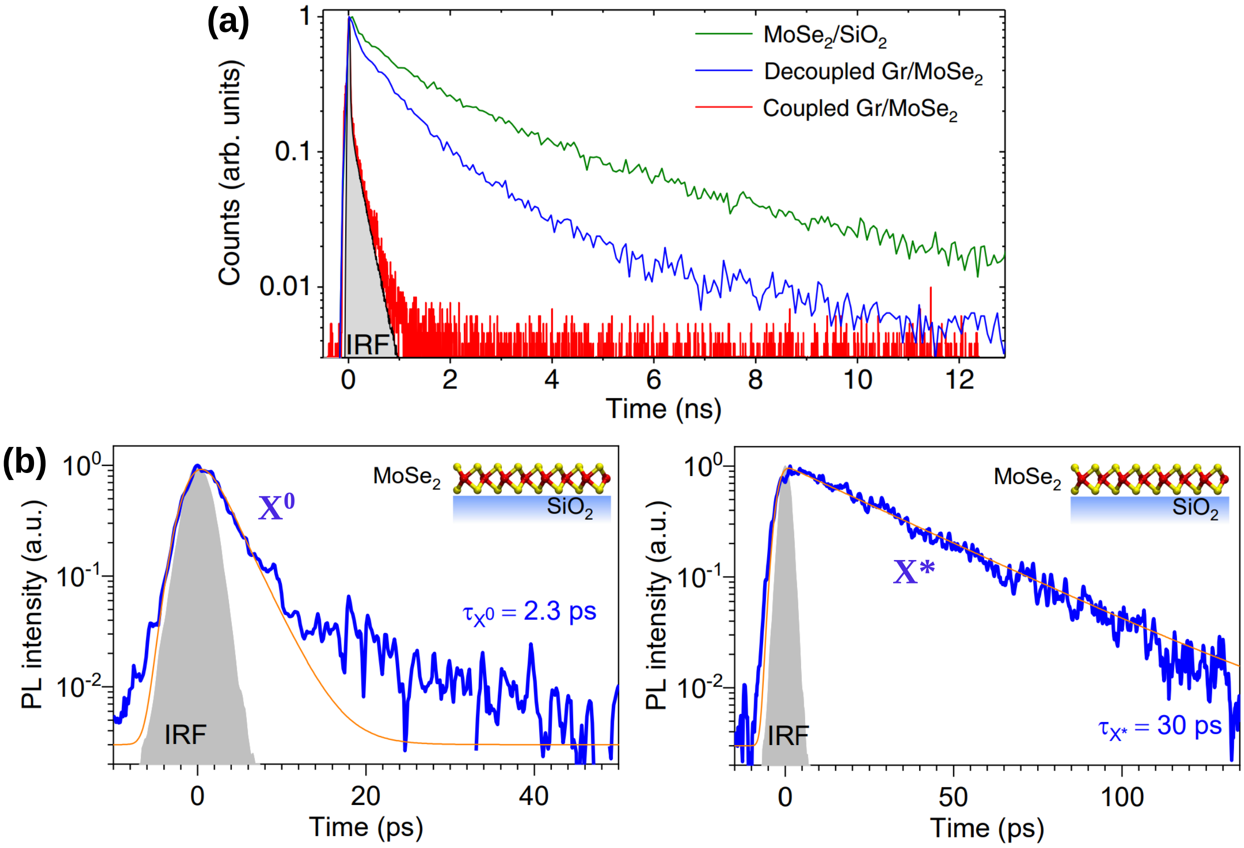

Figure 1.28: (a) PL decay measured with pulsed laser at room temperature (b) time-resolved PL of X^0 and (c) X^* of $MoSe_2$ at temperature of 14 K. The gray shaded areas show instrument response function (IRF). Adapted from [125, 9].

The exciton dynamics in TMD change due to addition of graphene to it. At low temperature, the non-radiative recombination pathways in exciton dynamics can be ignored and thus, the three-level model for TMD is shown in the top panel of figure 1.29b. When graphene is attached to TMD, this three-level model changes as shown in the bottom panel figure 1.29b with the opening two new non-radiative pathways: transfer of hot exciton from TMD to graphene (with timescale τ_G^h) and transfer of exciton from TMD to graphene (with timescale τ_G). The transfer of hot excitons to graphene hinders the formation of exciton population after relaxation [9].

The effects of coupling of graphene to TMDs described above are very prominent and intriguing. The underlying mechanisms between the layers causing these effects remain hidden.

Graphene/$MoSe_2$ as a building block

Among the TMDs discussed so far, the properties of $MoSe_2$ have been studied quite extensively by our research group as well by others. The PL spectra of $MoSe_2$ are very clean with well known features at both room temperature (see figure 1.27) and cryogenic temperatures (see figure 1.29a). The Dirac point of graphene lying between the conduction band and valence band (see figure 5.2) makes the heterostructure of graphene/$MoSe_2$ an excellent

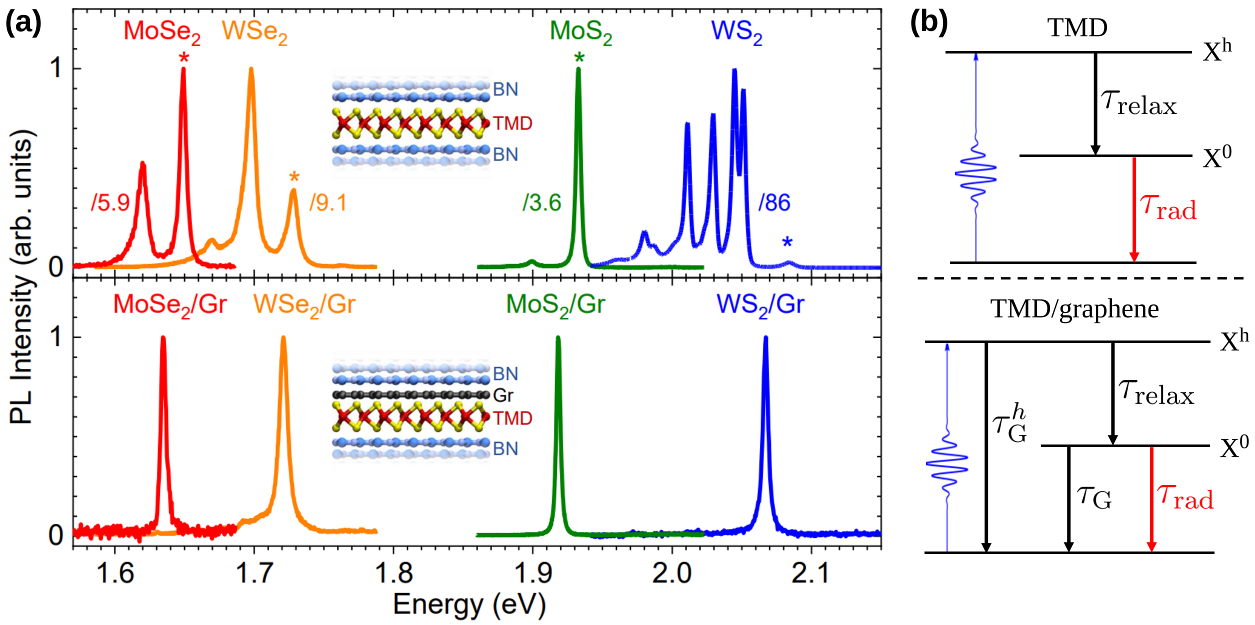

Figure 1.29: (a) PL spectra of (top panel) hBN encapsulated Mo and W based monolayer TMDs and (bottom panel) hBN encapsulated TMD/graphene measured below temperature of 20 K, the asterisks denote X^0 (b) the 3-level model of X^0 dynamics at low temperature for (top panel) TMD and (bottom panel) TMD/graphene, the blue wavy arrow denotes laser excitation. Adapted from [9].

donor-acceptor system for both electrons and holes.

In this thesis, we have used the heterostructure made up of different thicknesses of graphene and monolayer MoSe$_2$ as a building block to study the microscopic processes occurring at the 2D limit between these atomically thin layers and then to achieve the electrical control of their optical emission.

Conclusion

In this chapter, we have introduced the 2D materials, graphene and TMDs. Their electronic and optical properties have been explained along with how these properties can be used as a probe for observing intrinsic and external influence on these materials. We have also discussed about the vdWH that can be formed from these materials with using hBN as a protective material.

The important points in the sections of this chapter are as follows:

Graphene:

- Graphene is a zero-gap semimetal.
- Raman spectroscopy can be used as a probe to observe the intrinsic properties of graphene as well as the effect of external factors on it.

Monolayer TMDs:

- The optical emission of monolayer TMDs exhibiting a direct bandgap are dominated by stable excitons.
- The excitons are sensitive to external environmental conditions like temperature, applied voltage and surrounding layers.

hBN:

- Thin layers of hBN can be used as a protective layer for other 2D materials as well as a substrate for them to protect them from external perturbations.
- Encapsulating TMDs by particular thicknesses of hBN can be used to tune the radiative lifetime of excitons in TMDs.

vdWH:

- The vdWH of well coupled graphene and TMD is a system showing very interesting effects like neutralization, PL quenching and filtering of TMD when attached to graphene as compared to bare TMD.
- The addition of graphene to TMD causes new nonradiative transfer pathways from TMD to graphene to be opened up.

CHAPTER 2

Experimental methods

In this chapter, I will explain the experimental methods used during my PhD. The first section of this chapter gives details about sample fabrication and the second part explains the spectroscopy methods used in our setups.

2.1 Sample fabrication

In this section, the process of building van der Waals heterostructures used in the PhD work is described. For this work, a good sample needs to have large area with minimum defects like bubbles, contaminants, etc to ensure regions with well coupled thin layers. All the steps in making the sample were performed in 2D lab and ST-nano cleanroom platforms at IPCMS.

2.1.1 Mechanical exfoliation

The method of mechanical exfoliation, which was popularized by Novoselov and Geim [1] is a simple method that uses scotch tape to cleave bulk crystals in order to obtain high quality atomically thin layers up to the monolayer limit.

Before exfoliation, the substrates to be used were sonicated in acetone, ethanol and isopropanol, in that sequence, for 5 minutes each and then dried with Argon gun. The Si/SiO_2 substrates were exposed to oxygen plasma for 20 minutes in order to make their surfaces activated which increases the adhesion between SiO_2 and exfoliated material and thus, helps in yield of thin layers.

The figure 2.1 shows the process of mechanical exfoliation step by step:

1. Put the bulk crystal on the adhesive scotch tape piece (a blue nitto tape can be used as well).

2. Fold the tape onto the bulk crystal to cleave it and then remove the crystal from the tape.

3. Place a second piece of scotch tape onto it covering the material and apply pressure onto them gently to ensure adhesion.

4. Peel off the second piece of tape and repeat the steps mentioned so far until the material on step becomes transparent. These transparent areas look red for $MoSe_2$, gray for graphene and pink for hBN.

5. Put the scotch tape with transparent material on top of the target Si/SiO_2 substrate or on PDMS (PolyDiMethylSiloxane). Apply pressure on the tape gently for a few seconds.

6. In case of using Si/SiO_2 substrate for exfoliation, heat the substrate along with the tape on top of it for a few seconds at about 100°C to improve the yield of exfoliation and then, peel off the tape slowly. The substrate with tape should not be heated for too long as it results in higher amount of tape residue being left on the substrate after exfoliation.

   If material is exfoliated on PDMS, the tape has to be peeled off quickly.

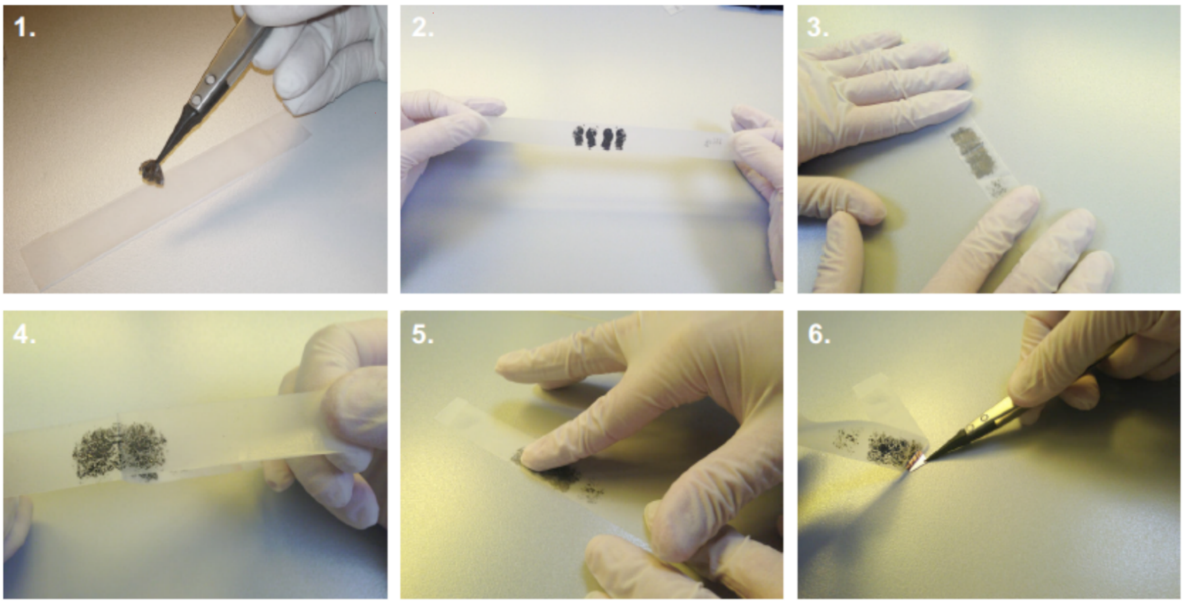

Figure 2.1: Steps in mechanical exfoliation. Adapted from [13].

For the heterostructures built during my PhD, graphene and hBN were mechanically exfoliated on Si/SiO_2 and $MoSe_2$ was exfoliated on PDMS. The layers of interest are found by looking at the substrate/PDMS after exfoliation under a microscope.

The method of mechanical exfoliation is non-deterministic i.e. the layers obtained are scattered randomly across the Si/SiO_2 substrates or PDMS randomly. To fabricate the van der Waals heterostructure efficiently, there has to be some control over the exfoliation, especially for a material like monolayer $MoSe_2$ that has low yield and is needed to make every sample in this work.

2.1.2 Transfer techniques

In order to make the heterostructure samples, the layers have to be stacked on top of each other and the substrate deterministically. This can be done via transfer methods which are described below.

Dry transfer method

This method is based on the work done in [128] in which a piece of PDMS polymer placed on a glass slide is used as a target to exfoliate two dimensional materials. After the exfoliation, the PDMS piece is looked under a microscope to spot the layers of interest from optical contrast. Once a layer of interest is identified, the PDMS around it is cut with a blade to make it as small as possible without inducing cracks in the layer.

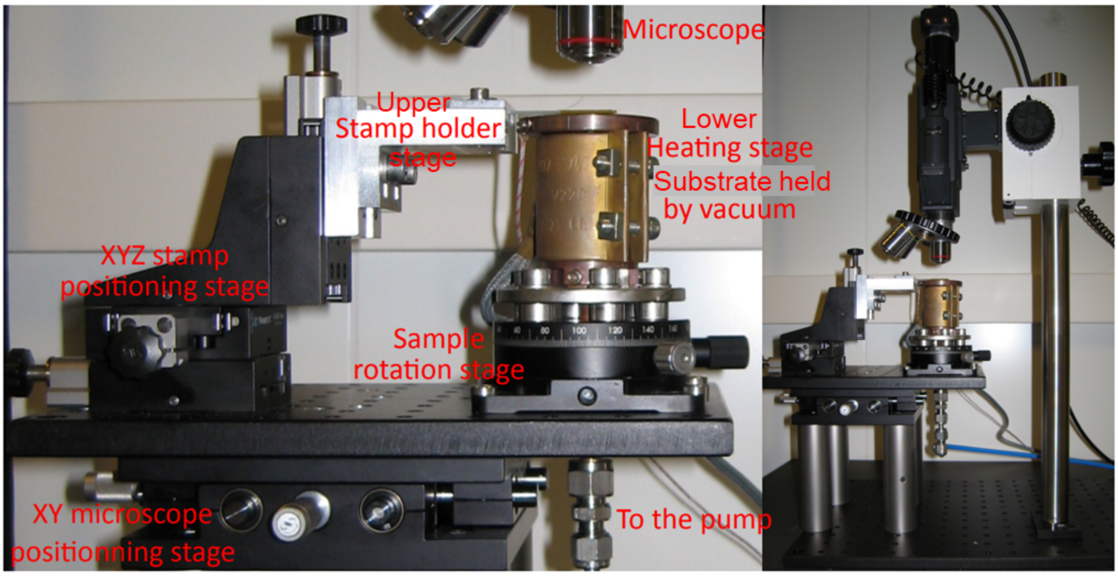

Figure 2.2: Transfer station in 2D lab. Adapted from [22].

The transfer station (figure 2.2) developed by E. Lorchat as part of his PhD was utilized in the next steps. The glass slide having the PDMS stamp with two dimensional layer on it is fixed inverted in the upper stamp holder stage with the PDMS over the lower stage. The target substrate is fixed using a vacuum pump on this lower stage which is heatable and sits on top of a rotation stage which can be rotated to align the layers on upper and lower stages with respect to each other. There is a microscope connected to the transfer station having three different long working distance microscope objectives with 5×, 10× and 20× magnifications. There are two positioning stages that can be moved independently of each other. The XY microscope positioning stage moves both the upper stamp holder stage and lower stage with respect to the microscope. This XY stage is used to find the layers on substrates. The XYZ stamp positioning stage can move the upper stamp holder stage with respect to the lower stage that remains stationary. This XYZ stage is used to align the layers with respect to each other.

Once the two layers of interest on PDMS and target substrate are well aligned vertically by using the two positioning stages and the sample rotation stage, the upper stamp holder stage is moved down towards the lower substrate stage using the XYZ stage. There is a very small tilt angle between the upper and lower stages, hence when they are close enough, the PDMS touches part of the target substrate and a contact line appears. The rotation stage can be rotated to control the position of tilt angle and thus, the direction from which the contact line appears. This contact line can be pushed further by either pushing in z axis of XYZ stamp positioning stage or by heating the target substrate which expands the PDMS. Typically, the target substrate is heated to 40°C and then, the stamp is pushed in z-axis by using the XYZ positioning stage until the contact line reaches a few tens of micrometers away from the layers of interest. The temperature is slowly increased (upto 90°C at most) after this so that the layers come in contact smoothly and the contact line moves past them. After this, the temperature is lowered so that the contact line recedes, leaving the layers on top of each other on the target substrate. The PDMS stamp is then retracted using the XYZ stage.

This process of depositing a layer from PDMS stamp onto target layer on substrate can be repeated multiple times to form the desired van der Waals heterostructure (figure 2.3). Upon each iteration of transfer process, the PDMS stamp comes in contact with the layers already transferred onto the target substrate which introduces the risk of parts of these layers coming off as the PDMS stamp is retracted and it also creates a high chance of these layers getting contaminated which reduces the coupling between layers because of formation of impurities like dirt particles and bubbles.

In the duration of my PhD, this dry transfer method has been mostly used to transfer monolayer $MoSe_2$ exfoliated on PDMS onto an intermediate substrate and then this transferred monolayer is utilized in fabrication of heterostructure onto the final substrate using the PC-method. The PDMS dry transfer method has also been used to fabricate many samples for collaborative work during my PhD (like shown in 2.3).

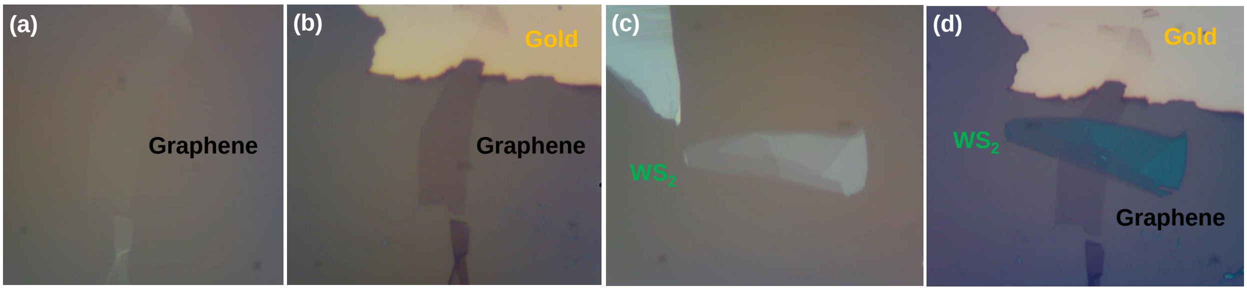

Figure 2.3: Formation of vdWH after vertical alignment with dry transfer method in steps: (a) exfoliated few layer graphene on PDMS (b) graphene deposited on Si/SiO_2 substrate with evaporated gold (c) WS_2 with many different thicknesses exfoliated on PDMS (d) WS_2 deposited on top of few layer graphene after vertical alignment.

PC-method

The PC method is an excellent way to fabricate complex vdWH with many layers [129]. Since this method needs the fabrication of all individual layers of heterostructure on intermediate substrates, it gives the opportunity to characterize the layers before the hetrostructure is fabricated.

Making PC films

This method uses a polymer named PC (Poly bisphenol A carbonate) to make a stamp with PDMS. For making this stamp, thin films of PC have to be made by dissolving PC in chloroform (6% PC by mass in chloroform) in a sealed vial and stirring this mixture with a magnetic stirrer at room temperature overnight. After this, a few drops of this mixture are put on a glass slide (cleaned with ethanol and isopropanol and then, dried with Argon gun) and they are sandwiched by putting a second glass slide on top. The glass slides are slid in opposite directions laterally and the PC films get formed on each of the glass slides. These PC films are left to be dried before use. A PC film can be used upto 6 months after it is made.

Making PC stamp

A small piece of PDMS is placed on a glass slide (figure 2.4a). A circle, bigger than the PDMS piece, is cut in a piece of kapton tape, which is very stable even at high temperatures. This piece of tape was placed on top of glass slide with a clean portion of PC film. The PC film alongside the tape is cut by a blade and the tape is removed from the glass slide, taking PC film underneath it. The tape was then stuck on top of the PDMS piece covering it completely (figure 2.4b). This stamp is heated for less than 30 seconds at 200°C to make it stable for use (care has to be taken because heating for longer time can completely melt the PC). A good PC stamp has the part of PC covering the PDMS piece elevated (with respect to glass slide plane) compared to the rest of the PC, which can be seen with unaided eyes. The PC stamp is checked under a microscope and if there are any bubbles, ripples or a number of dust particles on the stamp, it is discarded and a new one is made.

Picking up layers

The transfer station described for dry transfer method is used here as well. For the step of pick-up, the PC stamp is fixed inverted on the upper stamp holder stage while the substrate having the top layer of the hetrostructure that has to be made is fixed on the lower stage. The lower stage, fixed by vacuum, is heated to 40°C before the PC stamp is lowered towards it. Once the contact line forms between PC stamp and substrate, the lower stage is slowly heated to 80°C. This increase in temperature makes the contact line cover the whole PC stamp. Then, the PC stamp is slowly removed exclusively by vertical translation using the XYZ positioning stage while keeping the temperature at 80°C. The top layer of the heterostructure comes away with the PC stamp. Typically, like in this work, this top layer is hBN.

Once the top layer of stack has been picked up, this step of pick-up described above is iterated by picking up each next layer by the ones that are already present on PC stamp to stack all the layers required to make the heterostructure in sequence. This needs careful alignment

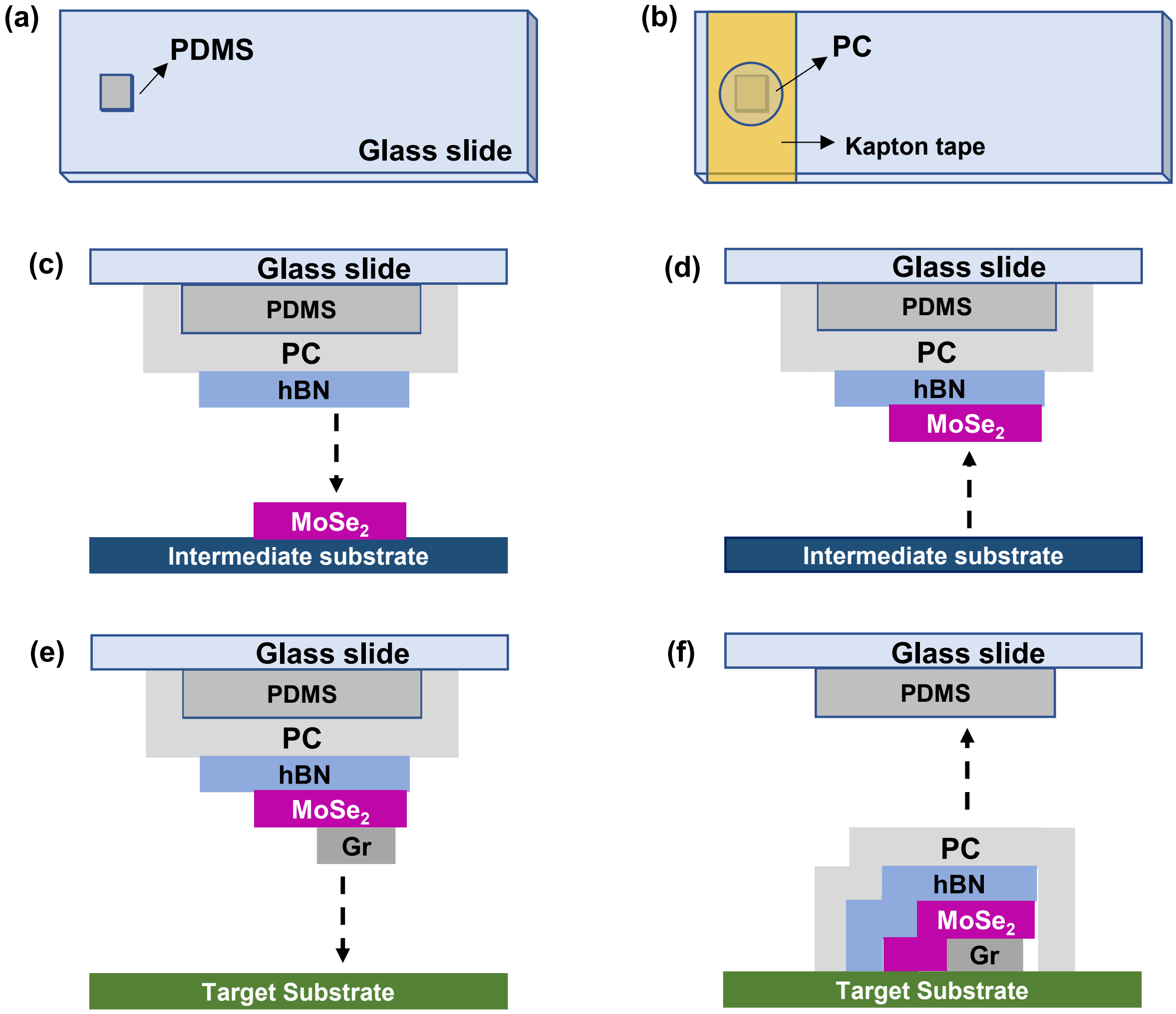

Figure 2.4: Steps involved in fabrication of samples with PC-method (a) and (b) depict making of PC stamp. (c) and (d) are the steps iterated to pick up all the layers from intermediate substrates to form the stack. (e) and (f) show the process of dropping the stack onto the target substrate.

of the layers on PC stamp with respect to the layers to be picked up from intermediate substrate on fixed lower stage (figure 2.4c and 2.4d).

Depositing the stack

Once all the two dimensional layers required to make the heterostructure are picked up onto the PC stamp (figure 2.4e), the stack is deposited onto the desired target substrate. For this step, the target substrate is preheated to 40°C. The stack is lowered by vertical translation till the stack comes a few tens of micrometers away from the contact line. Then, the lower stage is slowly heated to 180°C. The PC starts to melt at this high temperature and gets dropped onto the substrate along with the heterostructure. The PDMS piece left on the glass slide is pulled away from the substrate (figure 2.4f).

Cleaning

To get rid of the PC residue stuck to the sample, it is submerged in a vial filled with chloroform. This vial is sealed with paraffin and left for at least 15 hours for the PC to be dissolved in chloroform. After this, the sample is removed from this vial and submerged in ethanol and then in isopropanol before drying it with Argon gun to finish the fabrication of sample.

Once the sample fabrication is finished, it can be annealed under high vacuum (higher than 10^{-6} mbar) to get the bubbles between layers amalgamated and contaminants to be removed [130, 131]. In the samples fabricated for this work, there are multiple important regions of interest in each sample. Annealing our samples could merge the small bubbles and contaminants into a bigger one, rendering the part of the sample where this happens impossible to be studied well via optical spectroscopy techniques. Since the spot where this agglomeration of bubbles and contaminants happens is uncontrollable, the samples were not annealed.

In this PhD work, the PC method has been used extensively for sample fabrication by stacking the desired layers (individually obtained on intermediate substrate by PDMS dry transfer) in required sequence and dropping the layer stack onto the substrates, finishing the sample fabrication.

2.2 Optical spectroscopy techniques and setups

This section describes all the optical excitation based spectroscopy techniques and setups used for measurements at the laboratories in IPCMS as well as at the collaborative institute LPCNO.

2.2.1 Setup at IPCMS

The setup can be used for PL and Raman spectroscopy at room temperature or low temperatures under vacuum with the option to perform measurements under applied voltage.

The setup consists of home-built confocal microscope in backscattering geometry and is mounted on an optical table which stands on a pneumatic system for mechanical stability. In our setup, there are three lasers that have been used: two continuous wave (CW) lasers at 532 nm (2.33 eV) and at 633 nm (1.96 eV) and a third pulsed laser (mentioned as NKT laser from here onwards) with a tunable repetition rate between 2 MHz to 78 MHz and tunable wavelength between 480 nm (2.58 eV) and 2400 nm (0.52 eV). The CW lasers are filtered using BraggGrate ultra-narrow band pass filters before measurement.

Measurements under ambient conditions

The schematic of optical setup is shown in figure 2.5a and the picture is shown in figure 2.5b. After filtering using band pass filters, the CW laser beam that has to be used for measurements passes through a set of half wave-plate ($\lambda/2$) and polarising beamsplitter (PBS) to control the intensity of laser beam by rotating the angle of half wave-plate. Then the laser beam is reflected onto two mirrors in sequence (M1 and M2) and the mirrors are adjusted to align the laser beam. The beam then enters commercial Nikon inverted microscope Ti eclipse (figure 2.5c). The microscope is used to scan the sample to find the area of interest and see the alignment of laser spot on the sample. It also consists a turret that can hold up to six beamsplitters (BS/D) and this allows us to easily switch from one beamsplitter to another according to the requirements of the measurements to be performed. The microscope objective of 40× with numerical aperture (N.A.) of 0.6 is used for focusing the laser on sample. The objective can be moved in z direction for a course positioning of optical focus of sample or laser focus on the sample. The sample is fixed upside down in a sample holder which is fixed onto an XY mechanical stage which is utilized for coarse positioning as well as onto an XYZ piezo-stage for controlling micro positioning.

After the laser interacts with the sample, the backscattered laser passes through the objective and then through the beamsplitter again. For the microscope, there are two options of output that are used: first of which is linked to a webcam (by flipping the beamsplitter and mirror in microscope represented by curved arrows) and is used to observe the sample under white light illumination or under laser or to see the laser spot and the second option sends the white light or laser coming out of the microscope towards the spectrometer for detection.

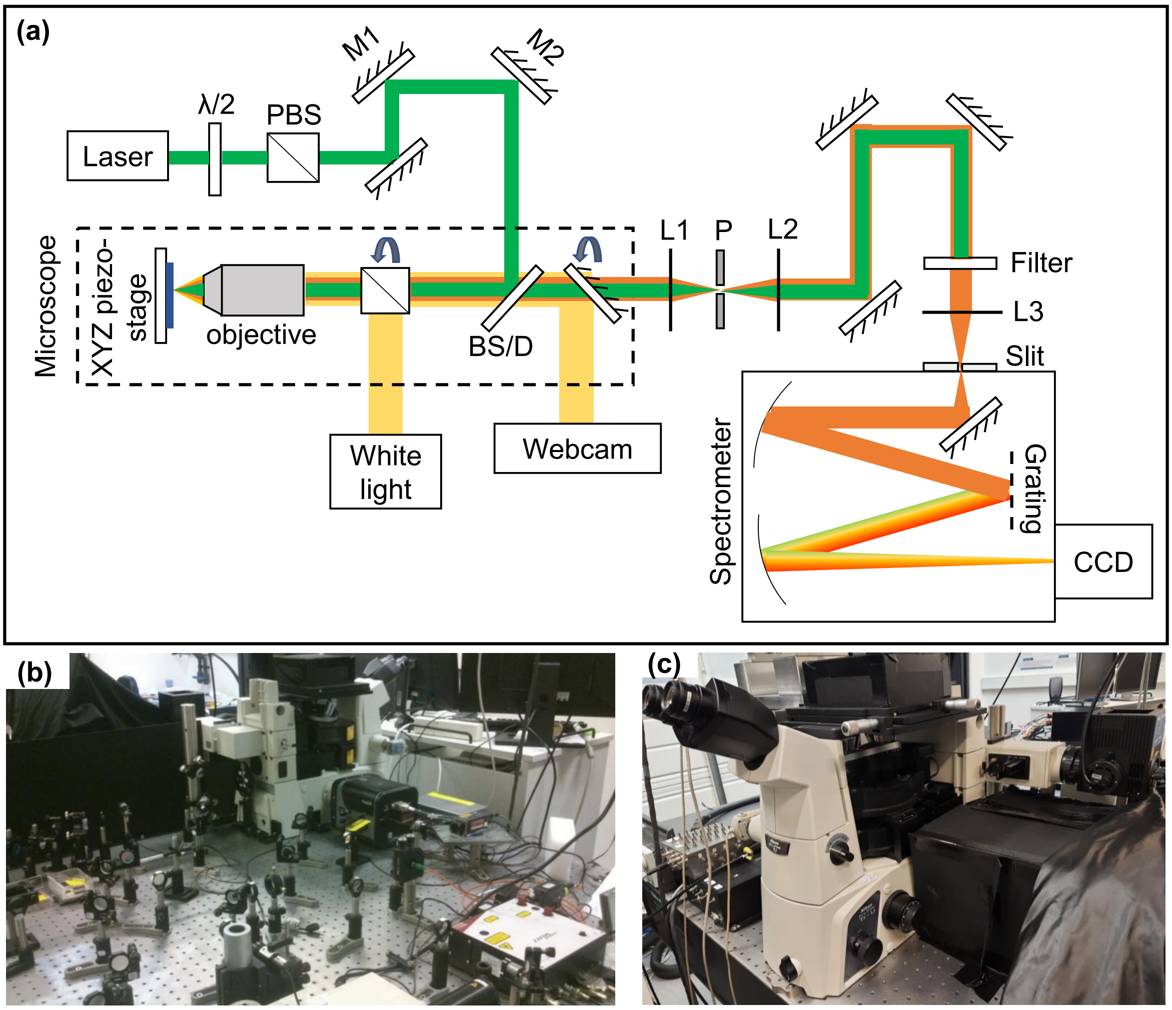

Figure 2.5: Optical spectroscopy setup at ambient conditions (a) Schematic of setup (b) Picture of setup (c) and of microscope.

For spectroscopy measurements, the laser coming out of microscope is incident on a first lens (L1) which concentrates the light onto the pinhole (P) which is aligned with respect to the laser and then passes through a second lens (L2) to collimate the beam. Then this laser beam is reflected by multiple mirrors to align it such that the beam is parallel to spectrometer and horizontal with respect to optical table. The laser passes though a filter corresponding to the laser wavelength used so that only the signal is passed on towards the spectrometer avoiding its saturation by the relatively intense laser. The remaining beam then passes through an adjustable lens (L3) with 5 cm focal length and falls onto the slit of the spectrometer. The width and horizontal position of the slit are adjustable so that the signal beam entering through it is maximized. The beam falls on a diffraction grating that can be chosen to have 150, 300, 900, 1200 or 2400 grooves/mm. For diffraction gratings, higher number of grooves/mm gives larger dispersion, which means higher spectral resolution and a smaller spectral window. For our measurements, we have either used a 300 grooves/mm grating or 900 grooves/mm (specifically for Raman spectroscopy of graphene with 2.33 eV laser) as a good balance between spectral resolution and spectral window. The beam is then incident on a monochromator with a 500 mm focal length which is coupled to a CCD (charge-coupled device) array cooled using a combination of Peltier effect and liquid nitrogen. The diffraction grating disperses the beam onto the CCD which has 1340 x 100 pixels and each pixel corresponds to a particular frequency and the intensity corresponds to the number of incident photons on each pixel over acqusition time window.

This setup under ambient conditions can be modified into a setup for measurements at low temperature and with variable laser wavelength. These are explained below along with acquisition methods of voltage dependent spectroscopy and hyperspectral mapping.

Measurements at low temperature using liquid Helium cryostat

For low temperature measurements under vacuum, we have used Helium flow cryostat from Cryo Industries of America (CIA). The sample is inserted on top of the cold finger in the cryostat. The cryostat is then sealed and a scroll pump and turbo pump are used in sequence to attain a vacuum of range 10^{-6} mbar. The sample is cooled via thermal conduction as cold finger is cooled with a continuous flow of liquid Helium. The low temperature measurements using CIA cryostat are typically done around 16 K in this work. The temperature is monitored and controlled using cryo-con 32B temperature controller which has a heater installed.

The optical measurements are performed the same way as the ones in ambient conditions, but with some changes. A long range microscope objective of 50× with N.A. 0.65 is fixed onto the XYZ piezo-stage and the XY mechanical stage is not moved during the measurements. The spotsize Δx with a laser wavelength of λ is given by the Abbe diffraction limit [132, 133]

$$\Delta x = 0.61 \frac{\lambda}{N.A.} \tag{2.1}$$

which comes to be 594 nm for the laser excitation of wavelength 633 nm (1.96 eV) which is used for many of the measurements in this manuscript.

The cryostat is then mounted on top of a stand such that the window covering the sample is directly over the microscope objective. This stand on which the cryostat is mounted also has an XYZ mechanical stage for coarse adjustment which helps in locating the sample and focusing on it; while the XYZ piezo-stage is used for micro positioning by moving the objective.

Measurements at low temperature using Helium free cryostat

The other setup that can be used to perform low temperature optical spectroscopy under vacuum uses the close-cycle attocube Attodry 800 cryostat (figure 2.6a) and was developed by L. Moczko as a part of his PhD. The closed circuit of helium cools down the cold head upto 4 K and the sample fixed on top of it cools down because of thermal conduction via an Attocube Thermal Coupler (ATC). Apart from the ATC, the stack on which the sample is mounted also consists of cryo-compatible piezoelectric positioners and scanners (figure 2.6b). The sample is mounted in a sample holder with a home made PCB (figure 2.6c). The rest of the optical setup is similar to the one described for ambient conditions and the optical measurements were performed in the same way at around 5.5 K sample temperature.

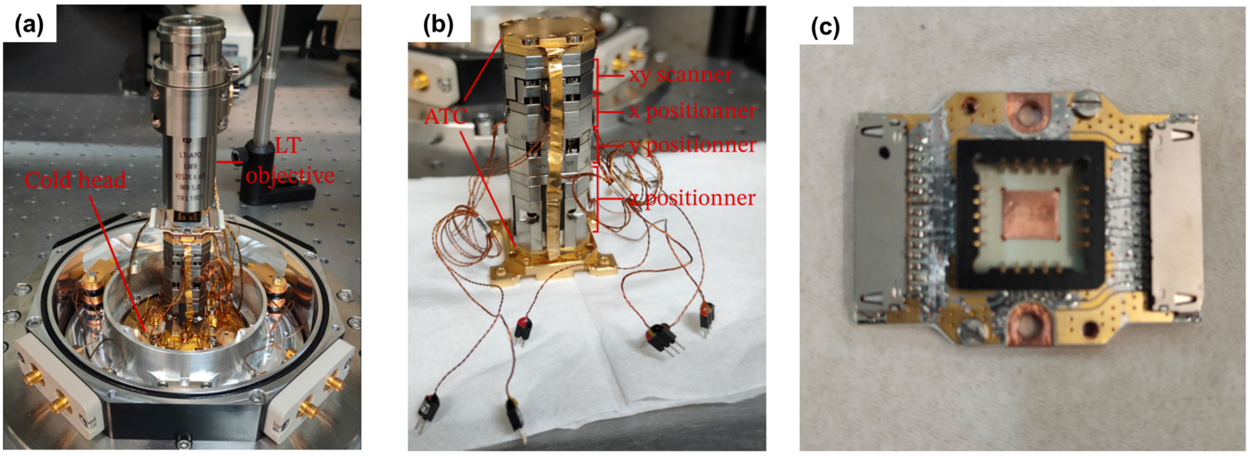

Figure 2.6: (a) Inside of sample chamber of helium free cryostat (b) stack consisting of ATC, positioners and scanners onto which (c) home made PCB with sample holder can be mounted. Adapted from [28].

Measurements for excitonic Rydberg states

Section 1.2.2 describes the band structure of TMDs. The energy positions of exciton states can be used to determine the exciton binding energy of the TMD layer. There are many ways to experimentally determine the higher energy exciton states. The first one is using the differential reflectance, but the signatures of higher energy exciton states observed by using this method are very weak and not shown in this work.

The second method is to perform PL spectroscopy with a high incoming laser photon intensity to observe the higher exciton states. Due to the high laser photon intensity, there is a high exciton generation and the non-linear processes dominate. This method is used in the

PhD work with CIA cryostat at low temperature and hyperspectral maps were also recorded at high incident laser intensity. The results are shown in section 3.3.5.

The third method is performing photoluminescence excitation spectroscopy (PLE) in order to observe exciton states. In this technique, PL spectrum is measured with respect to changing incident laser energy and the data can also be visualised by plotting PL intensity vs detuning (i.e. incident laser energy − 1s exciton energy position). We have measured PLE with CIA cryostat at low temperature on samples having $MoSe_2$ and the results are shown in section 3.3.5.

For our PLE measurements, we have used the tunable wavelength NKT laser from energies 1.69 eV to 2.57 eV. The schematic of operating NKT laser for PLE measurements is shown in figure 2.7. As the laser wavelength is changed, for each PL measurement, the laser beam has to be filtered before it enters the microscope because it could contain some contributions from laser wavelengths other than the desired laser wavelength. For this filtering, we have used one short-pass filter (F1). For the output, a long-pass filter (F2) is used to filter out the laser. Both the short-pass and long-pass filters have to be adjusted at each laser wavelength by adjusting the angles between the filters and the laser beam.

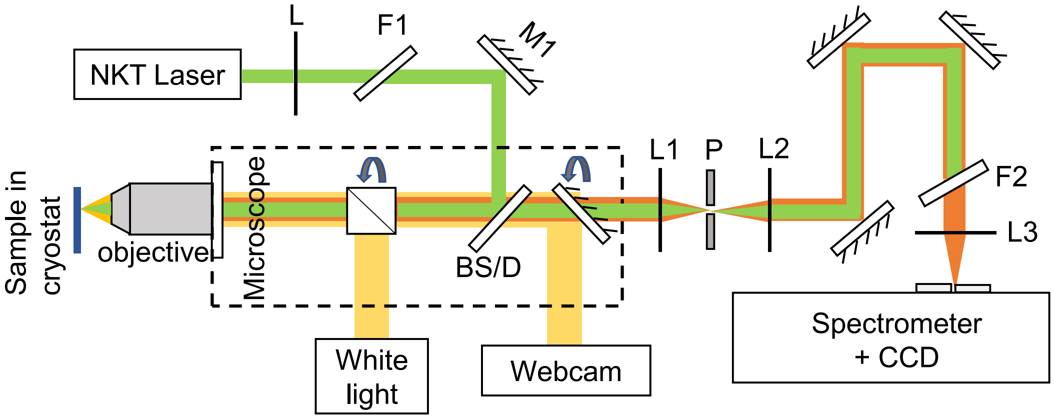

Figure 2.7: Schematic of photoluminescence excitation spectroscopy setup

Hyperspectral mapping

In order to observe the changes in optical properties of sample when it is probed at spatially different spots, we have used the hyperspectral mapping. The XYZ piezo-stage and the CCD were interfaced by Michelangelo Romeo, an engineer at IPCMS, for us to be able to perform the maps in an automatised manner. At ambient conditions, the sample fixed onto the XYZ piezo-stage is moved microscopically; while the microscope object mounted on XYZ piezo-stage is moved when CIA cryostat is used to perform the measurements of these maps. Thus, the sample is moved microscopically in x and y directions with respect to the incident laser and a hyperspectral map showing optical spectra at each point over an area of sample is obtained.

A hyperspectral PL map taken on a monolayer $MoSe_2$ deposited on ITO (Indium tin oxide) covered 170 µm thick glass coverslip (sample made using PDMS dry transfer method as part

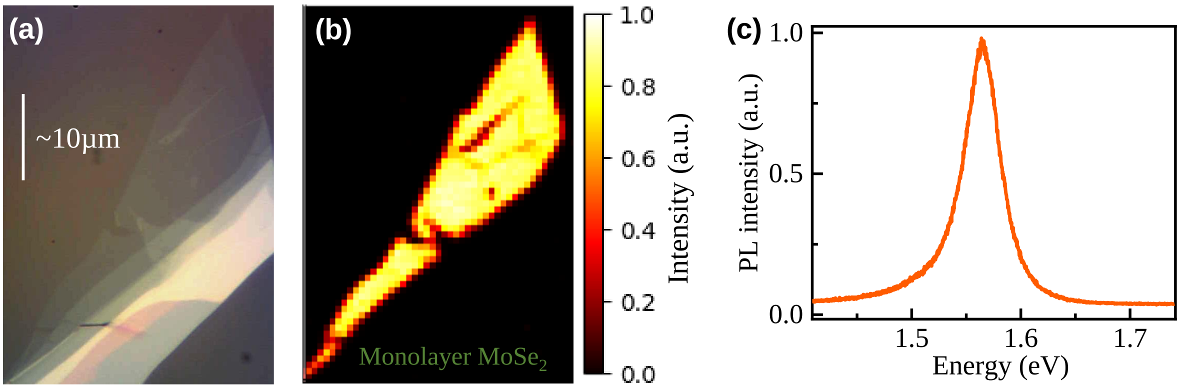

Figure 2.8: Hyperspectral mapping of a monolayer MoSe$_2$: (a) Optical image of sample (b) intensity seen in its corresponding PL map (c) and a typical PL spectrum obtained in PL map taken with 2.33 eV laser excitation and 25 µW/µm^2 at room temperature.

of a collaboration) is shown in figure 2.8. The PL map clearly reflects the inhomogeneities like cracks, folds, bubbles and dirt particles that are visible in the optical image of the sample (figure 2.8a). The individual spectra in the hyperspectral map (like shown in figure 2.8c) can be analyzed and fitted to get deeper insights into the sample homogeneity.

Voltage dependent optical spectroscopy

Some measurements in this PhD work consist of measuring PL and Raman spectra of heterostructures with respect to applied voltage. The CIA cryostat can be used for these voltage dependent optical measurements via the pins seen in figure 2.9 and fixing the sample into a PCB which connects to these pins. The source and measure unit Keithley 2612A is used to apply voltage in a controllable manner. The measurements detailed in section 4.2.4 were performed using the CIA cryostat at primary vacuum of 10^{-2} mbar and room temperature in an automatized way while recording voltage, current and time of measurement on virtue of the interfacing between XYZ piezo-stage, measuring softwares, spectrometer, CCD and Keithley.

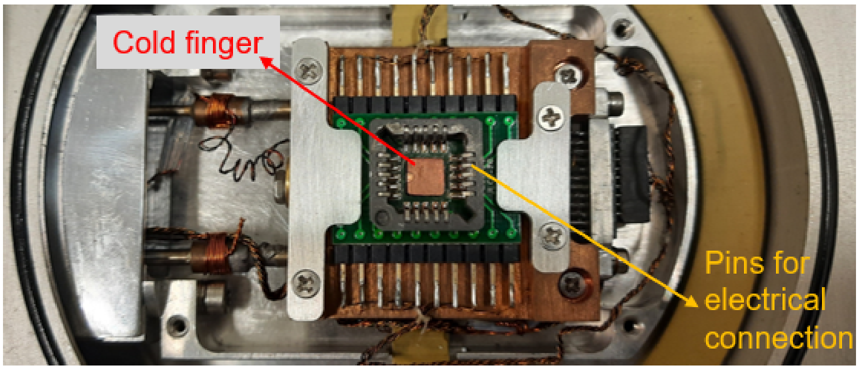

Figure 2.9: Inside of CIA cryostat when opened with pins for electrical connection

Reflectance measurements

Reflectance spectroscopy measurements are performed in low temperature cryostat by using incident white light and recording the light reflected by the sample. The differential reflectance is defined by

$$\text{Differential reflectance} = \frac{\mathrm{R}_{\text{heterostructure}} - \mathrm{R}_{\text{substrate}}}{\mathrm{R}_{\text{substrate}}} \tag{2.2}$$

where $\mathrm{R}_{\text{heterostructure}}$ and $\mathrm{R}_{\text{substrate}}$ are reflectance spectra taken on heterostructure and the substrate respectively, such that $\mathrm{R}_{\text{substrate}}$ is used as a baseline.

2.2.2 TRPL measurement setup at LPCNO

The TRPL (time resolved photoluminescence) measurements performed for results shown in upcoming section 3.3.6 in order to understand the exciton dynamics were performed at LPCNO, INSA, Toulouse by Delphine Lagarde, Maxime Mauguet, Cedric Robert and Xavier Marie because of a better resolution for TRPL measurements as compared to the setup at IPCMS. The schematic of setup for TRPL measurements at 6 K is shown in figure 2.10a. The sample is put on an XYZ-piezo stack in a cryostat. The setup uses a femtosecond pulsed Ti:Sa laser (150 fs) and a streak camera with a resolution of less than 1 ps. The instrument response function (IRF) comes from this resolution time of the streak camera. This setup has been used to measure PL using the spectrometer with grating of 600 grooves/mm and a mirror as well as TRPL using the streak camera at a spot on the sample. Because of this, the TRPL spectrum obtained at a spot can be correlated to the PL spectrum obtained at it and thus, the measurements at different spots can be compared.

Figure 2.10b shows the working principle of streak camera. The optical signal entering camera gets redirected towards a photocathode. When the signal falls on this photocathode, electrons are ejected from it with their number proportional to intensity of incident optical signal. Then, these electrons pass through two electrodes upon which a time varying voltage is applied. Due to this, the electrons reaching photocathode earlier get deflected differently as compared to the electrons reaching photocathode later. After this, the deflected electrons fall on a fluorescent screen which is coupled to the CCD camera. This gives a spatial distribution of signal. The signal is a streak of light containing the information about temporal properties.

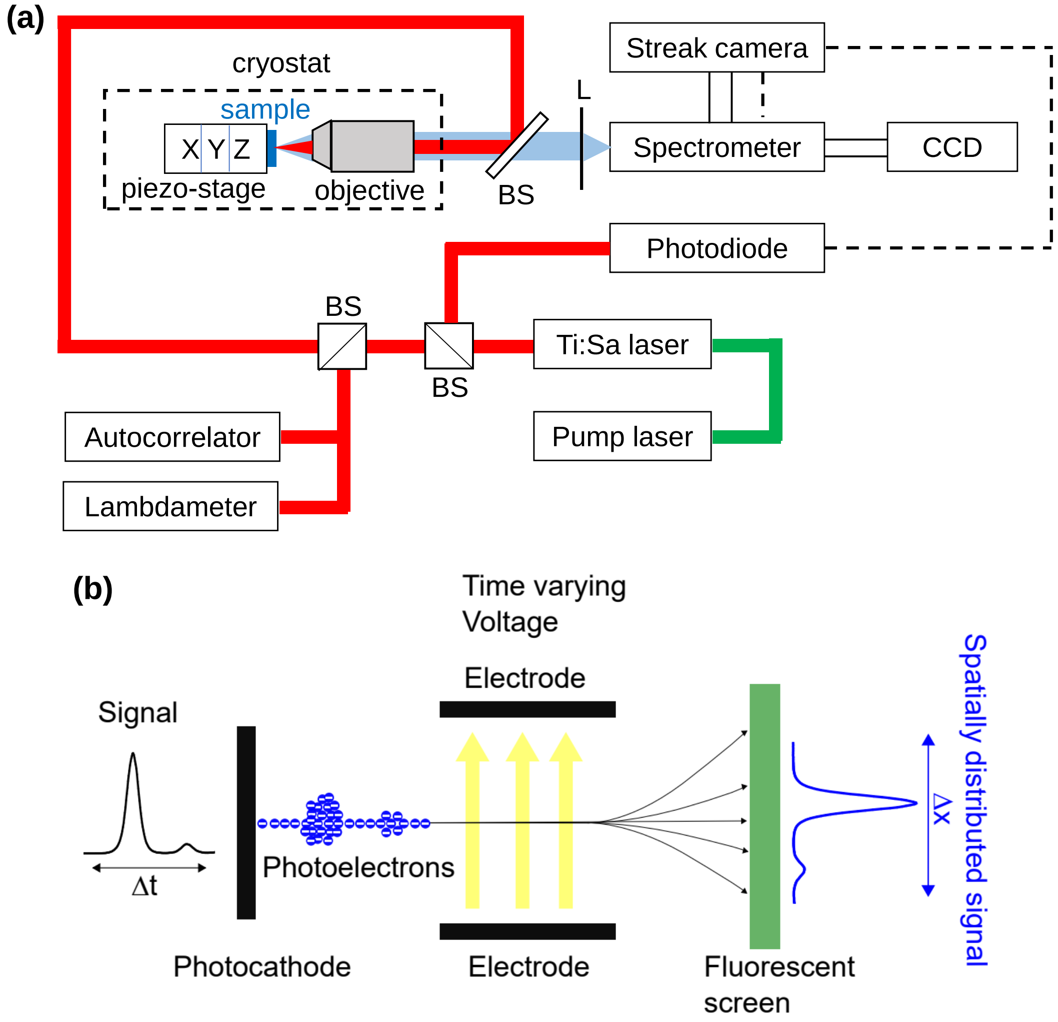

Figure 2.10: (a) Schematic of TRPL setup at LPCNO (b) schematic of working principle of streak camera, adapted from [62].

Conclusion

In this chapter, we have described all the experimental methods used in this PhD work. The process of sample fabrication involving mechanical exfoliation and the two transfer methods, namely dry transfer method and PC-method, are detailed with their advantages and disadvantages. Next, all the optical spectroscopy techniques and the setups in which they were performed have been described.

CHAPTER 3

Understanding near-field interactions between $MoSe_2$ and graphene

3.1 Motivation

The microscopic interactions and transfer mechanisms between materials of different dimensions, like from quantum wells to quantum dots [134], quantum wells to graphene [112], quantum dots to graphene [112, 135] and to MoS_2 [136], molecules to graphene [137, 138, 139], have been studied theoretically as well as through experiments. The interactions between different nm-thin sheets of 2D materials is still a rich field for research.

The vdWH made up of atomically thin 2D materials provide the opportunity to study the transfer processes occurring between these materials that are only a few angstroms away from each other. In contrast to the well-known transfer processes studied in bulk material heterojunctions with the formation of charge depletion regions, the 2D materials are thought to have superposition of bands of the materials at their interfaces giving rise to different physics related to transfer processes at the interfaces as compared to their bulk counterparts [120].

The TMD/graphene heterostructure is a very interesting system with strong influence of layers on each other that can be probed through optical spectroscopy techniques. The band alignment of TMD and graphene (shown in figure 5.2) makes it an excellent donor-acceptor system for both electrons and holes. Despite the intriguing effects like quenching of PL and filtering of trion in TMD by the attachment of graphene seen in TMD/graphene systems (detailed in section 1.4.2), the microscopic mechanisms taking place between TMD and graphene still remain unclear.

In this chapter, we have attempted to understand which type of transfer processes occur between the $MoSe_2$ and graphene layers by exploring the distance dependence of the transfer processes with varying graphene thicknesses in a microcavity tuned to have the longest radiative recombination lifetime of excitons in $MoSe_2$. We have used PL spectroscopy to probe the changes in PL of $MoSe_2$ with attachment of n-layer graphene and then, explore the dynamics of the system through TRPL.

Let us first take a look at the possible transfer processes between TMD and graphene.

3.2 Near-field transfer processes between TMD and Graphene

In this section, we will give details about the well-known near-field transfer processes between graphene and TMD. These processes depend upon many factors including laser energy and flux, band structures of layers, interlayer interactions, twist angle between layers, overlap between orbitals of layers, dipole-dipole interactions, etc. We will be discussing about the transfer processes possible for laser excitation above electronic gap.

3.2.1 Static charge transfer

This transfer process involves charges tunnelling from one layer to another under absence of illumination and results in charge redistribution to achieve equilibrium. The charge redistribution between the layers happens depending upon the band alignment between graphene and TMD (see section 1.4.2). As mentioned previously, the Dirac point of quasi-neutral graphene ($|E_\mathrm{F}| < 300$ meV) lies between the bandgap of the TMD, which makes the graphene act as an acceptor of charges from TMD (process shown in figure 3.1) resulting in the neutralization of the TMD [9, 62]. Thus, in TMD/graphene heterostructures, the PL spectrum taken at room temperature shows the neutralization of X* in TMD coupled to graphene (figure 1.27). In general, this transfer process can be probed via PL and Raman spectroscopy with the least possible laser power to avoid photoinduced effects.

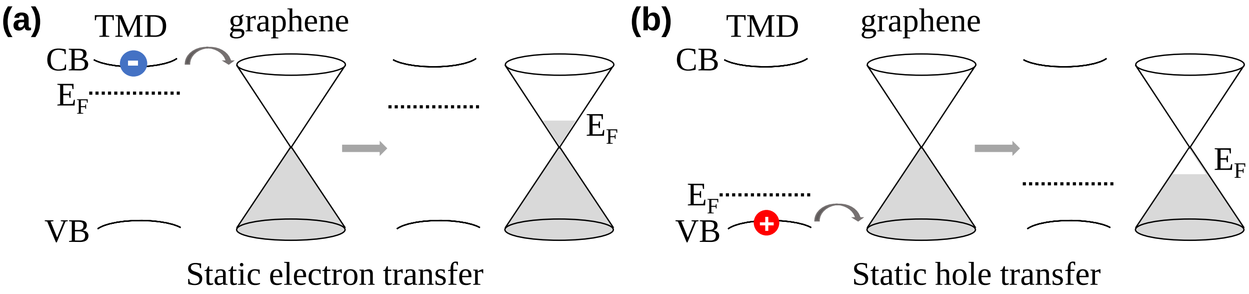

Figure 3.1: Schematic of (a) static electron transfer and (b) static hole transfer from monolayer TMD to monolayer graphene. The gray shaded part shows filled states. Adapted from [62, 125].

3.2.2 Photoinduced charge transfer

This transfer process occurs under illumination, which creates an exciton in TMD and then one of these charges tunnel to graphene coupled to it (process shown in figure 3.2). The relative band alignment between the layers decides which charge is tunneled to graphene and it creates a charge separated state leaving the TMD and graphene doped with opposite charges. The photoinduced charge transfer could originate from extrinsic factors (like defects, adsorbates, etc.) or intrinsic factors (induced by charge separation). The photoinduced charge transfer has a short range of ≈ 1 nm.

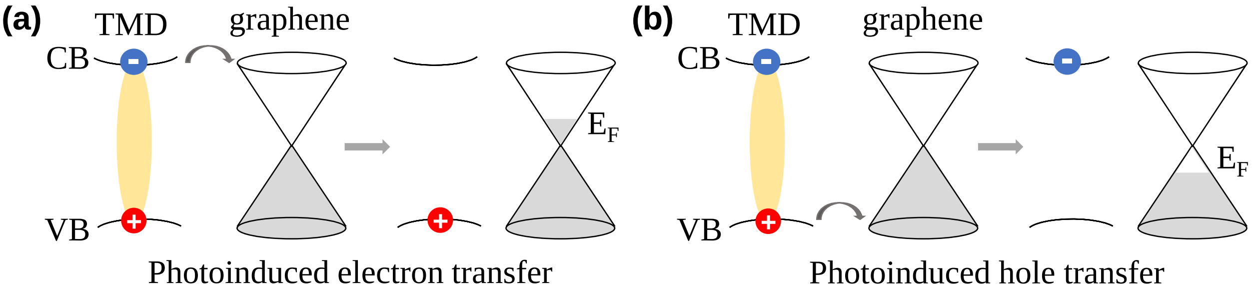

Figure 3.2: (a) Schematic of photoinduced electron transfer from monolayer TMD to monolayer graphene, which leaves TMD hole doped and graphene electron doped (b) schematic of photoinduced hole transfer from monolayer TMD to monolayer graphene, which leaves TMD electron doped and graphene hole doped. The gray shaded part shows filled states in graphene and yellow shaded area show excitons. Adapted from [62, 125].

The incoming photon flux strongly influences the photoinduced charge transfer. The doping level of graphene as a function of incoming photon flux (Φ_{ph}) estimated by Raman parameters and their correlations can be used to probe the transfer process. This approach used in [125] shows photoinduced electron transfer from $MoSe_2$ to graphene in samples with SiO_2 as the substrate, resulting in $MoSe_2$ and graphene getting hole doped and electron doped respectively (figures 3.3a and 3.3b).

Influence of environment and substrate

The photoinduced charge transfer originating from external factors is dependent on whether the measurements are performed in ambient air or under vacuum. In air, the contaminants in air are adsorbed on the surface of layers and these adsorbates work like efficient traps for charges [140, 141]. Due to the adsorbates acting like leakage channels, the charges can escape from the graphene layer because of desorption. The results in [125] show that the E_F in graphene in the TMD/graphene heterostructure increases with increasing Φ_{ph} up to a saturation value of $\sim$ 290 meV.

On the other hand, in vacuum, a significant fraction of adsorbates get removed from the layers suppressing the leakage channels formed because of them, making the transferred charges from TMD to graphene stay in the graphene layer as long as the laser illumination is on. Thus, the photoinduced rise of E_F in graphene can occur at any chosen Φ_{ph} on a long timescale of several minutes to reach a saturation value of $\sim$ 290 meV [125].

Moreover, the trapped charges between the heterostructure and substrate can cause similar photodoping effects. This can be avoided by encapsulating the heterostructure in hBN layers which is done in [104]. The correlation between ω_G and Γ_G (figure 3.3c) show no changes with increasing Φ_{ph}, implying no photodoping in the sample.

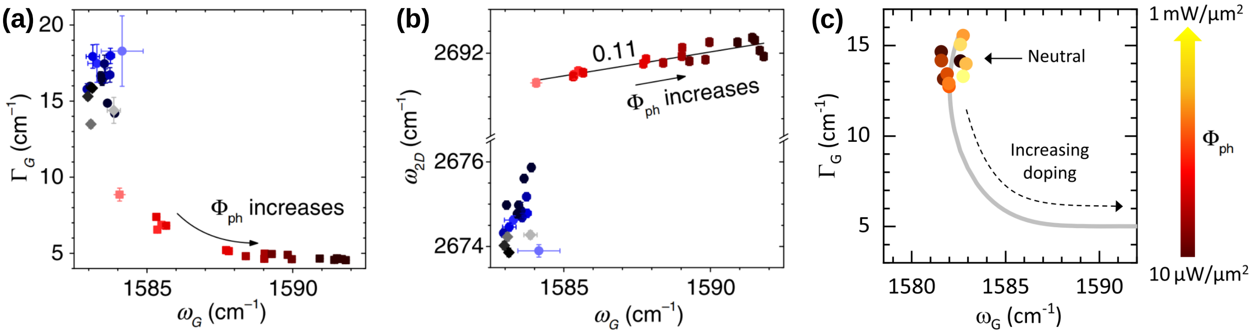

Figure 3.3: (a) Correlation between ω_G and Γ_G and (b) correlation between ω_G and ω_{2D} as a function of Φ_{ph} for coupled MoSe$_2$/graphene (red squares), decoupled MoSe$_2$/graphene (blue circles) and graphene (gray diamonds) on SiO$_2$ substrate. The two correlations show an electron doping in graphene with increasing Φ_{ph}. Adapted from [125]. (c) Correlation between ω_G and Γ_G as a function of increasing Φ_{ph} (scale shown) for MoSe$_2$/graphene encapsulated by hBN. Adapted from [104].

3.2.3 Charge separated state

Because of the relative band alignment between TMD and graphene, the available final states for electron and hole transfer from TMD to graphene are different. This causes the electron and hole transfer to have different efficiencies and transfer times [142]. After the creation of electron-hole pairs in TMD, the charge (electron or hole) with higher tunnelling probability to graphene gets transferred first, which creates a transient charge separated state (shown in figure left panel of 3.4a and 3.4b). Thus, in this transient state, both TMD and graphene are oppositely charged (like the photoinduced charge transfer). The remaining charge in TMD with lower tunnelling probability is then transferred to graphene, making the net charge transfer zero (shown in figure right side panel of 3.4a and 3.4b).

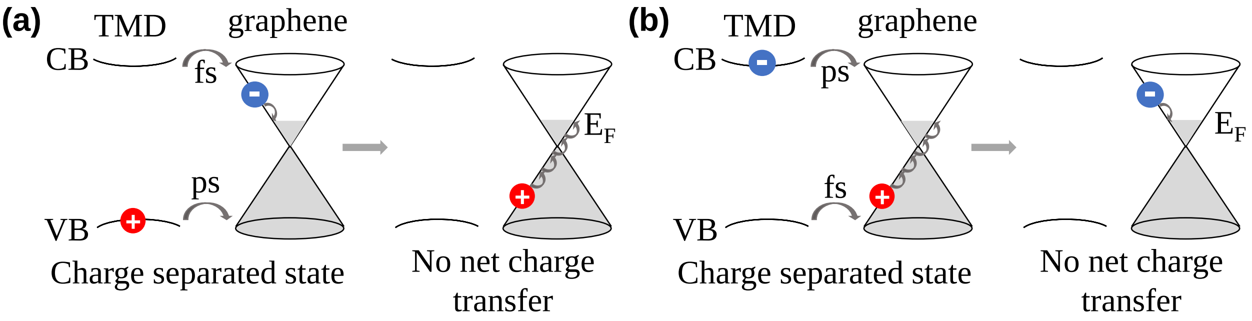

Figure 3.4: Schematic of short lived charge separated state with (a) efficient electron transfer and (b) efficient hole transfer. The gray shaded part shows filled states in graphene. Adapted from [62, 142].

The time- and angle-resolved photoemission spectroscopy (tr-ARPES) has been used extensively to study this transfer mechanism in monolayer TMD/graphene by [142, 143]. These studies reveal an efficient hole transfer from exciton in WS$_2$ to graphene with timescale $<$ 200 fs, which makes the WS$_2$ and graphene to be negatively and positively charged respectively. Then, the electron is transferred to graphene at a timescale $\sim$ 1 ps, possibly via defect-assisted charge tunneling. Whether this mechanism involves charge transfer from excitons or electron-hole pairs remains debatable. The tr-ARPES performed in [144] proposes a tuning of charge separation by varying the twist angle between WS_2 and graphene.

Time-resolved Raman spectroscopy has also been used by [126] in order to track the charge carriers transferred from monolayer WS_2 and monolayer graphene in well-coupled heterostructures by looking at its electronic temperature. This work demonstrates that even if a charge separated state exists, it was not observed beyond 3 ps, which is the upper limit of the short lived charge separated state.

3.2.4 Förster and Dexter Energy transfer

The near-field Coulomb interactions between TMD and graphene give rise to energy transfer processes. There are two energy transfer mechanisms: Förster Energy transfer (FRET) [145] and Dexter energy transfer (DET) [146]. In FRET, the exciton in TMD recombines, giving its energy to graphene which creates an electron-hole pair in graphene (figure 3.5a). In DET, the charges in exciton tunnel from TMD to graphene (figure 3.5b). In both processes, the electron-hole pair formed in/transferred to graphene relaxes to its Fermi level.

Despite the same initial and final states in these two processes, their underlying mechanisms and effects are different. Considering TMD as the donor and graphene as the acceptor, the interaction matrix element describing coupling between initial and final state consists of two terms: Direct coulombic term and exchange coulombic term [147].

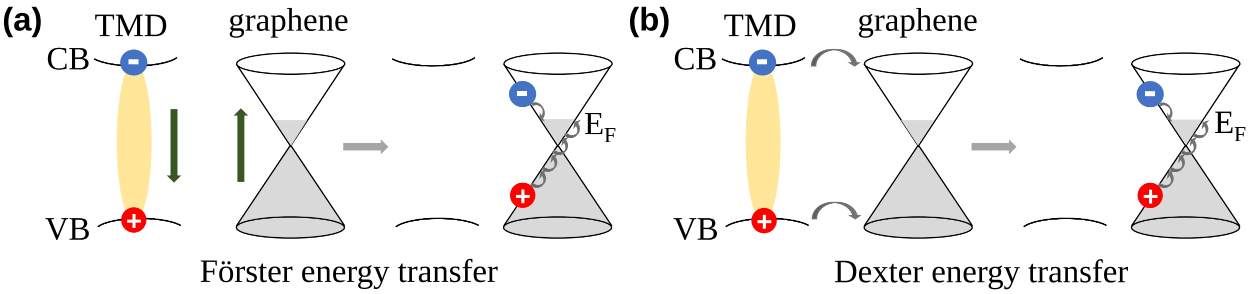

Figure 3.5: Schematic of (a) Förster Energy transfer and (b) Dexter energy transfer. The gray shaded part shows filled states in graphene and yellow shaded area show excitons. Adapted from [62, 125].

In quantum mechanical picture, only two electrons are considered, one in donor D and the other in acceptor A. Then the wavefunctions of initial excited state Ψ_i (D excited and A unexcited) and final excited state Ψ_f (D unexcited and A excited) are given by [147]

$$\Psi_i = \frac{1}{\sqrt{2}} [\Psi_{D*}(1)\Psi_A(2) - \Psi_{D*}(2)\Psi_A(1)] \tag{3.1}$$

and

$$\Psi_f = \frac{1}{\sqrt{2}} [\Psi_D(1)\Psi_{A*}(2) - \Psi_D(2)\Psi_{A*}(1)] \tag{3.2}$$

respectively, in which the * symbol corresponds to the excited part and the numbers 1 and 2 correspond to the two electrons involved. Then, the coupling between initial and final state is given by the interaction matrix

$$U = \langle \Psi_i | \hat{V} | \Psi_f \rangle \tag{3.3}$$

where $\hat{V}$ is the perturbation term in the total hamiltonian. The interaction matrix can be written as

$$U = \Big[\langle \Psi_{D*}(1)\Psi_A(2)|\hat{V}|\Psi_D(1)\Psi_{A*}(2)\rangle - \langle \Psi_{D*}(1)\Psi_A(2)|\hat{V}|\Psi_D(2)\Psi_{A*}(1)\rangle \Big] \tag{3.4}$$

The first term on the right hand side in this interaction matrix corresponds to direct Coulomb interaction. It can be approximated to dipole-dipole interaction between the transition dipole moments corresponding to transitions from unexcited to excited states [132]. This interaction leads to FRET where energy transfer occurs because of interaction of exciton transition dipole in TMD with delocalized transition dipoles in graphene [137, 148]. The FRET depends upon the extent of spectral overlap between donor emission and acceptor absorption and is a long range process. Moreover, FRET depends upon the dimensions of the materials involved [145, 132] and the Förster energy transfer rate Γ_F in the case of 2D materials depends upon the distance between donor and acceptor R as $\Gamma_F \propto R^{-4}$ [149]. Thus, FRET is a long range process with range over a few nm.

The second term in interaction matrix (of equation (3.4)) corresponds to the exchange coulombic term that represents DET that depends upon the orbital overlap of donor and acceptor layers. It is a short range mechanism that decays exponentially with distance [146, 147]. Typically, DET process becomes negligible beyond 1 nm distance between layers.

It should be noted that a Meitner-Auger type energy transfer [150] can occur under high laser fluence when the incident laser excitation cause the formation of excitons in TMD and photoexcited hot holes in graphene [151]. These photoexcited holes relax to just below E_F in graphene near a temporary chemical potential. The exciton in TMD recombines giving its energy to graphene. When graphene is intrinsically hole doped to begin with, the exciton energy is absorbed by electrons in deep valence band, which show a Meitner-Auger type transition to the vacant photoexcited hot holes. Thus, this process involves intraband transition in graphene and the necessarily required momentum for this transition is provided by the excitons having centre-of-mass momentum through processes like thermalization and phonon mediated dephasing [152]. The Meitner-Auger energy transfer can also occur with intraband transitions in conduction band of graphene when it is intrinsically doped with electrons. The extent to which this transfer process occurs is dependent upon the laser fluence as it controls the population of photoexcited hot holes in graphene, as well as on the doping level of graphene which influences the temporary chemical potential where the energy position of these hot holes lies.

3.3 Using PL quenching in $MoSe_2$/n-layer graphene to understand transfer processes

Out of all the possible transfer processes discussed in previous section, our goal here is to determine which ones of them occur and dominate between graphene and TMD. In order to probe these transfer processes, many measurement techniques have been employed, including transient absorption spectroscopy (or pump-probe spectroscopy) [153, 154], time-resolved Raman spectroscopy [126], tr-ARPES [142, 143, 151, 144], mega-electronvolt (MeV) ultrafast electron diffraction (UED) [155, 156] and optical-pump-THz probe spectroscopy [157].

In our work, we have used PL spectroscopy to understand interactions between monolayer $MoSe_2$ and graphene. As discussed in section 1.4.2, there are many intriguing changes in PL of $MoSe_2$ when it is coupled to graphene including the PL quenching and filtering of trion. We have used these changes in PL of $MoSe_2$ as a way to determine the microscopic transfer mechanisms occurring between these layered materials.

3.3.1 Experimental approach

PL spectroscopy has been used on hBN encapsulated heterostructures of monolayer TMD/hBN spacer/monolayer graphene to study the distance dependence of transfer processes between TMD and graphene through varying the thickness of hBN spacer in the work by [110] and by E. Lorchat, as part of his PhD thesis in our research group [22]. The fabrication of samples with an hBN spacer makes it difficult to distinguish the different regions optically because of the low optical contrast of hBN. The samples with an hBN spacer also makes it doubtful whether the region with hBN encapsulated TMD or the hBN encapsulated region with TMD/hBN spacer/graphene should be considered as a reference when comparing the PL of TMD/graphene.

$MoSe_2$/n-layer graphene

In this work, we have fabricated samples with schematics shown in figure 3.6a. The different thicknesses of graphene (n number of layers) covered by monolayer $MoSe_2$ make it possible to observe the distance dependence of transfer processes and thereby determine if one of the short range mechanisms (i.e. charge transfer and Dexter energy transfer) dominates or the long range (Förster Energy transfer) one does.

The hBN on top protects the monolayer $MoSe_2$/n-layer graphene heterostructure from the external disturbances. However, the heterostructure is directly fabricated on top of SiO_2/Si substrate, rather than on a bottom hBN layer. Since hBN layers having large area obtained from mechanical exfoliation tend to have small variations in thickness (in a few nm range) across the layer, making a large area sample becomes very difficult due to the $MoSe_2$ and graphene layers getting broken by these thickness variations in hBN at bottom during the fabrication process.

Moreover, the top hBN and the SiO_2 at bottom of the $MoSe_2$/n-layer graphene form a

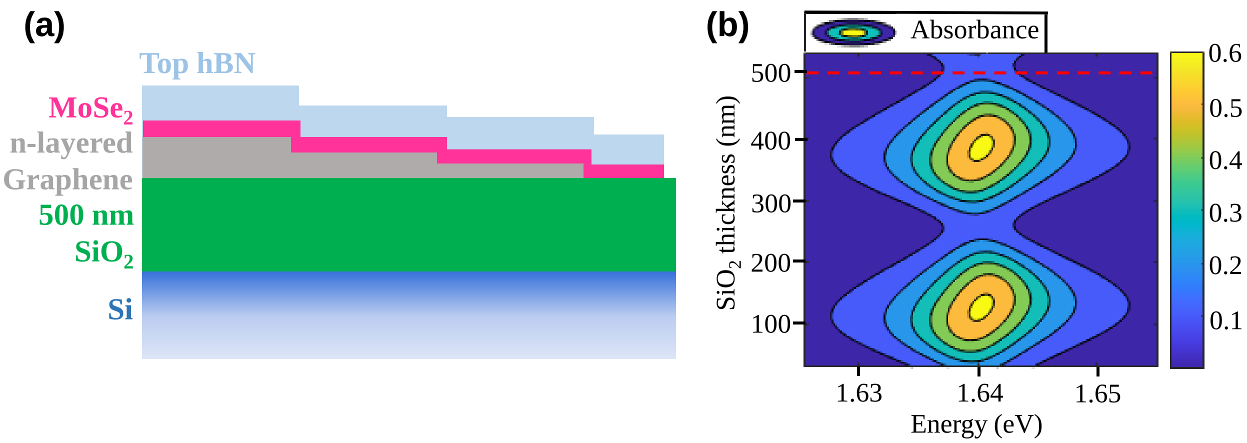

Figure 3.6: (a) Schematic of hBN covered $MoSe_2$/n-layer graphene samples on 500 nm thick SiO_2/Si substrate (b) Calculated absorbance of monolayer $MoSe_2$ with varying SiO_2 thickness at bottom centered at 1.64 eV exciton transition energy, the overall pattern remains similar for transition energies between 1.62 to 1.655 eV. A

microcavity-like structure. Similar to section 1.4.1, where controlling exciton radiative lifetime in TMDs with hBN is discussed, in this microcavity, the Purcell effect is the change in spontaneous emission probability because of variations in density of optical modes caused by changes in the surroundings [158, 159, 160]. The Purcell effect is based on weak coupling between $MoSe_2$ as an emitter and the optical microcavity explained in quantum electrodynamics [132, 161, 116]. Due to this Purcell effect, changing the thickness of SiO_2 can tune the excitonic radiative lifetime in $MoSe_2$ (similar to section 1.4.1, where bottom hBN thickness is varied to tune the exciton lifetime [115]). Figure 3.6b shows how the absorbance of the $MoSe_2$ layer changes with varying SiO_2 thickness calculated using transfer matrix method [115, 162] and we have chosen 500 nm thick SiO_2 to fabricate samples. This was done to place the sample at a node of the microcavity (dashed red line in figure 3.6b) which will give the longest possible radiative exciton lifetime of $MoSe_2$, in order to clearly observe the timescales over the ps range instrument response function (IRF) in TRPL measurements.

3.3.2 Sample fabrication

In this section, we will be describing the procedure of sample fabrication for the above discussed schematic using methods detailed in chapter 2.

The first step is to mechanically exfoliate graphene directly on 500 nm SiO_2/Si substrate. Figure 3.7a shows an optical image of the exfoliated graphene wherein the different thicknesses can be seen. The thicknesses/number of layers of these different regions of graphene is identified by looking at the intensity of Raman G modes shown in figure 3.7c from measured Raman spectra given in figure 3.7b (similar to the method of determining graphene thickness discussed with figure 1.13 [49]). Using this estimation of number of graphene layers, figure 3.7d shows the number of layers in each region on the optical image marked by the color coded dashed contours, finishing the step of obtaining n-layered graphene.

Next, monolayer $MoSe_2$ was exfoliated on PDMS and then transferred onto SiO_2/Si as an

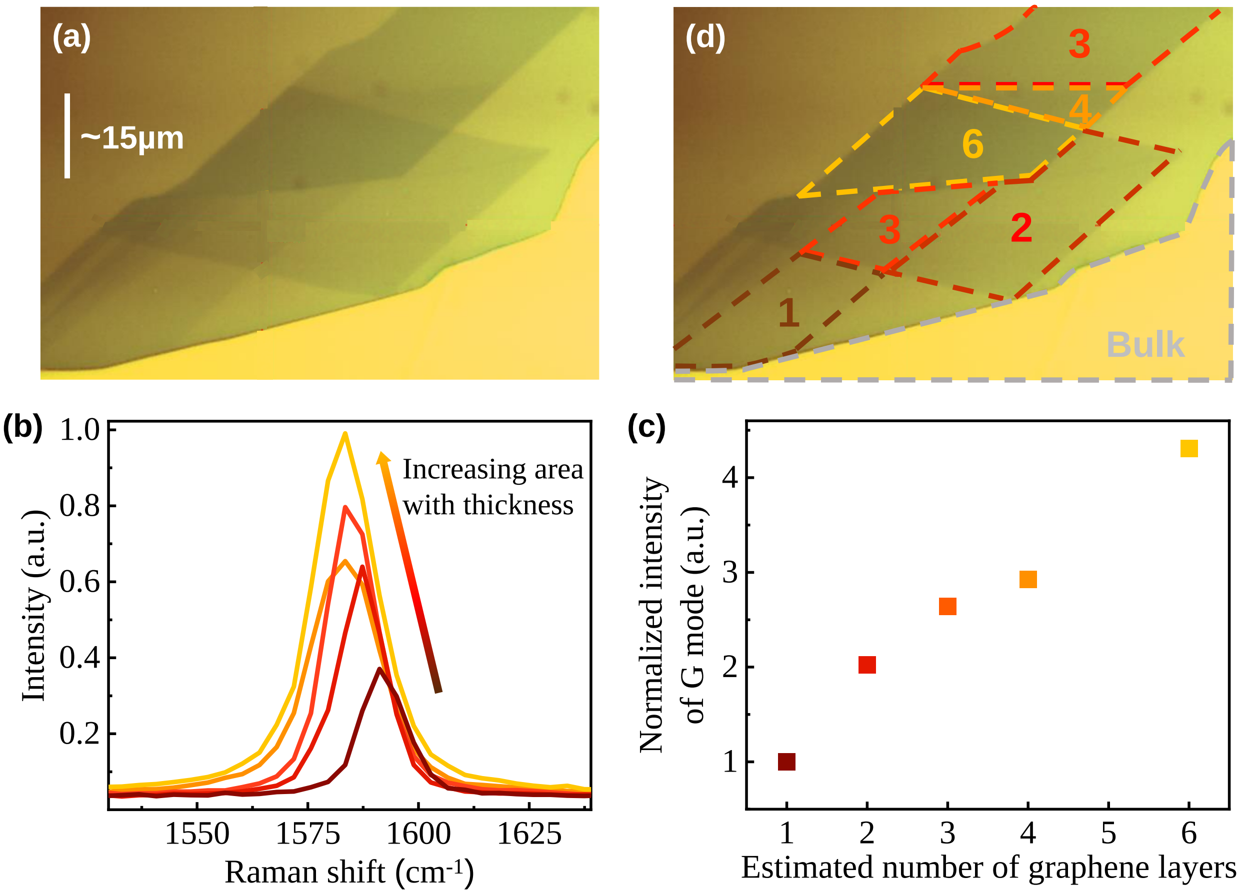

Figure 3.7: (a) Optical image of graphene exfoliated on 500 nm SiO_2/Si substrate (b) Raman G mode in Raman spectra taken on all the different regions with 2.33 eV laser at room temperature with intensity 160 μW/μm^2 (c) and the normalized area of G mode extracted from the Raman spectra used in estimating the number of graphene layers (d) the optical image of graphene with the number in dashed contours denoting the number of layers. The figures b, c and d are color co-ordinated.

intermediate substrate (optical image shown in figure 3.8a) by dry transfer method (described in section 2.1.2). Thin hBN (thickness < 10 nm, identified using optical contrast [106]) was mechanically exfoliated on SiO_2/Si substrates.

Using the PC-method (detailed in section 2.1.2), the hBN and monolayer $MoSe_2$ were deposited onto graphene finishing the sample fabrication, the optical image of sample is shown in figure 3.8b. The sample was made such that the $MoSe_2$ layer covers all the different thicknesses of graphene creating the $MoSe_2$/n-layer graphene regions, including an $MoSe_2$ reference denoted by $MoSe_2$/0 layer graphene in figure 3.8c. The hBN layer covers the whole sample and thus is not denoted by any contours.

The finished sample (named sample 1, optical image with regions shown in 3.8c) has $MoSe_2$ on top of 0 layer, 1 layer, 2 layer, 2 separate regions of 3 layer, 4 layer, 6 layer and bulk graphene. Another similar sample (named sample 2) is fabricated with graphene thicknesses varying from 1 layer to 4 layer.

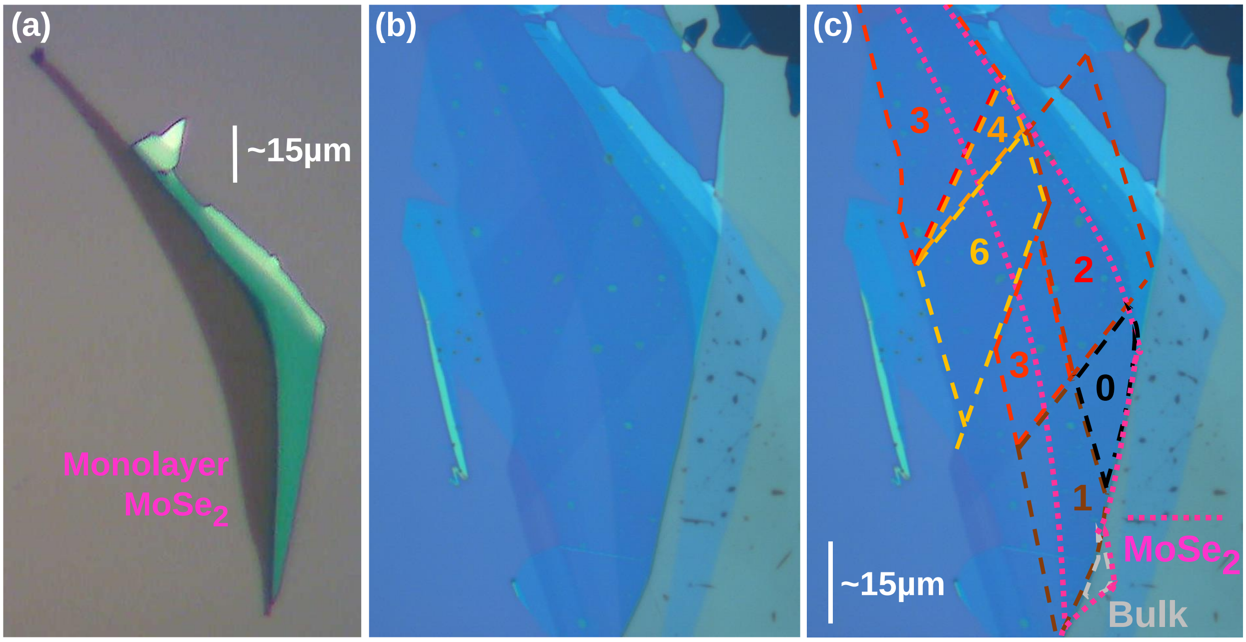

Figure 3.8: (a) Optical image of monolayer $MoSe_2$ transferred on SiO_2/Si substrate (b) the optical image of finished sample 1 having $MoSe_2$/n-layer graphene heterostructure covered by thin hBN (c) and the same optical image denoting the different n-layer graphene regions by dashed contours covered by $MoSe_2$ in the pink dotted contour.

3.3.3 Optical spectroscopy of $MoSe_2$/n-layer graphene

Avoiding non-linear regime

In order to exclude the transfer processes that happen in the non-linear regime, we have used the minimum laser intensity required to measure these PL spectra. This renders the photoinduced charge transfer and Meitner-Auger energy transfer process inefficient.

Auger recombination or exciton-exciton annihilation is a non-linear process in which one exciton recombines non-radiatively by giving its energy to another exciton through dipole-dipole interactions converting the latter into a free electron-hole pair. Auger recombination is a non-linear process whose extent depends upon exciton density and thus, upon the photon flux used for excitation.

In this work, the laser intensity used is around 25 $\mu W/\mu m^2$, which equates to a photon flux $\Phi_{ph} = 8 \times 10^{21}$ $cm^{-2}s^{-1}$. The exciton density generated from this photon flux assuming 10 % absorption [163] and intrinsic exciton lifetime of 2 ps [115] can be estimated to be around 10^9 cm^{-2}. As the exciton density is inversely related to the exciton-exciton distance, this obtained exciton density in our case is in the low regime because it corresponds to the exciton-exciton distance of more than $100a_B^{2D}$ [57].

Reflectance and PL spectra

The regions were first characterized with reflectance and PL spectroscopy. The first PL measurements performed at room temperature show a high PL quenching of PL of MoSe$_2$/0 layer graphene (referred by 'MoSe$_2$' from here onwards for simplicity) by all the different thicknesses of graphene (figure 3.9b). The PL spectrum of MoSe$_2$ can be fitted with two Voigt peaks corresponding to X^0 and X*; while the neutralized PL spectra of MoSe$_2$/nL graphene regions (where nL is n layered graphene for $n > 1$) can be fit with 1 Voigt profile corresponding to X^0, much like in figure 1.27.

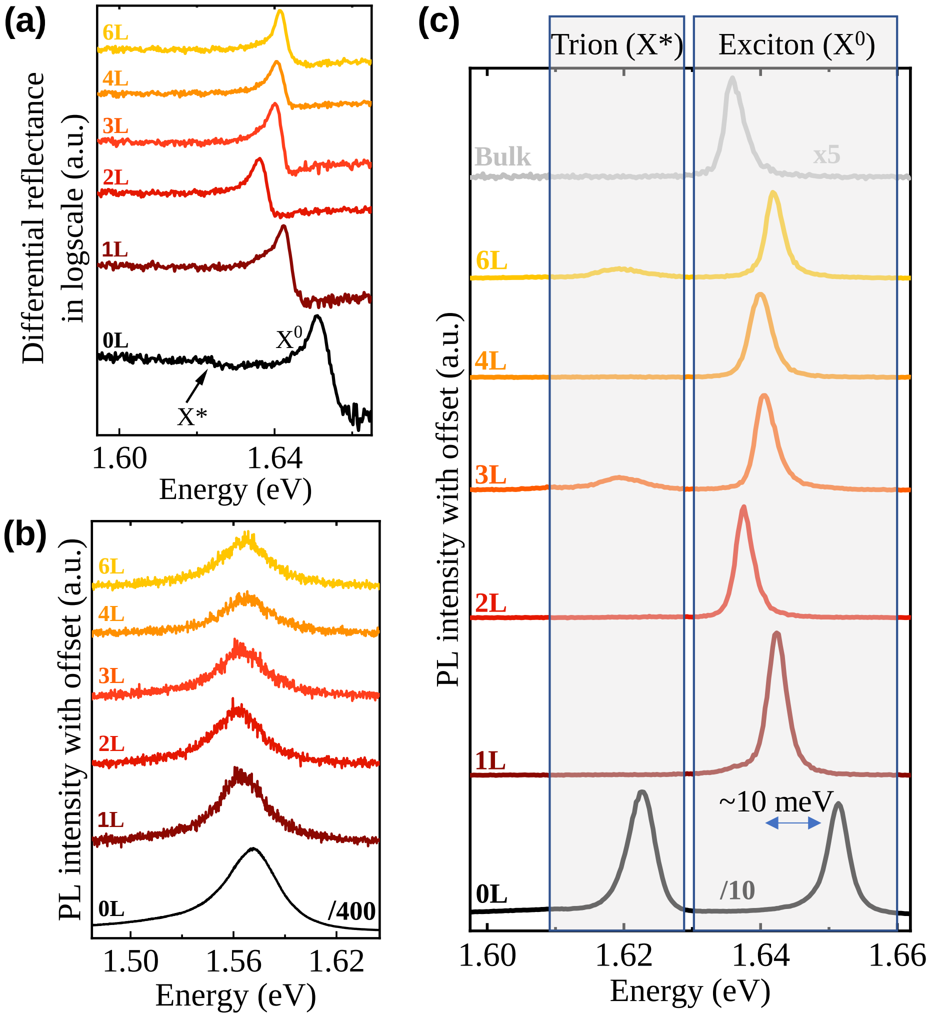

Figure 3.9: Optical spectroscopy spectra taken on all the MoSe$_2$/nL (where nL is n layer graphene) regions in sample 1, shown with vertical offset: (a) Differential reflectance spectra in logscale taken at temperature of 16 K, (b) PL spectra taken at room temperature with 2.33 eV laser and intensity close to 15 µW/µm^2 and (c) PL spectra taken at temperature of 16 K with laser excitation from 1.96 eV laser and intensity close to 25 µW/µm^2, the boxes highlight the X* and X^0 peaks.

Figures 3.9a and 3.9c show the differential reflectance spectra and PL spectra, respectively, taken on all regions at low temperature. Both differential reflectance and PL spectra of MoSe$_2$ have two features: X^0 and X*. On the other hand, MoSe$_2$/nL graphene regions have only one intense X^0 feature redshifted in energy by approximately 10 meV as compared to $MoSe_2$ due to dielectric screening. A very weak feature belonging to X* of $MoSe_2$ might be seen in PL spectra of $MoSe_2$/nL graphene regions after it being massively filtered by the attached graphene layer through transfer processes and charge neutralization. The PL spectra of $MoSe_2$/nL graphene regions for graphene thicknesses from 1 to 6 layers show a quenching comparable to each other when seen with respect to PL of $MoSe_2$; although the bulk graphene quenches the PL of $MoSe_2$ by a much higher factor.

To observe how the PL spectra of sample 1 change spatially over the regions and to obtain data from a large area rather than from just a few spots, we have taken hyperspectral PL maps over the sample.

3.3.4 Hyperspectral PL maps

The figure 3.10a shows the area in sample 1 over which a hyperspectral PL map is taken at low temperature with laser excitation of 1.96 eV. This map with an area of 111 µm × 35 µm was taken with a stepsize of 0.5 µm in order to have the best resolved map possible. The PL spectra in this map that are similar to the ones seen in 3.9c were fitted with Voigt profiles for both X* and X^0 peaks. The parameters extracted from this fitting are shown in figures 3.10b-i with respect to the $MoSe_2$/nL graphene regions in the PL map, where the white points in maps belong to spectra deviating from the expected features X* and X^0.

X^0 and X* positions

The figure 3.10b shows how the position of X^0 changes over the sample. The region with $MoSe_2$ has X^0 energy close to 1.65 eV, higher than nearly 10 meV when compared to $MoSe_2$/nL graphene regions. Although, the lower part of $MoSe_2$/1L graphene shows the X^0 close to 1.65 eV. This figure also shows that there is no significant strain on the heterostructure because such a strain will cause the X^0 position to change continuously in the direction of the strain [164].

The difference between positions of X^0 and X* varying over the sample is shown in figure 3.10d. This difference gets reduced wherever $MoSe_2$ is covering graphene of any thickness. All PL spectra taken over $MoSe_2$/nL graphene regions do not show a measurable X* peak due to its transfer to graphene and thus, figure 3.10d only depicts the points where an X* peak is clearly seen, the latter of which shows how the FWHM of X* varies over the sample. It should be noted that the intense X* peak in $MoSe_2$ has a slight asymmetry in some points of the map due to a tail on the low-energy side coming because of electron recoil effects (seen in figure 3.9 as well) [165].

X^0 FWHM

The FWHM of X^0, shown in figure 3.10e, is in the range of a few meV and shows a reduction with attachment of graphene.

PL intensity

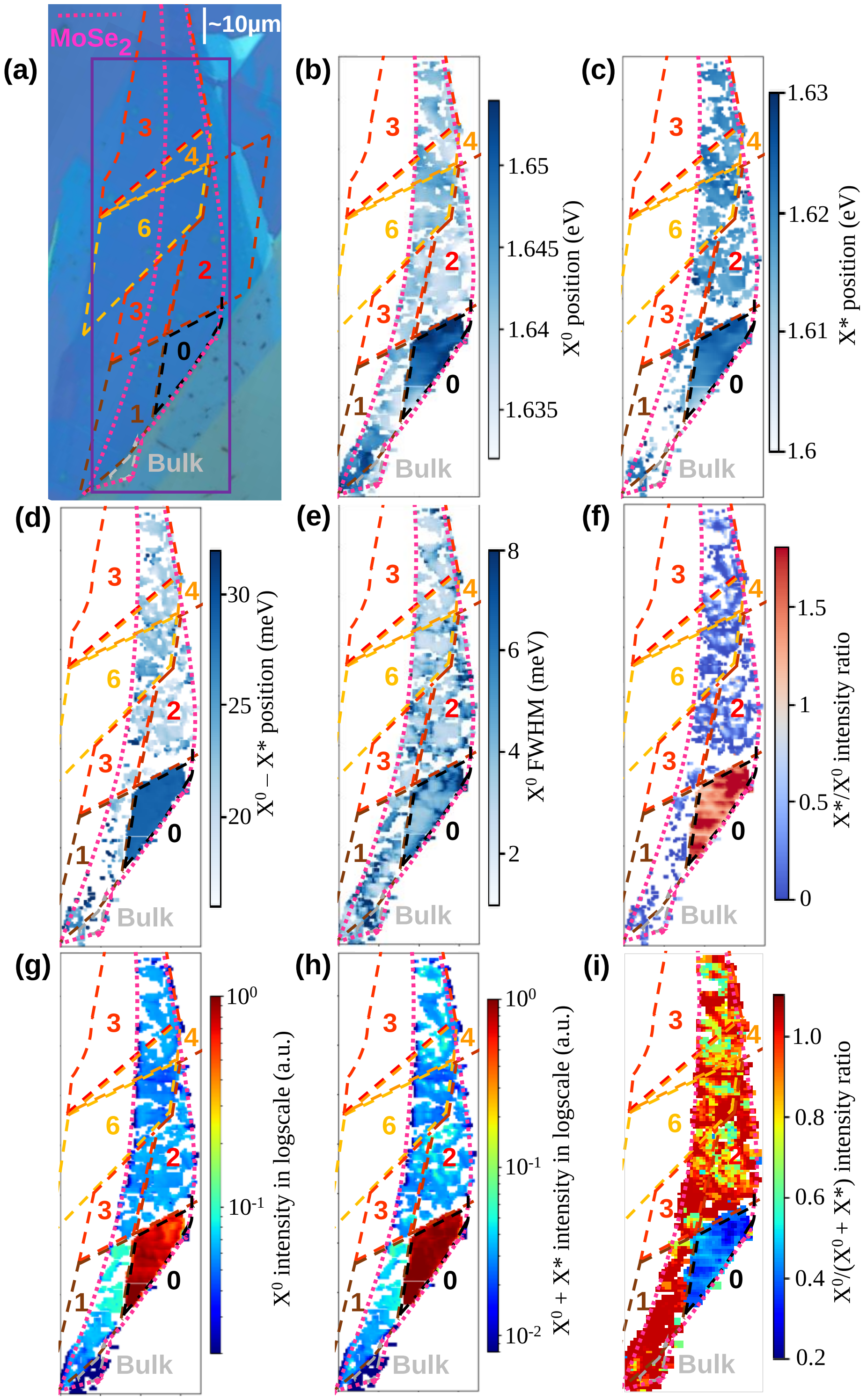

Figure 3.10: (a) Optical image of sample 1 with the purple rectangle denoting the area of hyperspectral PL map of MoSe$_2$ taken at 16 K with laser excitation of 1.96 eV and intensity close to 25 µW/µm^2, the extracted parameters: (b) X^0 position (c) X* position (d) X^0 − X* position (e) X^0 FWHM (f) ratio of intensities of X* to X^0 (g) X^0 intensity and (h) total PL intensity in logscale and (i) ratio of intensity of X^0 to total PL intensity. All images show the MoSe$_2$/n-layer graphene regions with dashed contours.

The figure 3.10g shows the variation of X^0 intensity over the sample when the intensity is almost saturated for the case of $MoSe_2$. This map helps in visualizing the reduction or quenching in X^0 intensity of $MoSe_2$ because of transfer to graphene when it is on top of different graphene thicknesses. The $MoSe_2$/1L graphene has a greater X^0 intensity compared to thicker $MoSe_2$/nL graphene regions.

The lower part of $MoSe_2$/1L graphene that has greater X^0 energy than the rest of it also shows a slightly smaller X^0 intensity. The reason for energy of X^0 in lower part of $MoSe_2$/1L graphene being close to that of $MoSe_2$ can be thought to be a very weak coupling between the $MoSe_2$ and 1L graphene layers; but then the X^0 intensity in this lower $MoSe_2$/1L graphene region should be nearly as high as that of $MoSe_2$, which is the opposite of the observed effect. Thus, this difference between the properties of upper and lower parts of $MoSe_2$/1L graphene and the unexpected behaviour of X^0 in the lower part cannot be easily explained by the difference in coupling between $MoSe_2$ and graphene layers and needs further study.

The total PL intensity (addition of X^0 + X^* intensities) is shown in figure 3.10h, almost saturated for $MoSe_2$ region. The intensity ratio of X^0 to total PL intensity given in figure 3.10i shows how the fraction of total PL intensity belonging to X^0 varies over the sample. The intensity of X^* peak is negligible for many points in $MoSe_2$/nL graphene regions, as can be seen in figure 3.10f that shows the intensity ratio of X^* to that of X^0 for the points with observable X^* peaks. This intensity ratio is higher than 1 for all points in the $MoSe_2$ region, making the total PL intensity of this region much higher than the rest.

The PL map also covers a small part of the sample having $MoSe_2$ attached to bulk graphene. The energies and FWHM of X^0 and X^* observed for this part are similar to the other regions with graphene, with the exception that the X^0 intensity is much lower compared to the other $MoSe_2$/nL graphene parts (3.10g). This could be explained by the quite thick bulk graphene changing the environment in the optical cavity so that the $MoSe_2$ covering it is not at the node shown in figure 3.6b, causing changes in the X^0 intensity.

Correlations

Some very interesting correlations can be plotted using the data extracted from the hyperspectral PL map in figure 3.10. The figure 3.11a shows the correlation between X^0 position and X^0 FWHM for all $MoSe_2$/nL graphene regions in sample 1. This correlation shows the spread of the position and FWHM of X^0 and the mean values for each region.

The figure 3.11b depicts the correlation between total PL intensity and the ratio of intensities of X^0 and total PL for each region. As the coupling between $MoSe_2$ and n-layered graphene decreases, the X^* intensity increases as its transfer from $MoSe_2$ to graphene becomes less efficient. Thus, the total PL intensity increases because of increasing X^* intensity, while the ratio of X^0 intensity to total PL intensity decreases. This results in a tail-like structure in the correlation for all different thicknesses of graphene. It can be considered that the points in the sample with high ratio of X^0 to total PL intensities have a strong coupling between $MoSe_2$ and graphene; while the points with weaker coupling between the layers have a smaller ratio. Although a particular value of this intensity ratio to divide the strong and weak coupling regimes cannot be determined, the figure 3.11b has square and triangular symbols

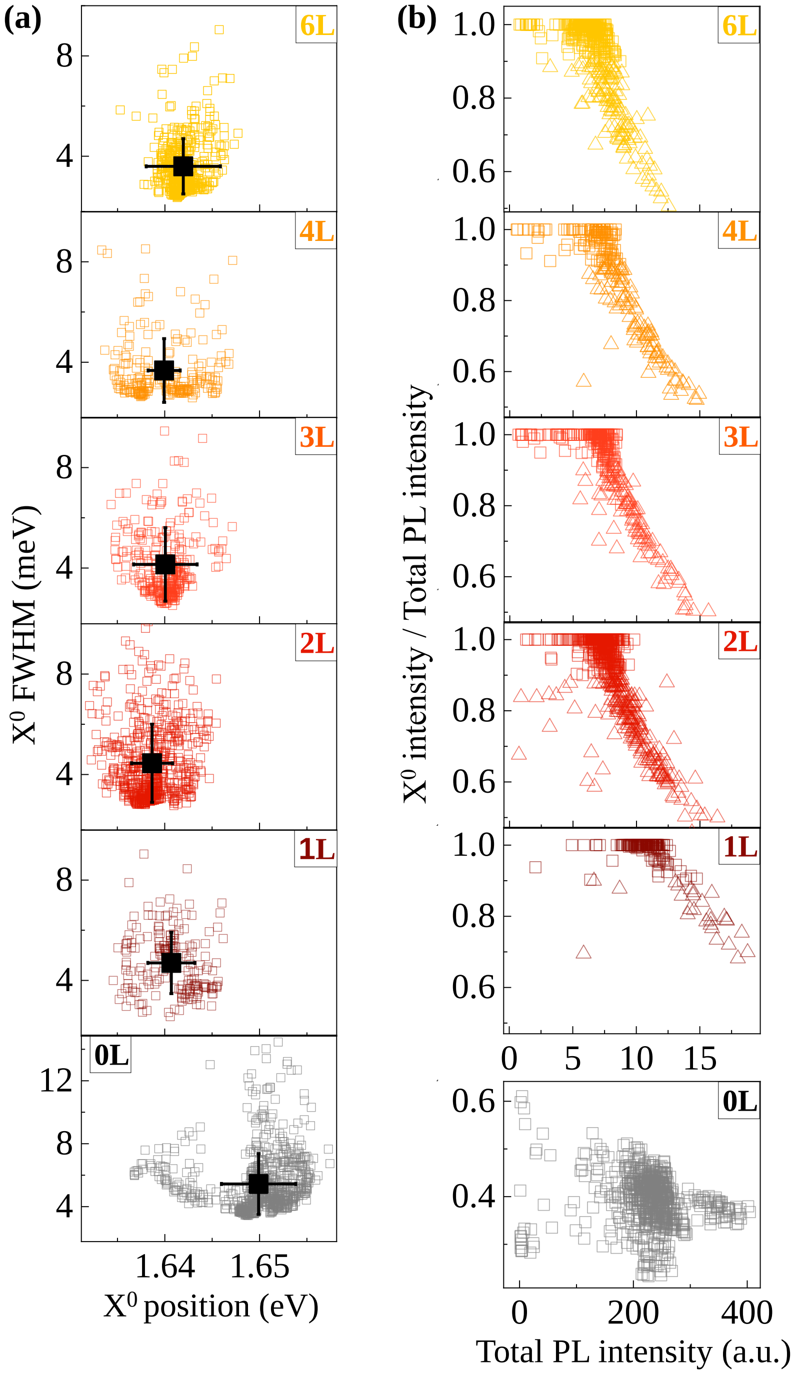

Figure 3.11: (a) Correlation between X^0 position and X^0 FWHM, the black filled squares show the mean values with standard deviations as error bars (b) Correlation between total PL intensity and ratio of X^0 intensity to total PL intensity, in which squares and triangles represent strongly and weakly coupled points respectively. Both correlations are obtained from map shown in figure 3.10. The data from only one of the two MoSe$_2$/3L graphene regions in sample 1 is given here for simplicity.

denoting the points having strongly and weakly coupled layers, respectively, corresponding to a threshold value of 0.9 for the ratio of X^0 intensity to total PL intensity to divide the coupling regimes.

Extracted mean values as a function of graphene thickness

The mean values of parameters extracted from the PL maps of $MoSe_2$ as a function of the number of graphene layers is shown in the figure 3.12 and in table 3.1. The mean values of X^0 position show an expected shift by $\approx$ 10 meV with addition of any of the graphene layers (figure 3.12a).

The difference between positions of X^0 and X^* defines the binding energy of X^*, which shows a reduction when $MoSe_2$ is covering graphene of any thickness (shown in figure 3.12b).

In order to quantify the PL quenching of $MoSe_2$ when it is coupled to graphene, we define the quenching factor of an $MoSe_2$/nL graphene region with respect to $MoSe_2$ by

$$\text{Quenching factor (QF)} = \frac{\text{Intensity of MoSe}_2}{\text{Intensity of MoSe}_2/\text{nL graphene}} \tag{3.5}$$

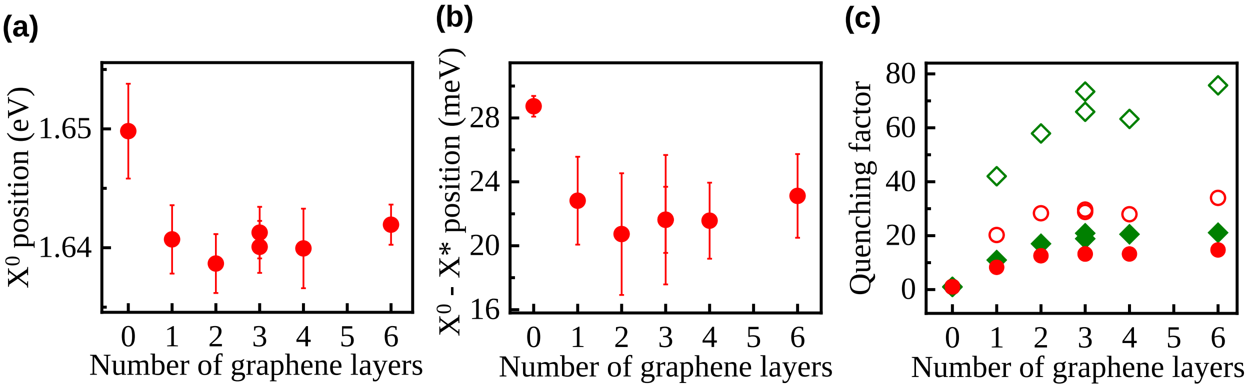

Figure 3.12: The mean values of (a) X^0 position (b) X^0 position − X^* position and (c) quenching factors as a function of number of graphene layers under $MoSe_2$ taken from the hyperspectral PL maps. The red and green symbols denote mean values from PL maps taken at temperature of 16 K with laser excitation of 1.96 eV and 2.33 eV respectively, while maintaining laser intensity close 25 $\mu W/\mu m^2$. The standard deviations are denoted by error bars. The open and filled symbols in (c) represent quenching factors for total PL and X^0 respectively.

This QF can be defined for X^0 and total PL separately. Figure 3.12c shows the QF for both X^0 and total PL when the laser energies 1.96 eV and 2.33 eV are used. It is quite clear that even if the QFs for the two incident laser excitations are different, the relative trend of change in QF as a function of number of graphene layers is the same. It is also important to note that this trend remains the same if the QFs are plotted separately for spots that have strong or weak coupling between layers, with the values of QFs becoming higher or lower respectively. The QF for X^0 shows a saturation beyond the thickness of 3 layers of graphene, implying that the interactions between $MoSe_2$ and graphene are of very short range.

The hyperspectral PL map taken with 2.33 eV from which the QF is calculated is shown in figure A.1 in appendix A. This map shows similar trends in PL of different regions to the one taken with laser energy 1.96 eV, alongwith the anomalous properties of lower $MoSe_2$/1L graphene region. The dependence of QF on the incident laser energy will be explored more in the next section.

$MoSe_2$ /nL Gr	X^0 position (eV)	X* position (eV)	X^0-X* position (meV)	X^0 FWHM (meV)	X* FWHM (meV)	X*/X^0 intensity ratio	QF (X^0)	QF (X^0+X*)
0L	1.650 ± 0.004	1.621 ± 0.004	28.7 ± 0.6	5.5 ± 2	6.0 ± 1.4	1.60 ± 0.4	–	–
1L	1.641 ± 0.003	1.618 ± 0.006	22.8 ± 5.6	4.7 ± 1.2	7.8 ± 2.5	0.13 ± 0.12	8.2	20.2
2L	1.639 ± 0.002	1.618 ± 0.004	20.7 ± 3.8	4.4 ± 1.6	8.1 ± 2.2	0.22 ± 0.23	12.5	28.3
3L	1.640 ± 0.002	1.618 ± 0.004	21.6 ± 2.1	4.1 ± 1.5	8.3 ± 2.3	0.21 ± 0.24	13.2	29.7
4L	1.640 ± 0.003	1.618 ± 0.003	21.6 ± 2.4	3.7 ± 1.3	8.0 ± 1.4	0.24 ± 0.24	13.2	27.9
6L	1.642 ± 0.002	1.619 ± 0.003	23.1 ± 2.6	3.6 ± 1.1	8.6 ± 2.3	0.15 ± 0.18	14.7	34.0

Table 3.1: The mean values of parameters of PL extracted from hyperspectral PL map taken with 1.96 eV shown in figure 3.10 dependent upon nL of graphene under $MoSe_2$.

3.3.5 High energy excitonic species

In order to understand the PL quenching in $MoSe_2$/nL graphene system, a deeper understanding about the formation of hot excitons is necessary, which will also help us explore their possible transfer to graphene and the effects of attachment of graphene on binding energy in $MoSe_2$.

Photoluminescence excitation spectroscopy

The PLE measurements were performed by measuring the PL spectra of sample 1 with changing incident laser energy from 1.69 eV to 2.57 eV at low temperature (method described in section 2.2.1). The measurements were mainly done on $MoSe_2$ and $MoSe_2$/1L graphene regions and the typical PL spectra at the chosen spots are shown in figure 3.13a denoting the fitting method for X* and X^0 peaks. Because of the prominent low-energy tail in spot of $MoSe_2$, it has been fit by two Voigt profiles. The PL spectra taken with incident laser energies of 1.85 eV (close to expected B exciton energy) and 1.69 eV (the closest measurement taken near X^0 resonances) are also shown in figures 3.13b and 3.13c respectively.

The intensity observed at each incident laser energy was normalized with respect to laser power and the spotsize. Figure 3.13d shows the contourplots of PL intensity of $MoSe_2$ and $MoSe_2$/1L graphene with varying laser energy. The onset of increase in PL intensity in these contourplots around the laser energy of 1.85-1.86 eV comes with the broadening of FWHM of the peaks in PL at these spots as given in figure 3.14 which shows FWHM a function of incident laser energy. The broad X* peak in $MoSe_2$/1L graphene is likely because of it being a combination of two separate trions arising from two adjacent spots under the laser.

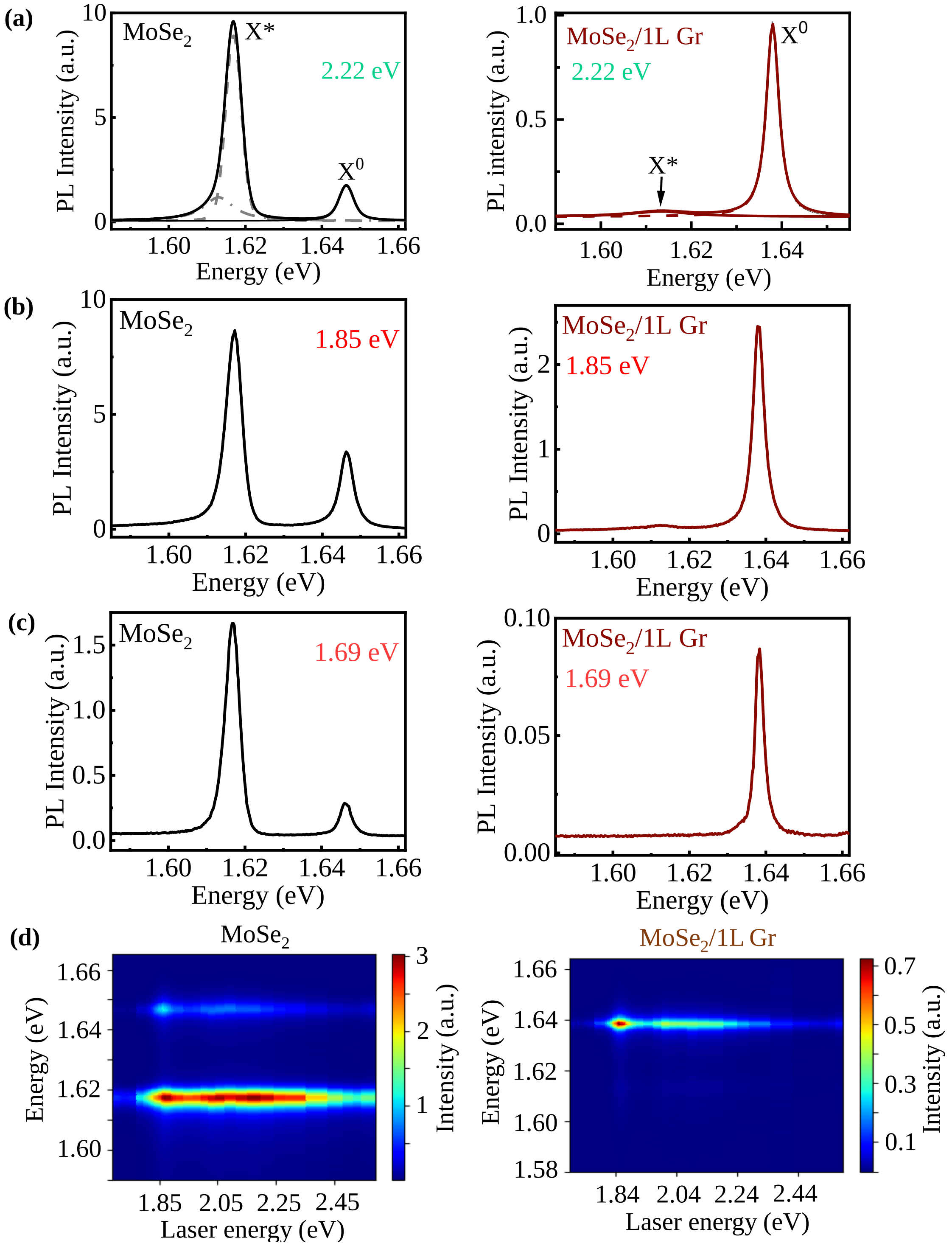

Figure 3.13: PL spectra of $MoSe_2$ (left panel) and $MoSe_2$/1L graphene (right panel) taken with laser energy of (a) 2.22 eV (b) 1.85 eV and (c) 1.69 eV, with (a) describing the fitting scheme of peaks. (d) Contourplots of PL intensity of $MoSe_2$ and $MoSe_2$/1L graphene with respect to the incident laser energy. All measurements are done at 16 K with laser intensity close to 10 µW/µm^2.

The PL intensity data obtained from PLE can be plotted as a function of incident laser energy (as done in figure 3.15) or the difference between laser energy and X^0 position called detuning (as done in figure 3.16). The X^0 and total PL intensities of $MoSe_2$ show an increase

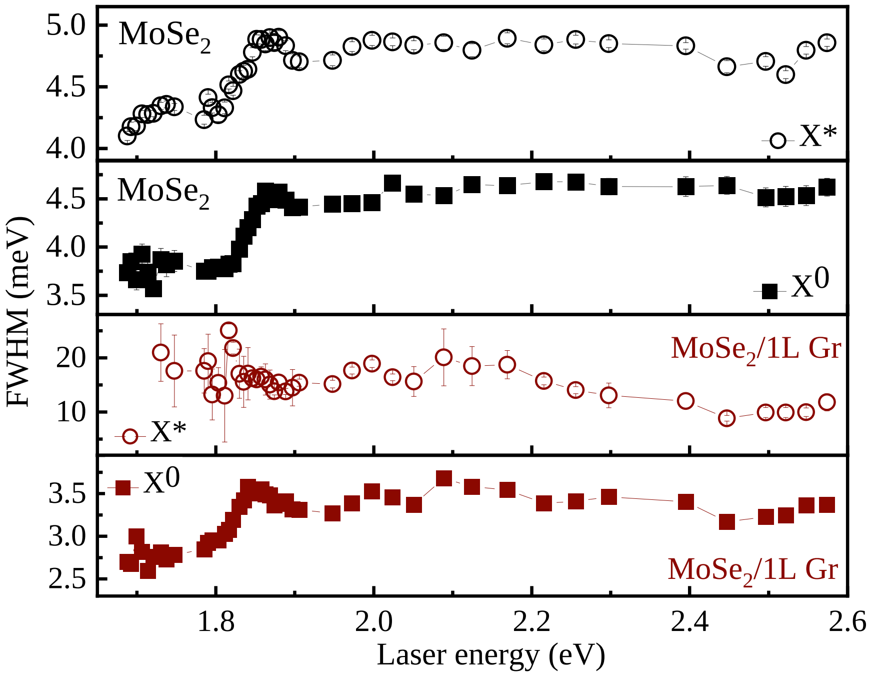

Figure 3.14: The FWHM of X* and X^0 peaks in PL spectra of MoSe$_2$ and MoSe$_2$/1L graphene shown in 3.13d as a function of incident laser energy. All measurements are done at 16 K with laser intensity close to 10 µW/µm^2.

around 1.856 eV where B$_{1s}$ exciton is expected [166, 9, 167]. The high energy A exciton species, namely X^0_{2s} and X^0_{3s}, do not show any fingerprint in the PLE data of MoSe$_2$ because of them being obscured by B$_{1s}$ exciton (as also observed by [166]). The B$_{1s}$ exciton in PL intensities of MoSe$_2$/1L graphene is redshifted as compared to the one in MoSe$_2$ due to dielectric screening.

Using the X^0 and total PL intensities, the QF for both are calculated and shown as a function of laser energy. Because of the different X^0 positions for MoSe$_2$ and MoSe$_2$/1L graphene, for calculating QF as a function of detuning, the data for MoSe$_2$/1L graphene is interpolated with respect to the detuning seen in the case of MoSe$_2$. In MoSe$_2$, the weight of X* i.e. ratio of X* intensity to total PL intensity increases as laser energy starts to reach X^0, resulting in the increase of QF for total PL. This X* weights in MoSe$_2$ and MoSe$_2$/1L graphene can also be visualized in the contourplots in figure A.2a of appendix A that show the PL intensity normalized by total PL intensity at each laser energy. The QFs seen here for the incident laser energies of 1.96 eV and 2.33 eV are smaller than the ones observed in from the hyperspectral PL maps (given in 3.12c); but this could be attributed to the fact that the latter is an average from all spots in the layers, while the QFs in PLE data are from singular spots. Thus, we should focus more on the trend of QFs in 3.15 and 3.16, rather than only on the particular values. The QF for X^0 show an increase beyond laser energy of 1.87 eV or detuning of 250 meV, making it clear that the hot excitons with energy higher than B$_{1s}$ exciton transfer from MoSe$_2$ to graphene more efficiently than the excitons with lower energy.

The figure A.2b in appendix A shows the PLE data of spots in MoSe$_2$, MoSe$_2$/1L graphene

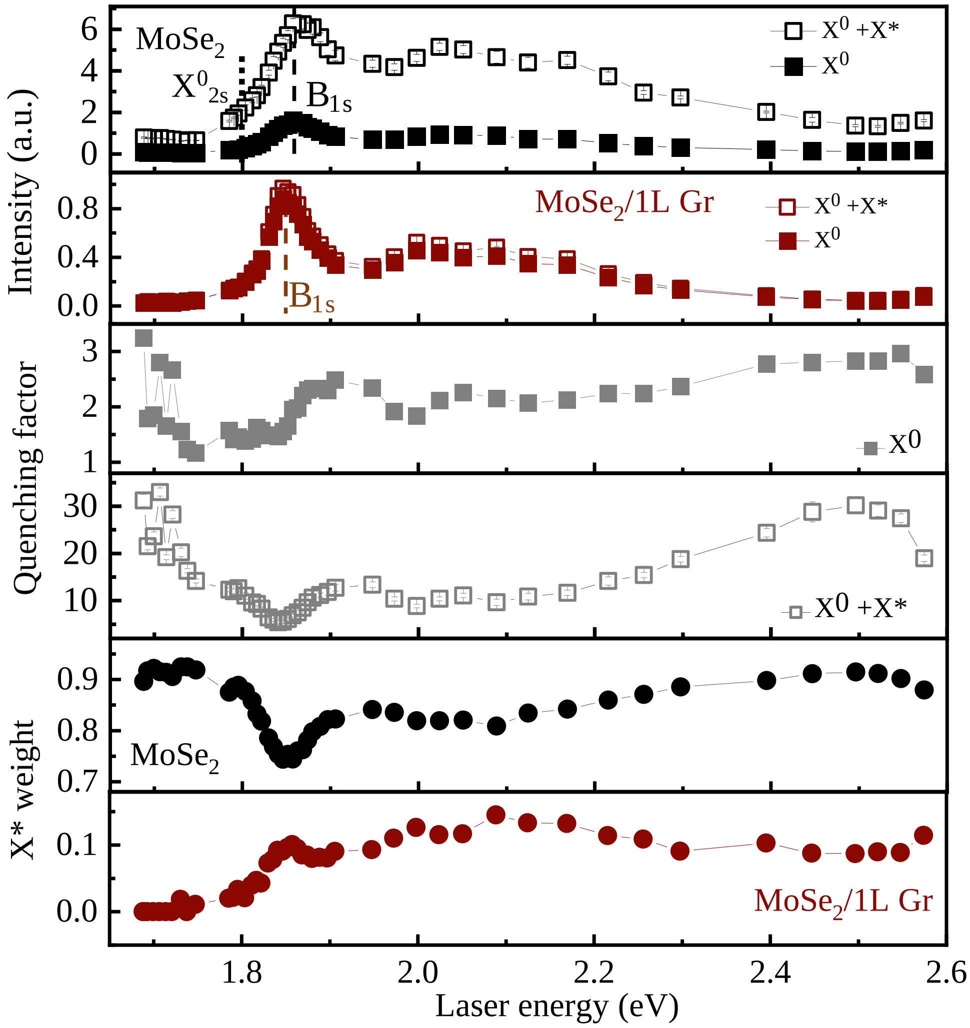

Figure 3.15: The panels from top to bottom showing PLE results: the X^0 intensity and total PL intensity, the quenching factors of X^0 and total PL and weight of X* in the PL intensity for MoSe$_2$ and MoSe$_2$/1L graphene as a function of incident laser energy. The dotted and dashed lines show positions of X^0_{2s} and B_{1s} exciton respectively. The intensities at each laser energy are normalized by the laser intensity. All measurements are done at 16 K with laser intensity close to 10 µW/µm^2.

and MoSe$_2$/2L graphene regions. Similar to the data seen so far, the X^0 intensity in MoSe$_2$/2L graphene has a peak near B_{1s} exciton.

Also, the PLE data measured on sample 2 which is given in appendix A.4 to confirm the data and trends seen in sample 1.

Estimation of binding energy

The binding energy of excitons in MoSe$_2$ changes with the addition of graphene because of screening effects. We have estimated the binding energies in the different regions of sample 1 by observing the high energy excitons in hot PL spectra given in figure 3.17. These are representative spectra taken from hyperspectral hot PL maps on each region with laser energy of 2.33 eV.

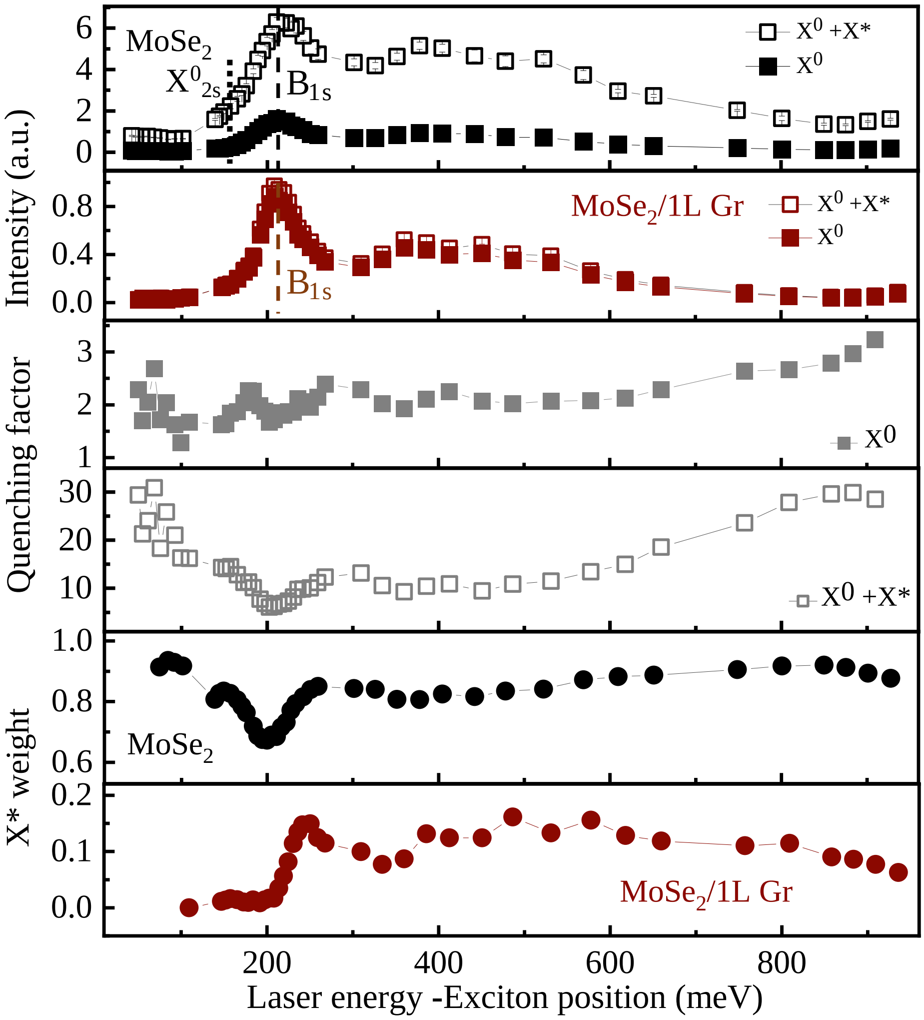

Figure 3.16: The panels from top to bottom showing PLE results: the X^0 intensity and total PL intensity, the quenching factors of X^0 and total PL and weight of X* in the PL intensity for MoSe$_2$ and MoSe$_2$/1L graphene as a function of difference between laser energy and X^0 position (detuning). The dotted and dashed lines show positions of X^0_{2s} and B_{1s} exciton respectively. The intensities at each laser energy are normalized by the laser intensity. All measurements are done at 16 K with laser intensity close to 10 µW/µm^2.

The lineshape of hot PL in MoSe$_2$ is depicted in black spectrum with the positions of X^0_{2s} and B_{1s} exciton (expected from [166, 167, 168] using the difference between positions of these peaks and X^0 as well as the PLE data in figures 3.16 and 3.15).

In the case of MoSe$_2$/1L graphene, the lineshape of hot PL changes as compared to MoSe$_2$, with a redshift of the peaks and significant reduction in intensity of B_{1s} exciton. The 2D Raman mode of 1-layer graphene can also be seen in this spectrum.

For MoSe$_2$/2-6L graphene i.e. MoSe$_2$ attached to graphene with thickness varying from 2 to 6 layers, the lineshape of hot PL changes again as compared to MoSe$_2$/1L graphene. The X^0_{2s} and X^0_{3s} peaks almost merge, making the determination of their exact positions a little difficult. The 2D mode of graphene can be seen in the spectra.

In these hyperspectral hot PL maps, most of the spots have the hot PL spectra corresponding

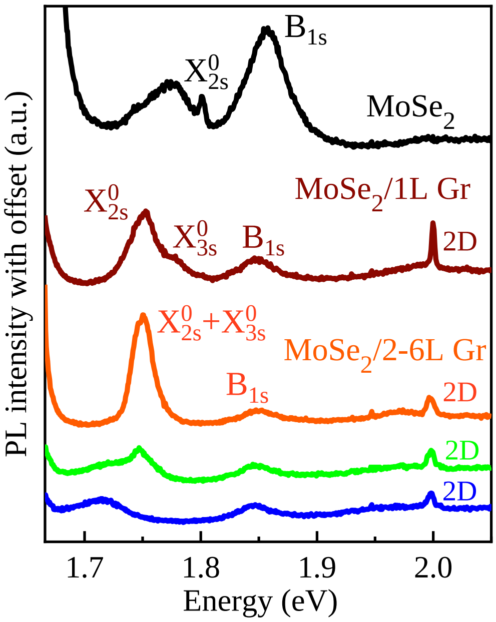

Figure 3.17: Lineshapes of hot PL spectra of $MoSe_2$, $MoSe_2$/1L graphene and $MoSe_2$/2-6L graphene (i.e. $MoSe_2$ attached to graphene with thickness varying from 2 to 6 layers) with vertical offset in intensity, the blue and green spectra are the anomalous hot PL spectra from some points in $MoSe_2$/2L graphene. All measurements done at 16 K with laser energy 2.33 eV and intensity smaller than 130 $\mu W/\mu m^2$.

to the number of graphene layers attached to $MoSe_2$ as discussed so far. But there are a few spots in $MoSe_2$/2L graphene region that have anomalous hot PL spectra, typically having the two lineshapes shown in green in blue colour in figure 3.17. It is important to note that these spots with anomalous hot PL spectra have PL spectra similar to the other spots that have the hot PL lineshape as in figure 3.17. The sample 2, on the other hand, has lineshapes of hot PL similar to the ones observed in sample 1 without any spots having such anomalous hot PL lineshapes (appendix A.3).

The difference between positions of X^0 and X^0_{2s} (Δ_{2s-1s}) and between X^0 and B_{1s} (Δ_{B1s-1s}) excitons averaged from the maps are given in table 3.2. Using the simplification that Δ_{2s-1s} is proportional to the changes in binding energy E_b of X^0 [169, 63] and taking the E_b for the case of $MoSe_2$ from [168], the E_b for $MoSe_2$/nL graphene is estimated.

$MoSe_2$/nL Gr	Δ_{2s-1s} (meV)	Δ_{B1s-1s} (meV)	E_b (meV)
0L	150 ± 1	206 ± 0.5	≈ 210
1L	107 ± 1	205 ± 1	≈ 150
2-6L	100 - 110	≈ 205	≈ 150

Table 3.2: The Δ_{2s-1s} and Δ_{B1s-1s} observed from hot PL spectra of $MoSe_2$/nL graphene and the binding energy estimated using these values.

Thus, the addition of nL graphene induces dielectric screening which results in reduced Δ_{2s-1s} and reduces the binding energy in $MoSe_2$ by ≈ 30 %. From equation (1.42), the radiative lifetime τ_{rad} for X^0 is related to E_{b} by

$$\tau_{\mathrm{rad}} \propto E_{\mathrm{b}}^{-2}. \tag{3.6}$$

Hence, there is an increase in τ_{rad} of X^0 with the coupling of nL graphene to MoSe$_2$.

3.3.6 Exciton dynamics

Upon coupling of graphene to MoSe$_2$, the 3-level model explaining the exciton dynamics changes by opening of non-radiative pathways for transfer of exciton and hot exciton from MoSe$_2$ to graphene, as depicted in figure 1.29b, the trion dynamics changes in an analogous manner. In order to study the exciton and trion dynamics and estimate the timescales involved in it, TRPL measurements were performed by our collaborators in INSA, Toulouse.

According to the 3-level model given in figure 1.29b, the rate equations for X^0 in MoSe$_2$ are

$$\frac{dn_{\mathrm{X^h}}}{dt} = -\frac{n_{\mathrm{X^h}}}{\tau_{\mathrm{relax}}} \tag{3.7}$$

and

$$\frac{dn_{\mathrm{X^0}}}{dt} = -\frac{n_{\mathrm{X^0}}}{\tau_{\mathrm{rad}}} + \frac{n_{\mathrm{X^h}}}{\tau_{\mathrm{relax}}} \tag{3.8}$$

where $n_{\mathrm{X^h}}$ and $n_{\mathrm{X^0}}$ are the populations of hot excitons and excitons respectively. Solving these two rate equations, one gets the PL intensity at time t as

$$I_{\mathrm{X^0(MoSe_2)}}(t) \propto \frac{n_{\mathrm{X^h}}(0)}{\tau_{\mathrm{relax}} - \tau_{\mathrm{rad}}}(\mathrm{e}^{-t/\tau_{\mathrm{relax}}} - \mathrm{e}^{-t/\tau_{\mathrm{rad}}}) \tag{3.9}$$

where $n_{\mathrm{X^h}}(0)$ is the initial photogenerated population of hot excitons.

For the case of MoSe$_2$ coupled to graphene, these rate equations become

$$\frac{dn_{\mathrm{X^h}}}{dt} = -\frac{n_{\mathrm{X^h}}}{\tau_{\mathrm{relax}}} - \frac{n_{\mathrm{X^h}}}{\tau_{\mathrm{G}}^{h}} \tag{3.10}$$

and

$$\frac{dn_{\mathrm{X^0}}}{dt} = -\frac{n_{\mathrm{X^0}}}{\tau_{\mathrm{rad}}} - \frac{n_{\mathrm{X^0}}}{\tau_{\mathrm{G}}} + \frac{n_{\mathrm{X^h}}}{\tau_{\mathrm{relax}}} \tag{3.11}$$

making the PL intensity in MoSe$_2$/graphene at time t:

$$I_{\mathrm{X^0(MoSe_2/Gr)}}(t) \propto \frac{n_{\mathrm{X^h}}(0)}{\tau_{\mathrm{rel}} - \tau_{\mathrm{decay}}}(\mathrm{e}^{-t/\tau_{\mathrm{rel}}} - \mathrm{e}^{-t/\tau_{\mathrm{decay}}}) \tag{3.12}$$

where $\tau_{\mathrm{rel}} = ((\tau_{\mathrm{relax}})^{-1} + (\tau_{\mathrm{G}}^{h})^{-1})^{-1}$ and $\tau_{\mathrm{decay}} = ((\tau_{\mathrm{rad}})^{-1} + (\tau_{\mathrm{G}})^{-1})^{-1}$ are the effective timescales of hot exciton relaxation and exciton decay of X^0 in MoSe$_2$/graphene respectively.

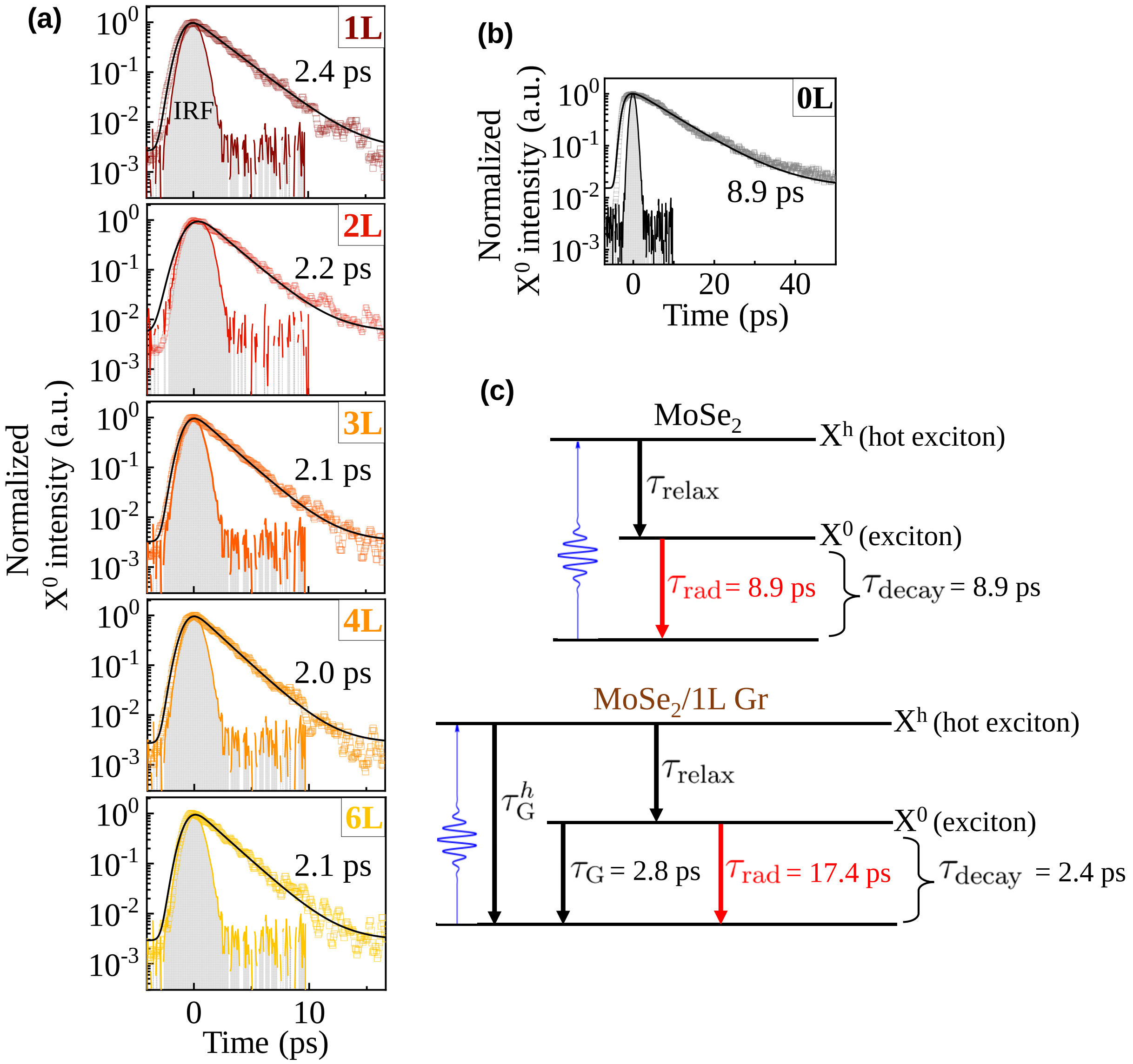

Figure 3.18: Different X^0 decay timescales seen in TRPL data of (a) MoSe$_2$/1-6L graphene and (b) MoSe$_2$, shown in logscale with gray shaded areas representing the IRF, taken using 1.71 eV laser excitation with intensity close to 10 µW/µm^2 and 1 ps resolution at cryogenic temperature. The X^0 dynamics depicted with 3-level models for (c) MoSe$_2$ and (d) MoSe$_2$/1L graphene with timescales extracted from the TRPL data.

X^0 dynamics

The TRPL of X^0 taken on MoSe$_2$/1-6 graphene and MoSe$_2$ are shown in figures 3.18a and 3.18b respectively. These figures are representative of the typical TRPL spectra observed on the MoSe$_2$/nL graphene regions. The spectra are fit with equations (3.9) and (3.12) for the case of MoSe$_2$ and MoSe$_2$/nL graphene respectively. The rise time of TRPL in MoSe$_2$ which is $\tau_{\text{relax}} \approx 1.4$ ps, very close to the expected value of 1.1 ps calculated in [64] for MoSe$_2$ on SiO$_2$. The τ_{relax} in MoSe$_2$/1-6L graphene regions remain unresolved. While MoSe$_2$/1-6L graphene show decay timescales in the range 2 -2.4 ps; longer decay timescale of $\sim$ 8.9 ps are seen in case of MoSe$_2$.

Since the TRPL spectra for $MoSe_2$/1-6L graphene are similar, we will be focusing on $MoSe_2$ and $MoSe_2$/1L graphene for further explanation by 3-level model in figure 3.18c. For $MoSe_2$, as the only channel of decay is radiative one, $\tau_{\mathrm{rad}} \approx 8.9$ ps. Using this τ_{rad} in $MoSe_2$, the estimated binding energies (E_{b} given in table 3.2) and the equation (3.6), τ_{rad} in $MoSe_2$/1L graphene is estimated to be ≈ 17.4 ps. In $MoSe_2$/1L Gr, other than the radiative recombination, the X^0 population can also transfer from $MoSe_2$ to graphene (with timescale τ_{G}). Thus, τ_{decay} in case of $MoSe_2$/1L graphene depends upon these two pathways as

$$\tau_{\mathrm{decay}} \approx \frac{\tau_{\mathrm{G}} \times \tau_{\mathrm{rad}}}{\tau_{\mathrm{G}} + \tau_{\mathrm{rad}}}. \tag{3.13}$$

Using the above equation (3.13), $\tau_{\mathrm{G}} \approx 2.8$ ps, which being much smaller than τ_{rad}, means that the X^0 transfer to graphene is a much more efficient pathway than the radiative recombination. To estimate the fraction of X^0 population that recombines radiatively, we estimate the X^0 emission yield η_{X^0} by

$$\eta_{\mathrm{X}^0} = \frac{1/\tau_{\mathrm{rad}}}{1/\tau_{\mathrm{rad}} + 1/\tau_{\mathrm{G}}} \tag{3.14}$$

which is ≈ 1 for $MoSe_2$ and ≈ 0.14 for $MoSe_2$/1L Gr. Comparing these two yields, one gets,

$$\frac{(\eta_{\mathrm{X}^0})_{\mathrm{MoSe_2}}}{(\eta_{\mathrm{X}^0})_{\mathrm{MoSe_2/1L\,Gr}}} \approx 7 \tag{3.15}$$

Further comparing this value to the quenching factor seen at these points: QF (X^0) ≈ 9.3, the difference between them implies that there is a pathway hindering the formation of X^0 population in $MoSe_2$/1L Gr, which is an evidence towards hot exciton transfer from $MoSe_2$ to graphene.

A similar calculation for timescales in X^0 dynamics of other $MoSe_2$/nL graphene can also be done and the estimated values, along with the ones mentioned so far are given in table 3.3. The similar TRPL data of X^0 and the comparable timescales observed for $MoSe_2$/1-6L graphene dynamics implies that the range of interactions between $MoSe_2$ and graphene is short. The differences between QF (X^0) and 1/(X^0 emission yield) observed in all $MoSe_2$/nL graphene region point out the hot exciton transfer from $MoSe_2$ to nL graphene.

X^0 dynamics in defected $MoSe_2$/1L graphene

The PL and TRPL of X^0 taken on the anomalous area seen in lower part of $MoSe_2$/1L graphene (detailed in section 3.3.4) is shown in figure 3.19. A contribution from some type of defect is seen in the PL spectrum even after filtering the X^0 peak during measurements (shown in figure 3.19a), which is a possible reason behind the anomalous behaviour observed in the PL spectra. The TRPL data on this defected region also shows a decay with different timescale (≈ 3.1 ps as given in 3.19b) than the ones observed so far in figure 3.18. These differences imply that the defect in this region causes a slight decoupling between $MoSe_2$ and 1L graphene, making the transfer to graphene less efficient which makes the X^0 lifetime longer than the one seen in coupled $MoSe_2$/1L graphene.

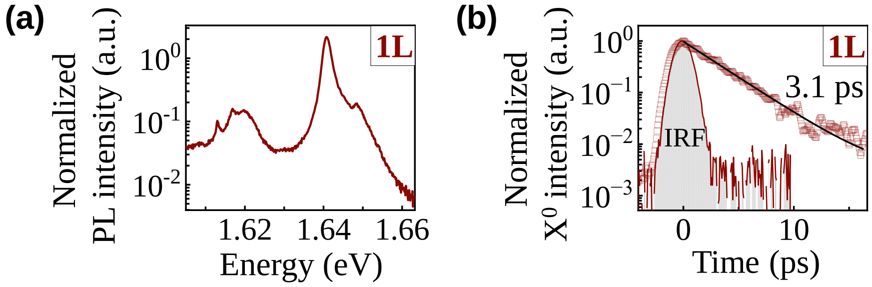

Figure 3.19: (a) PL showing defects and (b) TRPL of X^0 seen in lower part of MoSe$_2$/1L graphene in sample 1, data taken with 1.71 eV laser excitation at cryogenic temperature and 1 ps resolution.

MoSe$_2$ /nL Gr	0L	1L	2L	3L	4L	6L
X^0 τ_{decay} (ps)	8.9	2.4	2.2	2.1	2.0	2.1
X^0 τ_{rad} (ps)	8.9	17.4				
X^0 τ_{G} (ps)	–	2.8	2.5	2.4	2.3	2.4
X^0 emission yield	1	0.14	0.13	0.12	0.12	0.12
1/(X^0 emission yield)	1	7.0	7.9	8.2	8.5	8.3
QF (X^0)	–	9.3	11.7	18.8	16.6	13.1
QF (X^0+X*)	–	20.4	26.4	39.1	36.9	31.9

Table 3.3: The timescales estimated from TRPL data shown in figures 3.18a and 3.18b.

X* dynamics

The TRPL of X* taken on MoSe$_2$ shows a long decay timescale, i.e. $\tau_{\text{rad}} \approx 75$ ps (shown in figure 3.20a). Thus, in MoSe$_2$/nL Gr, X* is efficiently transferred from MoSe$_2$ to graphene through a pathway which is much shorter that τ_{rad}, giving rise to the filtering effect of X* (the neutralization by graphene layer also contributes in filtering).

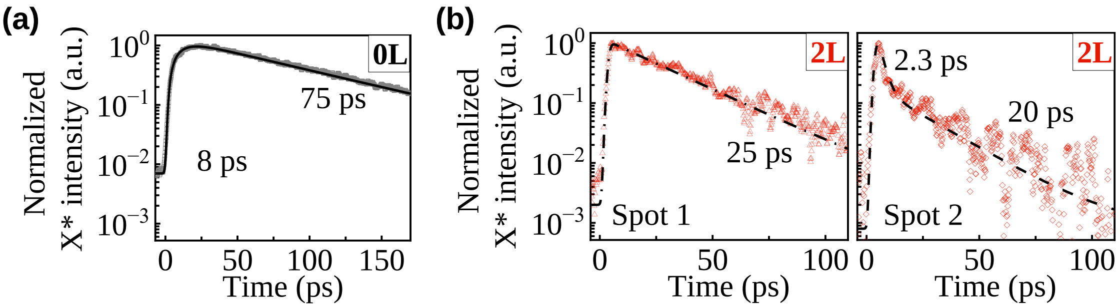

Figure 3.20: TRPL data of X* taken on (a) MoSe$_2$ and (b) MoSe$_2$/2L graphene at two different spots taken with 1.746 eV laser excitation and 1 ps resolution at cryogenic temperature, shown in logscale.

After this filtering of X*, measuring TRPL of X* on MoSe$_2$/nL graphene regions is quite difficult because of its very low intensity. The types of TRPL spectra observed on these regions show spot dependence as given in figure 3.20b only for the case of $MoSe_2$/2L graphene for simplicity. The TRPL data seen on a spot could have a monoexponential decay with a long timescale of > 20 ps (spot 1 in left panel of figure 3.20b) or a biexponential decay with a short timescale of ≈ 2.3 ps and a long one of > 20 ps (spot 2 in right panel of figure 3.20b). The weightage of the short and long exponential timescales in the TRPL having biexponential decay varies with the spots where measurements are performed.

3.3.7 Effects of hBN encapsulation

As the sample 1 discussed so far in this chapter and the sample 2 discussed in appendix are fabricated directly on top of the Si/SiO_2 substrate, the effects of hBN encapsulation on the $MoSe_2$/nL graphene regions have to be checked. In order to do this, sample 3 having hBN covered $MoSe_2$ as well as hBN encapsulated $MoSe_2$, $MoSe_2$/1L graphene, $MoSe_2$/2L graphene and $MoSe_2$/4L graphene regions was fabricated.

The X^0 position shows a redshift with addition of hBN at bottom and graphene layers (shown in figure 3.21a, it should be noted that the peak near 1.626 eV in $MoSe_2$/2L graphene is trion from hBN capped $MoSe_2$ as the measurement spots are very close). The FWHM of X^0 is ≈ 2.5 meV, approaching the homogeneous limit.

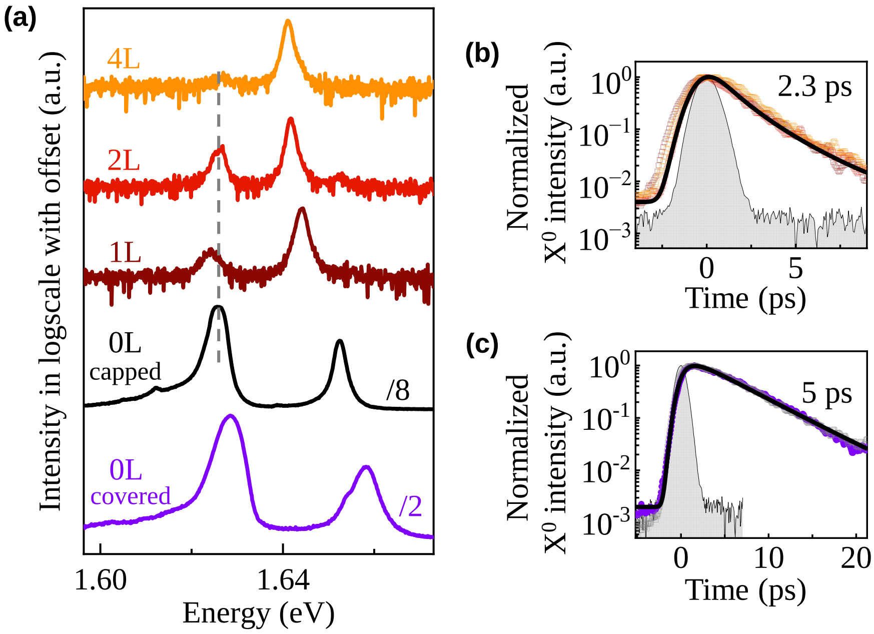

Figure 3.21: (a) PL spectra taken on hBN covered $MoSe_2$, hBN capped (encapsulated) $MoSe_2$ and hBN capped $MoSe_2$/1-4L graphene taken at around 4.5 K with laser excitation of 1.96 eV and intensity of 15 $\mu W/\mu m^2$. The dashed line shows X^* position in hBN capped $MoSe_2$. Different X^0 decay timescales seen in TRPL data of (b) hBN capped $MoSe_2$/1-4L graphene and (c) hBN capped $MoSe_2$ and hBN covered $MoSe_2$, shown in logscale with the same colour scheme as (a) where gray shaded areas represents the IRF, taken with 1.71 eV laser excitation and 1 ps resolution at cryogenic temperature.

The TRPL measurements done on sample 3 show that the timescales of X^0 $\tau_{\text{relax}} \approx 1.1$ ps and $\tau_{\mathrm{rad}} \approx 5$ ps are same for hBN covered $MoSe_2$ and hBN capped $MoSe_2$ (shown in figure 3.21c); while the X^0 dynamics for $MoSe_2$/1-4L graphene regions (shown in figure 3.21b) is similar to the ones seen for sample 1 (in figure 3.18) with decay timescale of 2.3 ps. This implies that having a bottom hBN layer between $MoSe_2$ and SiO_2 does not significantly affect the interactions between $MoSe_2$ and graphene.

3.4 Discussion and conclusions

In this chapter, we have explored the interactions between two-dimensional $MoSe_2$ and graphene layers. In order to understand the near-field interactions occurring between these materials, we wanted to exploit the distance dependence of these transfer processes by coupling different thicknesses of graphene to $MoSe_2$. The microcavity made up with the hBN layer at top and 500 nm thick SiO_2 at bottom with respect to $MoSe_2$/nL graphene to tune the radiative lifetime of X^0 in the $MoSe_2$ layer to the longest value possible by virtue of Purcell effect, which helps us in resolving the PL dynamics. To probe this $MoSe_2$/nL graphene heterostructure, we have used PL spectroscopy, which shows intriguing effects like filtering of X* emission and quenching of PL in $MoSe_2$ by n-layer graphene. The hyperspectral PL maps recorded at low temperature in order to observe the changes in PL spatially over the sample reveal:

- a redshift of 10 meV in X^0 due to dielectric screening by graphene
- a reduction in X* binding energy with the coupling of graphene
- filtering of X* by all different graphene thicknesses
- quenching factors of X^0 and total PL saturating beyond 3 layer graphene limit implying a short range interaction between $MoSe_2$ and graphene
- correlation between total PL intensity vs ratio of X^0 intensity/total PL intensity can be used to vizualize the effects of extent of coupling between layers on the PL

To explore the higher energy excitonic species, PLE measurements i.e. the dependence of incident laser excitation on the PL is also studied. There is an increase in PL intensity and QF of X^0 when laser excitation reaches B_{1s} exciton which comes with an increase in FWHM for $MoSe_2$ and $MoSe_2$/1L graphene.

Hot PL measurements were performed to see the high energy excitons and thereby estimate the binding energy of X^0. This study reveals:

- change in lineshape of hot PL between $MoSe_2$, $MoSe_2$/1L graphene and $MoSe_2$/2-6L graphene
- reduction in Δ_{2s-1s} from 150 meV in $MoSe_2$ to 100-110 meV with addition of graphene
- reduction in binding energy of X^0 from 210 meV to 150 meV with coupling of graphene to $MoSe_2$

- and subsequent increase in radiative lifetime of X^0 in $MoSe_2$/nL graphene as compared to that in $MoSe_2$.

The PL dynamics in $MoSe_2$/nL graphene heterostructure was studied by performing TRPL measurements by our collaborators in INSA, Toulouse. The TRPL measurements and the calculations done using them estimate the timescales and thereby we can conclude that:

- similar X^0 dynamics for $MoSe_2$/1-6L graphene indicate a short range interaction between $MoSe_2$ and graphene
- an efficient ps timescale X^0 transfer occurs from $MoSe_2$ to graphene
- difference between ratio of X^0 emission yields of $MoSe_2$ to that in $MoSe_2$/nL graphene and QF of X^0 in them evidences towards a hot exciton transfer from $MoSe_2$ to graphene.
- radiative lifetime of X^* in $MoSe_2$ is tens of ps, causing its filtering by transfer to graphene by shorter pathways
- TRPL of X^* in $MoSe_2$/nL graphene shows a spot dependence

The exciton dynamics observed for hBN encapsulated $MoSe_2$/n-layered graphene regions being similar to the ones seen in hBN covered $MoSe_2$/n-layered graphene regions as well as the similar exciton dynamics observed for hBN encapsulated $MoSe_2$ and hBN covered $MoSe_2$ show that the interactions between $MoSe_2$ and graphene are not significantly affected by $MoSe_2$ being in contact with the substrate.

We conclude that the interactions between $MoSe_2$ and graphene are of very short range ~ 1 nm, with the charge tunnelling mediated processes as the dominant ones.

CHAPTER 4

Control of light emission in charge tunable graphene/MoSe$_2$ heterostructures

4.1 Motivation

After developing a better understanding of interlayer transfer mechanisms in the previous chapter, we harness these mechanisms to tune the charge carrier density in heterostructures made up of monolayer graphene and monolayer MoSe$_2$ by applying external gate voltage and thereby achieve the electrical control of light emission in these heterostructures. The graphene and MoSe$_2$ layers are very sensitive to external charge doping and its effects on them can be accurately probed via optical spectroscopy methods.

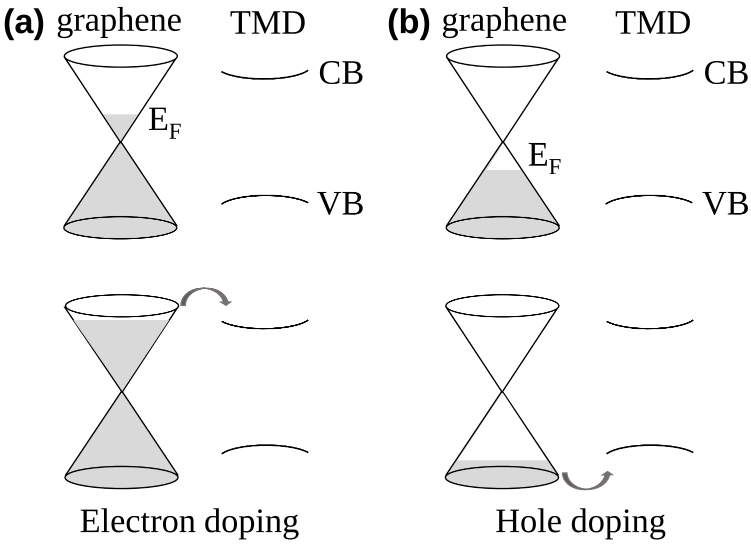

Figure 4.1: Schematic of (a) electron doping in graphene (top panel) and injection of electrons from graphene into TMD (bottom panel) and (b) hole doping in graphene (top panel) and injection of holes from graphene into TMD (bottom panel) in momentum-energy space.

Our approach to controlling the charge carrier density in graphene/MoSe$_2$ heterostructure is to first control the charge density in the graphene layer connected to gate electrodes. As the Raman response of graphene with changing external charge doping is well documented (detailed in section 1.1.4), we can use the Raman modes in graphene as a doping meter reference for the heterostructure to estimate the charge density at any applied gate voltage. The $MoSe_2$ layer is connected to graphene such that it creates two separate regions of graphene/$MoSe_2$ and $MoSe_2$, so that we can study the possible changes that can occur in $MoSe_2$ as the charge density in graphene is changed. As the charge doping in graphene changes, the band alignment between graphene and $MoSe_2$ dictates the possible effects on $MoSe_2$. The changes occurring in $MoSe_2$ as a function of charge doping can be probed through PL spectroscopy and the extracted parameters like X^0 position, FWHM and intensity can be compared with the available literature [92, 90, 89]. The injection of electrons and holes in graphene shifts the Fermi level in graphene up and down respectively (represented in top panels in figures 4.1a and 4.1b respectively). A possible scenario with these respective shifts in Fermi level of graphene is that when they reach the conduction band minimum and valence band maximum of $MoSe_2$, the charges can be directly injected from graphene into $MoSe_2$ (as represented in bottom panels of figures 4.1a and 4.1b respectively). This possible charge injection requires shifting the Fermi level in graphene by ≈ 500 meV and ≈ -1 eV, which correspond to charge carrier densities of 2×10^{13} cm^{-2} and -6×10^{13} cm^{-2} respectively. In order to reach beyond these rather high charge carrier densities, the gating material has to be chosen accordingly.

4.2 LaF_3 for reaching high doping regime

4.2.1 Comparing different substrates for doping

In order to reach the high doping regime of $|n| > 4 \times 10^{13}$ cm^{-2} in graphene to access the possible charge injection into $MoSe_2$, the substrate to be used has to be chosen carefully. The commonly used Si/SiO_2 substrate is easy to use with reversible doping [170], but the maximum carrier charge concentration that can be reached using it is only $\sim 10^{13}$ cm^{-2}.

Another method is to chemically dope the sample to reach the very high carrier charge density exceeding 10^{14} cm^{-2}, but this charge doping is irreversible and hard to control (as done by [171, 172, 173]). Intercalation of $FeCl_3$ has also been used in [174, 38, 175] for doping graphene, but it keeps the sample at a fixed charge carrier density.

Electrolytes (for example, $LiClO_4$ (PEO)) or ion gels (like DEME-TFSI) can be used to achieve the charge carrier concentration of $\geq 10^{14}$ cm^{-2} through ionic conduction as done in [30, 39, 31] and [176, 177, 178] respectively. But the possible electrochemical reactions and their liquid nature makes them difficult to handle and the sample fabrication and measurements can become tough. To avoid these issues that are caused by their liquid nature, solid electrolytes can be considered as a good alternative. The lithium based ion conducting glass ceramics have been used to as a substrate for doping TMDs upto $\sim 10^{14}$ cm^{-2}, but the high mobility of Li^+ ions can cause unwanted effects like intercalation within layers and chemical reactions [179, 180].

In our work, we have used the ionic glass [181] Lanthanum Trifluoride i.e. LaF_3 which can be used to reach a reversible charge carrier density of $\sim 10^{14}$ cm^{-2} through ion conduction, avoiding the several problems mentioned above that occur in case of other methods of sample doping. We have used LaF_3 in this study as it is a very robust substrate and shows insulating behaviour, which makes it work as both a gate dielectric and a substrate.

4.2.2 Doping mechanism in LaF$_3$

The LaF$_3$ crystal is a solid state superionic conductor with fluoride ion conductors [182, 183]. The fluoride ions (F^-) can jump through the crystal lattice (figure 4.2a) using the vacancies already present in the crystal; while the lanthanum ions (La^{3+}) remain motionless due to their large size and mass [184]. Figure 4.2b shows the schematic of charge doping using LaF$_3$ subtrate. When voltage is applied across the substrate, charges accumulate on the metal plates which forms an electric field that causes the motion of F^- ions. These F^- ions move towards the positively charged plate, while the negatively charged plate gathers F^- vacancies which are effectively positive charges. This causes the formation of electric double layer capacitors (EDLC) at the two metal plates due to the accumulation of F^- ions and F^- vacancies [185].

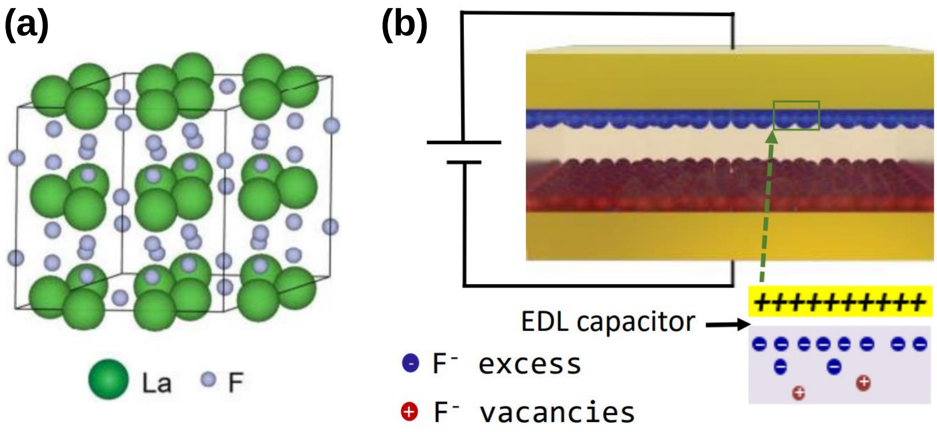

Figure 4.2: (a) Crystal structure of LaF$_3$, adapted from [185] (b) Charge doping in LaF$_3$ and EDLC of F^- ions formed in it after application of voltage, adapted from [186].

The formation of EDLCs depends upon movement of F^- ions, which depends upon the temperature. At low temperatures (typically below 180 K), mobility of F^- ions gets strongly reduced. Thus, the charges are effectively frozen and changing the applied voltage at low temperatures will not cause any significant changes in the EDLCs. At high temperatures (above 240 K), the movement of F^- ions is possible and the capacitance stays almost invariable with respect to temperature [186].

Capacitance in graphene

In usual cases, only the geometrical capacitance C_G of the system needs to be considered. The geometrical capacitance is given by $\epsilon A/d$, where A is the area of plates and d is the distance between plates of a parallel plate capacitor. But in our case, as the charges are injected in graphene through applying voltage, the Fermi level E_F in it changes accordingly as given in equation (1.25). This causes a quantum capacitance C_Q [187] to come into picture in series with the C_G [39]. The dependence of C_Q on E_F and charge carrier density n is given by

$$C_Q = \frac{e^2|n|}{E_F} = sgn(n)\frac{e^2}{\hbar\vartheta_F\sqrt{\pi}}\sqrt{|n|} \tag{4.1}$$

where $sgn(n)$ is the sign function.

The total capacitance C_{total} is thus calculated by

$$\frac{1}{C_{total}} = \frac{1}{C_Q} + \frac{1}{C_G} \tag{4.2}$$

4.2.3 Sample fabrication

The transparent LaF$_3$ substrates (of size 5 mm length × 5 mm width × 1mm height) used in these experiments were commercially purchased from Crystran (UK). They are doped with 0.3% europium for better crystal growth and it also creates more dislocations and vacancies in the crystal lattice which helps the ionic conduction [188, 189]. The top electrode of 3 nm thick Ti / 47 nm thick Au thickness was made by metal evaporation. The thin layer of titanium between gold layer and LaF$_3$ surface helps in the adhesion between the two.

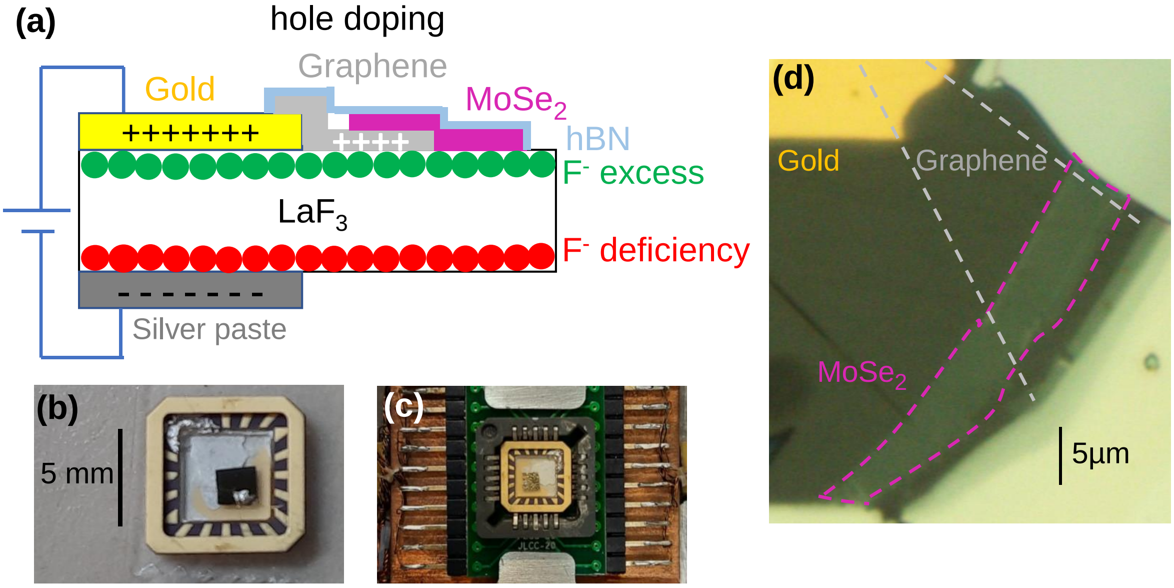

Figure 4.3: (a) Schematic of hole doping in hBN/MoSe$_2$/graphene heterostructure on LaF$_3$ substrate (b) picture of finished sample in a chip carrier (c) and in CIA cryostat (d) optical image of sample.

Figure 4.3a shows the schematic of the samples used in this work. To fabricate these samples, the heterostructure graphene/MoSe$_2$/hBN was deposited on the substrate using the PC method such that graphene touches the top gold electrode, while MoSe$_2$ does not. Next, some silver paste was used to connect the bottom part of the chip carrier to at least one of the pins in it, which forms the bottom electrode. The substrate with heterostructure was then glued to the chip carrier using more silver paste. The top electrode was connected to one of the pins using silver epoxy and wire bonding with gold and this finishes the sample fabrication. Figure 4.3a shows the sample in hole doping regime and figure 4.3b is a picture of one of the samples. After finishing the fabrication, the sample is put in CIA with pins for electrical connection (as shown in figure 4.3c). Figure 4.3d is an optical image of a sample which shows three different regions of interest in these heterostructure: graphene, graphene/$MoSe_2$ and $MoSe_2$, all of which are covered with thin (< 10 nm) hBN which works as a protective layer for the hetrostructure.

4.2.4 Methodology of voltage dependent measurements

The measurements were done using the voltage dependent measurements setup explained in section 2.2.1 at mostly room temperature to avoid problems caused because of immobility of F^- ions at low temperatures. Since the formation of EDLCs depends upon movement of F^- ions, the system has to be given some time to relax after every change in applied voltage. For the measurements done for this work, applied voltage is changed by a step of $\sim$ 0.2 V and the sample is given at least 100 seconds to relax before any measurements are performed. Since most measurements are performed at room temperature, the leakage current is quite high (as expected from [186]) and the measurements have to be performed slowly and carefully to avoid damaging the sample at high leakage currents. A voltage vs current plot observed in one of the measurement runs is shown in figure 4.4.

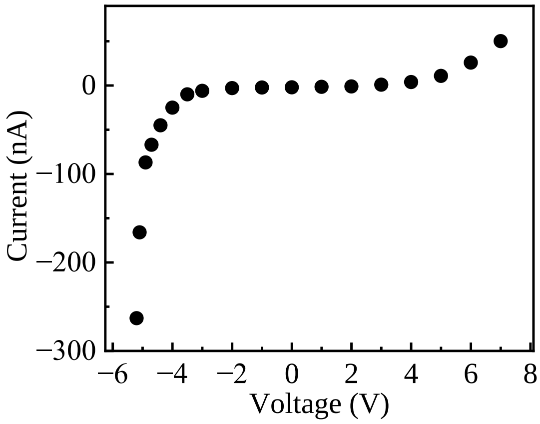

Figure 4.4: Measured current with respect to applied voltage to a sample on LaF_3 substrate in a typical voltage sweep done at room temperature.

The effects of applied voltage on these regions of heterostructure were probed using Raman and PL spectroscopy. The measurements were performed exclusively with 1.96 eV laser because the Raman peaks of LaF_3 seen when incident laser wavelength is of 2.33 eV coincides with the Raman G mode of graphene which makes its observation impossible and also hinders the observation of Raman 2D mode of graphene. Figure 4.5a and 4.5b show the Raman spectra of LaF_3 with incident laser wavelengths of 2.33 eV and 1.96 eV respectively. Whether the many peaks seen in the former comes from LaF_3 itself or from Europium doping in the crystal remains hidden. It should be noted that if these peaks are from the Europium doping, the percentage of this doping can also change the emission spectra of crystals [190, 191, 192].

In the next sections, we will discuss about controlling the light emission of these regions in several samples through gate voltage dependent optical spectroscopy.

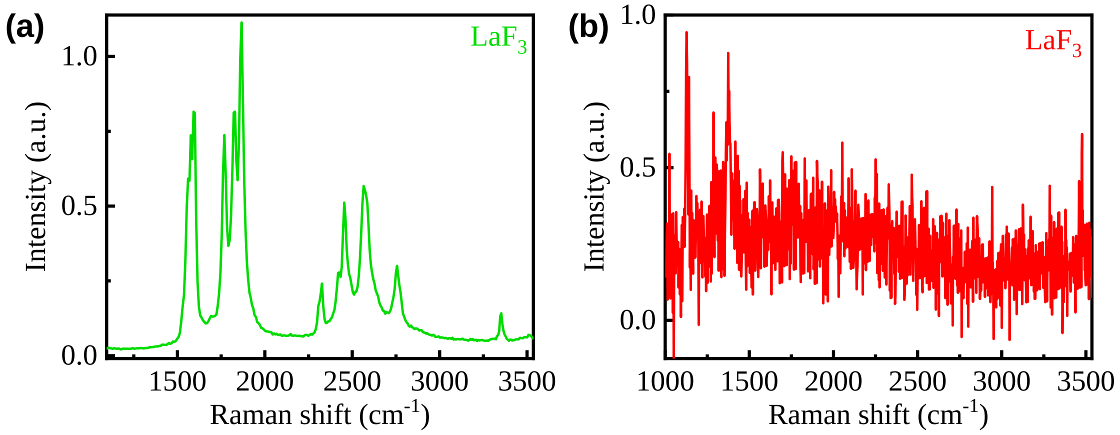

Figure 4.5: Raman spectra measured on LaF$_3$ with laser excitation of (a) 2.33 eV and intensity of 160 µW/µm^2 and (b) 1.96 eV at room temperature with intensity 90 µW/µm^2.

4.3 Charge doping in graphene

As detailed in section 1.1.4, Raman spectroscopy is an excellent probe to observe and quantify the effects of charge doping in graphene. We will discuss below the typical trends in the voltage dependent Raman spectra seen in samples with graphene on LaF$_3$ and their analysis.

4.3.1 Voltage dependent Raman spectra

The Raman spectra of graphene taken under applied gate voltage varying from 2.8 V to −4.9 V i.e. from electron doping to hole doping are shown in figure 4.6, focusing on some particular Raman modes. The measurements were performed with intensity of 600 µW/µm^2 and each spectrum was integrated for 200 seconds to get a good signal to noise ratio from sample on transparent LaF$_3$.

Although the range in frequency where defect related D mode in graphene should be observed is eclipsed by peaks from LaF$_3$, a shoulder from D mode can be observed at high hole doping near applied voltage of −4.9 V (seen along the dotted line in figure 4.6, which is at half the frequency of 2D mode), indicating the increase in defects. We will discuss about the effects of presence of defects on the Raman spectra in coming subsections.

The 2D' mode is relatively weaker in intensity as compared to G and 2D modes and its intensity gets further reduced with both hole and charge doping making its analysis very difficult.

The frequency of G mode ω_{G} shows continuous shifts with varying applied gate voltage and is highlighted by the dashed line in figure 4.6. The charge neutrality point (CNP), which is the applied gate voltage where $E_{\mathrm{F}} = 0$ is estimated by determining ω_{G}^0 and using the ratio of intensities $I_{\mathrm{2D}}/I_{\mathrm{G}}$ which is explained in more detail in the next subsection. The 2D mode intensity I_{2D} reduces with both electron and hole doping as compared to CNP and almost vanishes near gate voltage of −4.9 V. This vanishing of 2D mode implies a shift in E_{F} by $E_{\mathrm{L}}/2$, which is ~ -0.98 eV (as explained in section 1.1.4). As the G and 2D Raman modes

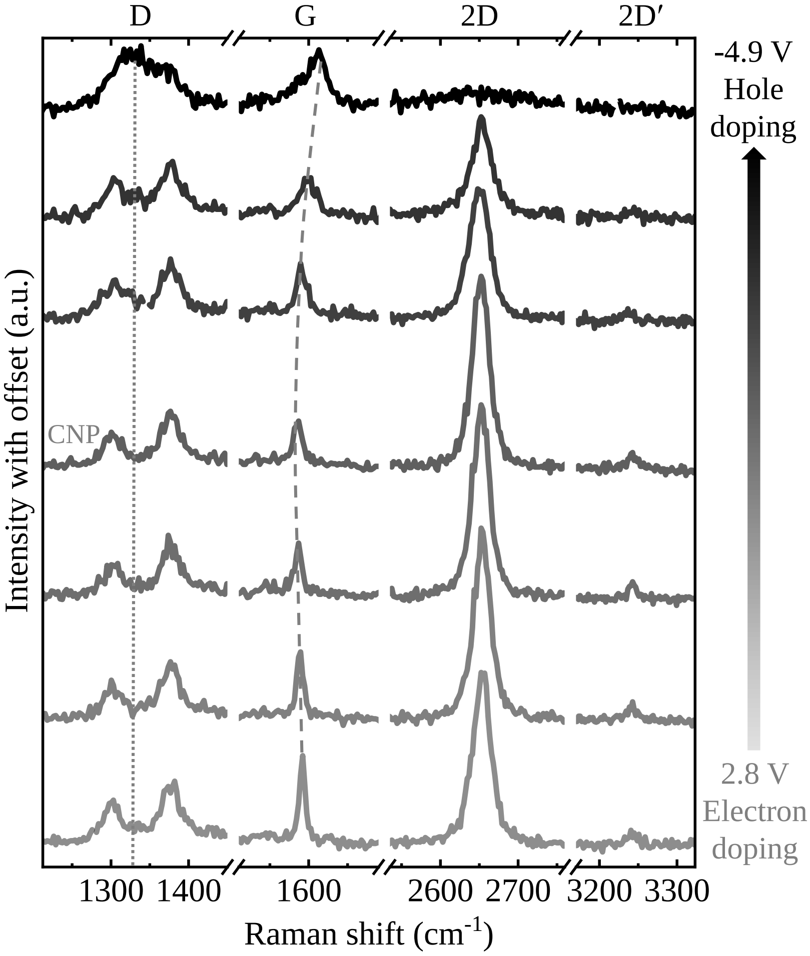

Figure 4.6: Gate voltage dependent Raman spectra showing D, G, 2D and 2D' Raman modes, taken on sample E (graphene on LaF_3) at room temperature with laser excitation of 1.96 eV and intensity close to 600 $\mu W/\mu m^2$. The dashed line is a guide to eye for shifts in G mode frequency, the dotted line shows expected position of D mode and the Raman spectrum corresponding to CNP is also given.

in graphene show a very nuanced dependence on charge doping, we will focus on these two modes and their correlations with respect to applied voltage hence forward.

Voltage dependence on G and 2D Raman modes

The dependence of parameters of G and 2D Raman modes on applied gate voltage, extracted after fitting them with Lorentzian and Voigt profiles respectively, is shown in figure 4.7. The expected changes in these modes with changing charge doping are detailed in section 1.1.4.

The 4.7a and 4.7b show the contourplots of G and 2D modes respectively with respect to gate voltage. A clear shift in ω_G is seen in the contourplot as well as in figure 4.7c. From the expected theoretical behaviour of ω_G with charge density given in figure 1.9, the ω_G^0 of this sample in this gate voltage sweep is $\sim$ 1585 cm^{-1} which is the minimum of ω_G with respect to applied voltage and accordingly, the CNP is at ~ -2.4 V. The CNP in voltage sweep being different from 0 V implies that the graphene layer is doped intrinsically. The

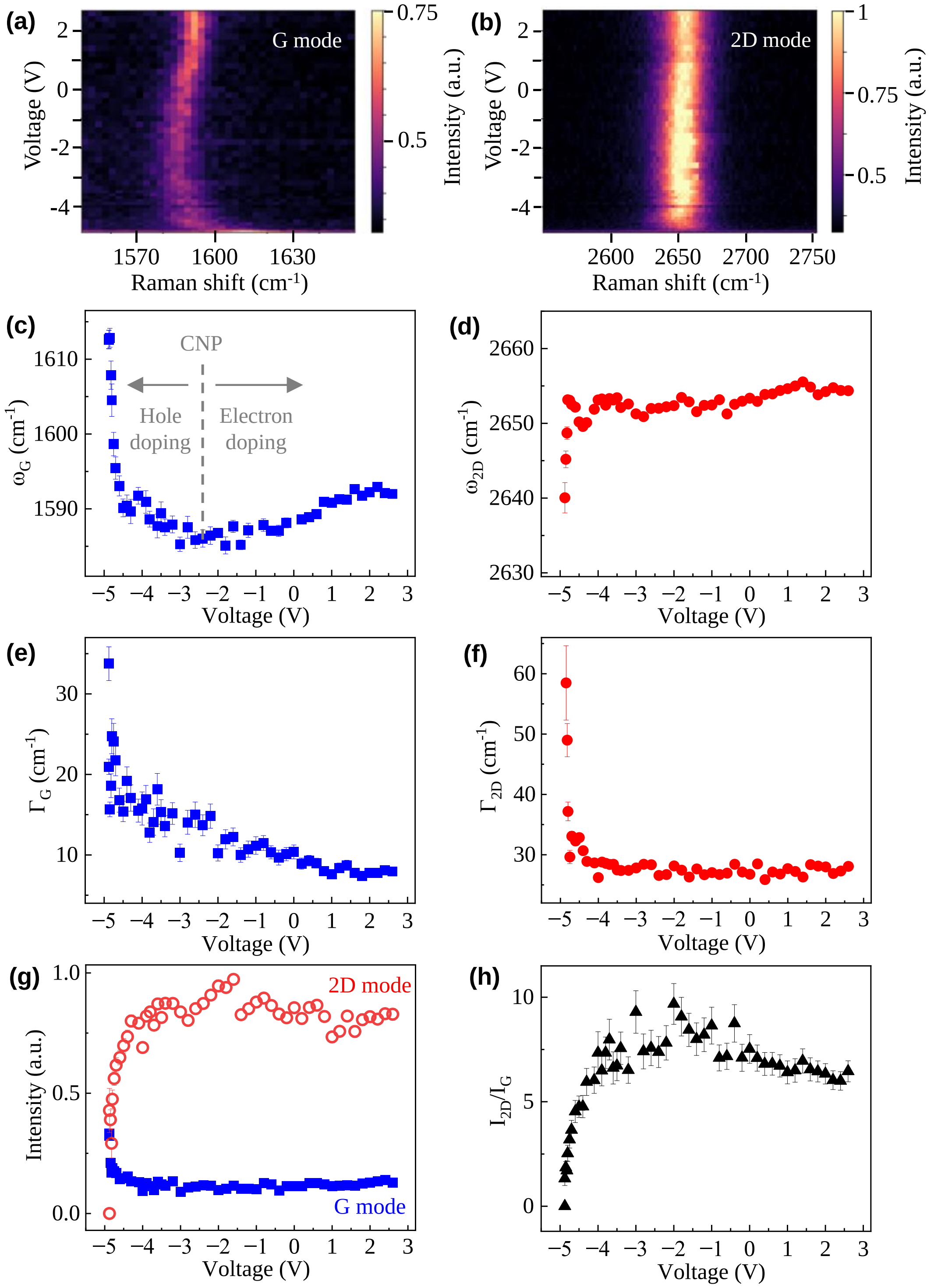

Figure 4.7: The contourplots of (a) G and (b) 2D mode as a function of applied gate voltage in same intensity scale. Variation in (c) G mode frequency (d) 2D mode frequency (e) FWHM of G mode (f) FWHM of 2D mode (g) intensities of G and 2D modes and (h) ratio of their intensities observed with respect to applied voltage. The CNP and directions of doping are denoted in (c). All data is taken on sample E at room temperature with laser excitation of 1.96 eV and intensity close to 600 µW/µm^2.

ω_{G} shows a rapid variation beyond -4 V in the hole doping regime and beyond 1 V in the electron doping regime. The FWHM of G mode Γ_{G} with respect to gate voltage shows an expected reduction as compared to Γ_{G}^{0} (Γ_{G} at CNP) under electron doping according to equation 1.30 (shown in figure 4.7e). Under hole doping, Γ_{G} shows a small decrease compared to Γ_{G}^{0} upto -3 V and then shows an increase. Such an increase in Γ_{G} under high charge concentration is also seen in [30, 43] and could be because of charge inhomogeneities. Moreover, the G mode lineshape might have some slight asymmetry on lower frequency side at very high hole density, for example in Raman spectrum taken at -4.9 V in figure 4.6. This type of asymmetry in G mode linehsape with increased charge density has been observed by [193, 194] and is attributed to Fano resonance originating from coupling between G mode phonon and electronic continuum [195, 196]. The intensity of G mode I_{G} remains almost constant through the voltage sweep (shown in figure 4.7g), but shows a significant increase beyond -4.7 V which also implies that E_{F} is approaching $E_{\mathrm{L}}/2$ (as explained in section 1.1.4).

The 2D mode frequency ω_{2D} changes very weakly between applied gate voltage of 2.8 V to -4.4 V, but reduces significantly beyond -4.4 V in high hole doping regime (as seen in figure 4.7d). The 2D mode FWHM Γ_{2D}, which remains constant between applied voltages of 2.8 V to -4.4 V, but starts to increase beyond -4.4 V (figure 4.7f). This increase in Γ_{2D} can be attributed to electron-electron interactions and possible electron-defect scattering because of increase in defects (as can be understood from the D mode shoulder seen at applied voltage of -4.9 V in figure 4.6). Figure 4.7g also shows the continuous decrease in I_{2D} with both electron and hole doping, the plummeting of it in high hole doping regime is of particular interest in this work. Intensity ratio $I_{\mathrm{2D}}/I_{\mathrm{G}}$ in figure 4.7h shows an expected reduction with increase in both electron and hole concentration.

4.3.2 Quantification of charge density

As the measurements done here are at room temperature, the equation (1.25) can undergo a slight modification and the relation between charge density n and E_{F} becomes

$$n = \frac{sgn(E_{\mathrm{F}})}{\pi\hbar^2\vartheta_F^2}\left[\left(E_{\mathrm{F}}^2 + \frac{\pi^4 k_{\mathrm{B}}^4 T^4}{36 E_{\mathrm{F}}^2}\right)\right] \tag{4.3}$$

where the first term is from equation (1.25) and the second term comes because of room temperature [197], but it is smaller than the first term by many orders of magnitude (for example, when the first term is of the order of 10^{14} cm^{-2}, the second term is only of the order 10^{7} cm^{-2}) and can be ignored without losing accuracy.

The $\Delta\omega_{\mathrm{G}}$ can be used to quantify the charge density in the sample from the equations (1.29), (1.26) and (1.27). In order to first theoretically estimate the $\Delta\omega_{\mathrm{G}}$ at all different n, the electron-phonon coupling constant at Γ point i.e. λ_{Γ} must be accurately determined for samples with graphene layers on LaF$_3$ to estimate the non-adiabatic term contribution $\Delta\omega_{\mathrm{G}}^{\mathrm{NA}}$ to $\Delta\omega_{\mathrm{G}}$. When $E_{\mathrm{F}} \approx E_{\mathrm{L}}/2$ (≈ -0.98 eV in this work), the I_{2D} becomes vanishingly small and $\Delta\omega_{\mathrm{G}}$ at this point can be used to determine λ_{Γ} using equations (1.29) and (1.25). The values of λ_{Γ} observed on multiple graphene samples are given in table 4.1. .

Sample	$\Delta\omega_G$ at $I_{2D} \rightarrow 0$ (cm^{-1})	λ_Γ
A	23.5	0.012
C	25.0	0.013
E	26.6	0.015

Table 4.1: The shift in G mode frequency observed when 2D mode becomes vanishingly small and the λ_Γ estimated using it for multiple samples at low defect density.

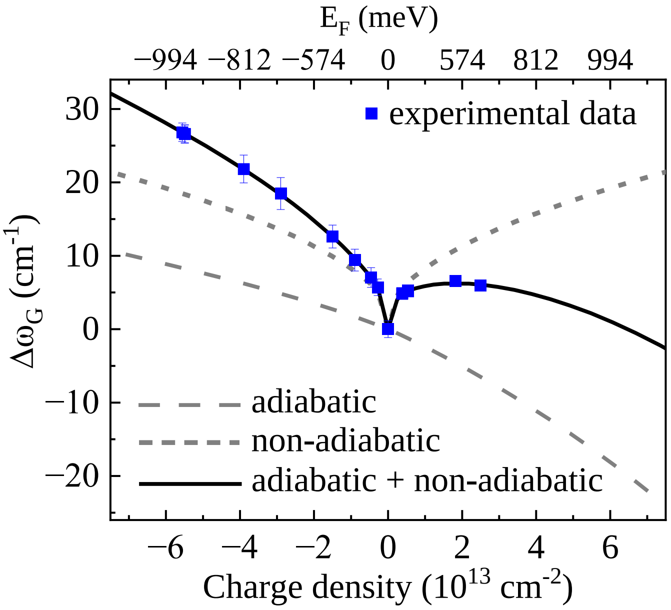

Figure 4.8: Calculated changes in frequency of G mode as a function of charge density (or Fermi level related to charge density by (1.25)) for adiabatic, non-adiabatic and total (adiabatic+non-adiabatic) contributions at room temperature. The experimental data is taken from figure 4.7c for sample E.

Using these values of λ_Γ, the theoretical $\Delta\omega_G^{NA}$ as a function of n and E_F is calculated using equation (1.27) and given in figure 4.8 (for the case of sample E), along with the theoretically estimated adiabatic contribution $\Delta\omega_G^{A}$ (from equation (1.26)) and thereby, the total $\Delta\omega_G$ (from equation(1.29)) estimated from these. As $\Delta\omega_G^{NA}$ is an even function of n, the asymmetry in $\Delta\omega_G$ between hole and electron doping directions comes from $\Delta\omega_G^{A}$. To compare this theoretical estimate with the experimental $\Delta\omega_G$, the values of $\Delta\omega_G$ seen in the experiments (given in figure 4.7c) are marked in figure 4.8 at their expected charge densities. It should be noted that since the $\Delta\omega_G^{NA}$ has a singularity at $E = \hbar\omega_G^0/2$, the $\Delta\omega_G$ between -200 meV $< E_F <$ 200 meV becomes a little doubtful and thus, only the $\Delta\omega_G$ values corresponding to E_F outside this window are considered for calculations in this work.

It can be seen from figure 4.8 that we can charge dope graphene on LaF$_3$ more efficiently in the hole doping direction as compared to electron doping direction. This behaviour is seen in multiple samples, as will be seen through all the figures with ω_G plots as a function of applied voltage in this chapter. This behaviour might be related to the LaF$_3$ crystal itself and the way F^- ions migrate across it. It is important to note that a relaxing time of at least 200 seconds was given to the crystal between every voltage change in order to give the F^- ions sufficient time for migration, indicating that this discrepancy in efficiency in doping directions is not because of the method of voltage dependent measurement itself.

From the results in this section, we can use the Raman modes in graphene as a doping meter to estimate the doping level at any applied voltage. We can now check the robustness of our charge doping methodology by observing the behaviour of ω_G shift (and in turn, charge density) with respect to applied voltage.

4.3.3 Reversibility and reproducibility of charge doping

We also studied the reversibility of charge doping in graphene samples on LaF_3 after they were subjected to the high gate voltages. As ω_G is very sensitive to changes in charge density, the dependence of it on applied voltage gives us a view of the charge doping in all doping regimes. The top panel of figure 4.9a shows the ω_G as a function of applied voltage changing from 0 V to −5.2 V (in blue symbols) and then back to 0 V (in orange symbols). It is clear that ω_G shows some hysteresis between the two voltage sweeps which occurs due to longer time being required for F^- ions to be moved and settled after they have been exposed to high negative voltages. Despite the CNP and ω_G^0 being moved slightly in this hysteresis, the overall charge doping is reversible. The extent of the hysteresis also depends upon the leakage current (bottom panel of figure 4.9a) experienced by the sample before the direction of charge doping is reversed and in the case of very high leakage currents, the sample might need longer time at each value of voltage for the leakage current to settle down as the doping is reversed.

Whether the charge doping in graphene layer is possible multiple times, Raman spectroscopy measurements as a function of applied voltage were performed multiple times. The ω_G extracted from two separate voltage sweeps on a sample are shown in top panel of figure 4.9b. The two voltage sweeps have slightly different CNP due to the intrinsic charge density being changed after the first voltage sweep measurements. A vanishing of 2D mode at the high negative voltages in both sweeps imply a shift in E_F by ≈ 0.98 eV and although $\Delta\omega_\mathrm{G}$ at any particular voltage is different when the two voltage sweeps are compared, the trend of changes in ω_G with respect to voltage seen in them are very similar. As this shows that the charge doping in graphene samples on LaF_3 is reproducible, up to a high hole doping regime, it also highlights the need to quantify the charge density in samples or looking at the shifts in ω_G rather than only considering the applied voltage.

Let us take a look at the effects of creation of defects on charge doping.

4.3.4 Doping dependence in defective graphene

The bottom panel in figure 4.10a shows the Raman spectra taken at CNP and under high hole density, the latter of which shows a shoulder from D mode indicating the creation of defects due to electrochemical reactions. It should also be noted that in this high hole doping regime, a broad hot luminescence can be present, which increases the baseline of the

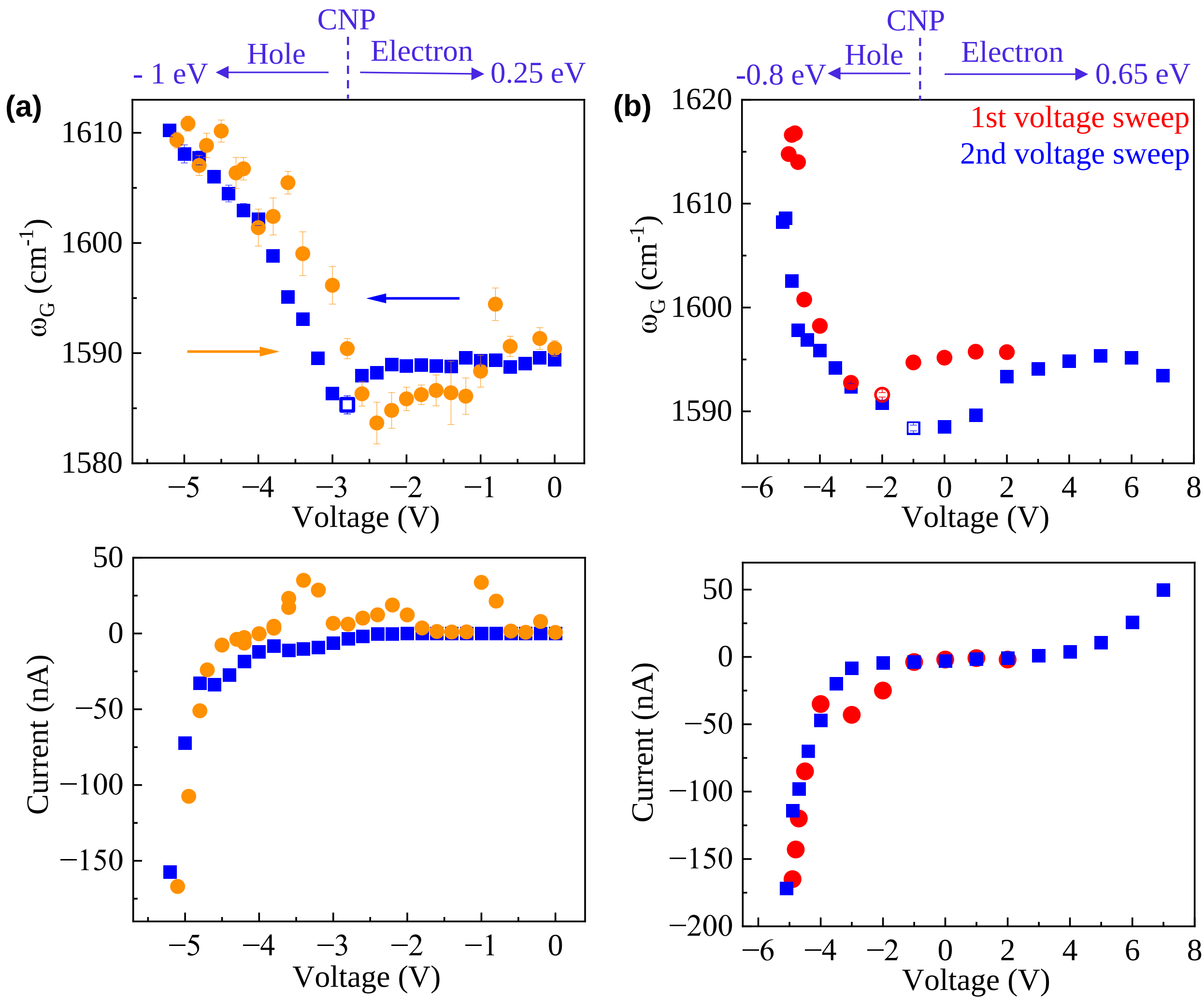

Figure 4.9: Frequency of G mode as a function of applied gate voltage in top panels to check (a) reversibility of charge doping with the arrows indicating directions of voltage sweeps and (b) the reprodubility of charge doping by performing two separate voltage sweeps. The open symbols indicate CNPs. The bottom panels in (a) and (b) show the leakage current measured at applied voltages. The directions of hole and electron doping with the maximum charge densities reached are also indicated. All data measured at room temperature with laser excitation of 1.96 eV and intensity 600 µW/µm^2 on (a) sample C and (b) sample A.

spectrum. After this voltage sweep, a population of defects is formed in the graphene layer and the defect related D, D' and a weak D+D' Raman modes (detailed in section 1.1.4) can be observed in Raman spectrum taken at CNP (given in top panel of figure 4.10a). The formation of defects does not hinder the further voltage dependent measurements that can be performed on LaF$_3$ samples. The figures 4.10b and 4.10c show the ω_G and I_{2D}/I_G as a function of applied voltage respectively for the voltage sweeps performed before and after the creation of defects (the spectra shown in figure 4.10a are from these measurements). Apart from the small shift in CNP between the two measurements, the $\frac{I_{2D}}{I_G}|_0$ (which is I_{2D}/I_G at CNP) shows a reduction after the creation of defects as compared to before, which happens because of increase in electron-defect scattering rate γ_D with the creation of defects that reduces this intensity ratio (as expected from equations (1.33) and (1.36)).

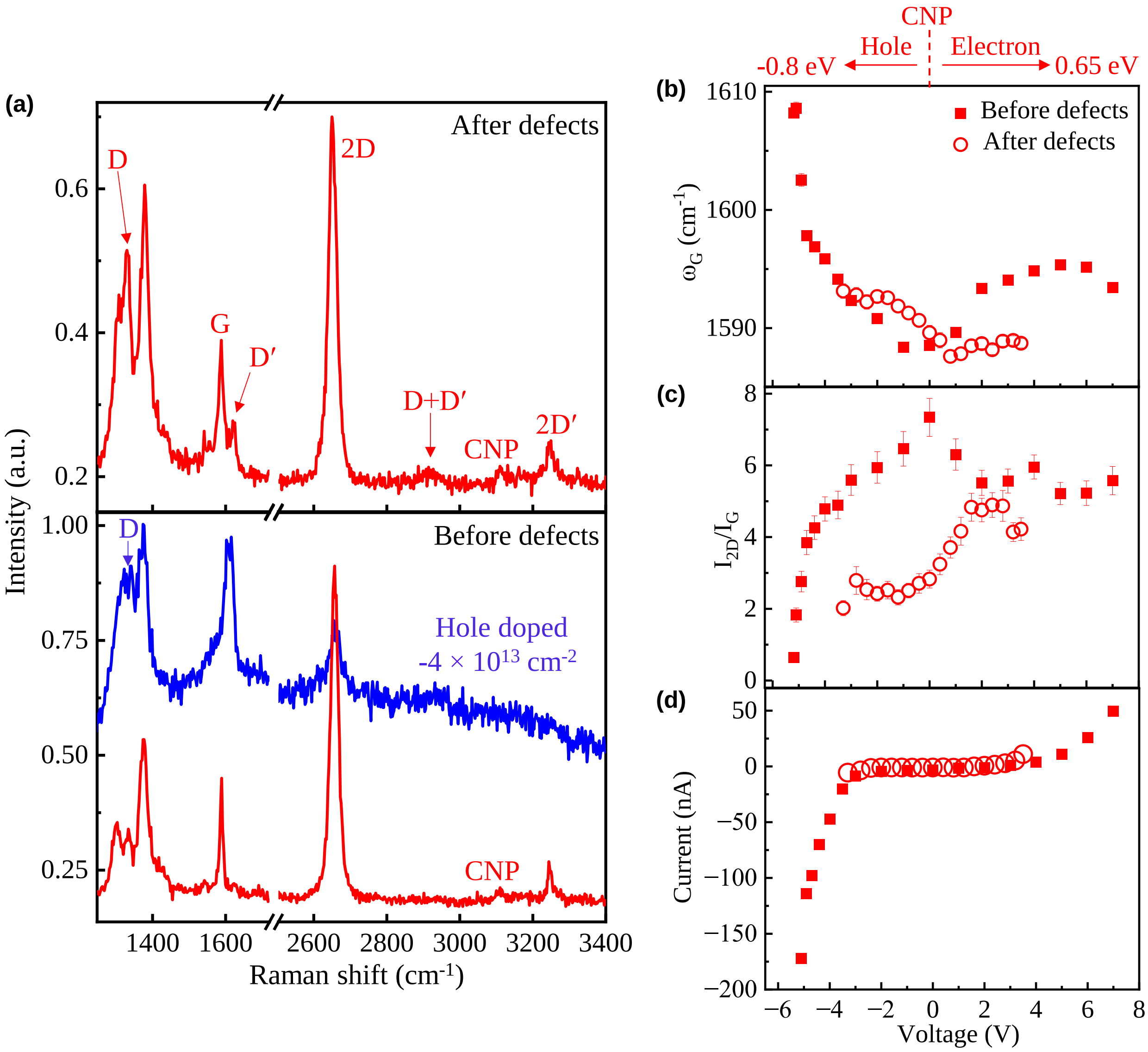

Figure 4.10: (a) Raman spectra taken at CNP and at highly hole doped state before the creation of defects (bottom panel) and at CNP after the creation of defects (top panel), with the observed Raman modes being mentioned. The (b) frequency of G mode, (c) ratio of intensities of 2D to G mode and (d) leakage current as a function of applied voltage for the measurements performed before and after the formation of high defect density. The directions of hole and electron doping with the maximum charge densities reached are also indicated for the case of before creation of defects. All measurements were performed at room temperature with laser excitation of 1.96 eV and intensity 600 µW/µm^2 on sample A.

4.3.5 Correlations

Apart from the estimation $\Delta\omega_G$ of charge density in samples, correlations between parameters of G and 2D Raman modes are also very useful in understanding changes in these modes with varying charge doping levels and compare the trends observed in multiple samples.

The correlation between $\Delta\omega_G$ and Γ_G for five different samples given in figure 4.11a shows that Γ_G reduces with electron doping as expected in equation (1.30). On the other hand, in

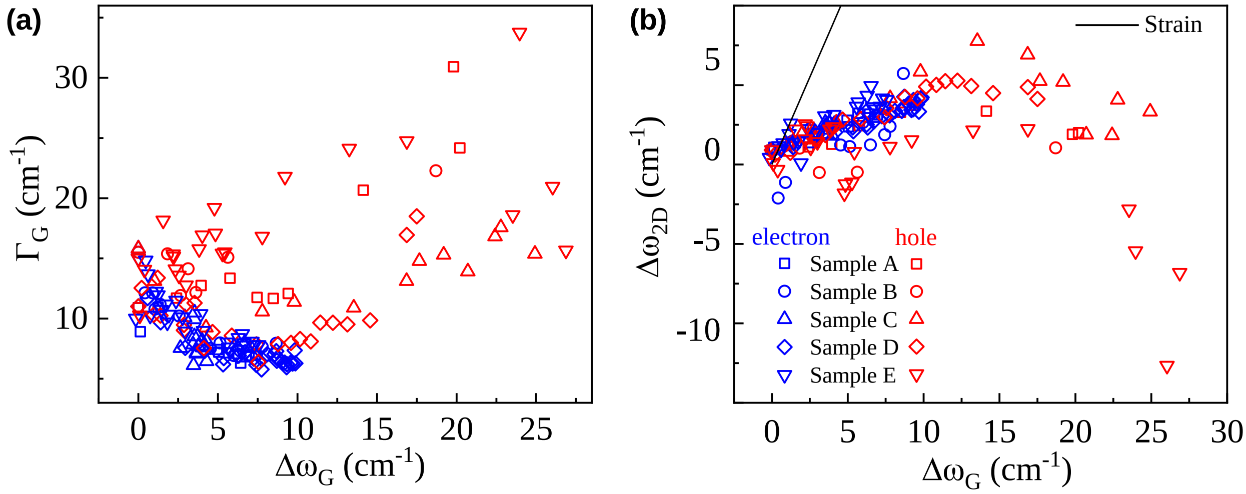

Figure 4.11: Correlations between (a) relative G mode frequency and FWHM of G mode (b) relative G mode frequency and relative 2D mode frequency with respect to the values at CNP for five samples with graphene on LaF$_3$. The blue and red symbols denote electron and hole doping respectively, with the black line having a slope of 2.2 in (b) corresponding to expected behaviour under strain with no charge doping.

hole doping scenario, Γ_G decreases at first until $\Delta\omega_G \approx 15$ cm^{-1}; while Γ_G increases for $\Delta\omega_G > 15$ cm^{-1}. This deviation of Γ_G from equation (1.30) is consistently observed in all the samples and has also been seen in [194, 43, 30]. The reason behind Γ_G broadening at high hole density is increasing charge inhomogeneity and possible increase in electron-phonon coupling.

The figure 4.11b shows the correlation between $\Delta\omega_G$ and $\Delta\omega_{2D}$ for the same voltage sweeps as in figure 4.11a. The expected trend in this correlation when the samples are under strain with no external charge doping is given with black line [30]. This figure shows that under moderate charge doping regime ($E_F < 600$ meV), $\Delta\omega_{2D}$ varies almost linearly with $\Delta\omega_G$ and then decreases nonlinearly under high hole doping ($E_F > 600$ meV).

4.4 Charge doping in MoSe$_2$ and MoSe$_2$/graphene through graphene

After performing extensive study of charge doping in graphene layers on LaF$_3$ substrate and obtaining a reliable method to quantify charge density from Raman spectroscopy, we move on to control the light emission in MoSe$_2$ and MoSe$_2$/graphene (denoted by MoSe$_2$/Gr here onwards for simplicity) by charge doping them through graphene.

As the monolayer MoSe$_2$ is very sensitive to charge doping and can get damaged at high charge density, the measurements were first performed in moderate doping regimes and then extended to high hole doping.

4.4.1 Optical spectroscopy in moderate charge doping regime

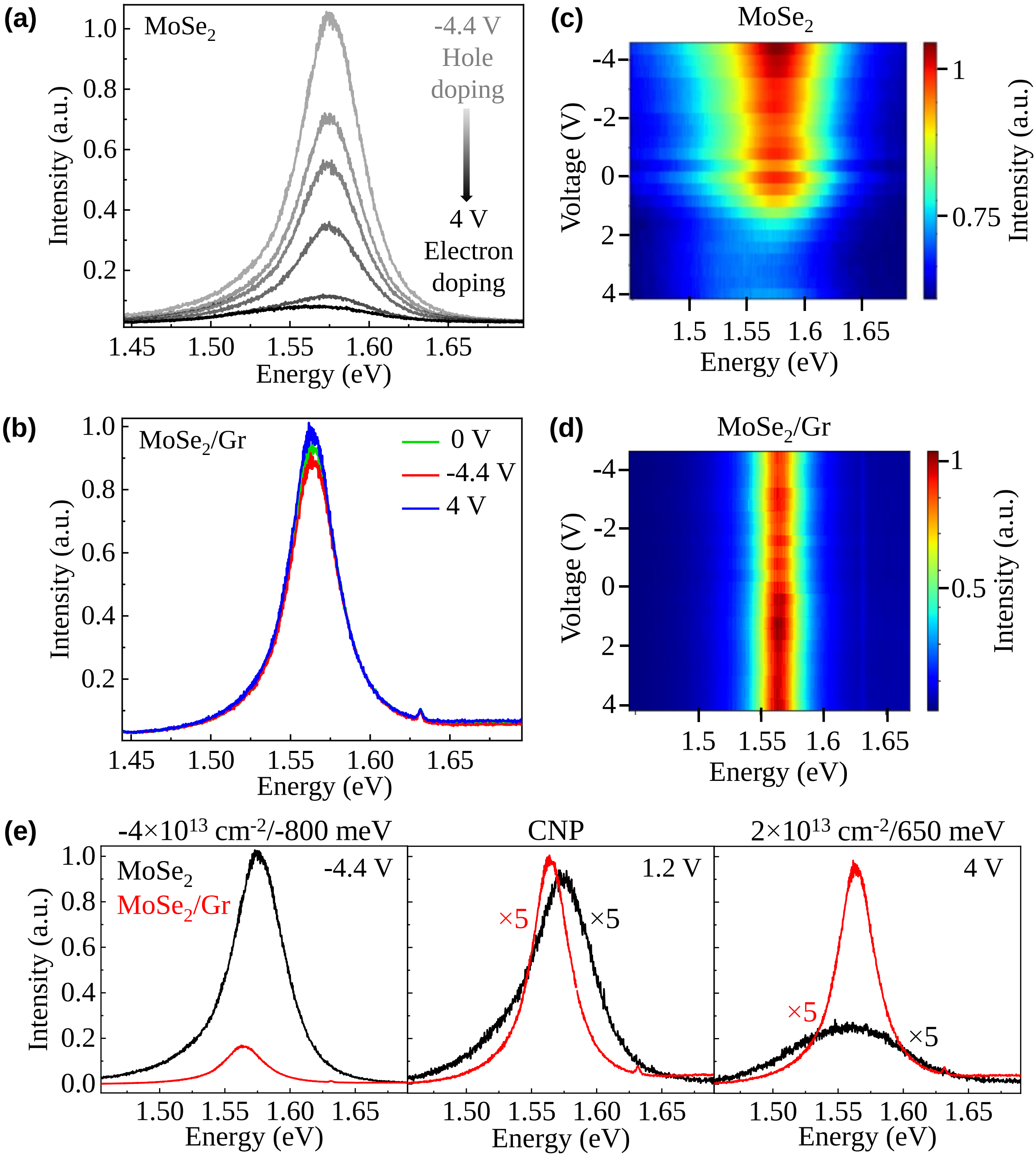

Figure 4.12: (a) PL spectra of $MoSe_2$ and (b) PL spectra of $MoSe_2$/Gr with varying gate voltage from 4 V to −4.4 V i.e. from electron to hole doping. Contourplots of PL spectra from (c) $MoSe_2$ and (d) $MoSe_2$/Gr with respect to applied gate voltage and (e) PL spectra of $MoSe_2$ and $MoSe_2$/Gr for different charge densities or Fermi levels obtained from Raman spectroscopy measurements in graphene. All measurements performed at room temperature with laser excitation of 1.96 eV and intensity 300 µW/µm^2 on sample B.

The figures 4.12 and 4.13 show the results observed on $MoSe_2$ and $MoSe_2$/Gr regions when the charge density in graphene was varied from −4.4 V (hole doping) to 4 V (electron doping) during a typical voltage sweep. Using the method to quantify the charge density in graphene from the voltage dependence of Raman modes described in previous section, the CNP can be estimated to be at 1.2 V and the maximum hole and electron densities are estimated to be around -4×10^{13} cm^{-2} (equivalently, $E_F = -0.8$ eV) and 2×10^{13} cm^{-2} (equivalently, $E_F = 0.65$ eV) at voltages −4.4 V and 4 V respectively.

Changes in PL spectra of $MoSe_2$

The PL spectra of $MoSe_2$ show continuous changes in lineshape as well as intensity when the gate voltage is varied with charge doping in graphene changing from electron to hole doping, as can be seen in figures 4.12a and 4.12c. These PL spectra of $MoSe_2$ were fit with two Voigt profiles for X^0 and X^*. The extracted total PL intensity along with the intensities of X^0 and X^* are given in figure 4.13a which show an increase with hole doping and a decrease with electron doping as compared to that at CNP. Beyond the applied voltage of 2 V towards higher electron density, the X^* peak becomes more dominant compared to X^0. These changes in relative intensities between X^0 and X^* also correspond to the start of blueshift in X^0 position (figure 4.13c) and broadening (figure 4.13e). Although, beyond the applied voltage of 2 V, as the X^* peak becomes more intense than X^0, the lineshape of PL spectra in $MoSe_2$ layer (like the one seen in figure 4.12c) makes the accuracy of FWHM extracted from the fits a little doubtful.

The changes we observe in total PL intensity and lineshape of PL in $MoSe_2$ with applied voltage on LaF_3 substrate are similar to the ones seen by [92]. A possible explanation for this behaviour in PL intensity of $MoSe_2$ with changing applied gate voltage is that as the layer is doped with increasing electron density, the population of X^* increases because of the larger population of X^0 getting converted into X^*. As we observe the relative intensity of X^* to X^0 increase with electron density, we can say that the X^* formed here is a negatively charged trion. The overall lower PL intensity in under electron doping could be because of the trions favouring non-radiative recombination or because of the electrons opening non-radiative recombination pathways [90]. Since the X^* intensity in our results shows a small decrease with electron density, it suggests that the electron population opens up non-radiative pathway for X^*. Thus, the probable reason for the decrease in PL intensity here is because of increase in non-radiative recombination rates of X^0 and X^* as the electron density increases.

In the other direction, i.e. under hole doping, the continuous increase in PL intensity, especially of the X^0 peak, can be understood as the $MoSe_2$ layer being intrinsically doped by electrons. Using the same mechanism described above, increasing hole density causes the layer to be neutralized, which in turn closes the non-radiative pathways of recombination. This increases the PL intensity and makes the X^0 peak narrower.

Changes in PL spectra of $MoSe_2$/Gr

On the other hand, PL spectra of $MoSe_2$/Gr show much smaller changes, even at the extremes of either type of charge doping than $MoSe_2$ in this moderate charge doping regime, as can be seen in figure 4.12e. All these spectra can be fit with a single Voigt profile corresponding

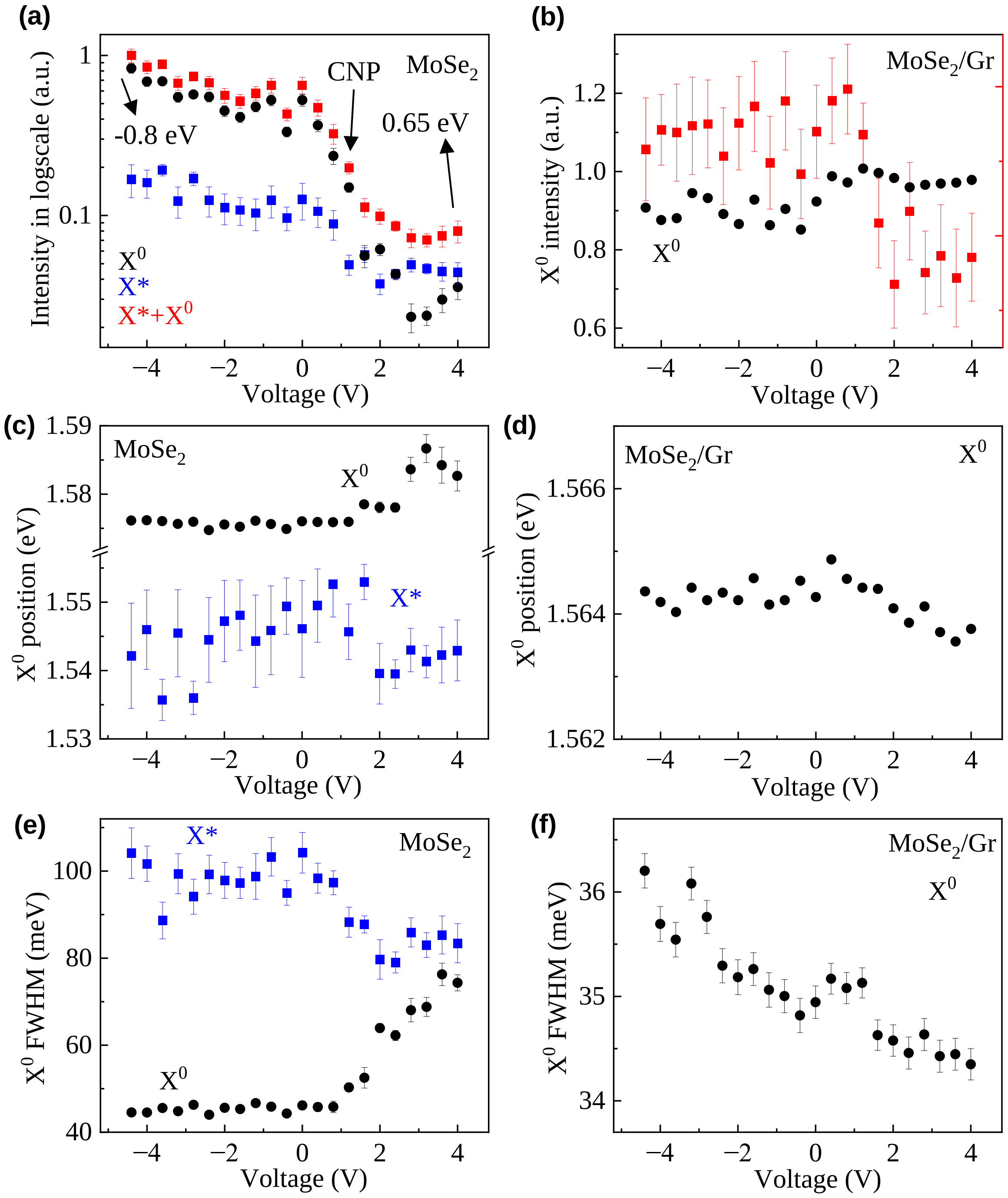

Figure 4.13: Applied gate voltage dependence of (a) the extracted PL intensity of $MoSe_2$ for X^0, X^* and total PL (X^0 +X^*) in logscale with marked CNP and maximum electron and hole densities observed at the ends of voltage sweep obtained from Raman spectroscopy measurements in graphene (b) X^0 intensity and 2D mode intensity in $MoSe_2$/Gr. (c) X^0 position in $MoSe_2$ with X^* position (d) X^0 position in $MoSe_2$/Gr, (e) X^0 FWHM in $MoSe_2$ with X^* FWHM and (f) X^0 FWHM $MoSe_2$/Gr. All measurements performed at room temperature with laser excitation of 1.96 eV and intensity 300 µW/µm^2 on sample B.

to X^0 because no signs of X^* are observed throughout the voltage sweep as can be seen from symmetric PL spectra shown in figure 4.12b. But the contourplot of PL of $MoSe_2$/Gr shown in 4.12d indicates a small decrease in intensity with hole doping as compared to at CNP. Although the X^0 position (figure 4.13d) does not change with applied voltage, a continuous broadening can be seen with increasing hole density (figure 4.13f). Also, the 2D mode intensity shows slight reduction with both electron and hole doping as compared to the CNP (figure 4.13b), implying that the CNP of the reference graphene layer and graphene in $MoSe_2$/Gr is similar.

The absence of changes in $MoSe_2$/Gr as the graphene layer is moderately doped imply that the shift in E_F of graphene with electrons and holes is not significant enough to reach beyond either of the minimum of conduction band and the maximum of valence band respectively. Although, the very small decrease in PL intensity (can be seen in contourplot figure 4.12d and figure 4.13b) compared to CNP with increase in hole density reaching -4×10^{13} cm^{-2} (equivalently, E_F = -0.8 eV at -4.4 V) tells us that the E_F of graphene is reaching towards the edge of valence band in $MoSe_2$.

These changes in $MoSe_2$/Gr region when graphene is doped with charges give us more motivation to explore the changes in PL of $MoSe_2$/Gr in the higher hole doping direction. Thus, we exposed the samples to even higher hole densities at room temperature since we have seen so far that we are able to charge dope graphene with holes much more efficiently than electrons. But as the $MoSe_2$ layer starts to degrade when $n > -4 \times 10^{13}$ cm^{-2}, we will only be discussing effects of high hole doping on graphene and $MoSe_2$/Gr in the next subsection.

4.4.2 Optical spectroscopy of $MoSe_2$/graphene in high hole doping regime

In order to observe the effects of high hole density in graphene region on the $MoSe_2$/Gr region, voltage dependent Raman and PL spectroscopy were performed from small electron density (applied gate voltage of 2.8 V) to high hole density regime (applied gate voltage of -4.9 V) in graphene at room temperature and the observations for Raman spectroscopy of graphene and $MoSe_2$/Gr figure 4.14 and the PL data for $MoSe_2$/Gr is given in 4.15. As the changes in $MoSe_2$/Gr, i.e. the region of interest in this section, depends upon what happens in both $MoSe_2$ and the graphene coupled to it, we will discuss our observations on them with applied gate voltage as well as that of reference graphene layer for comparison and quantification of charge density.

Raman response of graphene regions with respect to applied voltage

The contourplots of G and 2D modes in reference graphene layer with varying applied gate voltage are given in figures 4.14a and 4.14b respectively. The ω_G as a function of applied voltage is given in figure 4.14d for graphene and $MoSe_2$/Gr. From this, the CNP is identified to be at -0.75 V. The values of ω_G are quite similar for the two regions, but have a small difference between -4.4 V and -4.9 V, denoting a possible hole transfer from $MoSe_2$ to graphene in the $MoSe_2$/Gr region under high hole doping.

For the case of $MoSe_2$/Gr, the G and 2D modes can be seen riding the PL spectra in right panel of figure 4.15d. Thus, the parameters for G and 2D mode given in figure 4.14 for the

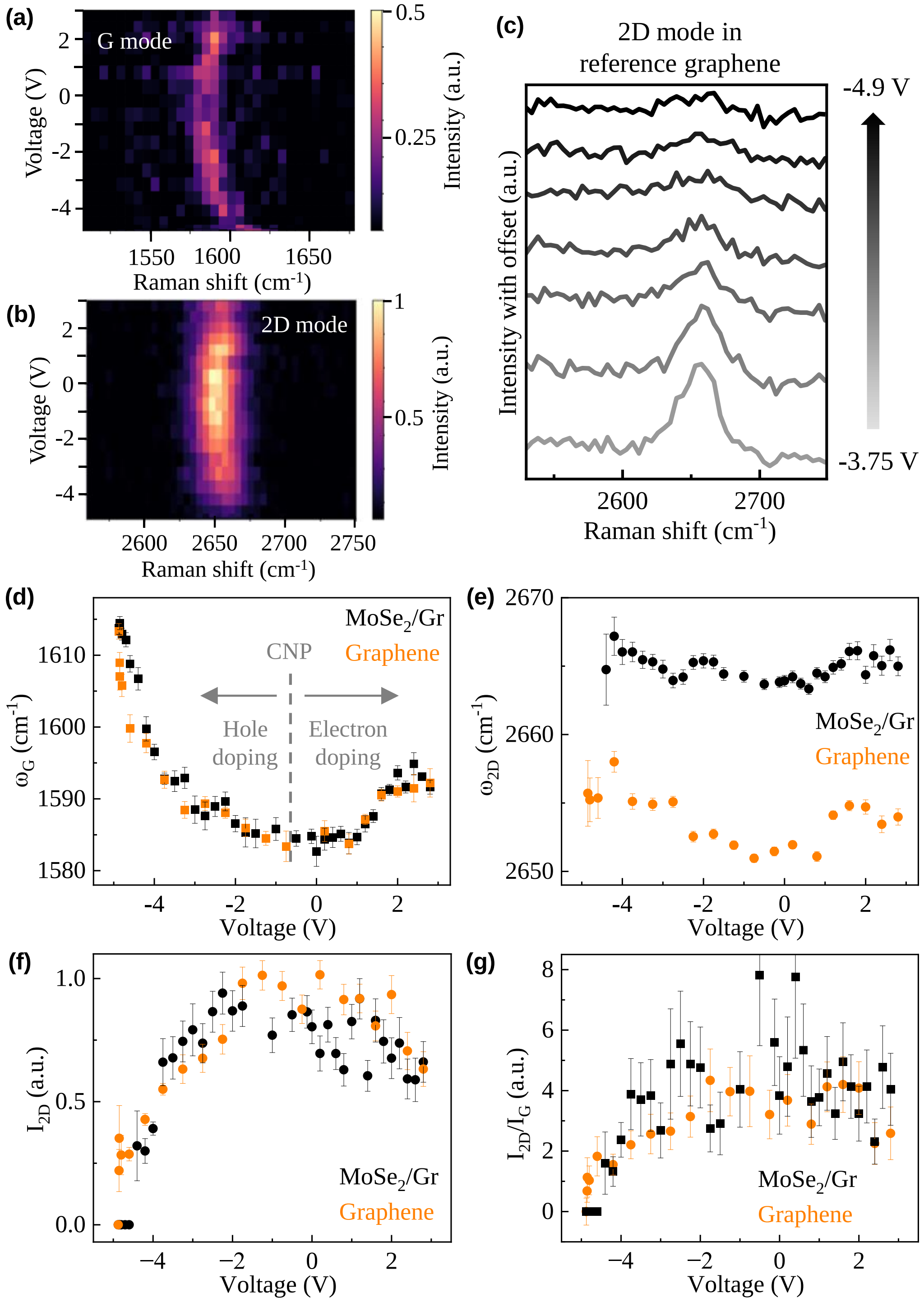

Figure 4.14: Countourplots of (a) G and (b) 2D modes in graphene with varying applied gate voltage. (c) 2D mode in graphene layer plotted with vertical offset for clarity with applied voltage changing from -3.75 V to -4.9 V. (d) G mode frequency and (e) 2D mode frequency as a function of gate voltage for MoSe$_2$/Gr and graphene. (d) also indicates the CNP in this voltage sweep and the directions of hole and electron doping. (f) Intensity of 2D mode and (g) intensity ratio of 2D to G mode in MoSe$_2$/Gr and graphene with varying voltage. All measurements performed at room temperature with laser excitation of 1.96 eV and intensity 100 µW/µm^2 on sample G.

case of MoSe$_2$/Gr region are extracted after removing the background of PL coming from MoSe$_2$, which results in comparatively larger error bars in Raman mode intensities.

The figure 4.14e shows that the trend of changes in $\omega_{2\mathrm{D}}$ with respect to applied voltage are quite similar for graphene and MoSe$_2$/Gr, with a difference between the values of $\omega_{2\mathrm{D}}$ at any given voltage between the two regions because of dielectric screening [198].

The contourplot of 2D mode (4.14b) and the Raman spectra (4.14c) show clearly that with the voltage increasing in hole doping direction, the intensity of 2D mode decreases continuously. At the end of this voltage sweep, when the applied gate voltage is at -4.9 V, the 2D mode intensity vanishes (as can be seen from figures 4.14c, 4.14f and can also be observed in the 2D mode contourplot shown in figure 4.14b), which is the evidence of hole density high enough to attain $E_\mathrm{F} \approx -1$ eV (equivalently, $n \approx -6 \times 10^{13}$ cm^{-2}) in the reference graphene layer. At this voltage of -4.9 V, the $\Delta\omega_\mathrm{G}$ is ≈ 29 cm^{-1}, a value slightly higher value than the ones seen in table 4.1.

Voltage dependent PL spectra of MoSe$_2$/Gr

The figure 4.15c shows PL spectra at different voltages including at CNP and -4.9 V (where $E_\mathrm{F} \approx -1$ eV) taken from Raman spectroscopy data described above. All PL of MoSe$_2$/Gr in this charge doping range can be fit with one Voigt fit for X^0 denoting the absence of trions, as can be seen from the symmetric peaks in this figures. The changes in PL with voltage can be clearly visualized in the contourplot given in figure 4.15b. This contourplot shows that a lot of changes happen in the PL spectra of MoSe$_2$/Gr for voltages beyond -4 V. To visualize the changes occurring beyond this value of voltage, the plot in figure 4.15e can be referred to.

As the graphene layer starts to have high hole density, the intensity of PL (also given in figure 4.15e) decreases as compared to CNP (similar to figure 4.12d, for the case of moderate hole doping regime), which can also be observed in the contourplot of PL spectra given in figure 4.15b. These figures also show a clear shift in X^0 as well as a change in FWHM for voltages beyond -4 V. The extracted X^0 intensity, X^0 position and X^0 FWHM as a function of applied gate voltage are plotted in figures 4.16a and 4.16c respectively, with the figures 4.16b and 4.16d showing the zoom in for higher negative voltages. The broadening of X^0 is similar to the one observed in figure 4.13f. Both X^0 position and FWHM as a function of voltage undergo a sharp kink beyond -4 V, this will be discussed more later on.

The PL spectra taken on MoSe$_2$/Gr region in higher energy range are shown in figure 4.15d for different applied voltages. The G and 2D Raman modes have expected changes in intensities with charge doping as in section 1.1.4. When the applied gate voltage reaches the value of -4.9 V, the G mode intensity in MoSe$_2$/Gr shows an increase as compared to that at CNP as well as the vanishing of 2D mode, denoting that $E_\mathrm{F} \approx -1$ eV. Moreover, these spectra also show changes in hot PL peaks with electron and hole doping when compared to that at CNP.

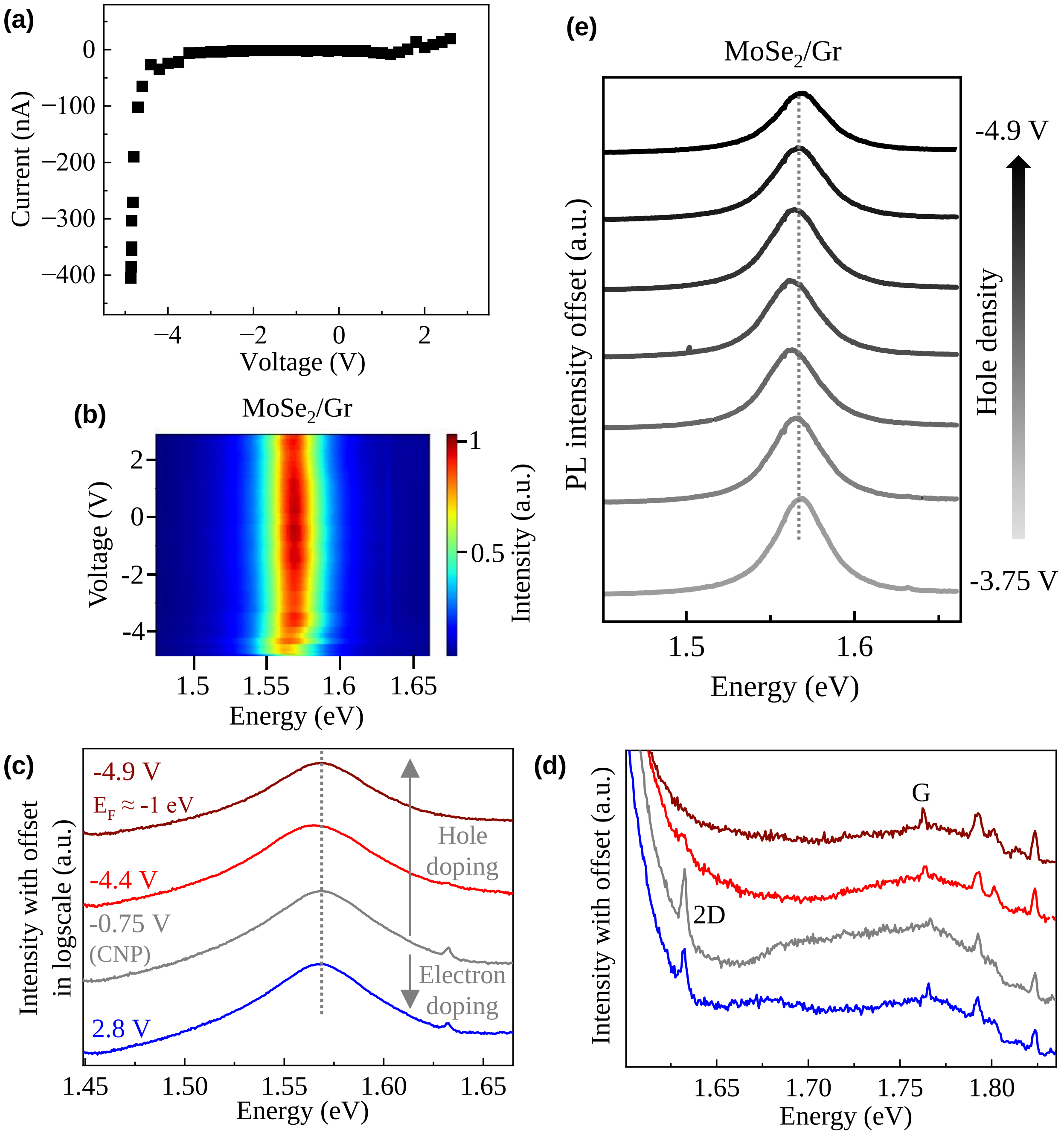

Figure 4.15: (a) Leakage current observed at applied gate voltages (b) Contourplot of PL spectra taken on $MoSe_2$/Gr as a function of gate voltage (c) PL spectra of $MoSe_2$/Gr in logscale with vertical offset for clarity measured at different applied gate voltages showing X^0 and (d) hot PL of $MoSe_2$/Gr with vertical offset also indicating the G and 2D modes. Figure (c) also indicates the PL spectra taken at CNP and at -4.9 V ($E_F \approx -1$ eV) as well as the directions of charge doping, the dotted line indicates the X^0 position at CNP, the same scheme applies for (d). (e) PL spectra of $MoSe_2$/Gr plotted in logscale for applied gate voltage changing from -3.75 V to -4.9 V. The dotted line denotes X^0 position for the applied gate voltage of -3.75 V. All measurements performed at room temperature with laser excitation of 1.96 eV and intensity 100 $\mu W/\mu m^2$ on sample G.

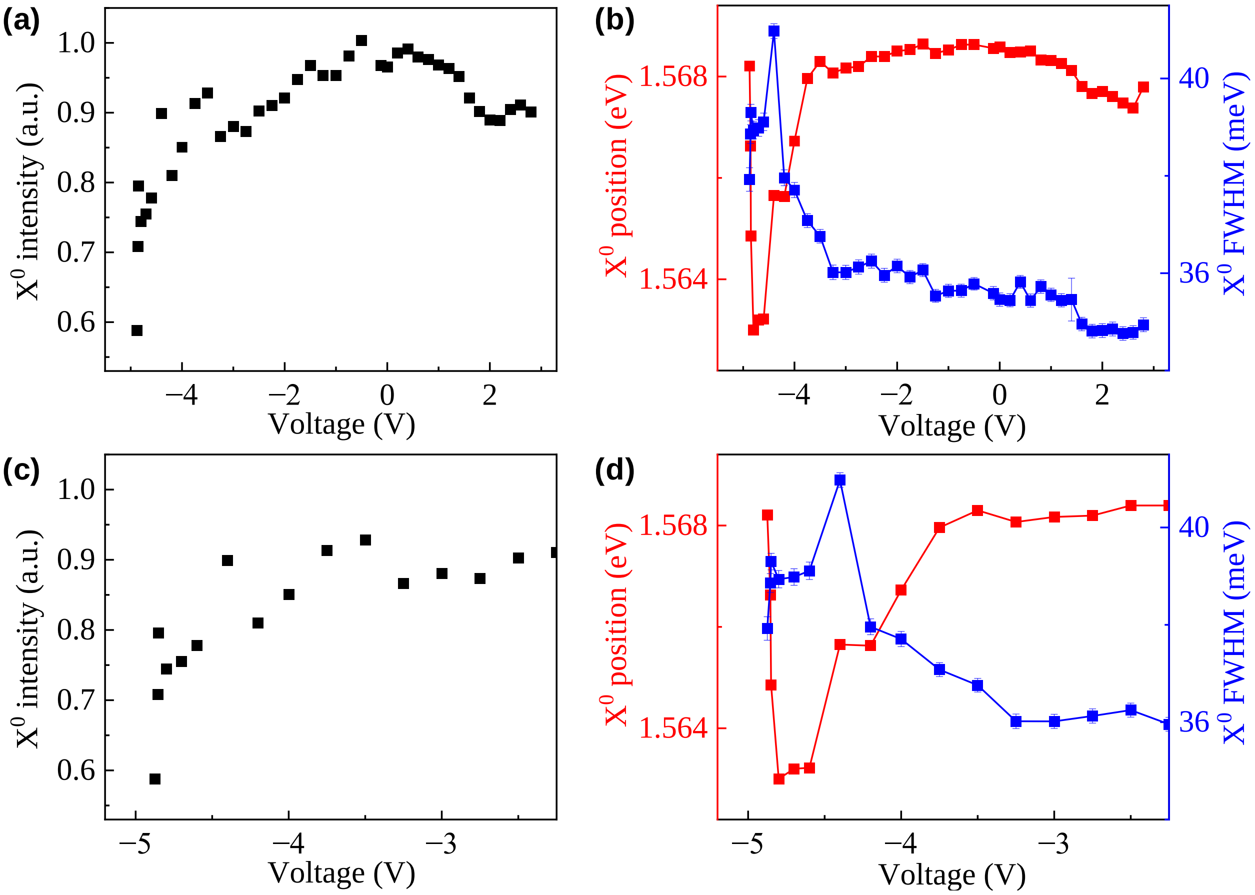

Figure 4.16: (a) X^0 intensity and (b) X^0 position and X^0 FWHM as a function of applied gate voltage for the data from figures 4.15 and 4.14. (c) shows a zoom in of (a) for voltages beyond −2.75 V and (d) shows a zoom in of (b) beyond −2.75 V.

X^0 in $MoSe_2$/Gr as a function of charge density in reference graphene layer

Using the methodology of quantification of charge density in graphene layer on LaF_3 substrate described in section 4.3.2, the E_F at the ends of the voltage sweep with applied gate voltage of 2.8 V (electron doping) and −4.9 V (hole doping) is estimated to be 0.6 eV and −1 eV respectively. Thus, we reach a moderate electron density and a high hole density at the end of voltage sweep.

To compare the behaviours of PL seen in $MoSe_2$/Gr region with the charge density in graphene without losing the many points in Raman data corresponding to $-200 \text{ meV} < E_F < 200 \text{ meV}$, the parameters in PL of $MoSe_2$/Gr are visualized with respect to $\Delta\omega_G$ in reference graphene layer caused by the changing charge density. The figures 4.17a, 4.17c and 4.17e show the X^0 energy, X^0 FWHM and X^0 position as a function of $\Delta\omega_G$ in graphene respectively. In this voltage sweep, since the electron density is still in the moderate regime, the $\Delta\omega_G$ increases continuously with the increase in both electron and hole densities (as expected from figure 4.8). As the intensity of 2D mode in graphene also varies continuously with the increasing applied voltage and charge density, X^0 intensity, X^0 FWHM and X^0 position are plotted with respect to it in figures 4.17b, 4.17d and 4.17f.

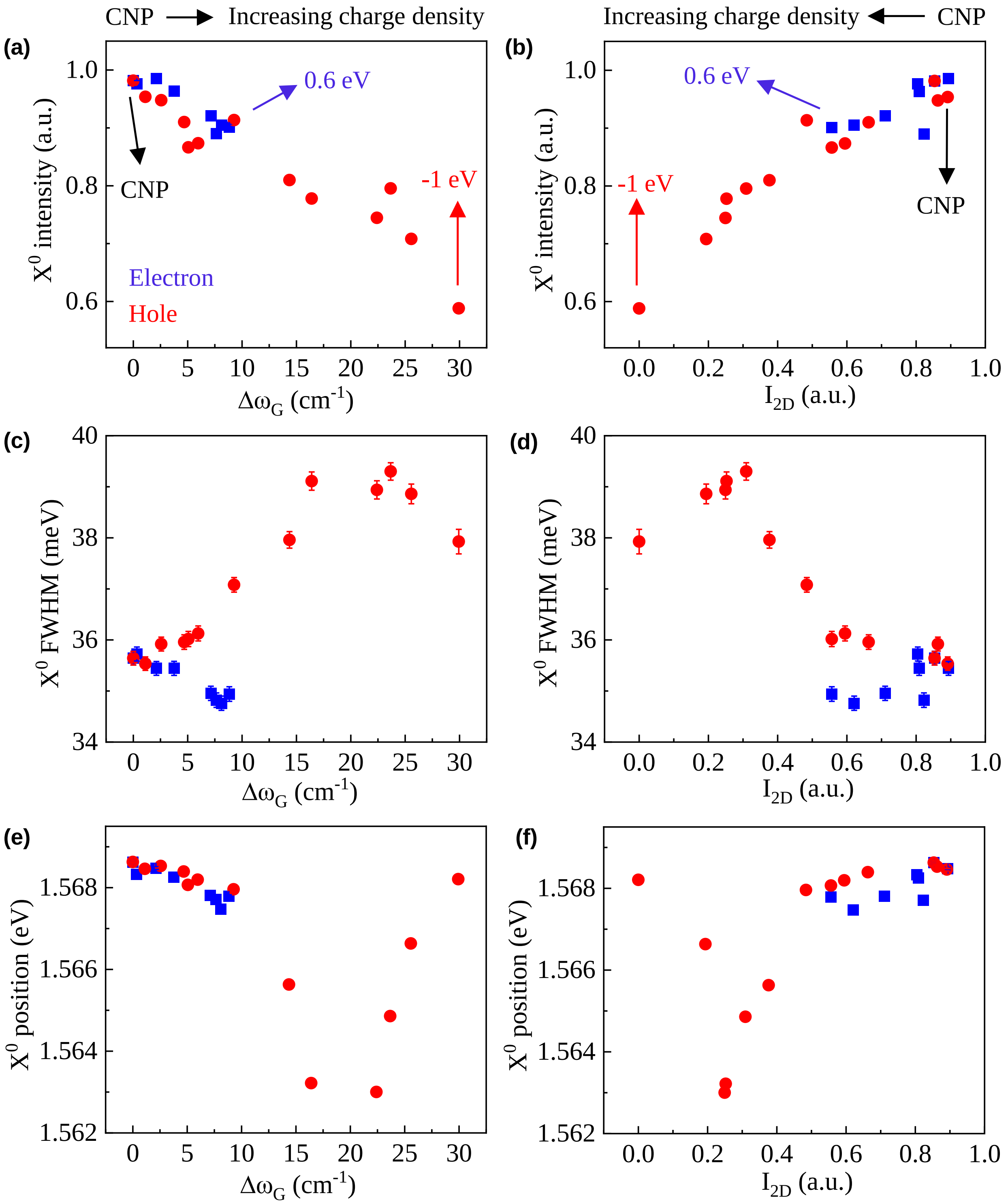

Figure 4.17: (a) X^0 intensity (c) X^0 FWHM and (e) X^0 position observed in MoSe$_2$/Gr (data in figure 4.15) with respect to changing relative G mode position compared to CNP in reference graphene (data in figure 4.14) as charge density is changed. (b) X^0 intensity (d) X^0 FWHM and (f) X^0 position observed in MoSe$_2$/Gr as a function of 2D mode intensity in reference graphene layer. The blue and red data points correspond to electron and hole doping respectively. The CNP and directions are given in and above (a) for (a), (c) and (e); in and above (b) for (b), (d) and (f).

The PL spectra shown with respect to applied voltage beyond -3.75 V in the figure 4.15e helps in clearly visualizing the variations in X^0 position as well as in X^0 intensity. The X^0 intensity shows a continuous decrease with increasing $\Delta\omega_G$ i.e. with increasing charge density with respect to the CNP, as can be seen in figure 4.17a. An explanation for the decrease in X^0 intensity is through the density of carrier charges increasing in $MoSe_2$ of $MoSe_2$/Gr with increasing charge density in reference graphene region. The increase in charge carriers density could open up more and more non-radiative recombination channels for X^0 population, reducing the efficiency of radiative recombination and thereby decreasing the X^0 intensity [90]. No signature of X^* is seen in the figure 4.15e. This implies that although the charge density is enough to change the PL intensity, it is not significant enough to form a X^* population so large that it cannot be filtered out by graphene.

With the increasing charge densities, X^0 position in $MoSe_2$/Gr shows a reduction until $\Delta\omega_G$ in graphene reaches the value of ≈ 20 cm^{-1} and then shows a continuous blueshift (figure 4.17e). This trend of X^0 position with respect to applied gate voltage is also seen clearly in figure 4.16b. The X^0 FWHM shows a broadening with increasing hole density up to $\Delta\omega_G$ ≈ 20 cm^{-1} and then experiences a reduction. These changes in the direction of shifts in X^0 position and X^0 FWHM with respect to a particular $\Delta\omega_G$ are quite intriguing and can also be observed in figures 4.17d and 4.17f as a function of intensity of 2D mode. They correspond to the gate voltage going beyond -4.4 V (figures 4.16a and 4.16b).

It is important to note that although the leakage current starts to shoot down beyond -4.4 V, these kinks seen in X^0 position and X^0 FWHM do not correspond to any sudden changes in leakage current observed as a function of applied gate voltage (see figure 4.15a). Thus, these observed changes are not because of damage in sample or a malfunction in application of gate voltage.

Beyond the threshold value of applied voltage of -4.4 V, the values of ω_G as a function of voltage in graphene and $MoSe_2$/Gr (figure 4.14d) starts to show a very small difference. The 2D mode in graphene of $MoSe_2$/Gr vanishes beyond -4.4 V (see figures 4.15d and 4.14f). The kinks seen behaviour of X^0 position and X^0 FWHM also start at -4.4 V. This all indicates that as the E_F approaches -1 eV, there is a hole transfer from $MoSe_2$ in $MoSe_2$/Gr to the graphene in $MoSe_2$/Gr. This is an evidence towards the band offset between Dirac point of graphene and valence band maximum in $MoSe_2$ being ≈ -1 eV.

4.4.3 Voltage dependent PL spectra at low temperature

The changing lineshape and intensity in PL of $MoSe_2$ under electron doping (seen in figure 4.12) was further studied by performing PL measurements at low temperature of 30 K as well as at room temperature with applied gate voltages of 0 and 4.5 V. The spectra observed are given in figure 4.18a which show a clear increase in intensity of X^* compared to that of X^0 under electron doping, confirming that intrinsically electron doped $MoSe_2$ layer is being neutralized with hole doping. The X^* peak seen in $MoSe_2$ can be concluded to be negatively charged trion because of its increasing intensity upon electron doping.

The PL spectra of $MoSe_2$/Gr at low temperature show a single peak corresponding to X^0 because X^* is filtered out by graphene (given in figure 4.18b). Moreover, much like the

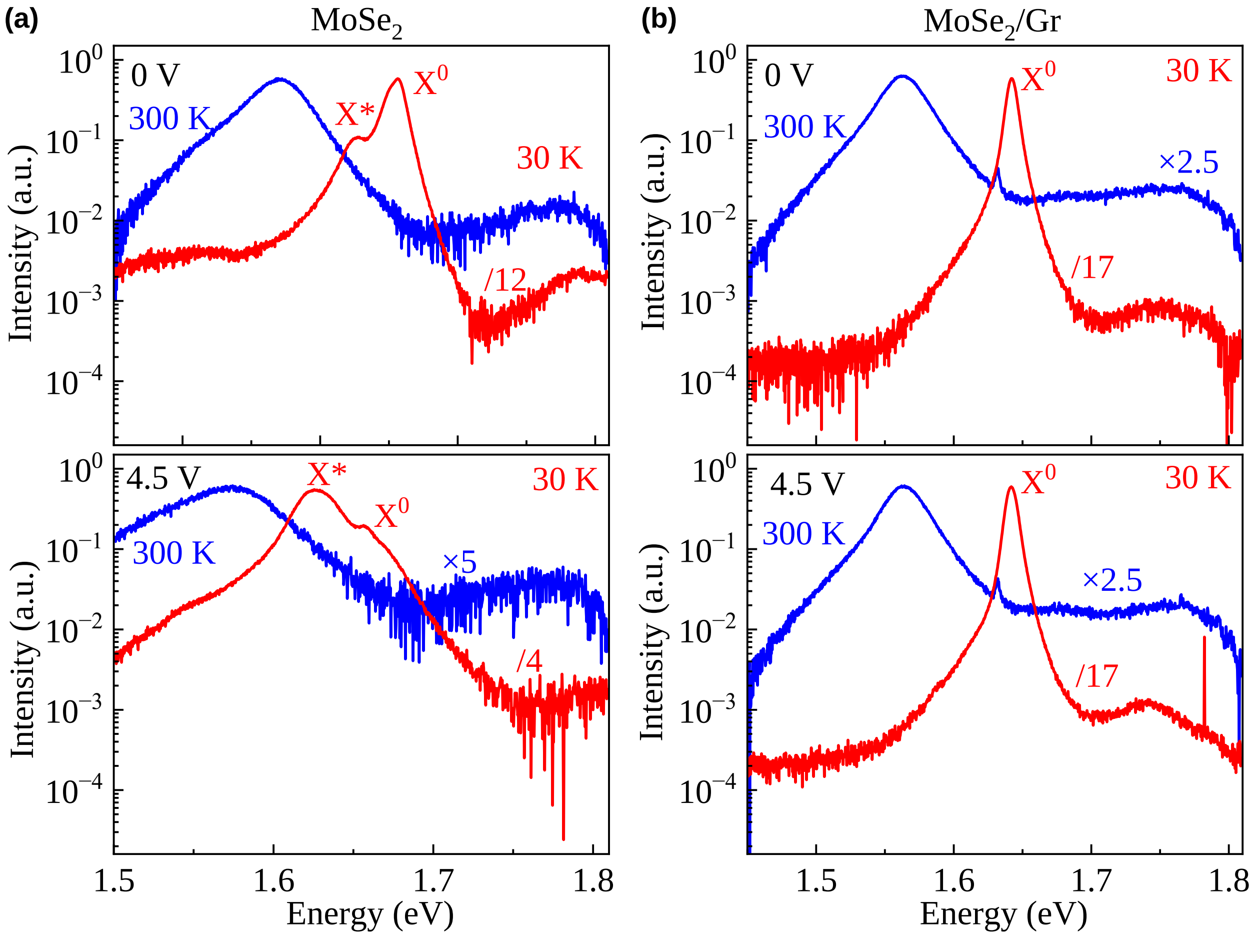

Figure 4.18: PL spectra taken under 0 V (top panel) and 4.5 V (bottom panel) for (a) $MoSe_2$ and (b) $MoSe_2$/Gr in logscale. The blue and red spectra denote temperature of 300 K and 30 K respectively. All spectra are normalized with respect to PL spectrum of $MoSe_2$ taken at 300 K under 0 V. All measurements performed with laser excitation of 1.96 eV and intensity close to 300 $\mu W/\mu m^2$ on sample B.

observations at room temperature, the intensity of X^0 remains similar for 0 V and under electron doping at 4.5 V, with no hints of a X* peak.

However, the X^0 peaks observed at 30 K (FWHM given in table 4.2) for both $MoSe_2$ and $MoSe_2$/Gr are much broader than the ones observed in the samples in chapter 3 (FWHM given in table 3.1), by a factor of 2.5 and 1.8 respectively. The broadening of X^0 can happen because of TMD being in an inhomogeneous environment. The layers in the heterostructures on LaF_3 samples studied here and the ones in chapter 3 are stacked in the same manner. The quenching of PL in $MoSe_2$/Gr as compared to $MoSe_2$ and the filtering of X* indicates that the interface between graphene and $MoSe_2$ is quite clean. Thus, we can attribute the broadening of X^0 to quality of interface between LaF_3 and the heterostructure and in particularly, to the roughness of LaF_3.

		300 K	300 K	30 K	30 K
	Voltage	X^0 position (eV)	X^0 FWHM (meV)	X^0 position (eV)	X^0 FWHM (meV)
$MoSe_2$	0 V	1.572	41	1.656	14.7
	4.5 V	1.578	52	1.660	27.0
$MoSe_2$/Gr	0 V	1.563	35.0	1.642	8.7
	4.5 V	1.564	34.3	1.642	9.4

Table 4.2: The extracted parameters of X^0 peaks from figure 4.18 for $MoSe_2$ and $MoSe_2$/Gr at temperatures of 300 K and 30 K and applied gate voltages of 0 V and 4.5 V.

4.5 Conclusion

In this chapter, we have achieved the control of light emission in heterostructures made up of graphene and $MoSe_2$ by tuning the charge density in the heterostructure by charge doping $MoSe_2$ through graphene. The ionic glass LaF_3 is used as a substrate to obtain charge density varying from moderate electron density of 2×10^{13} cm^{-2} to high hole density of -6×10^{13} cm^{-2}.

This charge density in samples is determined by using Raman spectroscopy of graphene as a sensitive probe. As the charge doping in samples fabricated on LaF_3 occurs through movement of F^- ions, a proper methodology of application of gate voltage and the optical spectroscopy measurements at these voltages has been established at room temperature. Our Raman spectroscopy results show that the charge doping in graphene is reversible and reproducible. The effects of formation of defects in graphene after exposing it to high charge density is also explored in this study. The variation of frequency of Raman G mode as well as the intensity ratio of 2D to G mode with respect to the applied gate voltage is used to quantify the charge density in several samples with the estimation of electron-phonon coupling constants. Thus, the Raman modes in graphene are used as precise doping meters to study the effects of charge doping on graphene, $MoSe_2$/Gr and $MoSe_2$ domains.

In the moderate charge doping regime, the intrinsically electron doped $MoSe_2$ gets neutralized with hole doping through graphene, which increases the intensity of exciton as compared to trion in PL spectra. This has been confirmed by measuring PL spectra on $MoSe_2$ and $MoSe_2$/Gr under no applied voltage and electron doping at room temperature and at low temperature. The $MoSe_2$/Gr region shows very small decrease in PL intensity as hole density in the heterostructure increases.

To explore these changes in PL of $MoSe_2$/Gr occurring with hole doping, the samples have been studied under higher hole density. The G and 2D Raman modes in $MoSe_2$/Gr and graphene can be compared and the charge density at each applied voltage was estimated through the latter. When the Fermi level in graphene reaches close to -1 eV under hole doping, hints of hole transfer from $MoSe_2$ to graphene in the $MoSe_2$/Gr region can be seen in the PL and Raman spectra, implying it to be the difference between the Dirac point in graphene and the valence band minimum of $MoSe_2$/Gr.

Conclusion and perspectives

In this manuscript, we reported on the study of the near-field interactions between monolayer $MoSe_2$ and graphene in chapter 3 and the control of light emission in their heterostructure by electrical tuning in chapter 4. The experimental methods including sample fabrication and optical spectroscopy methods are described in chapter 2.

In chapter 3, we have studied the near-field transfer mechanisms between monolayer $MoSe_2$ and graphene by exploiting the dependence of these mechanisms on the distance between layers. In order to do this, we have made heterostructures of monolayer graphene covering n-layered graphene with n from 1 to 6 layers. All the regions of $MoSe_2$ covering different thicknesses of graphene were probed using photoluminescence (PL) and time-resolved photoluminescence (TRPL) spectroscopy in linear regime to explore the excitonic species of $MoSe_2$ and the influence of n-layered graphene on them.

The coupling of graphene to $MoSe_2$ causes major changes in the PL of $MoSe_2$ like a reduction in PL intensity and filtering of charged excitons, which are a direct result of the interlayer processes. We study these changes in PL with respect to graphene layer thickness in detail as well as the homogeneity of sample, importance of extent of coupling between layers and other effects of dielectric screening. We observe that the quenching in PL of $MoSe_2$ saturates beyond the graphene thickness of 3 layers, indicating a short range process occurring between the layers. We also studied the high energy excitonic species in this heterostructure by observing the effects of varying incident laser excitation on PL as well as through hot PL spectroscopy from which we could estimate the binding energies of $MoSe_2$/n-layered graphene regions.

Moreover, the sample geometry is designed using engineering of the electromagnetic environment in order to obtain the longest possible radiative lifetime of excitons in $MoSe_2$ in our experimental geometry to have better resolved results in TRPL spectroscopy. The TRPL measurements revealed that the exciton dynamics stay similar for different thicknesses of graphene attached to $MoSe_2$ which confirms that the interaction between $MoSe_2$ and graphene layers is indeed of a very short range of ≈ 1 nm. These measurements also give evidence for efficient exciton and hot exciton transfer from $MoSe_2$ to graphene. The influence of presence of defects on the exciton intensity and its dynamics was also explored which showed a decoupling between layers because of the defect. The effects of hBN encapsulation on the PL and TRPL measurements were also studied which revealed that having an hBN layer between the $MoSe_2$/nL graphene structure and substrate does not significantly change the results as compared to the hBN covered heterostructure.

Our work has advanced the understanding regarding transfer mechanisms between 2D materials by revealing the dominant mechanism to be short range tunnelling mediated process through directly probing the effects of coupling of different thicknesses of graphene to TMD on its exciton physics via optical spectroscopy techniques.

In chapter 4, we show the results in the study of electrical control of light emission in $MoSe_2$/graphene heterostructure by charge doping through graphene. We have probed the changes in $MoSe_2$, $MoSe_2$/graphene and graphene regions at room temperature with increasing charge densities by PL and Raman spectroscopy. A high charge density in the order of -6×10^{13} cm^{-2} to possibly inject charges directly from graphene into $MoSe_2$ was achieved using ionic glass LaF_3 as a gate dielectric and substrate. The charge density in graphene was estimated using changes in Raman modes of graphene with changing gate voltage and this can be used as a reference charge density in the heterostructure. As the leakage current seen in LaF_3 substrates as a function of applied gate voltage at room temperature can be as high as a few hundreds of nA, a methodology was developed for spectroscopy measurements with varying voltage. The reversibility and reproducibility of charge doping in graphene layer on LaF_3 was also verified through Raman response.

The PL spectra of $MoSe_2$ with charge density in graphene changing in the moderate doping regime revealed that the PL intensity can be controlled by tuning the defect-assisted non-radiative channels. For $MoSe_2$/graphene, the changes in Raman spectra of reference graphene layer and that of graphene in $MoSe_2$/graphene alongwith the changes in PL of $MoSe_2$ in $MoSe_2$/graphene imply that when the Fermi level shifts by almost -1 eV, there is a hole transfer between $MoSe_2$ and graphene where they are coupled. This is an evidence towards the band offsets between valence band maximum $MoSe_2$ and Dirac point graphene being around 1 eV.

Perspectives

In this subsection, we will discuss about the perspectives related to the work done in this thesis.

hBN spacer between graphene and $MoSe_2$

The work done in this thesis to understand which transfer mechanism dominates between graphene and $MoSe_2$ can be complemented with optical spectroscopic measuerements on heterostructures with an hBN spacer between the monolayer $MoSe_2$ and monolayer graphene. Ideally, the hBN layer needed to perform this study should be at most three layers thick. Clean hBN layers can be exfoliated mechanically, but obtaining homogeneous thin layers with large area is a challenging task. Moreover, the experiments are also a bit challenging to perform as identifying areas with and without the hBN spacer optically is tough due to its low optical contrast. Nevertheless, our collaborators from INSA, Toulouse have provided us with some high quality, homogeneous, thin hBN layers for performing this study.

The study of microsocpic mechanisms between graphene and TMD with an hBN spacer between them was done by E. Lorchat, as part of his PhD thesis in our research group [22]. But the above mentioned challenges made it difficult to perform a comprehensive study with the hBN spacer. It should be noted that the distance dependence of transfer mechanisms between TMD and graphene using hBN spacer has been studied by [110] at room temperature. But we would be more interested to perform our measurements at low temperature to probe the exciton dynamics.

Interactions between graphene and WSe_2

The monolayer WSe_2, a dark TMD has very exotic excitonic species and emissions including bright exciton, intravalley trion, intervalley trion, spin-forbidden dark exciton, neutral biexciton, charged biexciton, dark trion as well as localized states [199]. This rich physics of emission lines coming from WSe_2 makes it a very intriguing to study the effect of coupling of graphene on them at low temperature.

Charge injection from graphene into other TMDs to map the band offsets

From the results in chapter 4, the LaF_3 substrate can be used to shift the Fermi level in graphene by -1 eV to reach high hole density regime. Since our study reveals that the band offset between $MoSe_2$ and graphene (valence band and Dirac point) is close to than 1 eV, a natural step to observe a possible direct hole injection is to perform similar studies with other TMDs having a smaller band offset with graphene. In case a high electron charge density remains unattainable using LaF_3, some other ionic glass or electrolyte can be used to achieve high charge doping in both electron and hole directions. Thus, a TMD like WSe_2 with the band offset of 700 meV could be a good candidate for this. Also, as mentioned above, WSe_2 being a dark exciton would make this study more interesting. A TMD like $MoTe_2$ can also be a good option to study this charge injection with the exciton energy in infrared regime.

Raman spectroscopy of graphene beyond $E_\mathrm{F} = E_\mathrm{L}/2$

As seen in section 4.3.1, we can dope the graphene layer on LaF_3 with hole density high enough to shift E_F by $E_\mathrm{L}/2$. When this Fermi level is reached with incident laser excitation of 1.96 eV, the current becomes of the order of a few hundred nA (as can be seen in figure 4.15a). This high current often damages graphene significantly enough to burn the layer. Hence, our measurements so far do not go beyond $E_\mathrm{F} = E_\mathrm{L}/2$ in graphene. In order to possibly see what happens to the Raman modes beyond this limit, laser excitation with lower energy can be chosen to reach E_F at lower values of applied gate voltages and hence, lower leakage currents to avoid damaging the graphene layer. This type of study can reveal more information about the interference of quantum pathways involved in the Raman modes of graphene as well as of its electronic structure.

$MoSe_2$ and $MoSe_2$/graphene under high hole density at low temperature

The optical spectroscopy measurements for $MoSe_2$ and $MoSe_2$/graphene at cryogenic temperatures as a function of applied gate voltage shown in section 4.4.3 are limited to electron doping direction. Below the temperature of 260 K, the F^- ions become immobile, making it impossible to apply the gate voltage. Hence, performing voltage dependent measurements on LaF_3 at low temperature involves changing the gate voltage at room temperature, then reducing the temperature to cryogenic temperatures and performing optical spectroscopy measurements, then increasing temperature beyond 260 K to change the gate voltage and this cycle has to be repeated for each applied gate voltage and therefore, any particular charge density. Although this process is too tedious to perform with the liquid helium cryostat because of the long time required in changing temperature for each cycle 2.2.1, such measurements can be performed to obtain voltage dependent data at low temperatures using the helium free cryostat. In our case, because of the compatibility issues of gating mechanism with the size of our LaF_3 substrates, these measurements could not be performed in the helium free cryostat until now. But as this is a home-built setup, changes are possible to be made to resolve this compatibility issue in order to perform charge density dependent optical spectroscopy measurements at low temperature on $MoSe_2$/graphene heterostructure on LaF_3 samples.

The control of light emission from $MoSe_2$/graphene and $MoSe_2$ under high hole density tuned by charge doping in graphene is a natural extension to the work done in this thesis so far. Moreover, as we see from figure 4.15d, the charge doping causes changes in the high energy excitonic species. These high energy excitons are much more clearly observed at low temperature, thus the changes in them with respect to charge doping can be efficiently probed at low temperature.

Tuning emission yield of single photon emitters

Although single photon emitters in 2D materials is an active field of research, the microscopic origins behind them remain hidden [200]. The emission spectra obtained from single photon emitters are often unclean. The electrical tuning of single photon emitters in TMD/graphene heterostructures can reveal information about their formation mechanism and control their emission yield which can potentially have usage in optoelectronic applications like light-emitting diodes [201, 202].

Expanding the study of tuning TMD/graphene interactions into infrared regime

The TMDs based on disulfides and diselenides have an optical gap in the visible range. On the other hand, monolayer 2H-$MoTe_2$ has an optical gap of ≈ 1 eV which lies in the near infrared regime [203]. This makes the monolayer $MoTe_2$ an excellent candidate to be used in optoelectronic devices related to application in near infrared regime [204] and especially, in telecommunication [205]. With the physics between $MoTe_2$ and graphene being similar to $MoSe_2$ and graphene, our study of tuning electrical properties of TMD by coupling it to graphene can be extended to $MoTe_2$/graphene heterostructures to explore the applications in near infrared regime.

Résumé en français

5.1 Introduction

Les matériaux bidimensionnels (2D) épais d'une seule ou de quelques couches atomiques peuvent être isolés de leurs cristaux massifs en grâce au fait que ces couches individuelles sont maintenues ensemble par de faibles forces de van der Waals et fortes liaisons covalentes dans le plan. L'isolation d'une couche de graphène atomiquement mince, qui est un le semi-métal, du graphite par [1] a été l'avènement de la découverte d'une large gamme de matériaux 2D avec différentes propriétés allant des semi-conducteurs comme les dichalcogénures de métaux de transition, isolants comme le nitrure de bore hexagonal, les métaux, les supraconducteurs ainsi que les matériaux magnétiques matériaux, les propriétés des matériaux 2D amincis étant différentes de leurs masses homologues. Afin d'isoler les matériaux 2D des cristaux massifs, de nombreuses techniques incluent exfoliation mécanique, dépôt chimique en phase vapeur, épitaxie par jet moléculaire et liquide l'exfoliation assistée a été explorée et utilisée.

Au-delà de l'isolement de ces matériaux 2D, du fait de l'absence de liaisons pendantes sur leurs surfaces, ces couches 2D peuvent être empilées les unes sur les autres dans n'importe quel ordre souhaité pour fabriquer des hétérostructures de van der Waals (vdWH) [2]. Lors de la fabrication de vdWH, le mécanisme d'auto-nettoyage [3] permet de regrouper les contaminants/impuretés qui fournissent des interfaces atomiquement plates et propres entre les matériaux 2D. À cause de ça, même si des ondulations ou des bulles se créent dans le vdWH, on peut facilement trouver des zones propres à étudier au vdWH. La large gamme de matériaux 2D connus signifie qu'un nombre énorme de différents vdWH sont possibles. L'alignement des bandes entre les matériaux 2D dans vdWH dépend de leurs décalages de bande les uns par rapport aux autres, ce qui permet d'obtenir différents types d'hétérojonctions en fonction des bandes interdites des matériaux 2D choisis. De plus, le défaut de paramètre de maille entre les matériaux 2D impliqués dans vdWH peut donner lieu à motifs moirés pour des angles de torsion spécifiques.

Les matériaux 2D sont très sensibles à leur environnement et aux propriétés d'un vdWH dépendent des propriétés de tous les matériaux individuels qui le composent ainsi que des interactions et couplages interfaciaux entre ces matériaux. Ainsi, les propriétés du 2D les matériaux peuvent être adaptés par les matériaux qui leur sont attachés dans le vdWH. De plus, les adsorbats, défauts et autres irrégularités peuvent fortement affecter les propriétés du vdWH. Dans ce système bidimensionnel, les interactions entre les matériaux dans ce champ proche sont différentes par rapport aux interactions entre des matériaux massifs tridimensionnels, ce qui rend le vdWH un système très idoine pour étudier des phénomène physiques dans la limite bidimensionnelle.

Cette thèse vise à comprendre le couplage intercouche entre vdWH constitué de graphène et les dichalcogénures de métaux de transition, puis, en réalisant le contrôle de l'émission de lumière en ajustant ses propriétés électriques. Les propriétés électriques et optiques du graphène peuvent être contrôlées en ajustant la densité de charge. La dispersion des phonons dans le graphène et la diffusion inélastique des photons avec ces phonons (c'est-à-dire la diffusion Raman) ont été bien étudiées au cours des dernières décennies. Cela permet de sonder avec précision les effets de paramètres externes tels que le dopage de charge, la déformation, la température, le écrantage diélectrique et plus encore sur la couche de graphène. La structure électronique du graphène monocouche est assez unique, car elle la bande interdite est nul.

D'autre part, les dichalcogénures de métaux de transition (TMD) ont une bande interdite directe dans la limite monocouche. Ainsi, ils fournissent une émission lumineuse intense et leurs propriétés d'émission sont dominé par une physique riche en excitons, les excitons dans les TMD étant stables même à température ambiante température. Pour cette raison, les TMD sont utilisés comme éléments de base efficaces en optoélectronique des applications comme le photovoltaïque [4] et les diodes électroluminescentes [5].

Lorsqu'un TMD monocouche est bien couplé à une couche de graphène, il est intéressant de se demander ce que des processus peuvent se produire entre ces deux couches et leur dépendance à différents niveaux externes conditions telles que l'éclairage, la température et le dopage de charge. Le vdWH composé de TMD et le graphène est un système intéressant à la fois pour la recherche fondamentale (voir chapitre 1, qui décrit également les propriétés pertinentes du graphène, du TMD et de leur vdWH) ainsi que dans les sciences appliquées telles que l'optoélectronique, l'électronique de spin et de vallée [6, 7] et la photodétection [8].

Dans ce travail, le vdWH composé de graphène et de $MoSe_2$ monocouche (un type de TMD) est utilisé comme élément de base (le schéma de vdWH est donné dans la figure 5.1) car il s'agit d'un système idéal étudié le couplage intercouche et les différents processus de transfert en champ proche se produisant entre les couches dans la limite 2D. En exploitant ces mécanismes de transfert, nous ajustons la densité de porteurs de charge dans cette hétérostructure de vdWH et contrôler ainsi leur photoluminescence.

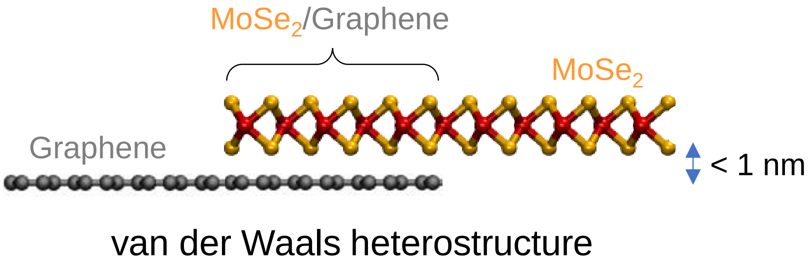

Figure 5.1: Schéma de vdWH composé de graphène monocouche et de $MoSe_2$ monocouche, ayant trois régions d'intérêt différentes : $MoSe_2$, $MoSe_2$/graphène et graphène.

Comme détaillée dans cette thèse, la question de savoir quel type de processus de transfert se produit et domine entre le graphène et les TMD est un domaine de recherche actif en cours à travers différentes techniques de mesure (voir chapitre 3). Comme ces mécanismes de transfert entre les matériaux 2D dépendent de la distance entre les couches, de l'étendue et de l'efficacité de ces processus peuvent être étudiés en exploitant leur dépendance à la distance. Dans ce travail, nous avons abordé cette question en utilisant le graphène en couches $MoSe_2$/n en forme d'escalier pour explorer la dépendance à la distance des processus de transfert en utilisant le changement épaisseur du graphène. Le couplage du graphène au TMD réduit fortement le rendement d'émission du TMD être fortement réduit et donne lieu à un filtrage des excitons chargés qui sont des résultats du transfert mécanismes entre eux. Bien que ces effets du couplage du graphène au TMD sur son excitonique propriétés ont été observées [9], les mécanismes qui les sous-tendent restent cachés. Cette étude vise à mieux comprendre les mécanismes de transfert de charge et d'énergie entre le graphène et TMD et la mesure dans laquelle ils peuvent survenir. Comme le transfert d'énergie Forster à longue portée fait l'objet de recherches actives pour des applications dans les dispositifs de collecte de lumière [10] et à courte portée les mécanismes de transfert de charge sont au cœur des photodétecteurs [11], étudiant ces processus est très important pour progresser vers leurs candidatures.

Après avoir étudié les mécanismes de transfert inter-couches, nous avons travaillé sur le contrôle des transferts inter-couches entre $MoSe_2$ et graphène et réalisant ainsi un contrôle électrique d'émission lumineuse de ce vdWH (voir chapitre 4). Cette étude est réalisée pour comprendre fondamentalement et estimer les décalages de bande entre le graphène et $MoSe_2$. Le contrôle des interactions lumière-matière offre de nombreuses perspectives en optoélectronique. Cela nécessite un contrôle de la densité des porteurs de charge dans $MoSe_2$/graphène et notre approche pour y parvenir consiste à doper le graphène avec des charges en appliquant une tension de grille, puis en dopant le $MoSe_2$ couche à travers le dopage de charge dans le graphène. Les couches de graphène sont souvent utilisées comme électrodes dans les dispositifs accordables en charge, mais leur photoréponse où la couche de graphène est couplée à TMD n'a pas encore été étudié de manière approfondie. Ces matériaux 2D sont très sensibles aux effets extérieurs comme le dopage de charge, qui provoque des modifications du niveau de Fermi dans ces matériaux. Dans ce travail, nous nous sommes concentrés sur le déplacement significatif du niveau de Fermi dans le graphène, de manière à ce que les charges puissent être éventuellement injecté du graphène dans $MoSe_2$, rendant la dépendance en tension de la région avec $MoSe_2$ couvrant le graphène très intrigant à étudier, qui est largement resté une déploré jusqu'à présent. De plus, la plupart des recherches dépendantes de la tension effectuées sur les TMD ont été réalisées les années ont été réalisées à des températures cryogéniques ; cependant, dans cette thèse, nous avons travaillé principalement à température ambiante ainsi qu'à des températures cryogéniques. Expérimentalement, ce décalage du niveau de Fermi dans le graphène de plusieurs centaines de meV nécessite une densité de charge de $\approx 10^{14}$ cm^{-2} et est très difficile à atteindre.

Dans ce travail, cette densité de charge élevée est obtenue en utilisant le verre ionique LaF_3 comme grille di électrique et substrat. Comme le courant de fuite dans LaF_3 est élevé à température ambiante (ce courant pourrait atteindre quelques centaines de nA), les expériences sont assez difficiles à réaliser, mais on sait que les échantillons sur substrat LaF_3 atteignent une densité de charge de $\approx 10^{14}$ cm^{-2}. Les changements produits par le dopage externe peuvent être sondés en observant des espèces excitoniques dans $MoSe_2$ par spectroscopie photoluminescence (PL) et pics dans les spectres Raman du graphène résultant de vibrationnels modes phonons traditionnels. La spectroscopie Raman est une sonde très précise pour déterminer la charge densité dans le graphène et nous l'avons utilisé comme compteur de dopage pour le vdWH. La robustesse de méthodologie de dopage de charge dans une couche de graphène sur un substrat LaF_3 à température ambiante a également été explorée en vérifiant sa réversibilité, sa reproductibilité et l'influence des défauts dessus via la spectroscopie Raman. Dans cette thèse, nous avons étudié les effets du dopage sur le graphène, le $MoSe_2$ ainsi que le $MoSe_2$/graphène et a réalisé le contrôle électrique d'interactions lumière-matière dans ce vdWH qui révèle également des détails sur l'alignement des bandes entre ces deux couches.

Ce projet a débuté en novembre 2020 avec pour objectif de faire avancer la recherche sur mécanismes de transfert intercouches entre matériaux 2D qui avaient été démarrés en 2017 chez mon au sein de mon équipe d'accueil à l'IPCMS, en explorant la dépendance à la distance de ces mécanismes avec hétérostructures des $MoSe_2$/n-couche de graphène dans une structure de type microcavité qui élimine le problèmes de résolution causés par la fonction de réponse de l'instrument observée pendant mesures TRPL (PL résolue en temps). Avec la compréhension des interactions entre les couches, l'étape suivante naturelle consistait à les contrôler. Bien que les effets du dopage de charge dans le graphène ainsi que dans certaines des monocouches TMD, ont été étudiées de manière approfondie; le contrôle du rendement de luminescence via la densité de charge dans les hétérostructures TMD/graphène est relativement peu exploré, ce qui nous a donné la motivation d'étudier cela dans le cas du $MoSe_2$/graphène dans une large plage de densité de charge pour mieux comprendre l'alignement de la bande ment entre ces couches. A cet effet, une méthodologie de fabrication de composants électriques hétérostructures à grille sur LaF_3 et réalisation de spécifications optiques dépendantes de la tension de grille appliquée des mesures troscopies sur ceux-ci ont été développées. Un ensemble complet de tensions de des mesures pendantes pourraient être effectuées avec cette méthodologie sur plusieurs échantillons pour observer des tendances constantes.

Ce manuscrit est divisé en quatre chapitres. Le chapitre 1 est consacré à l'introduction des matériaux 2D concernés par ce travail c'est-à-dire du graphène monocouche à quelques couches, des TMD monocouches, du nitrure de bore hexagonal également comme les hétérostructures TMD/graphène et la description de leurs propriétés pertinentes pour le prochains chapitres. Le chapitre 2 donne des détails sur les méthodes expérimentales utilisées dans ce travail. Il comprend des procédés de fabrication d'échantillons et techniques et configurations de mesure de spectroscopie optique où ils ont été exécutés. Le chapitre 3 est consacré à la compréhension des interactions en champ proche entre le $MoSe_2$ monocouche et le graphène utilisant des hétérostructures des $MoSe_2$/n-couche de graphène. Le chapitre présente d'abord les mécanismes de transfert connus entre matériaux 2D puis détaille les résultats observés pour comprendre les changements dans le PL de $MoSe_2$ provoqués par le couplage à des couches n graphène. Le chapitre 4 se concentre sur le réglage de la densité de charge sur une large plage en hétérostructures monocouche de $MoSe_2$/graphène monocouche par dopage de charge $MoSe_2$ à travers le graphène et contrôlant ainsi l'émission de lumière des trois régions d'intérêt : le graphène, $MoSe_2$/graphène et $MoSe_2$. La méthodologie de dopage de charge dans les échantillons utilisant LaF_3 est également décrite en détail. Le dernier chapitre est consacré à la conclusion et aux perspectives. Dans ce résumé, je vais présenter brièvement les principaux résultats détaillés dans les chapitres 3 et 4.

5.2 Hétérostructures de graphène et TMD

Les interactions en champ proche se produisant aux interfaces des couches dans vdWH influencent fortement ence ses propriétés optiques et électroniques. Les hétérostructures graphène/TMD sont excellents candidats pour comprendre les interactions en champ proche entre les couches ainsi que le contrôle de leurs propriétés optoélectroniques.

Dans la limite 2D, la taille typique de la zone de déplétion est beaucoup plus grande que les minces couches. Ainsi, la structure de bande pour l'hétérostructure des couches minces peut être considérée comme une superposition de bandes des matériaux impliqués [120]. Pour les hétérostructures graphène/TMD, le point Dirac du graphène neutre situé entre le minimum de la bande de conduction et le maximum de la bande de valence [123, 124] impliquent qu'il s'agit d'un modèle de système donneur-accepteur pour les électrons et les trous.

Un bon couplage entre les couches d'hétérostructure TMD/graphène est très important, car ces phénomènes peuvent provoquer un découplement des couches, affectant les propriétés optiques de l'hétérostructure. Le couplage du graphène aux TMD provoque de nombreux effets intéressants sur la physique excitonique dans TMD qui peut être sondé avec précision par spectroscopie PL.

À température ambiante, les TMD ont une durée de vie X^0 (exciton) de l'ordre de la nanoseconde [125, 127], beaucoup plus longue que le processus de transfert d'énergie typique de la gamme picoseconde. Le couplage du TMD au graphène ouvre un canal de recombinaison non-radiatif efficace pour l'exciton A dans les TMD transférés au graphène, ce qui entraîne une forte extinction de PL [125]. Les charges du TMD peuvent passer au graphène par transfert de charge statique entraînant la neutralisation de la couche TMD par le graphène [9, 125].

À basses températures (inférieures à 100 K), les TMD ont une durée de vie radiative X^0 dans la plage ps [127, 79], comparable à l'échelle de temps des mécanismes de transfert d'énergie du TMD vers le graphène [9]. Cela rend l'extinction de l'intensité du pic X^0 dans les spectres PL lorsque les TMD sont couplés au graphène observé à des températures cryogéniques bien moindre que celui observé à température ambiante. D'autre part, les espèces excitoniques des TMD ayant des durées de vie plus longues (par rapport à X^0), comme X^* (trion, ayant généralement une durée de vie de quelques dizaines de secondes à basse température), sont efficacement filtrés par la couche de graphène attachée en raison de processus de transfert d'énergie et de neutralisation par transfert de charge statique [9].

Parmi les TMD discutés jusqu'à présent, les propriétés de $MoSe_2$ ont été étudiées assez en profondeur par notre groupe de recherche ainsi que par d'autres. Les spectres PL de $MoSe_2$ sont très propres avec caractéristiques bien connues à température ambiante et à températures cryogéniques [9]. Dans cette thèse, nous avons utilisé l'hétérostructure constituée de différentes épaisseurs de graphène et $MoSe_2$ monocouche comme élément de base pour étudier les processus microscopiques se produisant à la limite 2D entre ces couches atomiquement minces puis pour réaliser le contrôle électrique de leur émission optique.

5.3 Utilisation de la quenching de PL dans le $MoSe_2$/n-layer graphène pour comprendre les processus de transfert

5.3.1 $MoSe_2$/n-layer graphène

Dans ce travail, nous avons fabriqué des échantillons selon le schéma présentés à la figure 5.2a. Les différentes épaisseurs de graphène (n nombre de couches) recouvrant la monocouche $MoSe_2$ permettent d'observer la dépendance à la distance des processus de transfert et déterminer ainsi si l'un des les mécanismes à courte portée (c'est-à-dire le transfert de charge et le transfert d'énergie de Dexter) dominent ou la longue portée (le transfert d'énergie de Förster). Le hBN sur le dessus protège l'hétérostructure de monocouche $MoSe_2$/n-couche graphène du perturbations extérieures.

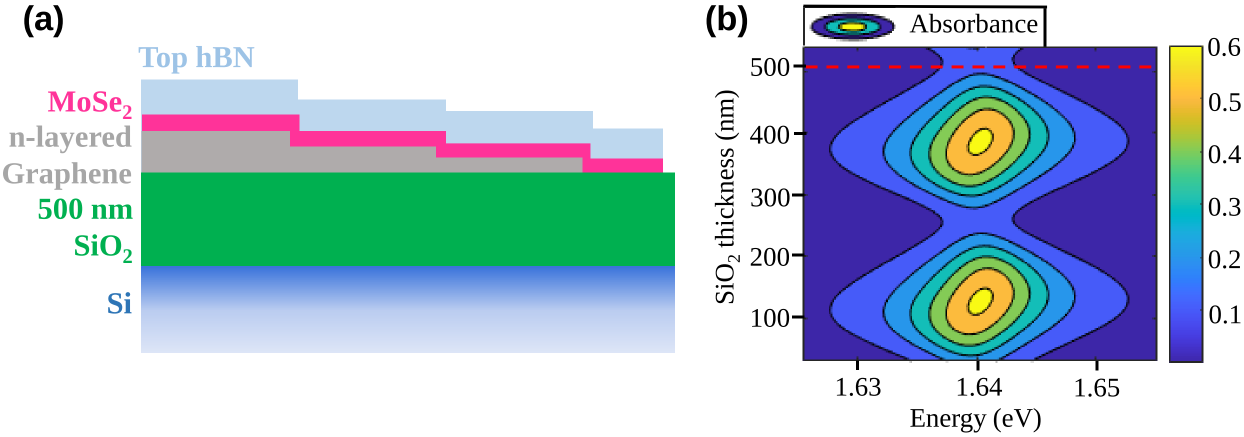

Figure 5.2: (a) Schéma des échantillons de $MoSe_2$/n-couche graphène recouverts de hBN sur un substrat SiO_2/Si de 500 nm d'épaisseur (b) Absorbance calculée du $MoSe_2$ monocouche avec une épaisseur variable de SiO_2 en bas centrée sur Énergie de transition d'exciton de 1,64 eV, le schéma global reste similaire pour les énergies de transition comprises entre 1,620 et 1,655 eV.

De plus, le hBN supérieur et le SiO_2 au bas du $MoSe_2$/n-couche graphène forment une structure de type microcavité. Dans cette microcavité, l'effet Purcell est la modification de probabilité d'émission spontanée en raison des variations de densité des modes optiques provoquées par des changements dans l'environnement [158, 159, 160]. L'effet Purcell est basé sur un couplage faible entre $MoSe_2$ en tant qu'émetteur et la microcavité optique expliquée en électrodynamique quantique [132, 159, 160]. En raison de cet effet Purcell, la modification de l'épaisseur du SiO_2 peut ajuster la durée de vie radiative excitonique dans $MoSe_2$ [115]. La figure 5.2b montre comment l'absorbance de la couche de $MoSe_2$ change avec l'épaisseur variable de SiO_2 calculé à l'aide de la méthode de matrice de transfert [115, 162] et nous avons choisi du SiO_2 de 500 nm d'épaisseur pour fabriquer des échantillons. Cela a été fait pour placer l'échantillon à un nœud de la microcavité (ligne pointillée rouge sur la figure 5.2b) qui permettra de donner la durée de vie de l'exciton radiatif la plus longue possible de $MoSe_2$, afin d'observer clairement les échelles de temps sur la fonction de réponse de l'instrument dans la plage ps dans les mesures TRPL.

5.3.2 Spectres de réflectance et photoluminescence

Les régions ont d'abord été caractérisées par réflectance et spectroscopie PL. Les figures 5.3a et 5.3c montre respectivement les spectres de réflectance différentielle et les spectres PL, prises sur toutes les régions à basse température. La réflectance différentielle et les spectres PL de la $MoSe_2$/0 couche graphène (appelé « $MoSe_2$ » à partir d'ici pour plus de simplicité) a deux caractéristiques : X^0 et X^*. D'autre part, les régions $MoSe_2$/nL de graphène (où nL est n graphène en couches pour $n > 1$) n'ont qu'une seule caractéristique X^0 intense décalée vers le rouge en énergie d'environ 10 meV par rapport à $MoSe_2$ en raison du écrantage diélectrique.

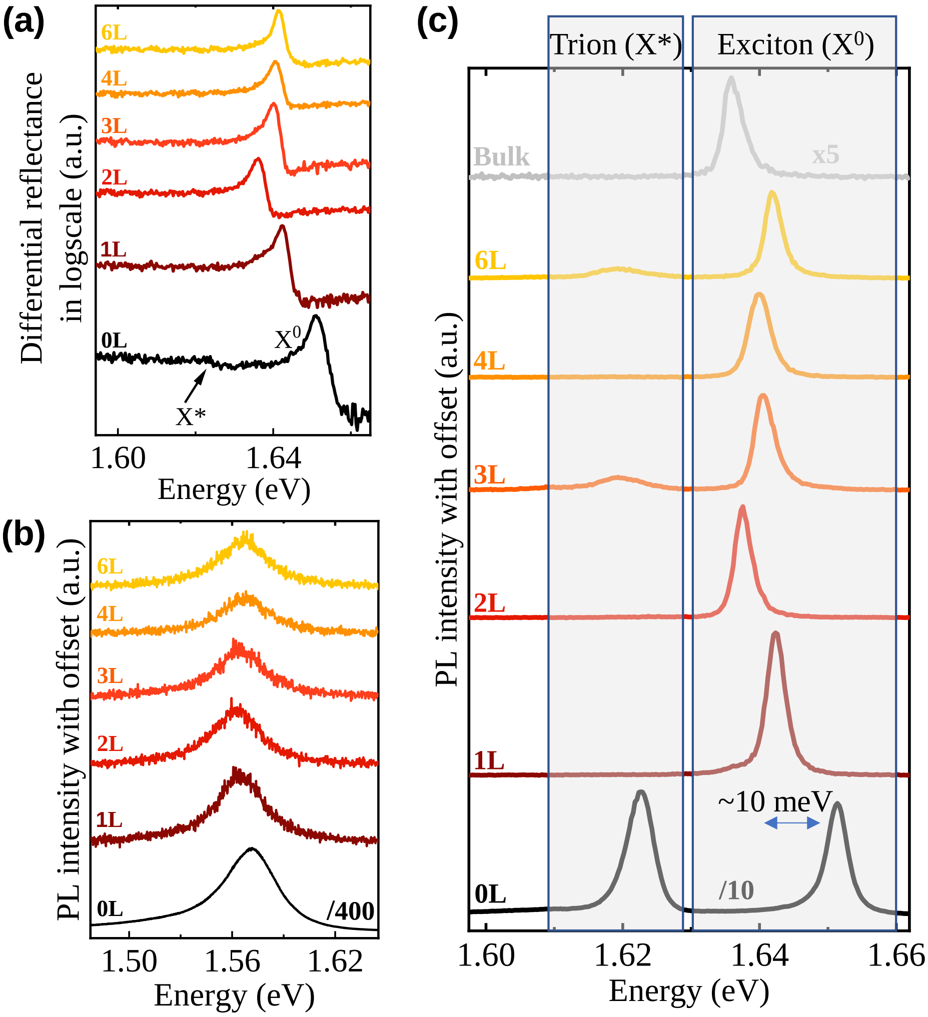

Figure 5.3: Spectres optiques pris sur toutes les régions $MoSe_2$/nL (où nL est n couche de graphène) dans l'échantillon 1, représentés avec un décalage vertical : (a) Spectres de réflectance différentielle en échelle logarithmique pris à une température de 16 K, (b) PL spectres pris à température ambiante avec un laser de 2,33 eV et une intensité proche de 15 µW/µm^2 et (c) spectres PL pris à une température de 16 K avec une excitation laser de Laser de 1,96 eV et intensité proche de 25 µW/µm^2, les cases mettent en évidence les pics X^* et X^0.

Un faible signal issu du trion (X^*) apparaît dans le $MoSe_2$ pourrait être vu dans les spectres PL des régions $MoSe_2$/nL de graphène après avoir été massivement filtré par la couche de graphène attachée grâce à des processus de transfert et de neutralisation de charge. Les spectres PL des régions $MoSe_2$/nL de graphène pour des épaisseurs de graphène de 1 à 6 couches montrent une trempe comparable les unes aux autres lorsqu'elles sont observées par rapport au PL de $MoSe_2$; bien que le graphène en vrac éteigne le PL de $MoSe_2$ d'un facteur beaucoup plus élevé. Pour observer comment les spectres PL de l'échantillon 1 changent spatialement au fil des régions et pour obtenir des données sur une vaste zone plutôt que sur quelques points seulement, nous avons pris des cartes de spectroscopie PL sur l'échantillon.

5.3.3 Cartes PL hyperspectrales

La figure 5.4a montre la zone de l'échantillon 1 sur laquelle une carte de spectroscopie PL est réalisée à basse température avec une excitation laser de 1,96 eV. Cette carte d'une superficie de 111 µm × 35 µm a été prise avec un pas de 0,5 µm afin d'avoir la carte la mieux résolue possible. Les spectres PL de cette carte, similaires à ceux observés dans 5.3c, ont été équipés de profils Voigt pour les pics X^* et X^0. Les paramètres extraits de cet ajustement sont représentés sur les figures 5.4b-i par rapport aux régions $MoSe_2$/nL de graphène dans la carte PL, où les points blancs dans les cartes appartiennent à des spectres s'écartant des caractéristiques attendu X^* et X^0.

La figure 5.4b montre comment la position du pic X^0 change au cours de l'échantillon. La région avec $MoSe_2$ a une énergie X^0 proche de 1,65 eV, supérieure à près de 10 meV par rapport aux régions $MoSe_2$/nL de graphène. La différence entre les positions des pics X^0 et X^* variant au cours de l'échantillon est illustrée dans la figure 5.4d. Tous les spectres PL pris dans les régions $MoSe_2$/nL de graphène ne montrent pas de pic X^* mesurable en raison de son transfert au graphène et donc, la figure 5.4d représente que les points où un pic X^* est clairement visible, ce dernier montre comment la largeur du pic X^* varie au cours de l'échantillon. Il convient de noter que le pic intense X^* dans $MoSe_2$ présente une légère asymétrie en certains points de la carte en raison d'un épaulement du côté des basses énergies due aux effets de recul des électrons (vu sur la figure 5.3 ainsi) [165].

La largeur du pic X^0, illustré sur la figure 5.4e, est de l'ordre de quelques meV et montre une réduction avec fixation du graphène.

La figure 5.4g montre la variation de l'intensité du pic X^0 sur l'échantillon lorsque l'intensité est presque saturée pour le cas de $MoSe_2$. Cette carte aide à visualiser la réduction ou l'extinction de l'intensité du pic X^0 de $MoSe_2$ en raison du transfert vers le graphène lorsqu'il se trouve au-dessus de différentes épaisseurs de graphène. Le $MoSe_2$/1L graphène a une intensité du pic X^0 plus grande que les régions $MoSe_2$/nL de graphène plus épaisses.

L'intensité totale de PL (l'ajout des intensités des pics $X^0 + X^*$) est indiquée sur la figure 5.4h, presque saturée pour la région $MoSe_2$. Le rapport d'intensité du pic X^0 à l'intensité totale de PL donné dans la figure 5.4i montre comment la fraction de l'intensité totale de PL appartenant à X^0 varie au cours de l'échantillon. L'intensité du pic X^* est négligeable pour de nombreux points dans les régions $MoSe_2$/nL de graphène, comme le montre la figure 5.4f qui montre le rapport d'intensité du pic X^* à celui de X^0 pour les points avec des pics X^* observables. Ce rapport d'intensité est supérieur à 1 pour tous les points de la région $MoSe_2$, ce qui rend l'intensité totale PL de cette région beaucoup plus élevée que le reste.

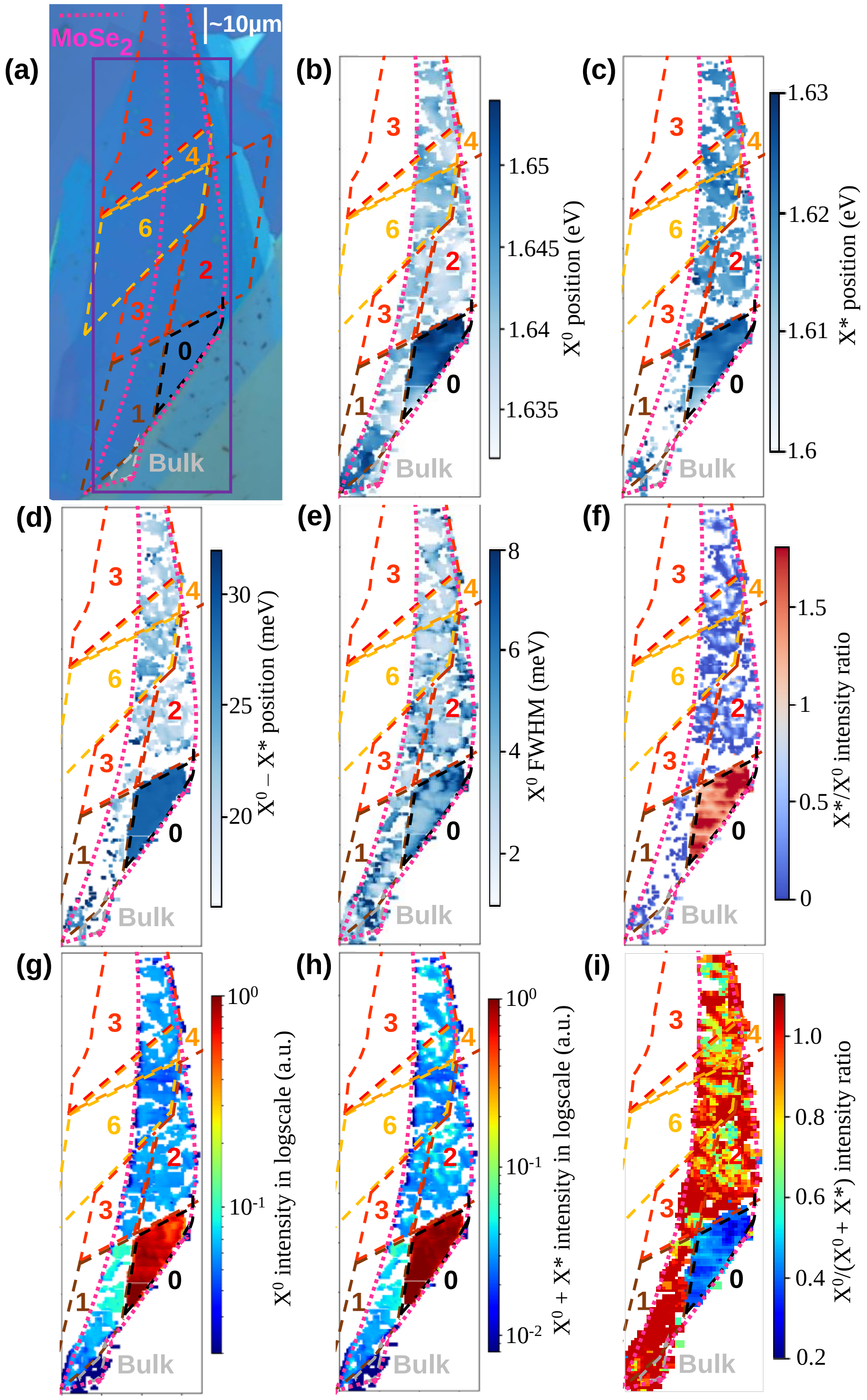

Figure 5.4: (a) Image optique de l'échantillon 1 avec le rectangle violet désignant la zone de carte de spectroscopie PL de $MoSe_2$ prise à 16 K avec une excitation laser de 1,96 eV et une intensité proche de 25 µW/µm^2, les paramètres extraits : (b) la position du pic X^0 (c) la position du pic X^* (d) la position du pic X^0 – la position du pic X^* (e) la largeur du pic X^0 (f) rapport des intensités du pic X^* à X^0 (g) l'intensité du pic X^0 et (h) intensité totale de PL en échelle logarithmique et (i) rapport de l'intensité du pic X^0 à l'intensité totale de PL. Toutes les images montrent les régions de graphène $MoSe_2$/n-layer avec des contours en pointillés.

Les valeurs moyennes des paramètres extraits des cartes PL de $MoSe_2$ en fonction du nombre de couches de graphène sont présentées dans la figure 5.5. La différence entre les positions des pics X^0 et X^* définit l'énergie de liaison de X^*, qui montre une réduction lorsque $MoSe_2$ recouvre du graphène de n'importe quelle épaisseur (illustré dans la figure 5.5b). Afin de quantifier l'extinction PL de $MoSe_2$ lorsqu'il est couplé au graphène, nous définissons le facteur d'extinction d'une région $MoSe_2$/nL de graphène par rapport à $MoSe_2$ par

$$\mathrm{Facteur\ d'extinction\ (QF)} = \frac{\mathrm{Intensit\acute{e}\ de\ MoSe_2}}{\mathrm{Intensit\acute{e}\ de\ MoSe_2/nL\ graphene}} \tag{5.1}$$

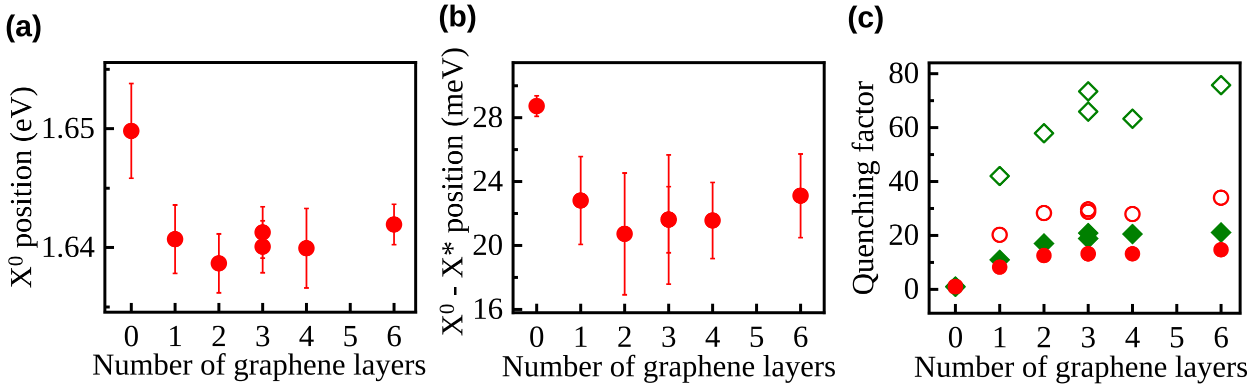

Figure 5.5: Les valeurs moyennes de (a) la position du pic X^0 (b) la position du pic X^0 − la position du pic X^* et (c) facteurs d'extinction en fonction du nombre de couches de graphène sous $MoSe_2$ tiré des cartes hyperspectrales PL. Les symboles rouges et verts désignent les valeurs moyennes des cartes PL prises à une température de 16 K avec une excitation laser de 1,96 eV et 2,33 eV respectivement, tout en maintenant une intensité laser proche de 25 µW/µm^2. Les écarts types sont indiqués par des barres d'erreur. Les symboles ouverts et remplis en (c) représentent respectivement les facteurs d'extinction pour le PL total et X^0.

Corrélations

La figure 5.6a montre la corrélation entre la position du pic X^0 et la largeur du pic X^0 pour toutes les régions $MoSe_2$/nL de graphène de l'échantillon 1. La figure 5.6b représente la corrélation entre l'intensité totale de PL et le rapport des intensités du pic X^0 et de PL total pour chaque région. À mesure que le couplage entre $MoSe_2$ et le graphène à n couches diminue, l'intensité du pic X^* augmente à mesure que son transfert de $MoSe_2$ au graphène devient moins efficace. Ainsi, l'intensité totale de PL augmente en raison de l'augmentation de l'intensité du pic X^*, tandis que le rapport entre l'intensité X^0 et l'intensité totale de PL diminue. Il en résulte une structure en forme de queue dans la corrélation pour toutes les différentes épaisseurs de graphène. On peut considérer que les points de l'échantillon avec un rapport élevé entre l'intensité du pic X^0 et l'intensité de PL totale ont un fort couplage entre $MoSe_2$ et le graphène ; tandis que les points avec un couplage plus faible entre les couches ont un rapport plus petit. Bien qu'une valeur particulière de ce rapport d'intensité pour isoler quantitativement des domaines plus ou moins fortement couplés ne peuvent pas être déterminés, la figure 5.6b comporte des symboles carrés et triangulaires désignant les points ayant respectivement des couches fortement et faiblement couplées, correspondant à une valeur seuil de 0,9 pour le rapport entre l'intensité du pic X^0 et l'intensité de PL totale pour diviser les régimes de couplage.

5.3.4 Dynamique des excitons

Afin d'étudier la dynamique des excitons et des trions et d'estimer les échelles de temps impliqués, les mesures TRPL ont été réalisées par nos collaborateurs de l'INSA de Toulouse. Lors du couplage du graphène à MoSe$_2$, le modèle à 3 niveaux expliquant la dynamique des excitons change en ouvrant des voies non-radiatives pour le transfert de l'exciton et de l'exciton chaud de MoSe$_2$ au graphène, comme le montre le figure 5.7c, la dynamique du trion change de manière analogue.

A partir du système à 3 niveaux, l'intensité de PL en MoSe$_2$ au temps t est :

$$I_{\mathrm{X}^0(\mathrm{MoSe}_2)}(t) \propto \frac{n_{\mathrm{X}^\mathrm{h}}(0)}{\tau_{\mathrm{relax}} - \tau_{\mathrm{rad}}}(\mathrm{e}^{-t/\tau_{\mathrm{relax}}} - \mathrm{e}^{-t/\tau_{\mathrm{rad}}}) \tag{5.2}$$

où $n_{\mathrm{X}^\mathrm{h}}(0)$ est la population photogénérée initiale d'excitons chauds.

L'intensité de PL en MoSe$_2$/graphène au temps t est :

$$I_{\mathrm{X}^0(\mathrm{MoSe}_2/\mathrm{Gr})}(t) \propto \frac{n_{\mathrm{X}^\mathrm{h}}(0)}{\tau_{\mathrm{rel}} - \tau_{\mathrm{decay}}}(\mathrm{e}^{-t/\tau_{\mathrm{rel}}} - \mathrm{e}^{-t/\tau_{\mathrm{decay}}}) \tag{5.3}$$

où $\tau_{\mathrm{rel}} = ((\tau_{\mathrm{relax}})^{-1} + (\tau_{\mathrm{G}}^{h})^{-1})^{-1}$ et $\tau_{\mathrm{decay}} = ((\tau_{\mathrm{rad}})^{-1} + (\tau_{\mathrm{G}})^{-1})^{-1}$ sont les échelles de temps efficaces de relaxation des excitons chauds et de désintégration des excitons de X^0 en MoSe$_2$/graphène respectivement.

Les TRPL de X^0 pris sur le graphène MoSe$_2$/1-6 et MoSe$_2$ sont représentés respectivement dans les figures 5.7a et 5.7b. Ces chiffres sont représentatifs des spectres TRPL typiques observés sur les régions MoSe$_2$/nL de graphène. Les spectres sont ajustés avec les équations (5.2) et (5.3) pour le cas du graphène MoSe$_2$ et MoSe$_2$/nL respectivement. Le temps de montée du TRPL dans MoSe$_2$ qui est de $\tau_{\mathrm{relax}} \approx$ 1,4 ps, très proche de la valeur attendue de 1,1 ps calculée dans [64] pour MoSe$_2$ sur SiO$_2$. Les τ_{relax} dans les régions MoSe$_2$/1-6L de graphène restent non résolus. Alors que le MoSe$_2$/1-6L graphène affiche des échelles de temps de décroissance comprises entre 2 et 2,4 ps ; une échelle de temps de désintégration plus longue de $\sim$ 8,9 ps est observée dans le cas de MoSe$_2$.

Étant donné que les spectres TRPL pour le MoSe$_2$/1-6L graphène sont similaires, nous nous concentrerons sur le graphène MoSe$_2$ et MoSe$_2$/1L pour une explication plus approfondie par le modèle à 3 niveaux de la figure 5.7c. Pour MoSe$_2$, comme le seul canal de désintégration est radiatif, $\tau_{\mathrm{rad}} \approx$ 8,9 ps. En utilisant ce τ_{rad} dans MoSe$_2$, les énergies de liaison estimées (E_{b} donné dans le tableau 3.2) et l'équation (3.6) , τ_{rad} dans MoSe$_2$/1L de graphène est estimé à $\approx$ 17,4 ps. Dans MoSe$_2$/1L Gr, outre la recombinaison radiative, la population X^0 peut également passer de MoSe$_2$ au graphène (avec une échelle de temps τ_{G}). Ainsi, τ_{decay} dans le cas du graphène MoSe$_2$/1L dépend de ces deux voies comme

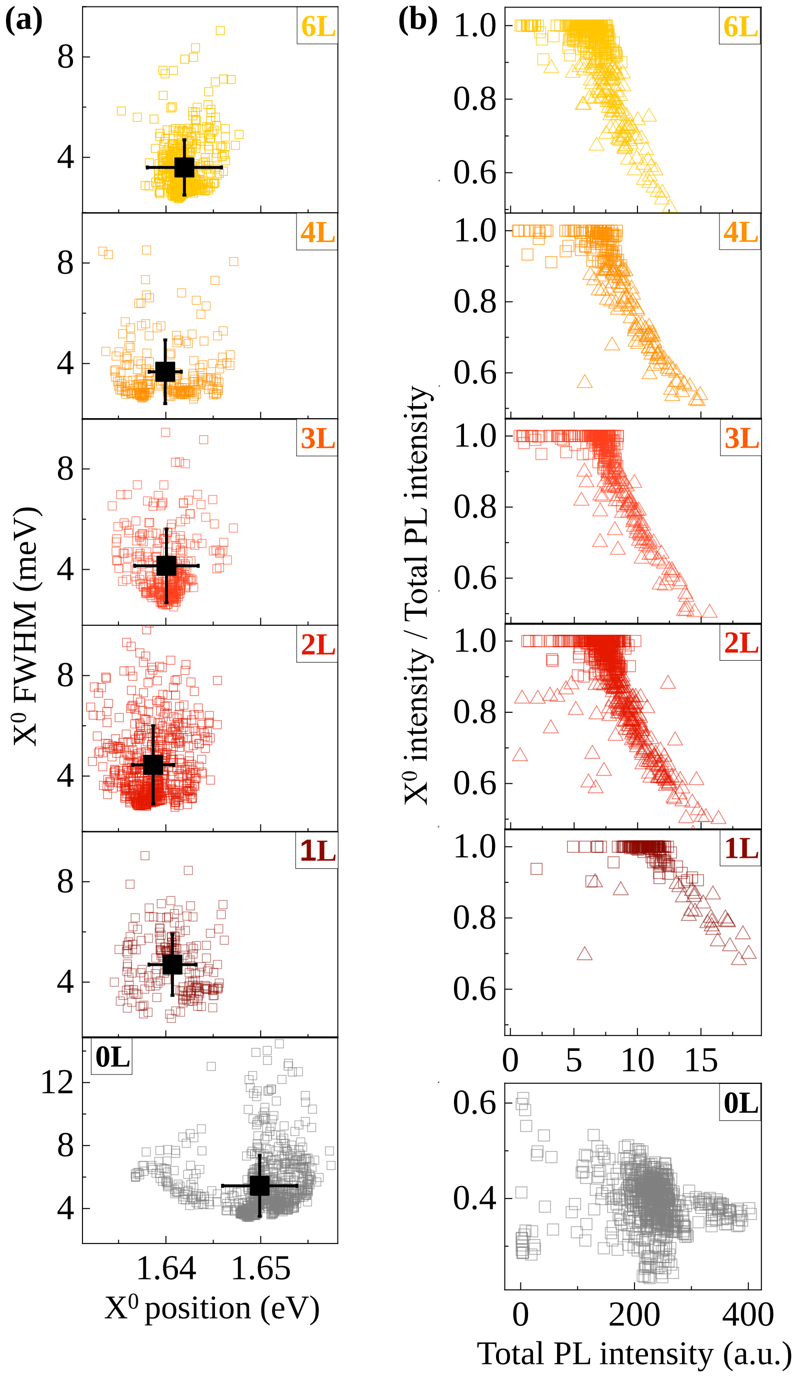

Figure 5.6: (a) Corrélation entre la position du pic X^0 et la largeur du pic X^0, les carrés remplis de noir montrent les valeurs moyennes avec les écarts types sous forme de barres d'erreur (b) Corrélation entre l'intensité totale de PL et rapport de l'intensité du pic X^0 à l'intensité totale PL, dans lequel les carrés et les triangles représentent respectivement des points fortement et faiblement couplés. Les deux corrélations sont obtenues à partir de la carte présentée dans la figure 3.10. Les données d'une seule des deux régions $MoSe_2$/3L de graphène de l'échantillon 1 sont données ici par souci de simplicité.

$$\tau_{\text{decay}} \approx \frac{\tau_{\text{G}} \times \tau_{\text{rad}}}{\tau_{\text{G}} + \tau_{\text{rad}}}. \tag{5.4}$$

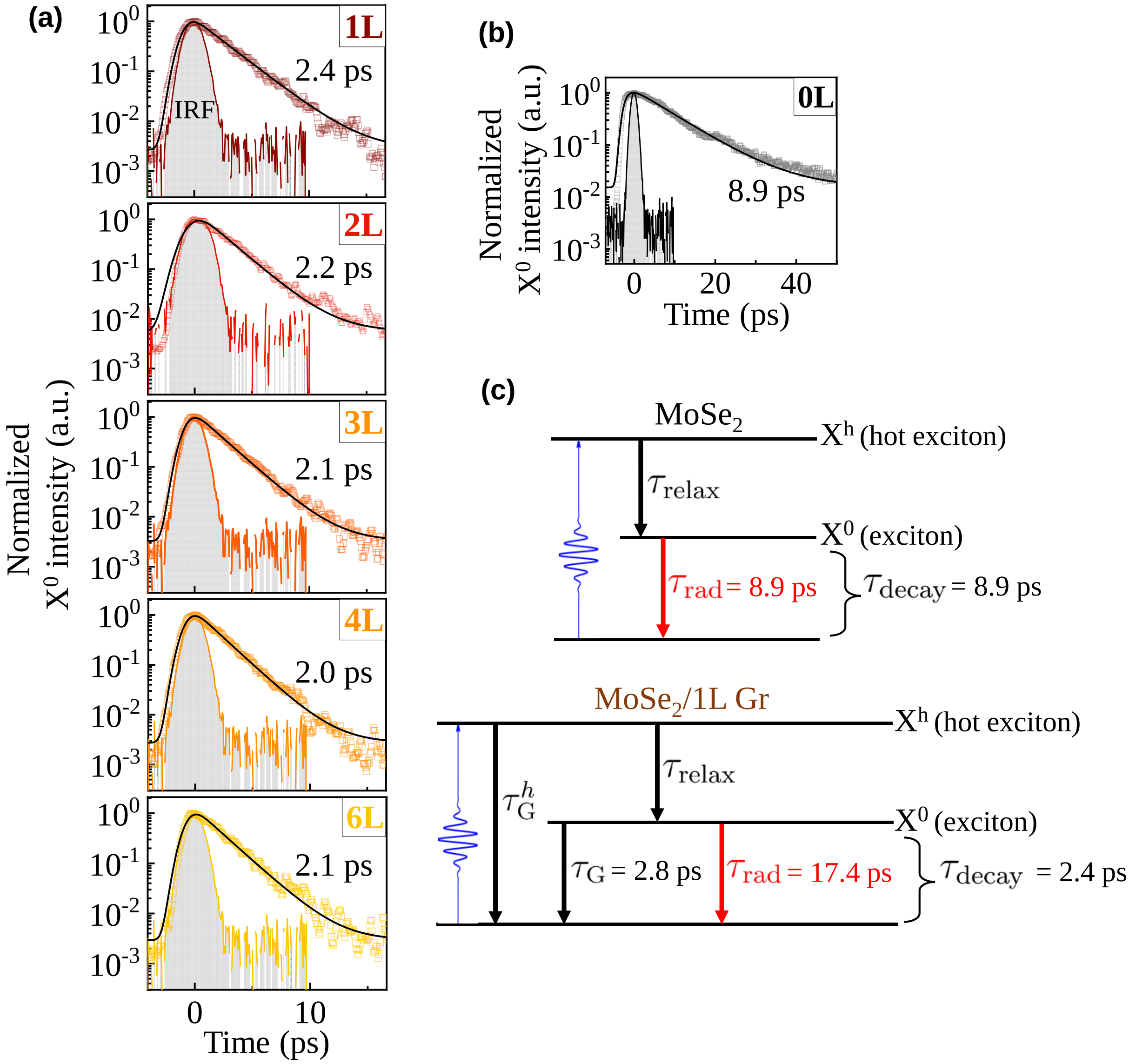

Figure 5.7: Différentes échelles de temps de désintégration X^0 observées dans les données TRPL de (a) MoSe$_2$/1-6L graphène et (b) MoSe$_2$, affichées en échelle logarithmique avec des zones ombragées en gris représentant l'IRF, prises utilisant une excitation laser de 1,71 eV avec une intensité proche de 10 µW/µm^2 et une résolution de 1 ps à température cryogénique. La dynamique X^0 représentée avec des modèles à 3 niveaux pour (c) MoSe$_2$ et (d) MoSe$_2$/1L graphène avec des échelles de temps extraites des données TRPL.

En utilisant l'équation ci-dessus (5.4), $\tau_G \approx 2{,}8$ ps, qui est beaucoup plus petit que τ_{rad}, signifie que le X^0 le transfert vers le graphène est une voie bien plus efficace que la recombinaison radiative. Pour estimer la fraction de la population X^0 qui recombine radiativement, nous estimons le rendement d'émission X^0 (η_{X^0}) par

$$\eta_{X^0} = \frac{1/\tau_{rad}}{1/\tau_{rad} + 1/\tau_G} \tag{5.5}$$

qui est ≈ 1 pour MoSe$_2$ et ≈ 0,14 pour MoSe$_2$/1L Gr. En comparant ces deux rendements,

$MoSe_2$ /nL Gr	0L	1L	2L	3L	4L	6L
X^0 τ_{decay} (ps)	8.9	2.4	2.2	2.1	2.0	2.1
X^0 τ_{rad} (ps)	8.9	17.4				
X^0 τ_G (ps)	–	2.8	2.5	2.4	2.3	2.4
X^0 emission yield	1	0.14	0.13	0.12	0.12	0.12
1/(X^0 emission yield)	1	7.0	7.9	8.2	8.5	8.3
QF (X^0)	–	9.3	11.7	18.8	16.6	13.1
QF (X^0+X*)	–	20.4	26.4	39.1	36.9	31.9

Table 5.1: Temps caractéristiques et facteurs de "quenching" estimés à partir des données TRPL présentées dans les figures 5.7a et 5.7b.

on obtient,

$$\frac{(\eta_{X^0})_{MoSe_2}}{(\eta_{X^0})_{MoSe_2/1L\,Gr}} \approx 7 \tag{5.6}$$

En comparant davantage cette valeur au facteur d'extinction observé à ces points : QF (X^0) ≈ 9,3, la différence entre eux implique qu'il existe une voie empêchant la formation de X^0 population en $MoSe_2$/1L Gr, ce qui est une preuve du transfert d'excitons chauds de $MoSe_2$ au graphène.

Un calcul similaire pour les échelles de temps dans la dynamique X^0 d'autres graphènes $MoSe_2$/nL peut également être effectué et les valeurs estimées, ainsi que celles mentionnées jusqu'à présent, sont données dans le tableau 5.1. Les données TRPL similaires de X^0 et les échelles de temps comparables observées pour les dynamiques des $MoSe_2$/1-6L graphène impliquent que la plage d'interactions entre $MoSe_2$ et le graphène est courte. Les différences entre QF (X^0) et 1/(X^0 rendement d'émission) observées dans toutes les régions de $MoSe_2$/nL graphène soulignent le transfert d'excitons chauds de $MoSe_2$ en nL graphène.

5.4 Contrôle de l'émission lumineuse en charge réglable Hétérostructures graphène/$MoSe_2$ utilisant un substrat LaF_3

Notre approche pour contrôler la densité des porteurs de charge dans l'hétérostructure graphène/$MoSe_2$ consiste à d'abord contrôler la densité de charge dans la couche de graphène connectée aux électrodes de grille et à doper la couche $MoSe_2$ à travers le graphène. Cette éventuelle injection de charge nécessite de décaler le niveau de Fermi (E_F) dans le graphène de ≈ 500 meV et ≈ −1 eV, ce qui correspond à des densités de porteurs de charge de 2×10^{13} cm^{-2} et -6×10^{13} cm^{-2} respectivement. Afin d'aller au-delà de ces densités de porteurs de charge plutôt élevées, le matériau de déclenchement doit être choisi en conséquence. Dans notre travail, nous avons utilisé le verre ionique [181] Trifluorure de Lanthane, c'est-à-dire

LaF$_3$ qui peut être utilisé pour atteindre réversiblement une densité de porteurs de charge de $\sim 10^{14}$ cm $^{-2}$ par conduction ionique et constitue un substrat très robuste avec un comportement isolant, ce qui le fait fonctionner à la fois comme diélectrique de grille et comme substrat.

La figure 5.8a montre le schéma des échantillons utilisés dans ce travail. Pour fabriquer ces échantillons, l'hétérostructure graphène/MoSe$_2$/hBN a été déposée sur le substrat de telle sorte que le graphène touche l'électrode supérieure (Ti de 3 nm d'épaisseur/Au de 47 nm d'épaisseur), contrairement à MoSe$_2$. La figure 5.8d est une image optique d'un échantillon qui montre trois régions d'intérêt différentes dans ces hétérostructures : graphène, graphène/MoSe$_2$ et MoSe$_2$, qui sont toutes recouvertes d'une fine couche (< 10 nm) hBN qui agit comme une couche protectrice pour l'hétérostructure.

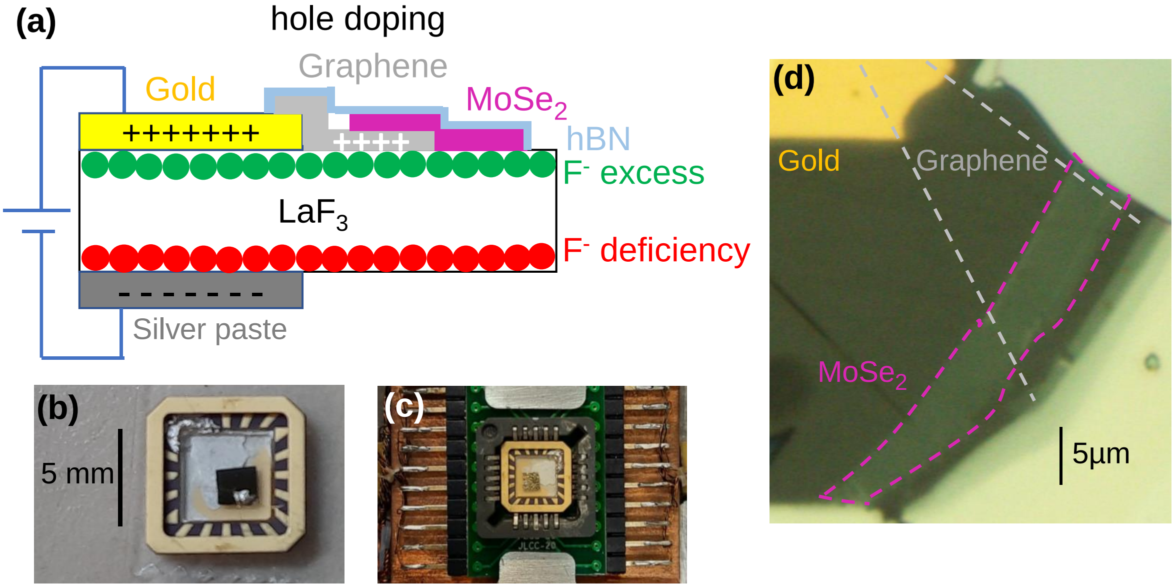

Figure 5.8: (a) Schéma du dopage de trous dans l'hétérostructure hBN/MoSe$_2$/graphène sur substrat LaF$_3$ (b) image de l'échantillon fini dans un support de puce (c) et dans le cryostat CIA (d) image optique de l'échantillon.

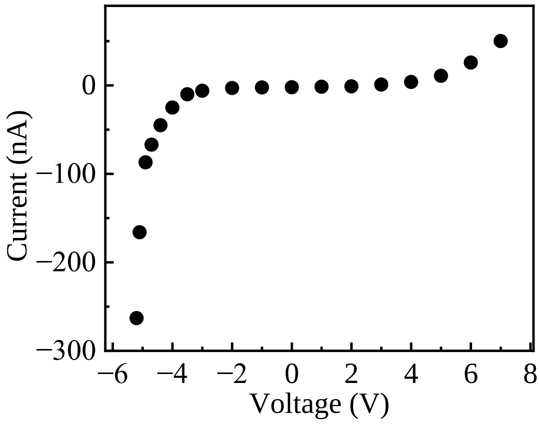

Figure 5.9: Courant mesuré par rapport à la tension appliquée à un échantillon sur un substrat LaF$_3$ lors d'un balayage de tension typique effectué à température ambiante.

Les mesures ont été effectuées en utilisant la configuration de mesures dépendantes de la tension principalement à température ambiante pour éviter les problèmes causés par l'immobilité des ions F^- à basse température. Depuis la formation du double électrique Les condensateurs à couche dépendent du mouvement des ions F^-, il faut laisser au système un certain temps pour se détendre après chaque changement de tension appliquée. Pour les mesures effectuées pour ce travail, la tension appliquée est modifiée par pas de $\sim$ 0,2 V et l'échantillon dispose d'au moins 100 secondes pour se détendre avant d'effectuer des mesures. Étant donné que la plupart des mesures sont effectuées à température ambiante, le courant de fuite est assez élevé (comme prévu par [186]) et les mesures doivent être effectuées lentement et avec précaution pour éviter d'endommager l'échantillon en cas de courants de fuite élevés. L'évolution typique du courant de fuite en fonction de la tension de grille est présentée sur la figure 5.9.

5.4.1 Dopage de charge dans le graphène

Comme détaillé dans la section 1.1.4, la spectroscopie Raman est une excellente sonde pour observer et quantifier les effets du dopage de charge dans le graphène. Nous discuterons ci-dessous des tendances typiques des spectres Raman dépendants de la tension observés dans les échantillons contenant du graphène sur LaF_3 et de leur analyse.

La figure 5.10 montre les spectres Raman du graphène pris du dopage électronique au dopage par trous lors d'un balayage de tension typique. Comme les modes Raman G et 2D dans le graphène montrent une dépendance très nuancée au dopage de charge, nous nous concentrerons donc sur ces deux modes et leurs corrélations par rapport à la tension appliquée.

La dépendance des paramètres des modes Raman G et 2D sur la tension de grille appliquée, extraite après les avoir ajustés respectivement aux profils Lorentzien et Voigt, est illustrée dans la figure 5.11. Les 5.11a et 5.11b montrent respectivement les tracés de contour des modes G et 2D en ce qui concerne la tension de grille. Un net changement de ω_{G} (la position du mode G) est visible sur le tracé de contour ainsi que sur la figure 5.11c. D'après le comportement théorique attendu de ω_{G} avec densité de charge [30, 35], le ω_{G}^0 (la position du mode G au CNP) de cet échantillon dans ce balayage de tension de grille est de $\sim$ 1585 cm^{-1} qui est le minimum de ω_{G} par rapport à la tension appliquée et par conséquent, le CNP est à $\sim -2{,}4$ V. Le CNP en balayage de tension étant différent de 0 V implique que la couche de graphène est intrinsèquement dopée. La fréquence ω_{G} montre une variation rapide au-delà de -4 V dans le régime de dopage par trous et au-delà de 1 V dans le régime de dopage par électrons.

La largeur du mode G (Γ_{G}) par rapport à la tension de grille montre une réduction attendue par rapport à Γ_{G}^0 (Γ_{G} à CNP) sous dopage électronique selon l'équation 1.30 (représentée sur la figure 5.11e). Sous dopage par trous, Γ_{G} montre une légère diminution par rapport à Γ_{G}^0 jusqu'à -3 V, puis montre une augmentation. Une telle augmentation de Γ_{G} sous une concentration de charges élevée est également observée dans [30, 43] et pourrait être due à des inhomogénéités de charge. De plus, la forme de la ligne en mode G peut présenter une légère asymétrie du côté des fréquences inférieures à une densité de trous très élevée, par exemple dans le spectre Raman pris à $-4{,}9$ V sur la figure 5.10. Ce type d'asymétrie

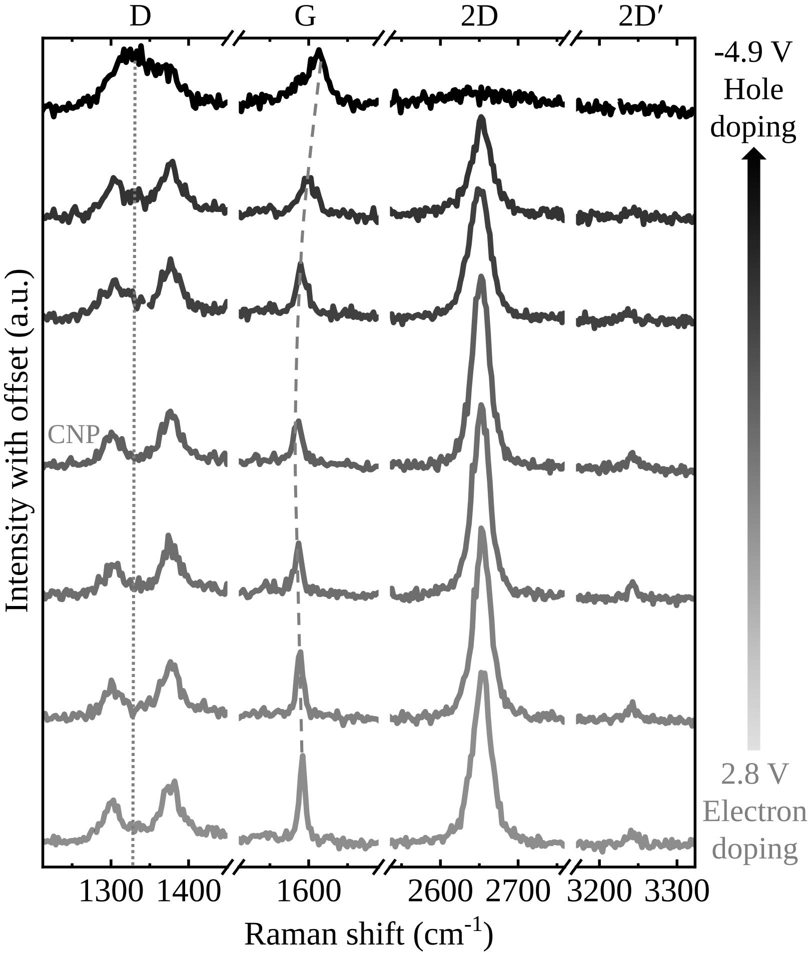

Figure 5.10: Spectres Raman dépendants de la tension de grille montrant les modes Raman D, G, 2D et 2D', prélevés sur l'échantillon E (graphène sur LaF$_3$) à température ambiante avec une excitation laser de 1,96 eV et une intensité proche de 600 µW/µm^2. La ligne pointillée est une guide pour détecter les changements de fréquence du mode G, la ligne pointillée montre la position attendue du mode D et le spectre Raman correspondant au point de neutralité de charge (CNP) est également donné.

du pic G avec une densité de charge accrue a été observé par [193, 194] et est attribué à la résonance de Fano provenant du couplage entre le phonon en mode G et le continuum électronique [195, 196]. L'intensité du mode G I_G reste presque constante tout au long du balayage de tension (illustré sur la figure 5.11g), mais montre une augmentation significative au-delà de $-4{,}7$ V, ce qui implique également que E_F s'approche de $E_L/2$ (comme expliqué dans la section 1.1.4 [36, 38]).

La fréquence du mode 2D (ω_{2D}) change très peu pour la tension de grille appliquée entre 2,8 V et $-4{,}4$ V, mais diminue considérablement au-delà de $-4{,}4$ V en régime de dopage à trous élevés (comme le montre la figure 5.11d). La largeur du mode 2D (Γ_{2D}), qui reste constant entre des tensions appliquées de 2,8 V à $-4{,}4$ V, mais commence à augmenter au-delà de $-4{,}4$ V (figure 5.11f). Cette augmentation de Γ_{2D} peut être attribuée aux interactions électron-électron et à une éventuelle diffusion des défauts électroniques en raison de l'augmentation des défauts [40, 41] (comme le montre l'épaulement en mode D vu à une tension appliquée

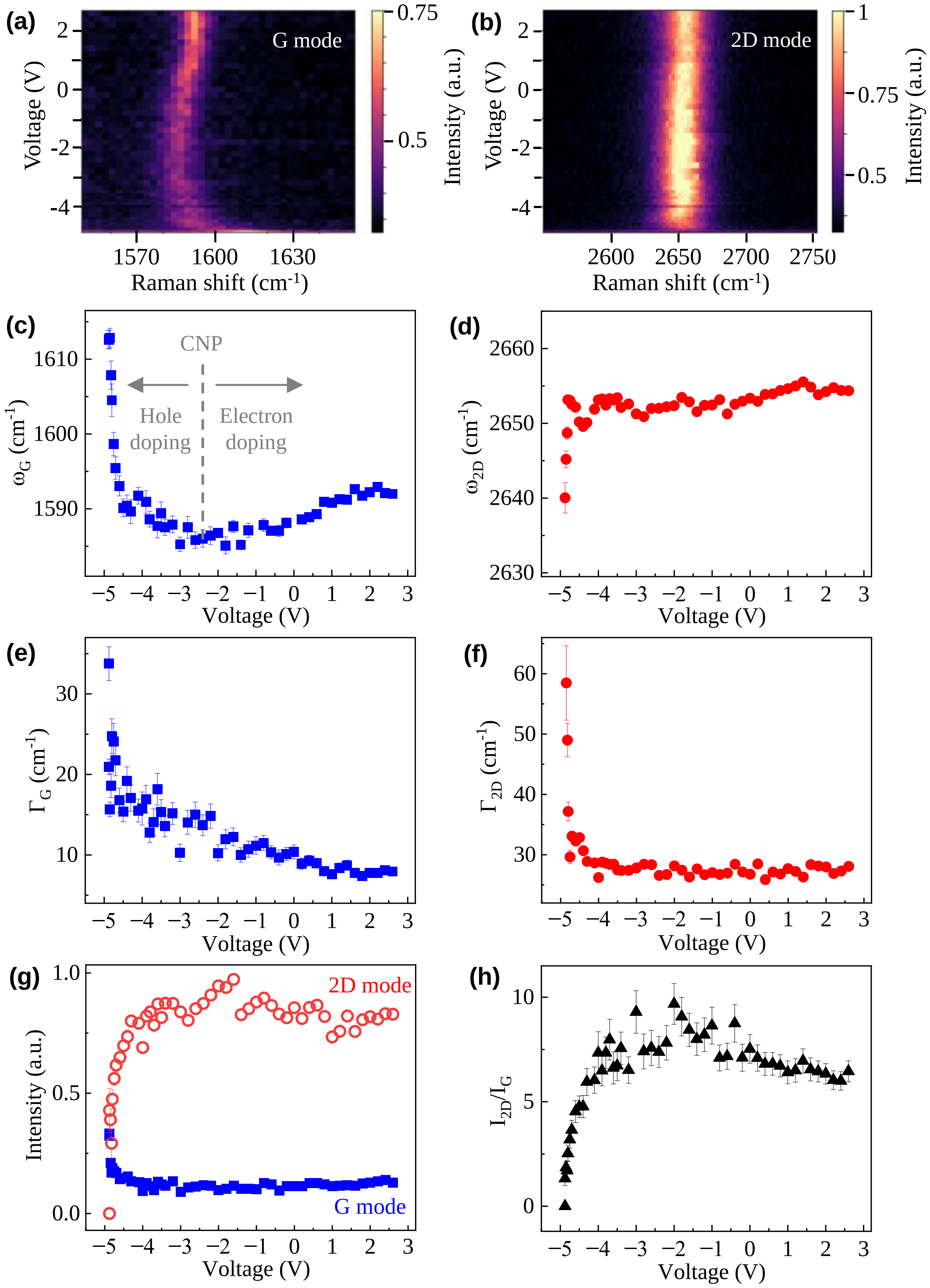

Figure 5.11: Les tracés de contour des modes (a) G et (b) 2D en fonction de la tension de grille appliquée dans la même échelle d'intensité. Variation de (c) fréquence du mode G (d) fréquence du mode 2D (e) la largeur du mode G (f) la largeur du mode 2D (g) intensités des modes G et 2D et (h) rapport de leurs intensités observées par rapport à celles appliquées tension. Le CNP et les directions de dopage sont indiqués en (c). Toutes les données sont prises sur l'échantillon E à température ambiante avec une excitation laser de 1,96 eV et une intensité proche de 600 µW/µm^2.

Échantillon	$\Delta\omega_{\mathrm{G}}$ à $I_{\mathrm{2D}} \to 0$ (cm^{-1})	λ_Γ
A	23.5	0.012
C	25.0	0.013
E	26.6	0.015

Table 5.2: Le décalage de fréquence du mode G observé lorsque le mode 2D devient extrêmement petit et le λ_Γ estimé en l'utilisant pour plusieurs échantillons à faible densité de défauts.

de −4,9 V dans la figure 5.10). La figure 5.11g montre également la diminution continue de I_{2D} avec le dopage par électrons et par trous (comme vu dans [34, 36]), sa chute dans un régime de dopage par trous élevé est d'un intérêt particulier dans ce travail. Le rapport d'intensité $I_{\mathrm{2D}}/I_{\mathrm{G}}$ sur la figure 5.11h montre une réduction attendue avec l'augmentation de la concentration d'électrons et de trous.

Quantification de la densité de charge

La densité des porteurs de charge n dans le graphène monocouche est liée à E_{F} comme [30]

$$E_F = \mathrm{sgn(n)}\hbar\vartheta_{\mathrm{F}}\sqrt{\pi|\mathrm{n}|} \tag{5.7}$$

Le décalage du pic G induit par le dopage ($\Delta\omega_{\mathrm{G}}$) peut être utilisé pour quantifier la densité de charge dans l'échantillon à partir d'équation [32, 33]:

$$\Delta\omega_{\mathrm{G}} = \Delta\omega_{\mathrm{G}}^{\mathrm{A}} + \Delta\omega_{\mathrm{G}}^{\mathrm{NA}}. \tag{5.8}$$

où

$$\Delta\omega_{\mathrm{G}}^{\mathrm{A}} = -2.13n_1 - 0.0360n_1^2 - 0.00329n_1^3 - 0.226|n_1|^{3/2} \tag{5.9}$$

dans lequel n_1 représente la densité des porteurs de charge en unités de 10^{13} cm^{-2} et $\Delta\omega_{\mathrm{G}}^{\mathrm{A}}$ est la contribution adiabatique en cm^{-1} et la contribution non-adiabatique est donnée par

$$\Delta\omega_{\mathrm{G}}^{\mathrm{NA}} = \frac{\lambda_\Gamma}{2\pi\hbar} P \int_{-\infty}^{\infty} \frac{[f(E - E_{\mathrm{F}}) - f(E)]E^2\mathrm{sgn}(E)}{E^2 - (\hbar\omega_{\mathrm{G}}^0)^2/4} \mathrm{d}E \tag{5.10}$$

où λ_Γ est le couplage électron-phonon constant au point Γ [34], P désigne la valeur principale de Cauchy et

$$f(E) = [1 + \exp((E)/k_{\mathrm{B}}T)]^{-1} \tag{5.11}$$

est la distribution de Fermi-Dirac.

Afin d'estimer d'abord théoriquement le $\Delta\omega_{\mathrm{G}}$ à différents n, la constante de couplage électron-phonon au point Γ, c'est-à-dire λ_Γ, doit être déterminée avec précision pour les échantillons avec des couches de graphène sur LaF. $_3$ pour estimer la contribution du terme non adiabatique $\Delta\omega_{\mathrm{G}}^{\mathrm{NA}}$ à $\Delta\omega_{\mathrm{G}}$. Lorsque $E_{\mathrm{F}} \approx E_{\mathrm{L}}/2$ ($\approx$ −0,98 eV dans ce travail), le I_{2D} devient extrêmement petit et $\Delta\omega_{\mathrm{G}}$ à ce stade peut être utilisé pour déterminer λ_Γ à l'aide des équations (5.8) et (5.7). Les valeurs de λ_Γ observées sur plusieurs échantillons de graphène sont données dans le tableau 5.2.

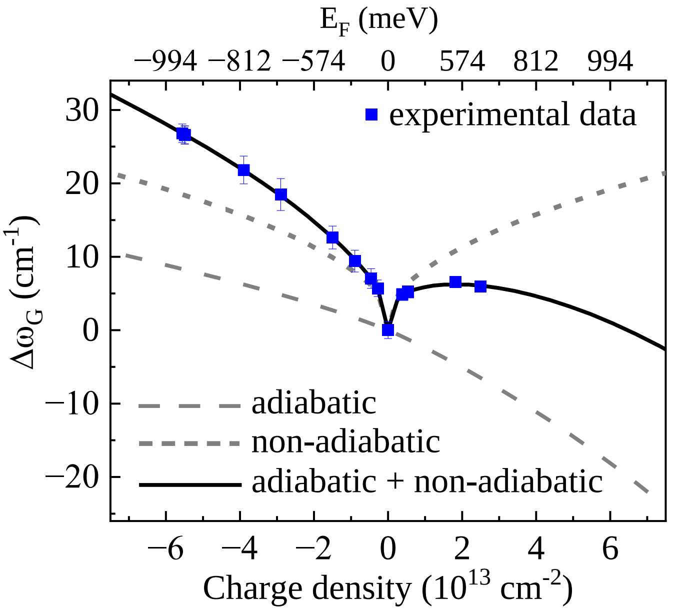

Figure 5.12: Modifications calculées de la fréquence du mode G en fonction de la densité de charge (ou niveau de Fermi lié à la densité de charge par (5.7)) pour les contributions adiabatiques, non-adiabatiques et totales (adiabatiques+non-adiabatiques) à température ambiante. Les données expérimentales sont extraites de la figure 5.11c pour l'échantillon E.

En utilisant ces valeurs de λ_Γ, le $\Delta\omega_G^{NA}$ théorique en fonction de n et E_F est calculé à l'aide de l'équation (5.10) et donné sur la figure 5.12 (pour le cas de l'échantillon E), ainsi que la contribution adiabatique théoriquement estimée $\Delta\omega_G^{A}$ (à partir de l'équation (5.9)) et ainsi, le total $\Delta\omega_G$ (à partir de l'équation(5.8)) estimé à partir de ceux-ci. Pour comparer cette estimation théorique avec le $\Delta\omega_G$ expérimental, les valeurs de $\Delta\omega_G$ vues dans les expériences (données dans la figure 5.11c) sont marquées dans la figure 5.12 à leurs densités de charge attendues. Ainsi, nous pouvons utiliser les modes Raman du graphène comme dopage pour estimer le niveau de dopage à n'importe quelle tension appliquée.

Robustesse de l'estimation du niveau de dopage

Nous avons également étudié la réversibilité du dopage de charge dans des échantillons de graphène sur LaF_3 après avoir soumis ces derniers à des tensions de grille élevées 5.13a. Il est clair que ω_G présente une certaine hystérésis entre les deux balayages de tension, qui se produit en raison du temps nécessaire plus long pour que les ions F^- soient déplacés et installés après avoir été exposés à des tensions négatives élevées. Bien que le CNP et ω_G^0 soient légèrement déplacés dans cette hystérésis, la charge globale de dopage est réversible. L'étendue de l'hystérésis dépend également du courant de fuite (panneau inférieur de la figure **??**a) subi par l'échantillon avant que la direction du dopage de charge ne soit inversée et dans le cas de courants de fuite très élevés, l'échantillon peut avoir besoin de plus de temps à chaque valeur de tension pour que le courant de fuite se stabilise à mesure que le dopage est inversé.

Si le dopage de charge dans la couche de graphène est possible plusieurs fois, les mesures de spectroscopie Raman en fonction de la tension appliquée ont été effectuées plusieurs fois. Les ω_G extraits de deux balayages de tension distincts sur un échantillon sont présentés dans le panneau supérieur de la figure 5.13b. Les deux balayages de tension ont un CNP légèrement différent en raison de la modification de la densité de charge intrinsèque après les premières mesures de balayage de tension. Une disparition du mode 2D aux tensions négatives élevées dans les deux balayages implique un décalage de E_F de $\approx$ 0,98 eV et bien que $\Delta\omega_\mathrm{G}$ à une tension particulière soit différent lorsque les deux tensions les balayages sont comparés, la tendance des changements de ω_G par rapport à la tension qui y est observée est très similaire. Comme cela montre que le dopage de charge dans les échantillons de graphène sur LaF$_3$ est reproductible, jusqu'à un régime de dopage de trous élevé, cela souligne également la nécessité de quantifier la densité de charge dans les échantillons ou d'examiner les déplacements de ω_G plutôt qu'en considérant uniquement la tension appliquée.

Le panneau inférieur de la figure 5.14a montre les spectres Raman pris au CNP et sous haute densité de trous, ce dernier montrant un épaulement du mode D indiquant la création de défauts dus à des réactions électrochimiques. Il convient également de noter que dans ce régime de dopage à trous élevés, une large luminescence chaude peut être présente, ce qui augmente la ligne de base du spectre. Après ce balayage de tension, une population de défauts se forme dans la couche de graphène et les défauts liés aux modes Raman D, D' et D+D' faibles (détaillés dans la section 1.1.4) peuvent être observés dans le spectre Raman pris à CNP (donné dans le panneau supérieur de la figure 5.14a). La formation de défauts n'entrave pas les mesures supplémentaires dépendantes de la tension qui peuvent être effectuées sur des échantillons LaF$_3$.

5.4.2 Dopage des charges en MoSe$_2$ et MoSe$_2$/graphène via le graphène

Comme la monocouche MoSe$_2$ est très sensible au dopage de charge et peut être endommagée à haute densité de charge, les mesures ont d'abord été effectuées dans des régimes de dopage modérés, puis étendues au dopage de trous élevé.

Spectroscopie optique en régime de dopage à charge modérée

Les figures 5.15 et 5.16 montrent les résultats observés sur les régions MoSe$_2$ et MoSe$_2$/graphène (noté MoSe$_2$/Gr ici pour plus de simplicité) lorsque la densité de charge dans le graphène varie de −4,4 V (dopage par trou) à 4 V (dopage électronique) lors d'un balayage de tension typique. En utilisant la méthode pour quantifier la densité de charge dans le graphène à partir de la dépendance en tension des modes Raman décrite dans la section précédente, le CNP peut être estimé à 1,2 V et les densités maximales de trous et d'électrons sont estimées à environ $4 - \times 10^{13}$ cm^{-2} (de manière équivalente, $E_\mathrm{F} = -0{,}8$ eV) et 2×10^{13} cm^{-2} (de manière équivalente, $E_\mathrm{F} = 0{,}65$ eV) à des tensions −4,4 V et 4 V respectivement.

Modifications des spectres PL de MoSe$_2$

Les changements que nous observons dans l'intensité totale de PL et la forme du spectre de

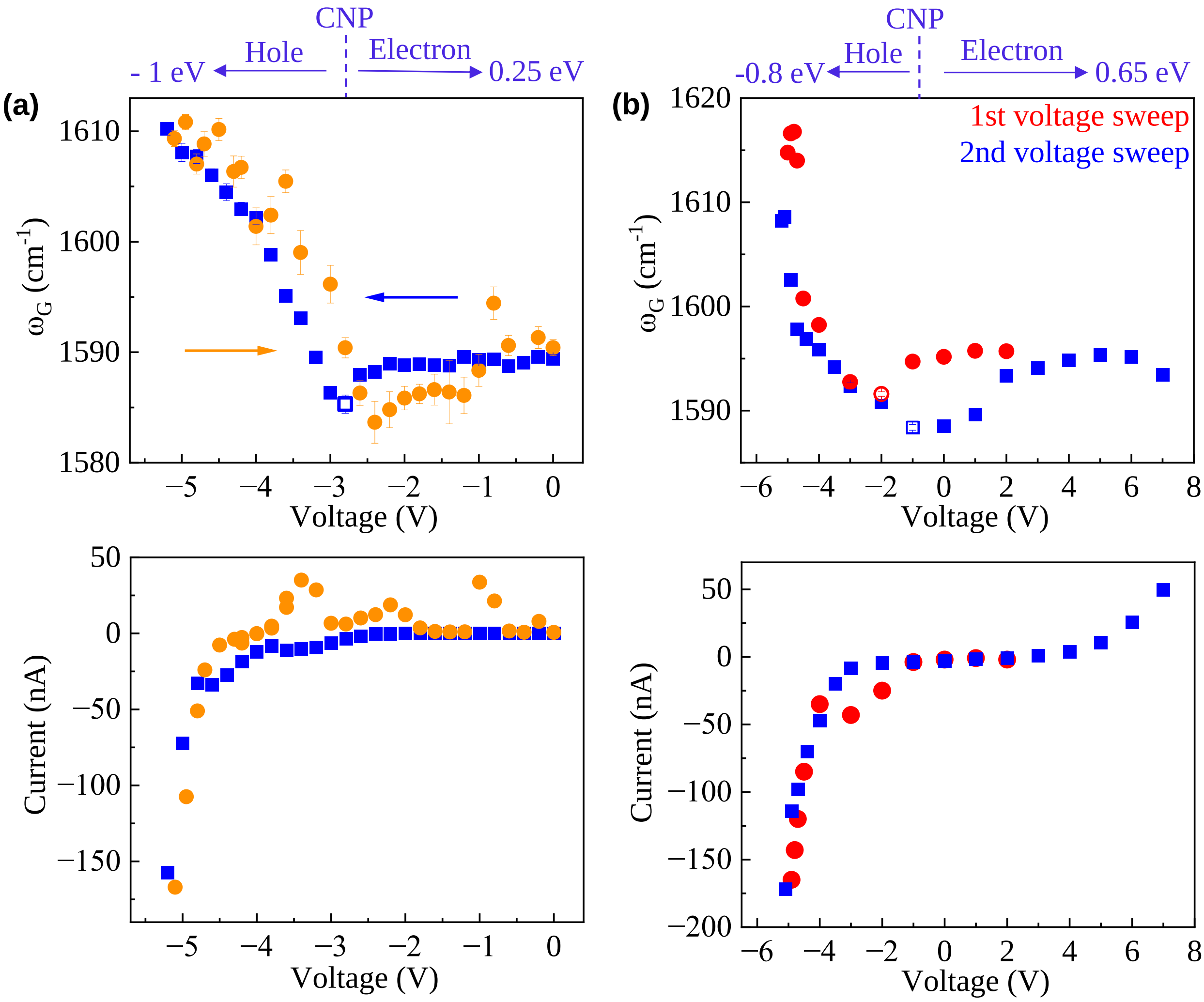

Figure 5.13: Fréquence du mode G en fonction de la tension de grille appliquée dans les panneaux supérieurs pour vérifier (a) la réversibilité du dopage de charge avec les flèches indiquant les directions des balayages de tension et (b) la reproductibilité du dopage de charge en effectuant deux balayages de tension séparés. Les symboles ouverts indiquent les CNP. Les panneaux inférieurs en (a) et (b) montrent le courant de fuite mesuré aux tensions appliquées. Les directions de dopage des trous et des électrons avec les densités de charge maximales atteintes sont également indiquées. Toutes les données mesurées à température ambiante avec une excitation laser de 1,96 eV et une intensité de 600 µW/µm^2 sur (a) l'échantillon C et (b) l'échantillon A.

photoluminescence dans $MoSe_2$ avec une tension appliquée sur le substrat LaF_3 (voir 5.15a, 5.15c, 5.15e, 5.16a, 5.16c and 5.16e) sont similaires à ceux observés par [92]. Une explication possible de ce comportement dans l'intensité de PL de $MoSe_2$ avec un changement de tension de grille appliquée est que, à mesure que la couche est dopée avec une densité électronique croissante, la population de X* augmente en raison de la plus grande population de X^0 convertie dans X*. Comme nous observons l'intensité relative du pic X* par rapport à X^0 augmenter avec la densité électronique, nous pouvons dire que le X* formé ici est un trion chargé négativement. L'intensité globale plus faible de PL sous dopage électronique pourrait être due aux trions favorisant la recombinaison non-radiative ou aux électrons ouvrant des voies de recombinaison non-radiative [90]. Étant donné que l'intensité du pic X* dans nos

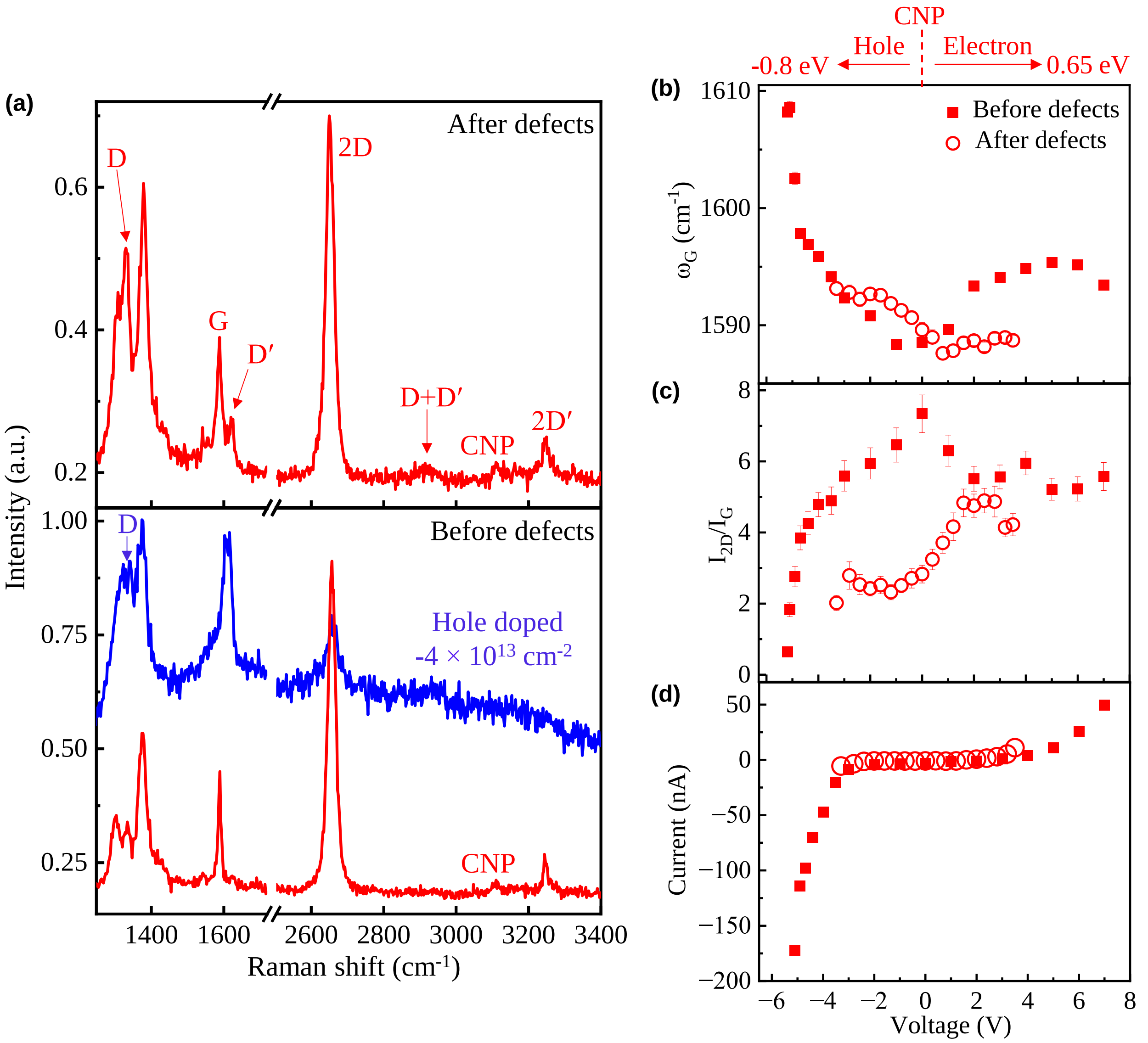

Figure 5.14: (a) Spectres Raman pris au CNP et à l'état fortement dopé par trous avant la création de défauts (panneau inférieur) et au CNP après la création de défauts (panneau supérieur), les modes Raman observés étant mentionnés. La (b) fréquence du mode G, (c) le rapport des intensités du mode 2D au mode G et (d) le courant de fuite en fonction de la tension appliquée pour les mesures effectuées avant et après la formation d'une densité de défauts élevée. Les directions de dopage des trous et des électrons avec les densités de charges maximales atteintes sont également indiquées pour le cas avant création de défauts. Toutes les mesures ont été effectuées à température ambiante avec une excitation laser de 1,96 eV et une intensité de 600 µW/µm^2 sur l'échantillon A.

résultats montre une légère diminution avec la densité électronique, cela suggère que la population électronique ouvre une voie non radiative pour X*. Ainsi, la raison probable de la diminution de l'intensité de PL ici est l'augmentation des taux de recombinaison non-radiative de X^0 et X* à mesure que la densité électronique augmente.

Dans l'autre sens, c'est-à-dire sous dopage par trous, l'augmentation continue de l'intensité de PL, en particulier du pic X^0, peut être comprise comme la couche MoSe$_2$ étant intrinsèquement dopée par des électrons. En utilisant le même mécanisme décrit ci-dessus, l'augmentation de la densité des trous entraîne la neutralisation de la couche, ce qui ferme les voies de recombinaison non-radiatives. Cela augmente l'intensité de PL et rend le pic X^0 plus étroit.

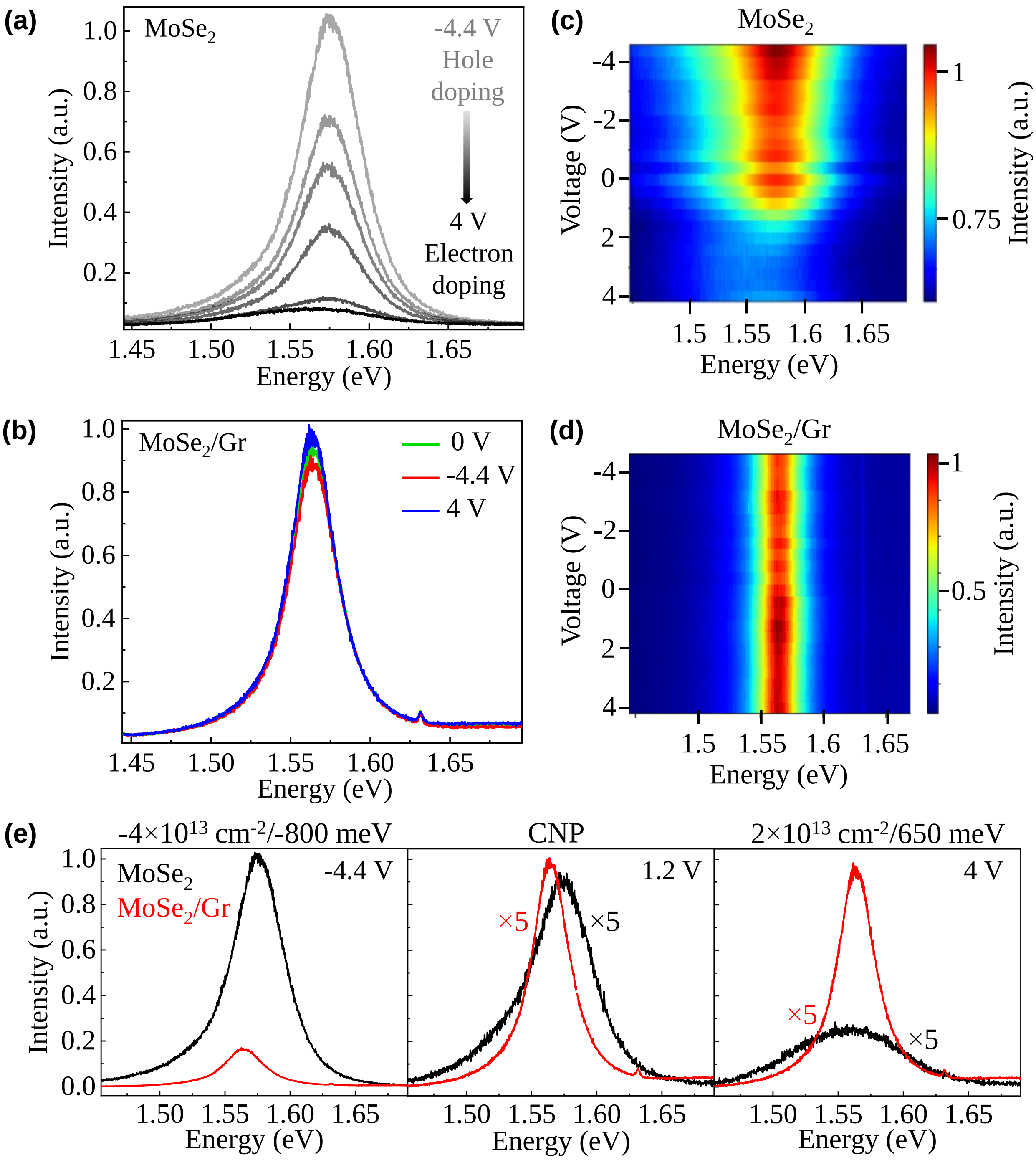

Figure 5.15: (a) Spectres PL de $MoSe_2$ et (b) Spectres PL de $MoSe_2$/Gr avec une tension de grille variable de 4 V à −4,4 V, c'est-à-dire du dopage électron au trou. Courbes de contour des spectres PL de (c) $MoSe_2$ et (d) $MoSe_2$/Gr par rapport à la tension de grille appliquée et (e) spectres PL de $MoSe_2$ et $MoSe_2$/Gr pour différentes densités de charge ou niveaux de Fermi obtenus à partir de mesures de spectroscopie Raman dans le graphène. Toutes les mesures effectuées à température ambiante avec une excitation laser de 1,96 eV et une intensité de 300 µW/µm^2 sur l'échantillon B.

Modifications des spectres PL de MoSe$_2$/Gr

D'un autre côté, les spectres PL de MoSe$_2$/Gr montrent des changements beaucoup plus faibles, même aux extrêmes de l'un ou l'autre type de dopage de charge, que MoSe$_2$ dans ce régime de dopage de charge modéré, comme le montre la figure 5.15e. Mais le tracé de contour de PL de MoSe$_2$/Gr présenté dans 5.15d indique une légère diminution de l'intensité avec le dopage par trous par rapport au CNP. Ces changements dans la région MoSe$_2$/Gr lorsque le graphène est dopé avec des charges nous donnent plus de motivation pour explorer les changements dans le PL de MoSe$_2$/Gr dans la direction de dopage du trou supérieur. Mais comme la couche MoSe$_2$ commence à se dégrader lorsque $n > -4 \times 10^{13}$ cm^{-2}, nous ne discuterons que du régime de fort dopage en trous dopage sur graphène et MoSe$_2$/Gr dans la sous-section suivante.

Spectroscopie optique de MoSe$_2$/graphène en régime de dopage à trous élevés

Réponse Raman des régions de graphène par rapport à la tension appliquée

Le tracé des modes G et 2D du graphène en fonction de la tension de grille sont présentés sur les figures 5.17a et 5.17b, respectivement. La fréquence du pic G, ω_{G} en fonction de la tension appliquée est donné sur la figure 5.17d pour le graphène et le MoSe$_2$/Gr. À partir de là, le CNP est identifié comme étant à $-0{,}75$ V. Pour le cas de MoSe$_2$/Gr, les modes G et 2D peuvent être vus chevauchant les spectres PL dans le panneau de droite de la figure 5.18d. Ainsi, les paramètres pour les modes G et 2D donnés dans la figure 5.17 pour le cas de la région MoSe$_2$/Gr sont extraits après suppression de l'arrière-plan de PL provenant de MoSe$_2$, ce qui entraîne des barres d'erreur comparativement plus grandes. en mode Raman intensités. La figure 5.17e montre que la tendance des changements de ω_{2D} par rapport à la tension appliquée est assez similaire pour le graphène et le MoSe$_2$/Gr, avec une différence entre les valeurs de ω_{2D} à n'importe quelle tension donnée entre les deux régions en raison du écrantage diélectrique [198]. Le tracé de contour du mode 2D (5.17b) et les spectres Raman (5.17c) montrent clairement qu'avec l'augmentation de la tension dans la direction du dopage du trou, l'intensité du mode 2D diminue continuellement. À la fin de ce balayage de tension, lorsque la tension de grille appliquée est de $-4{,}9$ V, l'intensité du mode 2D disparaît (comme le montrent les figures 5.17c, 5.17f et peut également être observé dans le tracé de contour en mode 2D illustré sur la figure 5.17b), qui est la preuve d'une densité de trous suffisamment élevée pour atteindre $E_{\mathrm{F}} \approx -1$ eV (de manière équivalente, $n \approx -6 \times 10^{13}$ cm^{-2}) dans la couche de graphène de référence.

Spectres PL dépendants de la tension de MoSe$_2$/Gr

La figure 5.18b montre le tracé des contours des spectres PL dépendants de la tension de grille de MoSe$_2$/Gr et les spectres PL sont donnés dans les figures 5.18c et 5.18d. La figure 5.18e montre les spectres PL sous une densité de trous élevée.

X^0 en MoSe$_2$/Gr en fonction de la densité de charge dans la couche de graphène de référence

Pour comparer les spectres de PL observés dans la région MoSe$_2$/Gr avec la densité de charge dans le graphène sans perdre les nombreux points dans les données Raman correspondant à

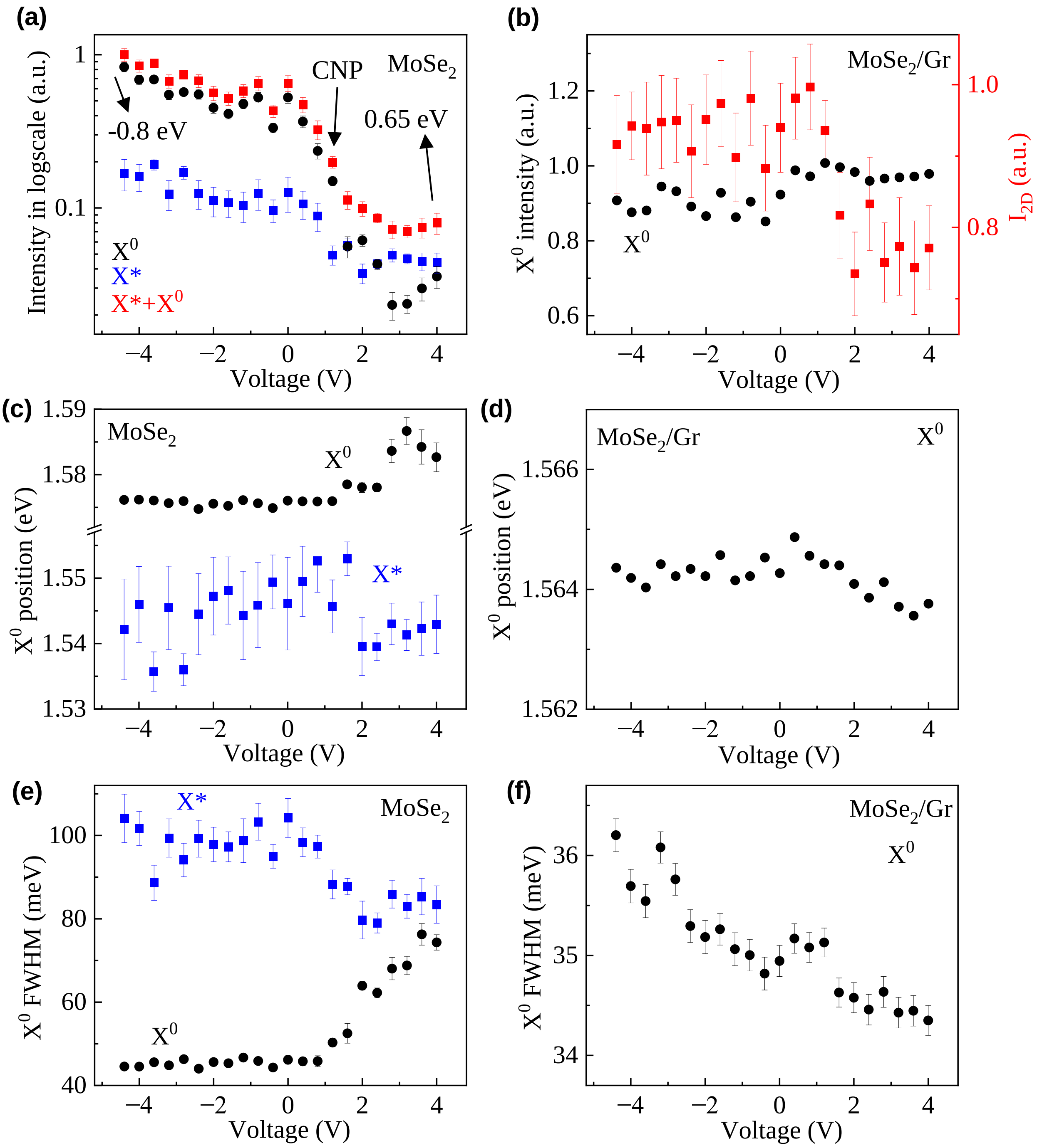

Figure 5.16: (a) L'intensité de PL extraite de $MoSe_2$ pour X^0, X^* et PL total ($X^0 + X^*$) en échelle logarithmique avec CNP marqué et densités maximales d'électrons et de trous observées aux extrémités du balayage de tension obtenu à partir des mesures de spectroscopie Raman dans le graphène (b) l'intensité du pic X^0 et intensité du mode 2D en $MoSe_2$/Gr (c) la position du pic X^0 dans $MoSe_2$ avec la position du pic X^* (d) la position du pic X^0 dans $MoSe_2$/Gr, (e) la largeur du pic X^0 dans $MoSe_2$ avec la largeur du pic X^* et (f) la largeur du pic X^0 dans $MoSe_2$/Gr en fonction de la tension de grille. Toutes les mesures effectuées à température ambiante avec une excitation laser de 1,96 eV et une intensité de 300 µW/µm^2 sur l'échantillon B.

-200 meV $< E_F <$ 200 meV, les paramètres en PL de $MoSe_2$/Gr sont visualisés par rapport à $\Delta\omega_{\mathrm{G}}$ dans la couche de graphène de référence provoquée par la densité de variation de la densité de charge. Les figures 5.19a, 5.19c et 5.19e montrent l'énergie X^0, la largeur du pic X^0 et la position du pic X^0 en fonction de $\Delta\omega_{\mathrm{G}}$ dans le graphène respectivement. Comme l'intensité du mode 2D dans le graphène varie également continûment avec l'augmentation de la tension appliquée et de la densité de charge, l'intensité du pic X^0, la largeur du pic X^0 et la position du pic X^0 sont tracées par rapport à celle-ci dans les figures 5.19b, 5.19d et 5.19f respectivement.

Les spectres PL présentés en fonction de la tension appliquée au-delà de −3,75 V sur la figure 5.18e aident à visualiser clairement les variations de la position du pic X^0 ainsi que d'intensité du pic X^0. L'intensité du pic X^0 montre une diminution continue avec l'augmentation de $\Delta\omega_{\mathrm{G}}$, c'est-à-dire avec l'augmentation de la densité de charge par rapport au CNP, comme on peut le voir sur la figure 5.19a. Une explication de la diminution de l'intensité du pic X^0 réside dans l'augmentation de la densité des charges de porteurs en MoSe$_2$ de MoSe$_2$/Gr avec une densité de charge croissante dans la région de graphène de référence. L'augmentation de la densité des porteurs de charge pourrait ouvrir de plus en plus de canaux de recombinaison non-radiative pour la population X^0, réduisant ainsi l'efficacité de la recombinaison radiative et diminuant ainsi l'intensité du pic X^0 [90]. Aucune signature de X^* n'est visible sur la figure 5.18e. Cela implique que même si la densité de charge est suffisante pour modifier l'intensité de PL, elle n'est pas suffisamment significative pour former une population X^* si grande qu'elle ne peut pas être filtrée par le graphène.

Avec les densités de charge croissantes, la position du pic X^0 dans MoSe$_2$/Gr montre une réduction jusqu'à ce que $\Delta\omega_{\mathrm{G}}$ dans le graphène atteigne la valeur de ≈ 20 cm^{-1}, puis montre un décalage vers le bleu continu (figure 5.19e). La largeur de l'exciton X^0 montre un élargissement avec une densité de trous croissante jusqu'à $\Delta\omega_{\mathrm{G}} \approx 20$ cm^{-1}, puis subit une réduction. Ces changements dans la direction des déplacements de la position du pic X^0 et la largeur du pic X^0 par rapport à un $\Delta\omega_{\mathrm{G}}$ particulier sont assez intrigants et peuvent également être observés dans les figures 5.19d et 5.19f en fonction de l'intensité du mode 2D. Il est important de noter que bien que le courant de fuite commence à descendre au-delà de −4,4 V, ces inflexions observés en position du pic X^0 et la largeur du pic X^0 ne correspondent à aucun changement soudain du courant de fuite observé comme une fonction de la tension de grille appliquée (voir figure 5.18a). Ainsi, ces changements observés ne sont pas dus à des dommages dans l'échantillon ou à un dysfonctionnement dans l'application de la tension de grille.

Au-delà de la valeur seuil de tension appliquée de −4,4 V, les valeurs de ω_{G} en fonction de la tension dans le graphène et MoSe$_2$/Gr (figure 5.17d) commencent à montrer une très petite différence. Le mode 2D dans le graphène de MoSe$_2$/Gr disparaît au-delà de −4,4 V (voir figures 5.18d et 5.17f). Les inflexions observés dans le comportement de la position du pic X^0 et de la largeur du pic X^0 commencent également à −4,4 V. Tout cela indique qu'à mesure que E_{F} s'approche de −1 eV, il y a un trou transfert de MoSe$_2$ en MoSe$_2$/Gr vers le graphène en MoSe$_2$/Gr. Ceci est une preuve que le décalage de bande entre le point Dirac du graphène et le maximum de la bande de valence dans MoSe$_2$ est de ≈ -1 eV.

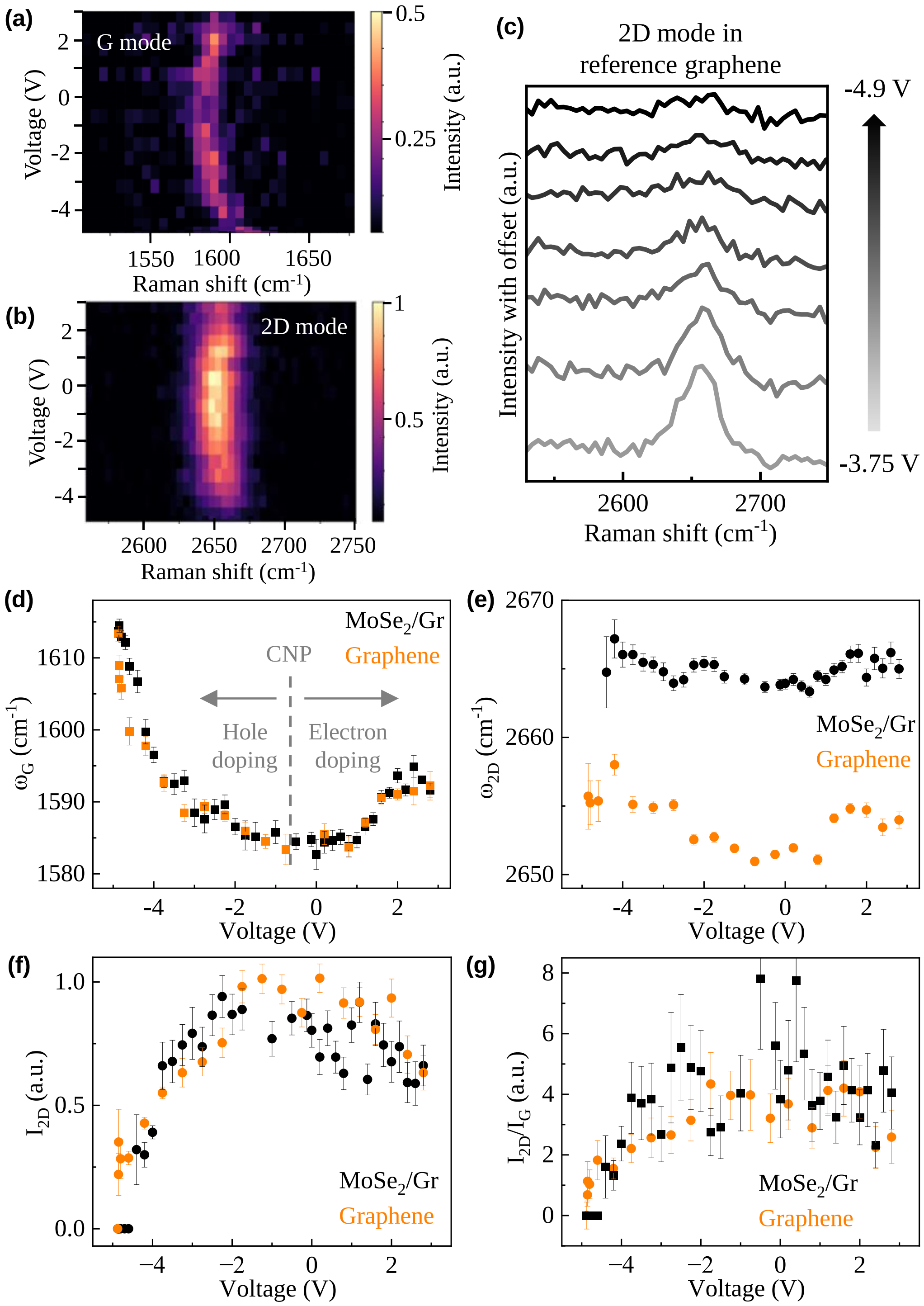

Figure 5.17: Graphiques de comptage des modes (a) G et (b) 2D dans le graphène avec une tension de grille appliquée variable. (c) Mode 2D dans la couche de graphène tracé avec un décalage vertical pour plus de clarté avec une tension appliquée passant de − 3,75 V à − 4,9 V. (d) Fréquence du mode G et (e) Fréquence du mode 2D en fonction de la tension de grille pour $MoSe_2$/Gr et graphène. (d) indique également le CNP dans ce balayage de tension et les directions de dopage des trous et des électrons. (f) Intensité du mode 2D et (g) rapport d'intensité du mode 2D au mode G en $MoSe_2$/Gr et graphène avec tension variable. Toutes les mesures sont effectuées à température ambiante avec une excitation laser de 1,96 eV et une intensité de 100 µW/µm^2 sur l'échantillon G.

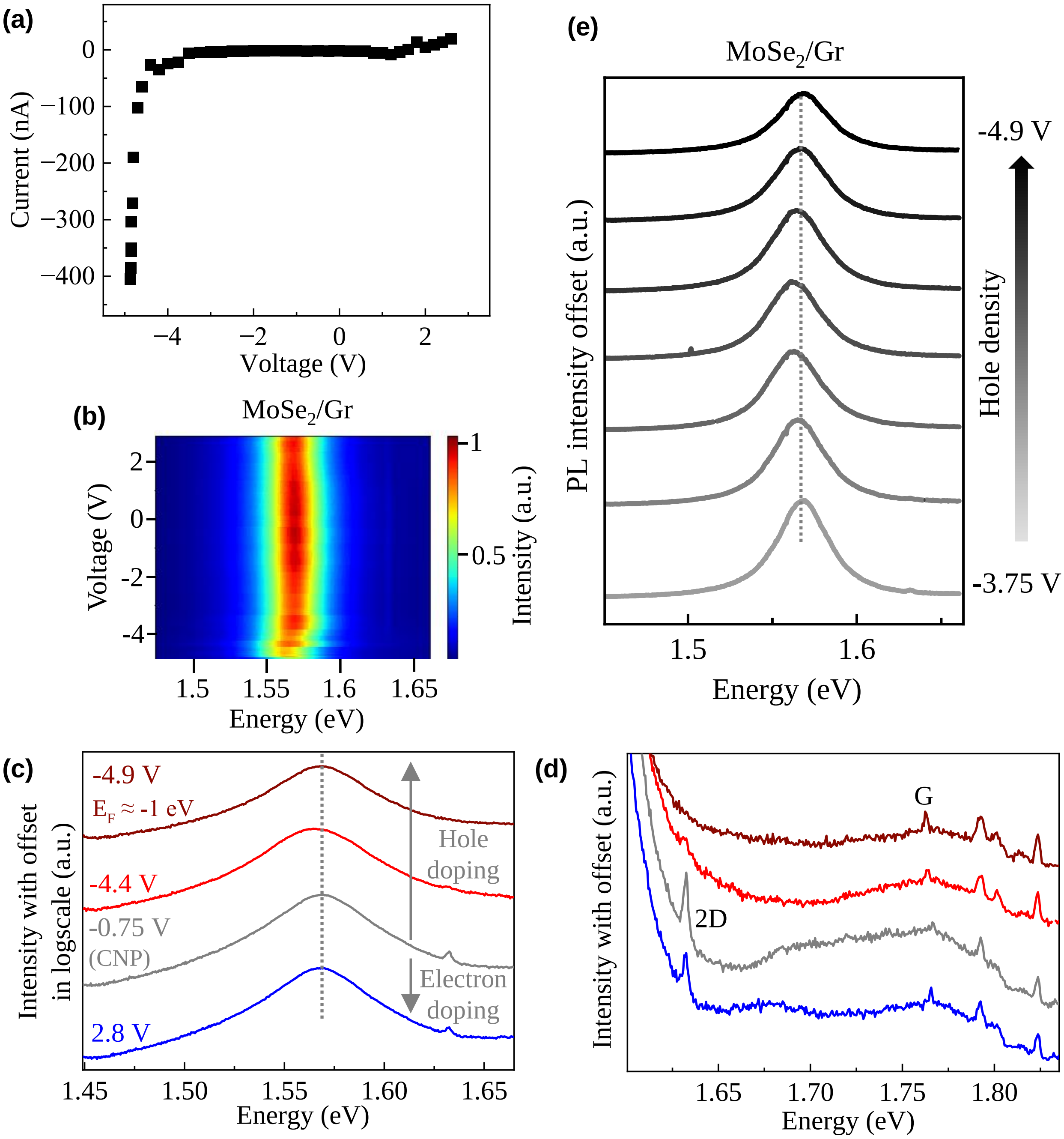

Figure 5.18: (a) Courant de fuite observé aux tensions de grille appliquées (b) Tracé de contour des spectres PL pris sur MoSe$_2$/Gr en fonction de la tension de grille (c) Spectres PL de MoSe$_2$/Gr en échelle logarithmique avec décalage vertical pour plus de clarté mesuré à différentes tensions de grille appliquées montrant X^0 et (d) PL chaud de MoSe$_2$/Gr avec un décalage vertical indiquant également les modes G et 2D. La figure (c) indique également les spectres PL pris au CNP et à −4,9 V ($E_F \approx -1$ eV) ainsi que les directions de dopage de charge, la ligne pointillée indique le Position X^0 chez CNP, le même schéma s'applique pour (d). (e) Spectres PL de MoSe$_2$/Gr tracés en échelle logarithmique pour la tension de grille appliquée passant de −3,75 V à −4,9 V. La ligne pointillée indique la position X^0 pour la tension de grille appliquée de $-3,75$. V. Toutes les mesures effectuées à température ambiante avec une excitation laser de 1,96 eV et une intensité de 100 µW/µm^2 sur l'échantillon G.

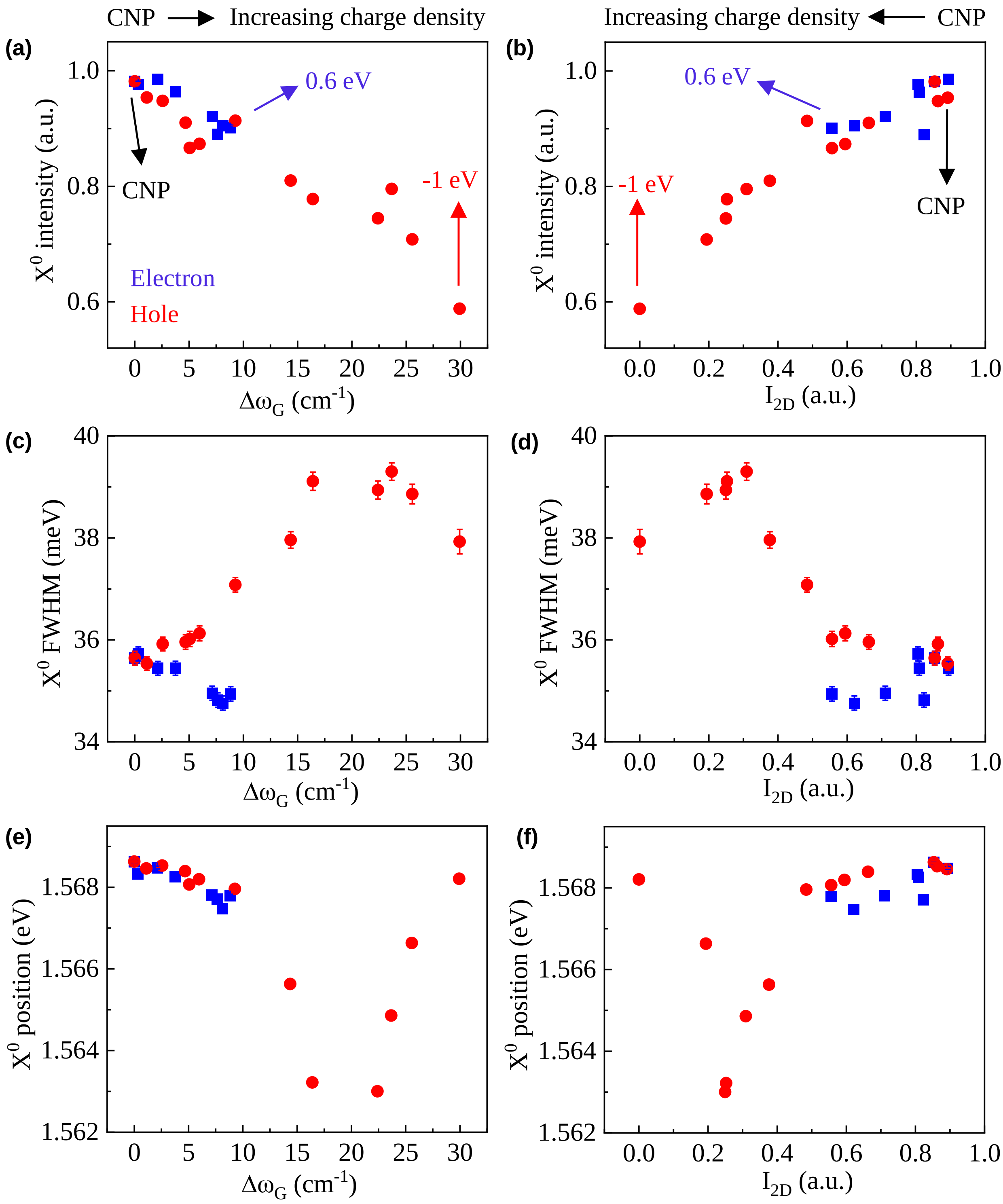

Figure 5.19: (a) l’intensité du pic X^0, (c) la largeur du pic X^0 et (e) position de X^0 observée dans $MoSe_2$/Gr (données dans la figure 4.15) par rapport au changement position relative du mode G par rapport au CNP dans le graphène de référence (données sur la figure 4.14) comme densité de charge est changé. (b) l’intensité du pic de X^0 (d) la largeur du pic X^0 et (f) position de X^0 observée dans $MoSe_2$/Gr en fonction de l’intensité du mode 2D dans la couche de graphène de référence. Les points de données bleus et rouges correspondent respectivement au dopage des électrons et des trous. Le CNP et les instructions sont donnés dans et ci-dessus (a) pour (a), (c) et (e) ; dans et au-dessus de (b) pour (b), (d) et (f).

APPENDIX A

Supplementary information for MoSe$_2$/n-layer graphene heterostructures

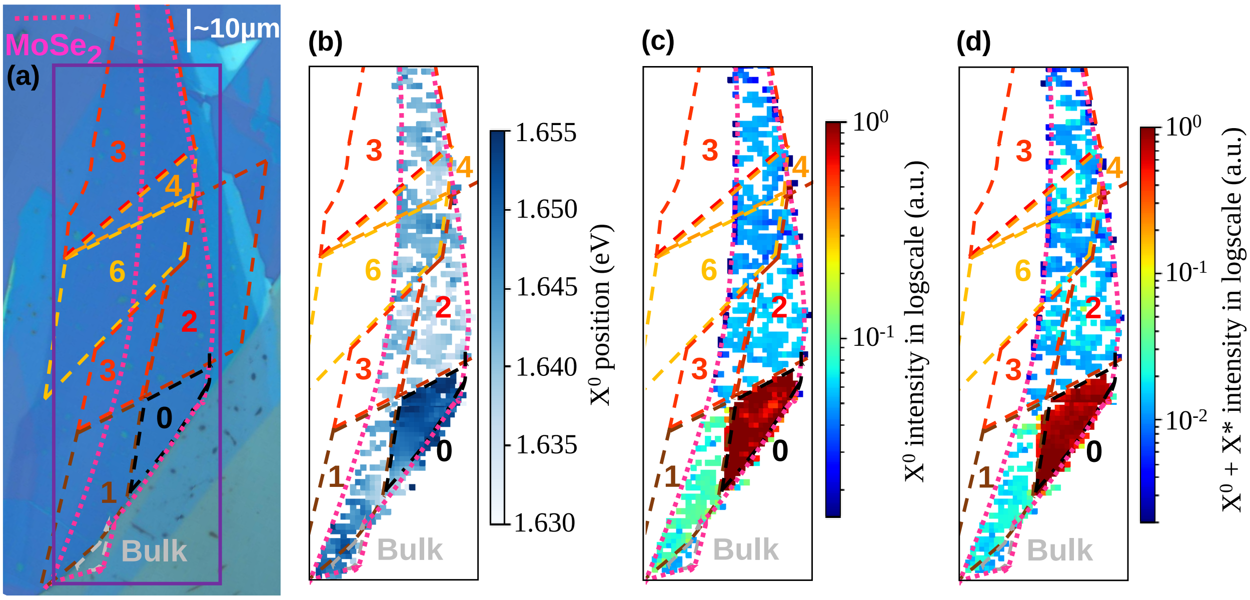

Figure A.1: (a) Optical image of sample 1 with the purple rectangle denoting the area of hyperspectral PL map of MoSe$_2$ taken at 16 K with laser excitation of 2.33 eV and intensity close to 25 µW/µm^2, the extracted parameters: (b) X^0 position (c) X^0 intensity and (d) total PL intensity in logscale. All images show the MoSe$_2$/n-layer graphene regions with dashed contours.

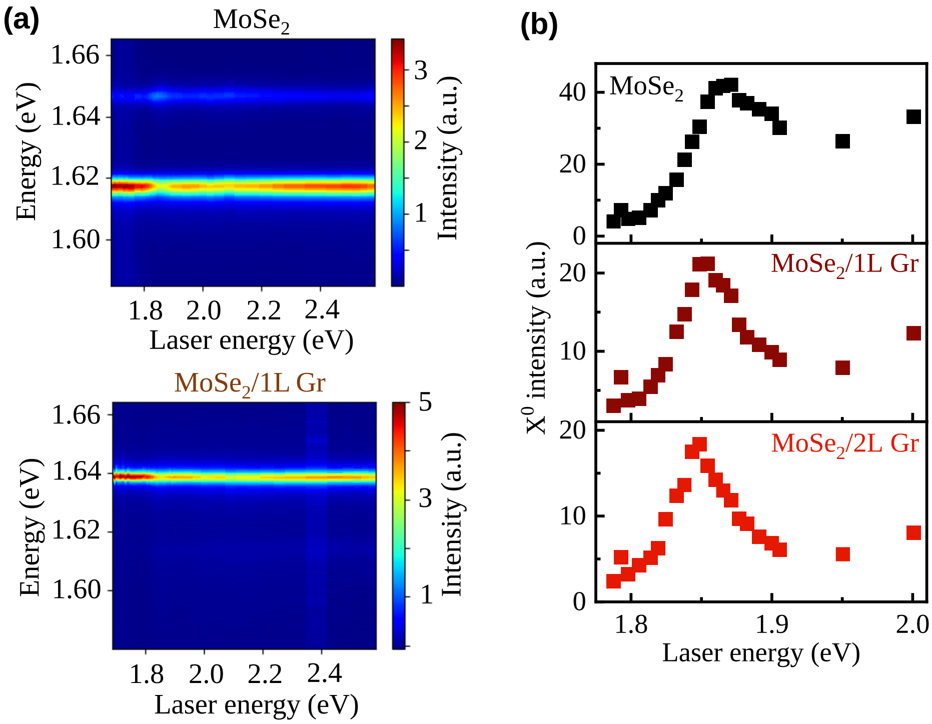

Figure A.2: PLE data on sample 1: (a) Contourplots of PL intensity normalized by the total PL intensity at each incident laser energy for $MoSe_2$ and $MoSe_2$/1L graphene (b) the X^0 intensity of $MoSe_2$, $MoSe_2$/1L graphene and $MoSe_2$/2L graphene with changing laser energy. All measurements are done at 16 K with laser intensity close to 10 µW/µm^2.

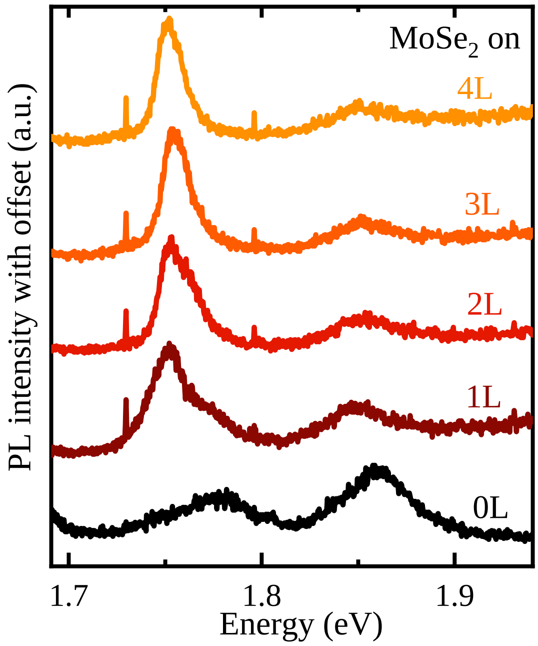

Figure A.3: Hot PL spectra on sample 2: Lineshapes of hot PL spectra of $MoSe_2$/n-layered graphene for n varying from 0 to 4 layers, with vertical offset in intensity. All measurements done at 16 K with laser energy 2.33 eV and intensity close to 80 µW/µm^2.

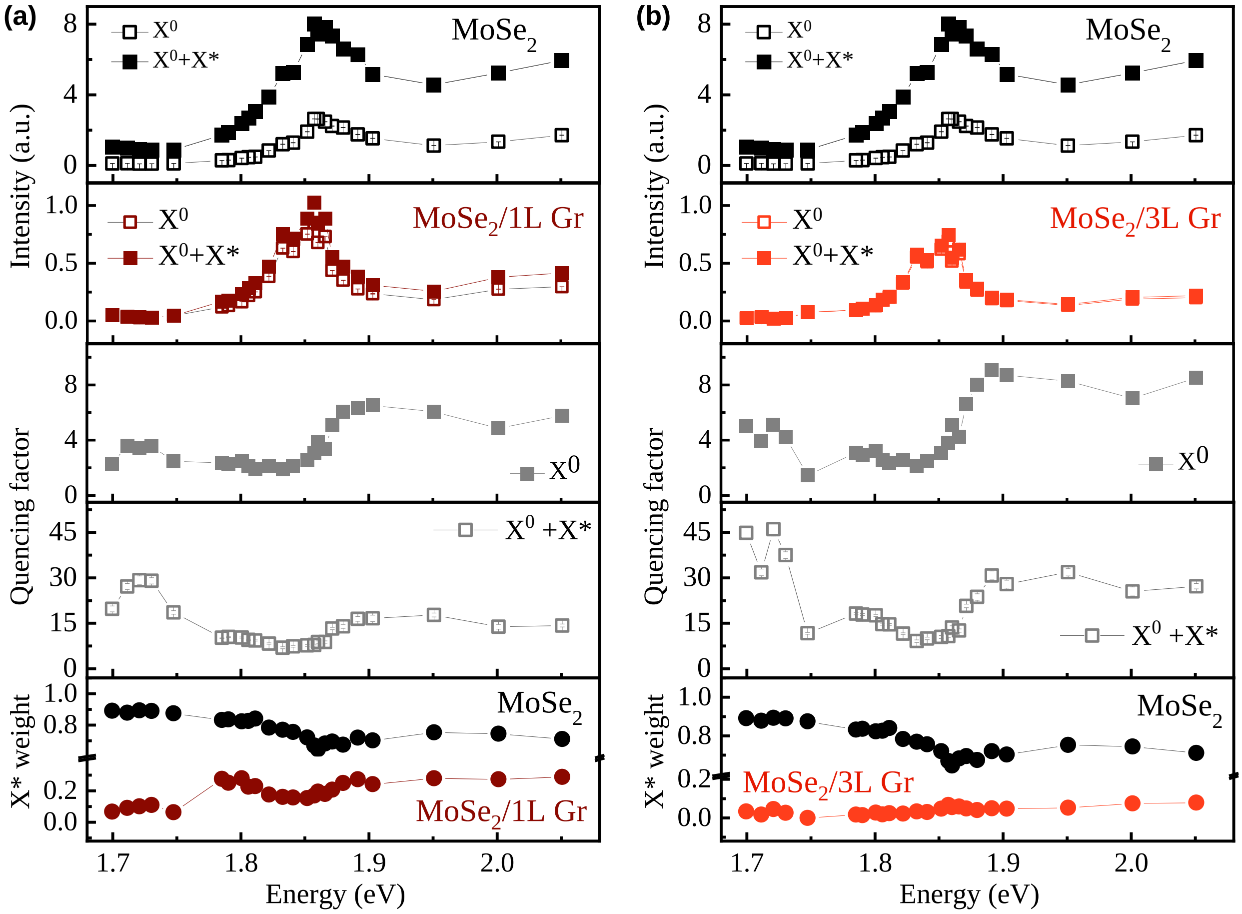

Figure A.4: PLE spectra on sample 2: The panels from top to bottom showing PLE results: the X^0 intensity and total PL intensity, the quenching factors of X^0 and total PL and weight of X* in the PL intensity for (a) $MoSe_2$ and $MoSe_2$/1L graphene and (b) $MoSe_2$ and $MoSe_2$/3L graphene as a function of incident laser energy. The data concerning $MoSe_2$ is same in (a) and (b). All measurements are done at 16 K with laser intensity close to 10 µW/µm^2.

Bibliography

[1] K. S. Novoselov, A. K. Geim, S. V. Morozov, D. Jiang, Y. Zhang, S. V. Dubonos, I. V. Grigorieva, and A. A. Firsov. Electric Field Effect in Atomically Thin Carbon Films. *Science*, 306(5696):666–669, 2004.

[2] A. K. Geim and I. V. Grigorieva. Van der Waals heterostructures. *Nature*, 499(7459):419–425, Jul 2013.

[3] Jia-Sheng Sun, Jin-Wu Jiang, Harold S. Park, and Sulin Zhang. Self-cleaning by harnessing wrinkles in two-dimensional layered crystals. *Nanoscale*, 10:312–318, 2018.

[4] Marco Bernardi, Maurizia Palummo, and Jeffrey C. Grossman. Extraordinary Sunlight Absorption and One Nanometer Thick Photovoltaics Using Two-Dimensional Monolayer Materials. *Nano Letters*, 13(8):3664–3670, 2013. PMID: 23750910.

[5] Jason S Ross, Philip Klement, Aaron M Jones, Nirmal J Ghimire, Jiaqiang Yan, DG Mandrus, Takashi Taniguchi, Kenji Watanabe, Kenji Kitamura, Wang Yao, et al. Electrically tunable excitonic light-emitting diodes based on monolayer WSe_2 p–n junctions. *Nature nanotechnology*, 9(4):268–272, 2014.

[6] Ahmet Avsar, Dmitrii Unuchek, Jiawei Liu, Oriol Lopez Sanchez, Kenji Watanabe, Takashi Taniguchi, Barbaros Özyilmaz, and Andras Kis. Optospintronics in Graphene via Proximity Coupling. *ACS Nano*, 11(11):11678–11686, 2017. PMID: 29068661.

[7] Yunqiu Kelly Luo, Jinsong Xu, Tiancong Zhu, Guanzhong Wu, Elizabeth J. McCormick, Wenbo Zhan, Mahesh R. Neupane, and Roland K. Kawakami. Opto-Valleytronic Spin Injection in Monolayer MoS_2/few-layer Graphene Hybrid Spin Valves. *Nano Letters*, 17(6):3877–3883, 2017. PMID: 28534400.

[8] Mathieu Massicotte, Peter Schmidt, Fabien Vialla, Kevin G Schädler, Antoine Reserbat-Plantey, Kenji Watanabe, Takashi Taniguchi, Klaas-Jan Tielrooij, and Frank HL Koppens. Picosecond photoresponse in van der Waals heterostructures. *Nature nanotechnology*, 11(1):42–46, 2016.

[9] Etienne Lorchat, Luis E. Parra López, Cédric Robert, Delphine Lagarde, Guillaume Froehlicher, Takashi Taniguchi, Kenji Watanabe, Xavier Marie, and Stéphane Berciaud. Filtering the photoluminescence spectra of atomically thin semiconductors with graphene. *Nature Nanotechnology*, 15(4):283–288, Apr 2020.

[10] Burak Guzelturk and Hilmi Volkan Demir. Near-Field Energy Transfer Using Nanoemitters for Optoelectronics. *Advanced Functional Materials*, 26(45):8158–8177, 2016.

[11] Simon M Sze, Yiming Li, and Kwok K Ng. *Physics of semiconductor devices.* John wiley & sons, 2021.

[12] A. H. Castro Neto, F. Guinea, N. M. R. Peres, K. S. Novoselov, and A. K. Geim. The electronic properties of graphene. *Rev. Mod. Phys.*, 81:109–162, Jan 2009.

[13] Guillaume Froehlicher. *Optical spectroscopy of two-dimensional materials : graphene, transition metal dichalcogenides and Van der Waals heterostructures.* PhD thesis, Université de Strasbourg, 2016.

[14] L.M. Malard, M.A. Pimenta, G. Dresselhaus, and M.S. Dresselhaus. Raman spectroscopy in graphene. *Physics Reports*, 473(5):51–87, 2009.

[15] R Saito, G Dresselhaus, and M S Dresselhaus. *Physical Properties of Carbon Nanotubes.* PUBLISHED BY IMPERIAL COLLEGE PRESS AND DISTRIBUTED BY WORLD SCIENTIFIC PUBLISHING CO., 1998.

[16] Jean-Noël Fuchs and Mark Oliver Goerbig. Introduction to the Physical Properties of Graphene. 2008.

[17] Masato Aoki and Hiroshi Amawashi. Dependence of band structures on stacking and field in layered graphene. *Solid State Communications*, 142(3):123–127, 2007.

[18] Kin Fai Mak, Matthew Y. Sfeir, James A. Misewich, and Tony F. Heinz. The evolution of electronic structure in few-layer graphene revealed by optical spectroscopy. *Proceedings of the National Academy of Sciences*, 107(34):14999–15004, 2010.

[19] Kevin R. Knox, Shancai Wang, Alberto Morgante, Dean Cvetko, Andrea Locatelli, Tevfik Onur Mentes, Miguel Angel Niño, Philip Kim, and R. M. Osgood. Spectromicroscopy of single and multilayer graphene supported by a weakly interacting substrate. *Phys. Rev. B*, 78:201408, Nov 2008.

[20] Stéphane Berciaud, Xianglong Li, Han Htoon, Louis E. Brus, Stephen K. Doorn, and Tony F. Heinz. Intrinsic Line Shape of the Raman 2D-Mode in Freestanding Graphene Monolayers. *Nano Letters*, 13(8):3517–3523, 2013. PMID: 23799800.

[21] R. R. Nair, P. Blake, A. N. Grigorenko, K. S. Novoselov, T. J. Booth, T. Stauber, N. M. R. Peres, and A. K. Geim. Fine Structure Constant Defines Visual Transparency of Graphene. *Science*, 320(5881):1308–1308, 2008.

[22] Etienne Lorchat. *Optical spectroscopy of heterostructures based on atomically-thin semiconductors.* PhD thesis, Université de Strasbourg, 05 2019.

[23] W. Kohn. Image of the Fermi Surface in the Vibration Spectrum of a Metal. *Phys. Rev. Lett.*, 2:393–394, May 1959.

[24] S. Piscanec, M. Lazzeri, Francesco Mauri, A. C. Ferrari, and J. Robertson. Kohn Anomalies and Electron-Phonon Interactions in Graphite. *Phys. Rev. Lett.*, 93:185503, Oct 2004.

[25] Peter Y. Yu and Manuel Cardona. *Fundamentals of Semiconductors.* Springer, 3rd edition, 2001.

[26] David J. Griffiths. *Introduction to electrodynamics.* Prentice Hall, 3rd edition, 1999.

[27] Andrea C. Ferrari and Denis M. Basko. Raman spectroscopy as a versatile tool for studying the properties of graphene. *Nature Nanotechnology*, 8:235–246, 04 2013.

[28] Loïc Moczko. *Suspended van der Waals heterostructures: from optical spectroscopy to opto-electro-mechanics.* PhD thesis, Université de Strasbourg, 03 2023.

[29] Giuseppe Grosso and Giuseppe Pastori Parravicini. *Solid State Physics.* Academic Press, London, 2000.

[30] Guillaume Froehlicher and Stéphane Berciaud. Raman spectroscopy of electrochemically gated graphene transistors: Geometrical capacitance, electron-phonon, electron-electron, and electron-defect scattering. *Phys. Rev. B*, 91:205413, May 2015.

[31] Martin Kalbac, Alfonso Reina-Cecco, Hootan Farhat, Jing Kong, Ladislav Kavan, and Mildred S. Dresselhaus. The Influence of Strong Electron and Hole Doping on the Raman Intensity of Chemical Vapor-Deposition Graphene. *ACS Nano*, 4(10):6055–6063, 2010. PMID: 20931995.

[32] Simone Pisana, Michele Lazzeri, Cinzia Casiraghi, Kostya S. Novoselov, A. K. Geim, Andrea C. Ferrari, and Francesco Mauri. Breakdown of the adiabatic Born–Oppenheimer approximation in graphene. *Nature Materials*, 6(3):198–201, Mar 2007.

[33] Michele Lazzeri and Francesco Mauri. Nonadiabatic Kohn Anomaly in a Doped Graphene Monolayer. *Phys. Rev. Lett.*, 97:266407, Dec 2006.

[34] D. M. Basko. Theory of resonant multiphonon Raman scattering in graphene. *Phys. Rev. B*, 78:125418, Sep 2008.

[35] Michele Lazzeri, S. Piscanec, Francesco Mauri, A. C. Ferrari, and J. Robertson. Phonon linewidths and electron-phonon coupling in graphite and nanotubes. *Phys. Rev. B*, 73:155426, Apr 2006.

[36] Chi-Fan Chen, Cheol-Hwan Park, Bryan W Boudouris, Jason Horng, Baisong Geng, Caglar Girit, Alex Zettl, Michael F Crommie, Rachel A Segalman, Steven G Louie, et al. Controlling inelastic light scattering quantum pathways in graphene. *Nature*, 471(7340):617–620, 2011.

[37] D M Basko. Calculation of the Raman G peak intensity in monolayer graphene: role of Ward identities. *New Journal of Physics*, 11(9):095011, sep 2009.

[38] Xue Chen, Sven Reichardt, Miao-Ling Lin, Yu-Chen Leng, Yan Lu, Heng Wu, Rui Mei, Ludger Wirtz, Xin Zhang, Andrea C. Ferrari, and Ping-Heng Tan. Control of Raman Scattering Quantum Interference Pathways in Graphene. *ACS Nano*, 17(6):5956–5962, 2023. PMID: 36897053.

[39] Anindya Das, Simone Pisana, Biswanath Chakraborty, Stefano Piscanec, Srijan K Saha, Umesh V Waghmare, Konstantin S Novoselov, Hulikal R Krishnamurthy, Andre K Geim, Andrea C Ferrari, et al. Monitoring dopants by Raman scattering in an electrochemically top-gated graphene transistor. *Nature nanotechnology*, 3(4):210–215, 2008.

[40] Pedro Venezuela, Michele Lazzeri, and Francesco Mauri. Theory of double-resonant Raman spectra in graphene: Intensity and line shape of defect-induced and two-phonon bands. *Phys. Rev. B*, 84:035433, Jul 2011.

[41] D. M. Basko, S. Piscanec, and A. C. Ferrari. Electron-electron interactions and doping dependence of the two-phonon Raman intensity in graphene. *Phys. Rev. B*, 80:165413, Oct 2009.

[42] Zuzana Melníková-Komínková, Václav Valeš, Otakar Frank, and Martin Kalbáč. Evolution of the Raman 2D' mode in monolayer graphene during electrochemical doping. *Microchemical Journal*, 181:107739, 2022.

[43] Matteo Bruna, Anna K. Ott, Mari Ijäs, Duhee Yoon, Ugo Sassi, and Andrea C. Ferrari. Doping Dependence of the Raman Spectrum of Defected Graphene. *ACS Nano*, 8(7):7432–7441, 2014. PMID: 24960180.

[44] L. G. Cançado, A. Jorio, E. H. Martins Ferreira, F. Stavale, C. A. Achete, R. B. Capaz, M. V. O. Moutinho, A. Lombardo, T. S. Kulmala, and A. C. Ferrari. Quantifying Defects in Graphene via Raman Spectroscopy at Different Excitation Energies. *Nano Letters*, 11(8):3190–3196, 2011. PMID: 21696186.

[45] Junku Liu, Qunqing Li, Yuan Zou, Qingkai Qian, Yuanhao Jin, Guanhong Li, Kaili Jiang, and Shoushan Fan. The Dependence of Graphene Raman D-band on Carrier Density. *Nano Letters*, 13(12):6170–6175, 2013. PMID: 24283411.

[46] PH Tan, WP Han, WJ Zhao, ZH Wu, K Chang, H Wang, YF Wang, N Bonini, N Marzari, Nicola Pugno, et al. The shear mode of multilayer graphene. *Nature materials*, 11(4):294–300, 2012.

[47] Xin Luo, Xin Lu, Chunxiao Cong, Ting Yu, Qihua Xiong, and Su Ying Quek. Stacking sequence determines Raman intensities of observed interlayer shear modes in 2D layered materials–A general bond polarizability model. *Scientific reports*, 5(1):14565, 2015.

[48] Chun Hung Lui, Zhipeng Ye, Courtney Keiser, Eduardo B. Barros, and Rui He. Stacking-dependent shear modes in trilayer graphene. *Applied Physics Letters*, 106(4), January 2015.

[49] Yun Hwangbo, Choong-Kwang Lee, Alexander E. Mag-Isa, Jae-Won Jang, Hak-Joo Lee, Soon-Bok Lee, Seong-Su Kim, and Jae-Hyun Kim. Interlayer non-coupled optical properties for determining the number of layers in arbitrarily stacked multilayer graphenes. *Carbon*, 77:454–461, 2014.

[50] K. S. Novoselov, D. Jiang, F. Schedin, T. J. Booth, V. V. Khotkevich, S. V. Morozov, and A. K. Geim. Two-dimensional atomic crystals. *Proceedings of the National Academy of Sciences*, 102(30):10451–10453, 2005.

[51] Andrea Splendiani, Liang Sun, Yuanbo Zhang, Tianshu Li, Jonghwan Kim, Chi-Yung Chim, Giulia Galli, and Feng Wang. Emerging Photoluminescence in Monolayer MoS_2. *Nano Letters*, 10(4):1271–1275, 2010.

[52] Kin Fai Mak, Changgu Lee, James Hone, Jie Shan, and Tony F. Heinz. Atomically Thin MoS_2: A New Direct-Gap Semiconductor. *Phys. Rev. Lett.*, 105:136805, Sep 2010.

[53] Yajing Sun, Dong Wang, and Zhigang Shuai. Indirect-to-Direct Band Gap Crossover in Few-Layer Transition Metal Dichalcogenides: A Theoretical Prediction. *The Journal of Physical Chemistry C*, 120(38):21866–21870, 2016.

[54] Z. Y. Zhu, Y. C. Cheng, and U. Schwingenschlögl. Giant spin-orbit-induced spin splitting in two-dimensional transition-metal dichalcogenide semiconductors. *Phys. Rev. B*, 84:153402, Oct 2011.

[55] J. Ribeiro-Soares, R. M. Almeida, E. B. Barros, P. T. Araujo, M. S. Dresselhaus, L. G. Cançado, and A. Jorio. Group theory analysis of phonons in two-dimensional transition metal dichalcogenides. *Phys. Rev. B*, 90:115438, Sep 2014.

[56] Philipp Tonndorf, Robert Schmidt, Philipp Böttger, Xiao Zhang, Janna Börner, Andreas Liebig, Manfred Albrecht, Christian Kloc, Ovidiu Gordan, Dietrich RT Zahn, et al. Photoluminescence emission and Raman response of monolayer MoS_2, $MoSe_2$, and WSe_2. *Optics express*, 21(4):4908–4916, 2013.

[57] Gang Wang, Alexey Chernikov, Mikhail M. Glazov, Tony F. Heinz, Xavier Marie, Thierry Amand, and Bernhard Urbaszek. Colloquium: Excitons in atomically thin transition metal dichalcogenides. *Rev. Mod. Phys.*, 90:021001, Apr 2018.

[58] Won Seok Yun, S. W. Han, Soon Cheol Hong, In Gee Kim, and J. D. Lee. Thickness and strain effects on electronic structures of transition metal dichalcogenides: 2H-MX_2 semiconductors (M = Mo, W; X = S, Se, Te). *Phys. Rev. B*, 85:033305, Jan 2012.

[59] Di Xiao, Gui-Bin Liu, Wanxiang Feng, Xiaodong Xu, and Wang Yao. Coupled Spin and Valley Physics in Monolayers of MoS_2 and Other Group-VI Dichalcogenides. *Phys. Rev. Lett.*, 108:196802, May 2012.

[60] Andor Kormányos, Viktor Zólyomi, Neil D. Drummond, and Guido Burkard. Spin-Orbit Coupling, Quantum Dots, and Qubits in Monolayer Transition Metal Dichalcogenides. *Phys. Rev. X*, 4:011034, Mar 2014.

[61] K. Kośmider, J. W. González, and J. Fernández-Rossier. Large spin splitting in the conduction band of transition metal dichalcogenide monolayers. *Phys. Rev. B*, 88:245436, Dec 2013.

[62] Luis Enrique Parra Lòpez. *Tailoring the luminescence of atomically-thin semiconductors at the sub-nanometer scale.* PhD thesis, Université de Strasbourg, 07 2021.

[63] Alexey Chernikov, Timothy C. Berkelbach, Heather M. Hill, Albert Rigosi, Yilei Li, Burak Aslan, David R. Reichman, Mark S. Hybertsen, and Tony F. Heinz. Exciton Binding Energy and Nonhydrogenic Rydberg Series in Monolayer WS_2. *Phys. Rev. Lett.*, 113:076802, Aug 2014.

[64] Samuel Brem, Malte Selig, Gunnar Berghaeuser, and Ermin Malic. Exciton relaxation cascade in two-dimensional transition metal dichalcogenides. *Scientific reports*, 8(1):1–8, 2018.

[65] Claus F. Klingshirn. *Semiconductor Optics.* Springer, 4th edition, 2012.

[66] Miguel M Ugeda, Aaron J Bradley, Su-Fei Shi, Felipe H Da Jornada, Yi Zhang, Diana Y Qiu, Wei Ruan, Sung-Kwan Mo, Zahid Hussain, Zhi-Xun Shen, et al. Giant bandgap renormalization and excitonic effects in a monolayer transition metal dichalcogenide semiconductor. *Nature materials*, 13(12):1091–1095, 2014.

[67] A. Molina-Sánchez and L. Wirtz. Phonons in single-layer and few-layer MoS_2 and WS_2. *Phys. Rev. B*, 84:155413, Oct 2011.

[68] Timothy C. Berkelbach, Mark S. Hybertsen, and David R. Reichman. Theory of neutral and charged excitons in monolayer transition metal dichalcogenides. *Phys. Rev. B*, 88:045318, Jul 2013.

[69] J. S. Blakemore. Semiconducting and other major properties of gallium arsenide. *Journal of Applied Physics*, 53(10):R123–R181, 1982.

[70] Pierluigi Cudazzo, Ilya V. Tokatly, and Angel Rubio. Dielectric screening in two-dimensional insulators: Implications for excitonic and impurity states in graphane. *Phys. Rev. B*, 84:085406, Aug 2011.

[71] Jack Deslippe, Mario Dipoppa, David Prendergast, Marcus V. O. Moutinho, Rodrigo B. Capaz, and Steven G. Louie. Electron-Hole Interaction in Carbon Nanotubes: Novel Screening and Exciton Excitation Spectra. *Nano Letters*, 9(4):1330–1334, 2009.

[72] L. V. Keldysh. Coulomb interaction in thin semiconductor and semimetal films. *ZhETF Pisma Redaktsiiu*, 29:716, June 1979.

[73] Jason S. Ross, Sanfeng Wu, Hongyi Yu, Nirmal J. Ghimire, Aaron M. Jones, Grant Aivazian, Jiaqiang Yan, David G. Mandrus, Di Xiao, Wang Yao, and Xiaodong Xu. Electrical control of neutral and charged excitons in a monolayer semiconductor. *Nature Communications*, 4(1474), 2 2013.

[74] Kin Fai Mak, Keliang He, Changgu Lee, Gwan Hyoung Lee, James Hone, Tony F. Heinz, and Jie Shan. Tightly bound trions in monolayer MoS_2. *Nature Materials*, 12(3):207–211, Mar 2013.

[75] Kevin O'Donnell and X Chen. Temperature Dependence of Semiconductor Band Gaps. *Applied Physics Letters*, 58:2924 – 2926, 07 1991.

[76] Y.P. Varshni. Temperature dependence of the energy gap in semiconductors. *Physica*, 34(1):149 – 154, 1967.

[77] F. Cadiz, E. Courtade, C. Robert, G. Wang, Y. Shen, H. Cai, T. Taniguchi, K. Watanabe, H. Carrere, D. Lagarde, M. Manca, T. Amand, P. Renucci, S. Tongay, X. Marie, and B. Urbaszek. Excitonic Linewidth Approaching the Homogeneous Limit in mos_2-Based van der Waals Heterostructures. *Phys. Rev. X*, 7:021026, May 2017.

[78] Malte Selig, Gunnar Berghäuser, Archana Raja, Philipp Nagler, Christian Schüller, Tony F Heinz, Tobias Korn, Alexey Chernikov, Ermin Malic, and Andreas Knorr. Excitonic linewidth and coherence lifetime in monolayer transition metal dichalcogenides. *Nature communications*, 7(1):13279, 2016.

[79] C. Robert, D. Lagarde, F. Cadiz, G. Wang, B. Lassagne, T. Amand, A. Balocchi, P. Renucci, S. Tongay, B. Urbaszek, and X. Marie. Exciton radiative lifetime in transition metal dichalcogenide monolayers. *Phys. Rev. B*, 93:205423, May 2016.

[80] Lucio Claudio Andreani, Francesco Tassone, and Franco Bassani. Radiative lifetime of free excitons in quantum wells. *Solid State Communications*, 77(9):641–645, 1991.

[81] Galan Moody, Chandriker Kavir Dass, Kai Hao, Chang-Hsiao Chen, Lain-Jong Li, Akshay Singh, Kha Tran, Genevieve Clark, Xiaodong Xu, Gunnar Berghäuser, et al. Intrinsic homogeneous linewidth and broadening mechanisms of excitons in monolayer transition metal dichalcogenides. *Nature communications*, 6(1):8315, 2015.

[82] Nardeep Kumar, Qiannan Cui, Frank Ceballos, Dawei He, Yongsheng Wang, and Hui Zhao. Exciton-exciton annihilation in $MoSe_2$ monolayers. *Phys. Rev. B*, 89:125427, Mar 2014.

[83] Yiling Yu, Yifei Yu, Chao Xu, Andy Barrette, Kenan Gundogdu, and Linyou Cao. Fundamental limits of exciton-exciton annihilation for light emission in transition metal dichalcogenide monolayers. *Phys. Rev. B*, 93:201111, May 2016.

[84] Guillaume Froehlicher, Etienne Lorchat, and Stéphane Berciaud. Direct versus indirect band gap emission and exciton-exciton annihilation in atomically thin molybdenum ditelluride $MoTe_2$. *Physical Review B*, 94, 02 2016.

[85] Haining Wang, Changjian Zhang, Weimin Chan, Christina Manolatou, Sandip Tiwari, and Farhan Rana. Radiative lifetimes of excitons and trions in monolayers of the metal dichalcogenide MoS_2. *Phys. Rev. B*, 93:045407, Jan 2016.

[86] G. Wang, L. Bouet, D. Lagarde, M. Vidal, A. Balocchi, T. Amand, X. Marie, and B. Urbaszek. Valley dynamics probed through charged and neutral exciton emission in monolayer WSe_2. *Phys. Rev. B*, 90:075413, Aug 2014.

[87] Andrey Sushko, Kristiaan De Greve, Madeleine Phillips, Bernhard Urbaszek, Andrew Y. Joe, Kenji Watanabe, Takashi Taniguchi, Alexander L. Efros, C. Stephen Hellberg, Hongkun Park, Philip Kim, and Mikhail D. Lukin. Asymmetric photoelectric effect: Auger-assisted hot hole photocurrents in transition metal dichalcogenides. *Nanophotonics*, 10(1):105–113, 2021.

[88] Bumho Kim, Yue Luo, Daniel Rhodes, Yusong Bai, Jue Wang, Song Liu, Abraham Jordan, Baili Huang, Zhaochen Li, Takashi Taniguchi, Kenji Watanabe, Jonathan Owen, Stefan Strauf, Katayun Barmak, Xiaoyang Zhu, and James Hone. Free Trions with Near-Unity Quantum Yield in Monolayer $MoSe_2$. *ACS Nano*, 16(1):140–147, 2022. PMID: 34935357.

[89] Bo Wen, Yi Zhu, Didit Yudistira, Andreas Boes, Linglong Zhang, Tanju Yidirim, Boqing Liu, Han Yan, Xueqian Sun, Yu Zhou, Yunzhou Xue, Yupeng Zhang, Lan Fu, Arnan Mitchell, Han Zhang, and Yuerui Lu. Ferroelectric-Driven Exciton and Trion Modulation in Monolayer Molybdenum and Tungsten Diselenides. *ACS Nano*, 13(5):5335–5343, 2019. PMID: 31017755.

[90] Der-Hsien Lien, Shiekh Zia Uddin, Matthew Yeh, Matin Amani, Hyungjin Kim, Joel W. Ager, Eli Yablonovitch, and Ali Javey. Electrical suppression of all nonradiative recombination pathways in monolayer semiconductors. *Science*, 364(6439):468–471, 2019.

[91] Kyounghwan Kim, Stefano Larentis, Babak Fallahazad, Kayoung Lee, Jiamin Xue, David C. Dillen, Chris M. Corbet, and Emanuel Tutuc. Band Alignment in WSe_2–Graphene Heterostructures. *ACS Nano*, 9(4):4527–4532, 2015. PMID: 25768037.

[92] Yuze Meng, Tianmeng Wang, Chenhao Jin, Zhipeng Li, Shengnan Miao, Zhen Lian, Takashi Taniguchi, Kenji Watanabe, Fengqi Song, and Su-Fei Shi. Electrical switching between exciton dissociation to exciton funneling in $MoSe_2/WS_2$ heterostructure. *Nature Communications*, 11(1):2640, 2020.

[93] Yang Li, Jing-Kai Qin, Cheng-Yan Xu, Jian Cao, Zhao-Yuan Sun, Lai-Peng Ma, Ping An Hu, Wencai Ren, and Liang Zhen. Electric Field Tunable Interlayer Relaxation Process and Interlayer Coupling in WSe_2/Graphene Heterostructures. *Advanced Functional Materials*, 26(24):4319–4328, 2016.

[94] H Judith Milledge, E Nave, and FH Weller. Transformation of cubic boron nitride to a graphitic form of hexagonal boron nitride. *Nature*, 184(4687):715–715, 1959.

[95] Darshana Wickramaratne, Leigh Weston, and Chris G. Van de Walle. Monolayer to Bulk Properties of Hexagonal Boron Nitride. *The Journal of Physical Chemistry C*, 122(44):25524–25529, 2018.

[96] G. Cassabois, P. Valvin, and B. Gil. Hexagonal boron nitride is an indirect bandgap semiconductor. *Nature Photonics*, 10(4):262–266, Apr 2016.

[97] C. E. Ekuma, V. Dobrosavljević, and D. Gunlycke. First-Principles-Based Method for Electron Localization: Application to Monolayer Hexagonal Boron Nitride. *Phys. Rev. Lett.*, 118:106404, Mar 2017.

[98] Jiamin Xue, Javier Sanchez-Yamagishi, Danny Bulmash, Philippe Jacquod, Aparna Deshpande, K Watanabe, T Taniguchi, Pablo Jarillo-Herrero, and Brian J LeRoy. Scanning tunnelling microscopy and spectroscopy of ultra-flat graphene on hexagonal boron nitride. *Nature materials*, 10(4):282–285, 2011.

[99] Kailiang Zhang, Yulin Feng, Fang Wang, Zhengchun Yang, and John Wang. Two dimensional hexagonal boron nitride (2D-hBN): synthesis, properties and applications. *J. Mater. Chem. C*, 5:11992–12022, 2017.

[100] Lu Hua Li, Jiri Cervenka, Kenji Watanabe, Takashi Taniguchi, and Ying Chen. Strong Oxidation Resistance of Atomically Thin Boron Nitride Nanosheets. *ACS Nano*, 8(2):1457–1462, 2014. PMID: 24400990.

[101] Tania Roy, Mahmut Tosun, Jeong Seuk Kang, Angada B. Sachid, Sujay B. Desai, Mark Hettick, Chenming C. Hu, and Ali Javey. Field-Effect Transistors Built from All Two-Dimensional Material Components. *ACS Nano*, 8(6):6259–6264, 2014. PMID: 24779528.

[102] Régis Decker, Yang Wang, Victor W. Brar, William Regan, Hsin-Zon Tsai, Qiong Wu, William Gannett, Alex Zettl, and Michael F. Crommie. Local Electronic Properties of Graphene on a BN Substrate via Scanning Tunneling Microscopy. *Nano Letters*, 11(6):2291–2295, 2011. PMID: 21553853.

[103] Cory R Dean, Andrea F Young, Inanc Meric, Chris Lee, Lei Wang, Sebastian Sorgenfrei, Kenji Watanabe, Takashi Taniguchi, Phillip Kim, Kenneth L Shepard, et al. Boron nitride substrates for high-quality graphene electronics. *Nature nanotechnology*, 5(10):722–726, 2010.

[104] Luis Enrique Parra López, Loïc Moczko, Joanna Wolff, Aditya Singh, Etienne Lorchat, Michelangelo Romeo, Takashi Taniguchi, Kenji Watanabe, and Stéphane Berciaud. Single- and narrow-line photoluminescence in a boron nitride-supported $MoSe_2$/graphene heterostructure. *Comptes Rendus. Physique*, 22(S4):77–88, 2021.

[105] Archana Raja, Lutz Waldecker, Jonas Zipfel, Yeongsu Cho, Samuel Brem, Jonas D Ziegler, Marvin Kulig, Takashi Taniguchi, Kenji Watanabe, Ermin Malic, et al. Dielectric disorder in two-dimensional materials. *Nature nanotechnology*, 14(9):832–837, 2019.

[106] Yuto Anzai, Mahito Yamamoto, Shingo Genchi, Kenji Watanabe, Takashi Taniguchi, Shuhei Ichikawa, Yasufumi Fujiwara, and Hidekazu Tanaka. Broad range thickness identification of hexagonal boron nitride by colors. *Applied Physics Express*, 12(5):055007, apr 2019.

[107] Dheeraj Golla, Kanokporn Chattrakun, Kenji Watanabe, Takashi Taniguchi, Brian J. LeRoy, and Arvinder Sandhu. Optical thickness determination of hexagonal boron nitride flakes. *Applied Physics Letters*, 102(16):161906, 04 2013.

[108] Cedric Robert, Sangjun Park, Fabian Cadiz, Laurent Lombez, Lei Ren, Hans Tornatzky, Alistair Rowe, Daniel Paget, Fausto Sirotti, Min Yang, et al. Spin/valley pumping of resident electrons in WSe_2 and WS_2 monolayers. *Nature communications*, 12(1):5455, 2021.

[109] Sotirios Papadopoulos, Lujun Wang, Takashi Taniguchi, Kenji Watanabe, and Lukas Novotny. Energy transfer from tunneling electrons to excitons, 2022.

[110] David Tebbe, Marc Schütte, K. Watanabe, T. Taniguchi, Christoph Stampfer, Bernd Beschoten, and Lutz Waldecker. Distance Dependence of the Energy Transfer Mechanism in WS_2-Graphene Heterostructures. *Phys. Rev. Lett.*, 132:196902, May 2024.

[111] Xue Liu, Jiajie Pei, Zehua Hu, Weijie Zhao, Sheng Liu, Mohamed-Raouf Amara, Kenji Watanabe, Takashi Taniguchi, Han Zhang, and Qihua Xiong. Manipulating Charge and Energy Transfer between 2D Atomic Layers via Heterostructure Engineering. *Nano Letters*, 20(7):5359–5366, 2020. PMID: 32543201.

[112] François Federspiel, Guillaume Froehlicher, Michel Nasilowski, Silvia Pedetti, Ather Mahmood, Bernard Doudin, Serin Park, Jeong-O Lee, David Halley, Benoît Dubertret, Pierre Gilliot, and Stéphane Berciaud. Distance Dependence of the Energy Transfer Rate from a Single Semiconductor Nanostructure to Graphene. *Nano Letters*, 15(2):1252–1258, 2015. PMID: 25607231.

[113] L. Gaudreau, K. J. Tielrooij, G. E. D. K. Prawiroatmodjo, J. Osmond, F. J. García de Abajo, and F. H. L. Koppens. Universal Distance-Scaling of Nonradiative Energy Transfer to Graphene. *Nano Letters*, 13(5):2030–2035, 2013. PMID: 23488979.

[114] Jiye Lee, Wei Bao, Long Ju, P. James Schuck, Feng Wang, and Alexander Weber-Bargioni. Switching Individual Quantum Dot Emission through Electrically Controlling Resonant Energy Transfer to Graphene. *Nano Letters*, 14(12):7115–7119, 2014. PMID: 25383700.

[115] H. H. Fang, B. Han, C. Robert, M. A. Semina, D. Lagarde, E. Courtade, T. Taniguchi, K. Watanabe, T. Amand, B. Urbaszek, M. M. Glazov, and X. Marie. Control of the Exciton Radiative Lifetime in van der Waals Heterostructures. *Phys. Rev. Lett.*, 123:067401, Aug 2019.

[116] Christian Schneider, Mikhail M Glazov, Tobias Korn, Sven Höfling, and Bernhard Urbaszek. Two-dimensional semiconductors in the regime of strong light-matter coupling. *Nature communications*, 9(1):2695, 2018.

[117] You Zhou, Giovanni Scuri, Jiho Sung, Ryan J. Gelly, Dominik S. Wild, Kristiaan De Greve, Andrew Y. Joe, Takashi Taniguchi, Kenji Watanabe, Philip Kim, Mikhail D. Lukin, and Hongkun Park. Controlling Excitons in an Atomically Thin Membrane with a Mirror. *Phys. Rev. Lett.*, 124:027401, Jan 2020.

[118] Christopher Rogers, Dodd Gray, Nathan Bogdanowicz, Takashi Taniguchi, Kenji Watanabe, and Hideo Mabuchi. Coherent feedback control of two-dimensional excitons. *Phys. Rev. Res.*, 2:012029, Jan 2020.

[119] Emmanuel Rosencher and Borge Vinter. *Optoelectronics*. Cambridge University Press, 2002.

[120] Debora Pierucci, Hugo Henck, Jose Avila, Adrian Balan, Carl H. Naylor, Gilles Patriarche, Yannick J. Dappe, Mathieu G. Silly, Fausto Sirotti, A. T. Charlie Johnson, Maria C. Asensio, and Abdelkarim Ouerghi. Band Alignment and Minigaps in Monolayer MoS_2-Graphene van der Waals Heterostructures. *Nano Letters*, 16(7):4054–4061, 2016. PMID: 27281693.

[121] Horacio Coy Diaz, José Avila, Chaoyu Chen, Rafik Addou, Maria C. Asensio, and Matthias Batzill. Direct Observation of Interlayer Hybridization and Dirac Relativistic Carriers in Graphene/MoS_2 van der Waals Heterostructures. *Nano Letters*, 15(2):1135–1140, 2015. PMID: 25629211.

[122] Neil R. Wilson, Paul V. Nguyen, Kyle Seyler, Pasqual Rivera, Alexander J. Marsden, Zachary P. L. Laker, Gabriel C. Constantinescu, Viktor Kandyba, Alexei Barinov, Nicholas D. M. Hine, Xiaodong Xu, and David H. Cobden. Determination of band offsets, hybridization, and exciton binding in 2D semiconductor heterostructures. *Science Advances*, 3(2):e1601832, 2017.

[123] Yufeng Liang, Shouting Huang, Ryan Soklaski, and Li Yang. Quasiparticle band-edge energy and band offsets of monolayer of molybdenum and tungsten chalcogenides. *Applied physics letters*, 103(4), 2013.

[124] Young-Jun Yu, Yue Zhao, Sunmin Ryu, Louis E. Brus, Kwang S. Kim, and Philip Kim. Tuning the Graphene Work Function by Electric Field Effect. *Nano Letters*, 9(10):3430–3434, 2009. PMID: 19719145.

[125] Guillaume Froehlicher, Etienne Lorchat, and Stéphane Berciaud. Charge Versus Energy Transfer in Atomically Thin Graphene-Transition Metal Dichalcogenide van der Waals Heterostructures. *Physical Review X*, 8, 01 2018.

[126] Carino Ferrante, Giorgio Di Battista, Luis E Parra López, Giovanni Batignani, Etienne Lorchat, Alessandra Virga, Stéphane Berciaud, and Tullio Scopigno. Picosecond energy transfer in a transition metal dichalcogenide–graphene heterostructure revealed by transient raman spectroscopy. *Proceedings of the National Academy of Sciences*, 119(15):e2119726119, 2022.

[127] Maurizia Palummo, Marco Bernardi, and Jeffrey C. Grossman. Exciton Radiative Lifetimes in Two-Dimensional Transition Metal Dichalcogenides. *Nano Letters*, 15(5):2794–2800, 2015. PMID: 25798735.

[128] Andres Castellanos-Gomez, Michele Buscema, Rianda Molenaar, Vibhor Singh, Laurens Janssen, Herre S J van der Zant, and Gary A Steele. Deterministic transfer of

two-dimensional materials by all-dry viscoelastic stamping. *2D Materials*, 1(1):011002, apr 2014.

[129] PJ Zomer, MHD Guimarães, JC Brant, N Tombros, and BJ Van Wees. Fast pick up technique for high quality heterostructures of bilayer graphene and hexagonal boron nitride. *Applied Physics Letters*, 105(1), 2014.

[130] D Kwabena Bediako, Mehdi Rezaee, Hyobin Yoo, Daniel T Larson, SY Frank Zhao, Takashi Taniguchi, Kenji Watanabe, Tina L Brower-Thomas, Efthimios Kaxiras, and Philip Kim. Heterointerface effects in the electrointercalation of van der waals heterostructures. *Nature*, 558(7710):425–429, 2018.

[131] Zhujun Huang, Abdullah Alharbi, William Mayer, Edoardo Cuniberto, Takashi Taniguchi, Kenji Watanabe, Javad Shabani, and Davood Shahrjerdi. Versatile construction of van der Waals heterostructures using a dual-function polymeric film. *Nature communications*, 11(1):3029, 2020.

[132] Lukas Novotny and Bert Hecht. *Principles of Nano-Optics.* Cambridge University Press, 2nd edition, 2012.

[133] E. Abbe. Beiträge zur theorie des mikroskops und der mikroskopischen wahrnehmung. *Archiv für Mikroskopische Anatomie*, 9:413–468, 1873.

[134] Š. Kos, M. Achermann, V. I. Klimov, and D. L. Smith. Different regimes of förster-type energy transfer between an epitaxial quantum well and a proximal monolayer of semiconductor nanocrystals. *Phys. Rev. B*, 71:205309, May 2005.

[135] Zheyuan Chen, Stéphane Berciaud, Colin Nuckolls, Tony F. Heinz, and Louis E. Brus. Energy Transfer from Individual Semiconductor Nanocrystals to Graphene. *ACS Nano*, 4(5):2964–2968, 2010. PMID: 20402475.

[136] Archana Raja, Andrés Montoya-Castillo, Johanna Zultak, Xiao-Xiao Zhang, Ziliang Ye, Cyrielle Roquelet, Daniel A. Chenet, Arend M. van der Zande, Pinshane Huang, Steffen Jockusch, James Hone, David R. Reichman, Louis E. Brus, and Tony F. Heinz. Energy Transfer from Quantum Dots to Graphene and MoS_2: The Role of Absorption and Screening in Two-Dimensional Materials. *Nano Letters*, 16(4):2328–2333, 2016. PMID: 26928675.

[137] R. S. Swathi and K. L. Sebastian. Resonance energy transfer from a dye molecule to graphene. *The Journal of Chemical Physics*, 129(5):054703, 2008.

[138] RS Swathi and KL Sebastian. Long range resonance energy transfer from a dye molecule to graphene has (distance)- 4 dependence. *The Journal of chemical physics*, 130(8), 2009.

[139] Yansheng Liu, Miguel Angel Niño Ortí, Feng Luo, and Reinhold Wannemacher. Electrical control of förster resonant energy transfer across single-layer graphene. *Nanophotonics*, 11(14):3247–3256, 2022.

[140] Sunmin Ryu, Li Liu, Stephane Berciaud, Young-Jun Yu, Haitao Liu, Philip Kim, George W. Flynn, and Louis E. Brus. Atmospheric Oxygen Binding and Hole Doping in Deformed Graphene on a SiO_2 Substrate. *Nano Letters*, 10(12):4944–4951, 2010.

[141] Sefaattin Tongay, Jian Zhou, Can Ataca, Jonathan Liu, Jeong Seuk Kang, Tyler S. Matthews, Long You, Jingbo Li, Jeffrey C. Grossman, and Junqiao Wu. Broad-Range Modulation of Light Emission in Two-Dimensional Semiconductors by Molecular Physisorption Gating. *Nano Letters*, 13(6):2831–2836, 2013. PMID: 23627637.

[142] Sven Aeschlimann, Antonio Rossi, Mariana Chávez-Cervantes, Razvan Krause, Benito Arnoldi, Benjamin Stadtmüller, Martin Aeschlimann, Stiven Forti, Filippo Fabbri, Camilla Coletti, and Isabella Gierz. Direct evidence for efficient ultrafast charge separation in epitaxial WS_2/graphene heterostructures. *Science Advances*, 6(20):eaay0761, 2020.

[143] R. Krause, S. Aeschlimann, M. Chávez-Cervantes, R. Perea-Causin, S. Brem, E. Malic, S. Forti, F. Fabbri, C. Coletti, and I. Gierz. Microscopic Understanding of Ultrafast Charge Transfer in van der Waals Heterostructures. *Phys. Rev. Lett.*, 127:276401, Dec 2021.

[144] Niklas Hofmann, Leonard Weigl, Johannes Gradl, Neeraj Mishra, Giorgio Orlandini, Stiven Forti, Camilla Coletti, Simone Latini, Lede Xian, Angel Rubio, et al. Link between interlayer hybridization and ultrafast charge transfer in WS_2-graphene heterostructures. *2D Materials*, 2023.

[145] Th. Förster. Zwischenmolekulare energiewanderung und fluoreszenz. *Annalen der Physik*, 437(1-2):55–75, 1948.

[146] D. L. Dexter. A theory of sensitized luminescence in solids. *The Journal of Chemical Physics*, 21(5):836–850, 1953.

[147] Alexander Govorov, Pedro Ludwig Hernández Martínez, and Hilmi Volkan Demir. *Understanding and Modeling Förster-type Resonance Energy Transfer (FRET): Introduction to FRET, Vol. 1.* Springer, 2016.

[148] Ermin Malic, Heiko Appel, Oliver T. Hofmann, and Angel Rubio. Förster-Induced Energy Transfer in Functionalized Graphene. *The Journal of Physical Chemistry C*, 118(17):9283–9289, 2014.

[149] Malte Selig, Ermin Malic, Kwang Jun Ahn, Norbert Koch, and Andreas Knorr. Theory of optically induced förster coupling in van der Waals coupled heterostructures. *Phys. Rev. B*, 99:035420, Jan 2019.

[150] Lara Greten, Robert Salzwedel, Manuel Katzer, Henry Mittenzwey, Dominik Christiansen, Andreas Knorr, and Malte Selig. Dipolar Coupling at Interfaces of Ultrathin Semiconductors, Semimetals, Plasmonic Nanoparticles, and Molecules. *physica status solidi (a)*, 221(1):2300102, 2024.

[151] Shuo Dong, Samuel Beaulieu, Malte Selig, Philipp Rosenzweig, Dominik Christiansen, Tommaso Pincelli, Maciej Dendzik, Jonas D Ziegler, Julian Maklar, R Patrick Xian, et al. Observation of ultrafast interfacial Meitner-Auger energy transfer in a van der Waals heterostructure. *Nature Communications*, 14(1):5057, 2023.

[152] Shuo Dong, Michele Puppin, Tommaso Pincelli, Samuel Beaulieu, Dominik Christiansen, Hannes Hübener, Christopher W. Nicholson, Rui Patrick Xian, Maciej Dendzik, Yunpei Deng, Yoav William Windsor, Malte Selig, Ermin Malic, Angel Rubio, Andreas Knorr, Martin Wolf, Laurenz Rettig, and Ralph Ernstorfer. Direct measurement of key exciton properties: Energy, dynamics, and spatial distribution of the wave function. *Natural Sciences*, 1(1):e10010, 2021.

[153] Jiaqi He, Nardeep Kumar, Matthew Z Bellus, Hsin-Ying Chiu, Dawei He, Yongsheng Wang, and Hui Zhao. Electron transfer and coupling in graphene–tungsten disulfide van der Waals heterostructures. *Nature communications*, 5(1):5622, 2014.

[154] Zongpeng Song, Haiou Zhu, Wentao Shi, Dalin Sun, and Shuangchen Ruan. Ultrafast charge transfer in graphene-WS_2 van der Waals heterostructures. *Optik*, 174:62–67, 2018.

[155] Duan Luo, Jian Tang, Xiaozhe Shen, Fuhao Ji, Jie Yang, Stephen Weathersby, Michael E. Kozina, Zhijiang Chen, Jun Xiao, Yusen Ye, Ting Cao, Guangyu Zhang, Xijie Wang, and Aaron M. Lindenberg. Twist-Angle-Dependent Ultrafast Charge Transfer in MoS_2-Graphene van der Waals Heterostructures. *Nano Letters*, 21(19):8051–8057, 2021. PMID: 34529439.

[156] Ming-Fu Lin, Vidya Kochat, Aravind Krishnamoorthy, Lindsay Bassman Oftelie, Clemens Weninger, Qiang Zheng, Xiang Zhang, Amey Apte, Chandra Sekhar Tiwary, Xiaozhe Shen, et al. Ultrafast non-radiative dynamics of atomically thin $MoSe_2$. *Nature communications*, 8(1):1745, 2017.

[157] Shuai Fu, Indy du Fossé, Xiaoyu Jia, Jingyin Xu, Xiaoqing Yu, Heng Zhang, Wenhao Zheng, Sven Krasel, Zongping Chen, Zhiming M. Wang, Klaas-Jan Tielrooij, Mischa Bonn, Arjan J. Houtepen, and Hai I. Wang. Long-lived charge separation following pump-wavelength dependent ultrafast charge transfer in graphene/WS_2 heterostructures. *Science Advances*, 7(9):eabd9061, 2021.

[158] E. M. Purcell. Spontaneous Emission Probabilities at Radio Frequencies. *Physical Review*, 69:681, 1946.

[159] Chad Ropp, Zachary Cummins, Sanghee Nah, John T Fourkas, Benjamin Shapiro, and Edo Waks. Nanoscale imaging and spontaneous emission control with a single nano-positioned quantum dot. *Nature Communications*, 4(1):1447, 2013.

[160] Kerry J Vahala. Optical microcavities. *nature*, 424(6950):839–846, 2003.

[161] Galina Khitrova, HM Gibbs, M Kira, Stephan W Koch, and Axel Scherer. Vacuum Rabi splitting in semiconductors. *Nature physics*, 2(2):81–90, 2006.

[162] C. Robert, M. A. Semina, F. Cadiz, M. Manca, E. Courtade, T. Taniguchi, K. Watanabe, H. Cai, S. Tongay, B. Lassagne, P. Renucci, T. Amand, X. Marie, M. M. Glazov, and B. Urbaszek. Optical spectroscopy of excited exciton states in MoS_2 monolayers in van der Waals heterostructures. *Phys. Rev. Mater.*, 2:011001, Jan 2018.

[163] Yilei Li, Alexey Chernikov, Xian Zhang, Albert Rigosi, Heather M. Hill, Arend M. van der Zande, Daniel A. Chenet, En-Min Shih, James Hone, and Tony F. Heinz. Measurement of the optical dielectric function of monolayer transition-metal dichalcogenides: MoS_2, $MoSe_2$, WS_2, and WSe_2. *Phys. Rev. B*, 90:205422, Nov 2014.

[164] Ryan J Gelly, Dylan Renaud, Xing Liao, Benjamin Pingault, Stefan Bogdanovic, Giovanni Scuri, Kenji Watanabe, Takashi Taniguchi, Bernhard Urbaszek, Hongkun Park, et al. Probing dark exciton navigation through a local strain landscape in a WSe_2 monolayer. *Nature Communications*, 13(1):232, 2022.

[165] Axel Esser, Erich Runge, Roland Zimmermann, and Wolfgang Langbein. Photoluminescence and radiative lifetime of trions in GaAs quantum wells. *Phys. Rev. B*, 62:8232–8239, Sep 2000.

[166] Gang Wang, Iann C Gerber, Louis Bouet, Delphine Lagarde, Andrea Balocchi, Maël Vidal, Thierry Amand, Xavier Marie, and Bernhard Urbaszek. Exciton states in monolayer $MoSe_2$: impact on interband transitions. *2D Materials*, 2(4):045005, 2015.

[167] B. Han, C. Robert, E. Courtade, M. Manca, S. Shree, T. Amand, P. Renucci, T. Taniguchi, K. Watanabe, X. Marie, L. E. Golub, M. M. Glazov, and B. Urbaszek. Exciton States in Monolayer $MoSe_2$ and $MoTe_2$ Probed by Upconversion Spectroscopy. *Phys. Rev. X*, 8:031073, Sep 2018.

[168] M Goryca, Jing Li, Andreas V Stier, Takashi Taniguchi, Kenji Watanabe, Emmanuel Courtade, Shivangi Shree, Cedric Robert, Bernhard Urbaszek, Xavier Marie, et al. Revealing exciton masses and dielectric properties of monolayer semiconductors with high magnetic fields. *Nature communications*, 10(1):4172, 2019.

[169] Archana Raja, Andrey Chaves, Jaeeun Yu, Ghidewon Arefe, Heather M. Hill, Albert F. Rigosi, Timothy C. Berkelbach, Philipp Nagler, Christian Schüller, Tobias Korn, Colin Nuckolls, James Hone, Louis E. Brus, Tony F. Heinz, David R. Reichman, and Alexey Chernikov. Coulomb engineering of the bandgap and excitons in two-dimensional materials. *Nature Communications*, 8(1):15251, May 2017.

[170] Jun Yan, Yuanbo Zhang, Philip Kim, and Aron Pinczuk. Electric Field Effect Tuning of Electron-Phonon Coupling in Graphene. *Phys. Rev. Lett.*, 98:166802, Apr 2007.

[171] Andrew C. Crowther, Amanda Ghassaei, Naeyoung Jung, and Louis E. Brus. Strong Charge-Transfer Doping of 1 to 10 Layer Graphene by NO_2. *ACS Nano*, 6(2):1865–1875, 2012. PMID: 22276666.

[172] Zheyuan Chen, Pierre Darancet, Lei Wang, Andrew C. Crowther, Yuanda Gao, Cory R. Dean, Takashi Taniguchi, Kenji Watanabe, James Hone, Chris A. Marianetti,

and Louis E. Brus. Physical Adsorption and Charge Transfer of Molecular Br_2 on Graphene. *ACS Nano*, 8(3):2943–2950, 2014. PMID: 24528378.

[173] Romain Parret, Matthieu Paillet, Jean-Roch Huntzinger, Denise Nakabayashi, Thierry Michel, Antoine Tiberj, Jean-Louis Sauvajol, and Ahmed A. Zahab. In Situ Raman Probing of Graphene over a Broad Doping Range upon Rubidium Vapor Exposure. *ACS Nano*, 7(1):165–173, 2013. PMID: 23194077.

[174] M. S. Dresselhaus and G. Dresselhaus. Intercalation compounds of graphite. *Advances in Physics*, 51(1):1–186, 2002.

[175] Weijie Zhao, Ping Heng Tan, Jian Liu, and Andrea C. Ferrari. Intercalation of Few-Layer Graphite Flakes with $FeCl_3$: Raman Determination of Fermi level, layer by layer decoupling, and stability. *Journal of the American Chemical Society*, 133(15):5941–5946, 2011. PMID: 21434632.

[176] Guangliang Hu, Gaind P. Pandey, Qingfeng Liu, Radhika S. Anaredy, Chunrui Ma, Ming Liu, Jun Li, Scott K. Shaw, and Judy Wu. Self-Organization of Ions at the Interface between Graphene and Ionic Liquid DEME-TFSI. *ACS Applied Materials & Interfaces*, 9(40):35437–35443, 2017. PMID: 28920423.

[177] Xiaoyu Jia, Min Hu, Karuppasamy Soundarapandian, Xiaoqing Yu, Zhaoyang Liu, Zongping Chen, Akimitsu Narita, Klaus Müllen, Frank H. L. Koppens, Jun Jiang, Klaas-Jan Tielrooij, Mischa Bonn, and Hai I. Wang. Kinetic Ionic Permeation and Interfacial Doping of Supported Graphene. *Nano Letters*, 19(12):9029–9036, 2019. PMID: 31742413.

[178] Matin Amani, Der-Hsien Lien, Daisuke Kiriya, Jun Xiao, Angelica Azcatl, Jiyoung Noh, Surabhi R Madhvapathy, Rafik Addou, Santosh Kc, Madan Dubey, et al. Near-unity photoluminescence quantum yield in MoS_2. *Science*, 350(6264):1065–1068, 2015.

[179] Marc Philippi, Ignacio Gutiérrez-Lezama, Nicolas Ubrig, and Alberto F Morpurgo. Lithium-ion conducting glass ceramics for electrostatic gating. *Applied Physics Letters*, 113(3), 2018.

[180] Md Hasibul Alam, Zifan Xu, Sayema Chowdhury, Zhanzhi Jiang, Deepyanti Taneja, Sanjay K Banerjee, Keji Lai, Maria Helena Braga, and Deji Akinwande. Lithium-ion electrolytic substrates for sub-1v high-performance transition metal dichalcogenide transistors and amplifiers. *Nature communications*, 11(1):3203, 2020.

[181] Andrea Paradisi, Johan Biscaras, and Abhay Shukla. Space charge induced electrostatic doping of two-dimensional materials: graphene as a case study. *Applied Physics Letters*, 107(14), 2015.

[182] J. Schoonman, G. Oversluizen, and K.E.D. Wapenaar. Solid electrolyte properties of LaF_3. *Solid State Ionics*, 1(3):211–221, 1980.

[183] A. Sher, R. Solomon, K. Lee, and M. W. Muller. Transport properties of LaF_3. *Phys. Rev.*, 144:593–604, Apr 1966.

[184] C. Hoff, H.-D. Wiemhöfer, O. Glumov, and I.V. Murin. Orientation dependence of the ionic conductivity in single crystals of lanthanum and cerium trifluoride. *Solid State Ionics*, 101-103:445–449, 1997.

[185] Chun-Lan Wu, Hongtao Yuan, Yanbin Li, Yongji Gong, Harold Y. Hwang, and Yi Cui. Gate-Induced Metal–Insulator Transition in MoS_2 by Solid Superionic Conductor LaF_3. *Nano Letters*, 18(4):2387–2392, 2018. PMID: 29580055.

[186] Ulrich NOUMBE NGUETCHUISSI. *2D materials, colloidal nanocrystals and mixed dimensional van der Waals heterostructures for nanoelectronics and optoelectronics in high doping regime*. PhD thesis, Université de Strasbourg, 11 2020.

[187] Serge Luryi. Quantum capacitance devices. *Applied Physics Letters*, 52(6):501–503, February 1988.

[188] D.A. Jones and W.A. Shand. Crystal growth of flourides in the lanthanide series. *Journal of Crystal Growth*, 2(6):361–368, 1968.

[189] Michael J. D. Brand and Garry A. Rechnitz. Mechanistic studies on crystal-membrane ion-selective electrodes. *Analytical Chemistry*, 42(4):478–483, 1970.

[190] Shinobu Fujihara, Takayoshi Kato, and Toshio Kimura. Sol–Gel Synthesis of Silica-Based Oxyfluoride Glass-Ceramic Thin Films: Incorporation of Eu_3^+ Activators into Crystallites. *Journal of the American Ceramic Society*, 84(11):2716–2718, 2001.

[191] Larisa B. Gulina, Valeri P. Tolstoy, Igor A. Kasatkin, Ilya E. Kolesnikov, and Denis V. Danilov. Formation of oriented LaF_3 and LaF_3:Eu_3^+ nanocrystals at the gas - Solution interface. *Journal of Fluorine Chemistry*, 200:18–23, 2017.

[192] Emille M. Rodrigues, Ernesto R. Souza, Jorge H. S. K. Monteiro, Rafael D. L. Gaspar, Italo O. Mazali, and Fernando A. Sigoli. Non-stabilized europium-doped lanthanum oxyfluoride and fluoride nanoparticles well dispersed in thin silica films. *J. Mater. Chem.*, 22:24109–24123, 2012.

[193] Duhee Yoon, Dongchan Jeong, Hu-Jong Lee, Riichiro Saito, Young-Woo Son, Hyun Cheol Lee, and Hyeonsik Cheong. Fano resonance in Raman scattering of graphene. *Carbon*, 61:373–378, 2013.

[194] C. A. Howard, M. P. M. Dean, and F. Withers. Phonons in potassium-doped graphene: The effects of electron-phonon interactions, dimensionality, and adatom ordering. *Phys. Rev. B*, 84:241404, Dec 2011.

[195] U. Fano. Effects of Configuration Interaction on Intensities and Phase Shifts. *Phys. Rev.*, 124:1866–1878, Dec 1961.

[196] Eddwi H. Hasdeo, Ahmad R. T. Nugraha, Mildred S. Dresselhaus, and Riichiro Saito. Breit-Wigner-Fano line shapes in Raman spectra of graphene. *Phys. Rev. B*, 90:245140, Dec 2014.

[197] Qiuzi Li, E. H. Hwang, and S. Das Sarma. Disorder-induced temperature-dependent transport in graphene: Puddles, impurities, activation, and diffusion. *Phys. Rev. B*, 84:115442, Sep 2011.

[198] Loïc Moczko, Sven Reichardt, Aditya Singh, Xin Zhang, Luis E. Parra López, Joanna L. P. Wolff, Aditi Raman Moghe, Etienne Lorchat, Rajendra Singh, Kenji Watanabe, Takashi Taniguchi, Hicham Majjad, Michelangelo Romeo, Arnaud Gloppe, Ludger Wirtz, and Stéphane Berciaud. Symmetry-dependent dielectric screening of optical phonons in monolayer graphene, 2023.

[199] Matthias Paur, Aday J Molina-Mendoza, Rudolf Bratschitsch, Kenji Watanabe, Takashi Taniguchi, and Thomas Mueller. Electroluminescence from multi-particle exciton complexes in transition metal dichalcogenide semiconductors. *Nature communications*, 10(1):1709, 2019.

[200] Shaimaa I Azzam, Kamyar Parto, and Galan Moody. Prospects and challenges of quantum emitters in 2D materials. *Applied Physics Letters*, 118(24), 2021.

[201] Luca Sortino, Panaiot G Zotev, Catherine L Phillips, Alistair J Brash, Javier Cambiasso, Elena Marensi, A Mark Fox, Stefan A Maier, Riccardo Sapienza, and Alexander I Tartakovskii. Bright single photon emitters with enhanced quantum efficiency in a two-dimensional semiconductor coupled with dielectric nano-antennas. *Nature communications*, 12(1):6063, 2021.

[202] Bruno Schuler, Katherine A. Cochrane, Christoph Kastl, Edward S. Barnard, Edward Wong, Nicholas J. Borys, Adam M. Schwartzberg, D. Frank Ogletree, F. Javier García de Abajo, and Alexander Weber-Bargioni. Electrically driven photon emission from individual atomic defects in monolayer WS_2. *Science Advances*, 6(38):eabb5988, 2020.

[203] Claudia Ruppert, Burak Aslan, and Tony F. Heinz. Optical Properties and Band Gap of Single- and Few-Layer $MoTe_2$ Crystals. *Nano Letters*, 14(11):6231–6236, 2014. PMID: 25302768.

[204] Ya-Qing Bie, Gabriele Grosso, Mikkel Heuck, Marco M Furchi, Yuan Cao, Jiabao Zheng, Darius Bunandar, Efren Navarro-Moratalla, Lin Zhou, Dmitri K Efetov, et al. A $MoTe_2$-based light-emitting diode and photodetector for silicon photonic integrated circuits. *Nature nanotechnology*, 12(12):1124–1129, 2017.

[205] P. Ma, N. Flöry, Y. Salamin, B. Baeuerle, A. Emboras, A. Josten, T. Taniguchi, K. Watanabe, L. Novotny, and J. Leuthold. Fast $MoTe_2$ Waveguide Photodetector with High Sensitivity at Telecommunication Wavelengths. *ACS Photonics*, 5(5):1846–1852, 2018.

Aditi Raman MOGHE

Interfacial coupling and electrical control of light-matter interactions in van der Waals heterostructures made of two-dimensional semiconductors and graphene

Résumé

Nous avons réalisé une étude fondamentale des interactions en champ proche dans des hétérostructures de van der Waals constituées de graphène et de dichalcogénures de métaux de transition (TMD), afin de contrôler les caractéristiques de photoluminescence de monocouches de TMD intégrées dans des hétérostructures TMD/graphène à densité de charge ajustable.

Afin d'étudier les mécanismes de transfert de charge et d’énergie en champ proche, des hétérostructures composées de monocouches de diséléniure de molybdène ($MoSe_2$) couplées à des feuillets de graphène épais de seulement quelques monocouches (N = 1 à 6) ont fabriquées par exfoliation mécanique et transfert. Nous avons alors sondé les états excitoniques de $MoSe_2$ par spectroscopie de photoluminescence (PL) et de photoluminescence résolue dans le temps (TRPL). L’évolution de l'énergie des excitons, de leur largeur de raie de photoluminescence et de leur durée de vie avec le nombre de couches de graphène adjacentes révèle que les interactions entre le $MoSe_2$ et le graphène sont à très courte portée (~ 1 nm), ce qui suggère une contribution importante des processus de transfert par effet tunnel.

Pour contrôler la photoluminescence d’une monocouche de $MoSe_2$ couplée au graphène et estimer les alignements de bandes entre $MoSe_2$ et le graphène, nous avons utilisé un verre ionique (LaF_3) en tant que substrat et matériau de grille. Le LaF_3 permet d’injecter réversiblement des charges (électrons et trous) dans le graphène et dans le $MoSe_2$ à des densités supérieures à 10^{13} cm^{-2} à température ambiante. Les densités de charge ont été estimées en utilisant la sensibilité des modes Raman du graphène au dopage. L’évolution, en fonction du dopage, de la photoluminescence de $MoSe_2$ et de l’hétérostructure graphène/$MoSe_2$, ainsi que des modes Raman du graphène a permis d’extraire des informations importantes sur les voies de recombinaison excitonique, les processus de transfert de charge et les alignements de bandes entre $MoSe_2$ et le graphène.

Mots clés : matériaux bidimensionnels, graphène, dichalcogénures de métaux de transition, hétérostructures de van der Waals, excitons, transfert de charge et d'énergie, couplage interfacial, spectroscopie de photoluminescence, spectroscopie Raman.

Résumé en anglais

We have performed a fundamental study of the near-field interactions in van der Waals heterostructures made from graphene and transition metal dichalcogenides (TMD), with the aim to control the light emission characteristics of TMD monolayers in charge-tunable TMD/graphene heterostructures.

In order to investigate near-field charge and energy transfer mechanisms, heterostructures made from monolayer molybdenum diselenide ($MoSe_2$) covering thin graphene of different thicknesses (N= 1 to 6 layers) were fabricated by mechanical exfoliation and transfer. The excitonic manifold of $MoSe_2$ was probed through photoluminescence (PL) and time-resolved photoluminescence (TRPL) spectroscopy. Through the dependence of the exciton energy, photoluminescence linewidth and lifetime on the number of underlying graphene layers, our work reveals that the interactions between $MoSe_2$ and graphene are very short range (~ 1 nm), suggesting a prominent contribution from charge tunnelling mediated processes.

To control the photoluminescence from the graphene/$MoSe_2$ heterostructure through charge doping and thereby estimate the band offsets between these materials, we have used an ionic glass (namely LaF_3) as a substrate and gating material. LaF_3 enables reversible injection of electrons and holes into graphene and $MoSe_2$ at densities greater than 10^{13} cm^{-2} at room temperature. Charge densities were estimated using the sensitivity of the Raman modes of graphene to doping. The dependence of the PL of $MoSe_2$ and graphene/$MoSe_2$ regions and of the Raman features of graphene on the doping level revealed details about exciton recombination pathways, charge transfer processes and band offsets.

Keywords: two-dimensional materials, graphene, transition metal dichalcogenides, van der Waals heterostructures, excitons, charge and energy transfer, interfacial coupling, photoluminescence spectroscopy, Raman spectroscopy.